
Hybrid systems of molecular ruthenium catalyst anchored on oxide films for water oxidation: Functionality of the interface

Dissertation

zur Erlangung des mathematisch-naturwissenschaftlichen Doktorgrades
'Doctor rerum naturalium'
der Georg-August-Universität Göttingen

im Promotionsprogramm ProPhys
der Georg-August University School of Science (GAUSS)

vorgelegt von

Julius Scholz

aus Berlin

Göttingen, 2017

Betreuungsausschuss:

Prof. Dr. Christian Jooß, Institut für Materialphysik

Prof. Dr. Franc Meyer, Institut für Anorganische Chemie

Prof. Dr. Martin Wenderoth, IV. Physikalisches Institut

Mitglieder der Prüfungskommission:

Referent: Prof. Dr. Christian Jooß, Institut für Materialphysik

Korreferent: Prof. Dr. Sven Schneider, Institut für Anorganische Chemie

Weitere Mitglieder der Prüfungskommission:

Prof. Dr. Vasily Moshnyaga, I. Physikalisches Institut

Prof. Dr. Inke Siewert, Institut für Anorganische Chemie

Dr. Martin Wenderoth, IV. Physikalisches Institut

Tag der mündlichen Prüfung: 26.06.2017

Contents

1	Introduction	5
2	Scientific Background	10
2.1	Oxygen evolution reaction on perovskites	10
2.2	Stability of hybrid systems for artificial photosynthesis	16
3	Rotating Ring-Disk Electrode Study of Oxygen Evolution at a Perovskite Surface: Correlating Activity to Manganese Concentration	22
3.1	Introduction	22
3.2	Experimental section	25
3.3	Results and Discussion	29
3.3.1	Physical Properties of LSMO Films.	31
3.3.2	Electrochemistry of Semiconducting LSMO.	32
3.3.3	Activity and Stability of LSMO during Oxygen Evolution.	35
3.3.4	Correlating Trends in OER Activity to Surface Composition of the Electrode.	40
3.4	Conclusions	45
4	Tailoring the oxygen evolution activity and stability using defect chemistry	47
4.1	Introduction	47
4.2	Results	49
4.2.1	Structural and electronic characterization	51
4.2.2	Electrochemical characterization	57
4.2.3	Stability characterization	59
4.3	Discussion	63
4.4	Materials and Methods	67
4.5	Conclusion	70
5	Backbone Immobilization of the Bis(bipyridyl)pyrazolate Diruthenium Catalyst for Electrochemical Water Oxidation	71
5.1	Introduction	72
5.2	Results and Discussion	75
5.3	Conclusions	89

6	Chasing the Achilles' Heel in Hybrid Systems of Diruthenium Water Oxidation Catalysts Anchored on Indium Tin Oxide: the Stability of the Anchor	91
6.1	Introduction	92
6.2	Results and discussion	94
6.3	Conclusion	108
7	Conclusion	111
8	Appendix A	116
8.1	Supporting information for chapter 3	116
8.1.1	Supporting discussion	124
8.1.2	Supporting Tables	130
8.2	Supporting information for chapter 4	134
9	Appendix B	147
9.1	Electrode preparation	147
9.2	Experimental Section	150
9.2.1	Electrochemistry	150
9.2.1.1	RRDE setup:	152
9.2.1.2	Water Oxidation Experiments:	160
9.2.2	XPS Measurements:	162
9.2.3	X-ray Absorption Spectroscopy:	163
9.2.4	Atomic force microscopy:	165
9.3	Discussion	166
10	Appendix C	170

1 Introduction

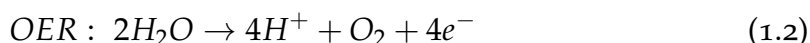
'On the arid lands there will spring up industrial colonies without smoke and without smokestacks; forests of glass tubes will extend over the plains and glass buildings will rise everywhere; inside of these will take place the photochemical processes that hitherto have been the guarded secret of the plants, but that will have been mastered by human industry which will know how to make them bear even more abundant fruit than nature, for nature is not in a hurry and mankind is.'

Giacomo Ciamician, Science, 36(926), 1912

This vision was not part of a science-fiction novel but the call of *Giacomo Ciamician* to enforce the effort towards photochemical, sustainable energy more than a century ago^[1]. The realization of a sustainable energy supply is more urgent than ever with ever growing population and energy demand, depletion of fossil fuel reserves and increasing effects of global warming - yet it still remains visionary. One of the approaches to obtain benign, renewable energy is provided by nature itself and is one of if not the most important reaction in the history of life on earth - photosynthesis.

Photosynthesis is the natural process to store photon energy in chemical bonds via several steps. The photochemical process requires the absorption of photons in photosystem II (PSII) to generate excited charge carriers that are used to drive the oxidation of water on one site and the reduction of carbon dioxide on the other site. Taking photosynthesis as blueprint, the most simplistic approach is the photochemical reaction of water splitting as it evolves gaseous oxygen and hydrogen which can be stored separately as fuel.

The water splitting reaction is a four electron process which can be separated in two half reactions of the hydrogen evolution reaction (HER) and the oxygen evolution reaction (OER) (shown for acidic media):



The overall reaction is predominantly limited by the sluggish kinetics of the half reaction of the OER fueling extensive research on numerous both homogeneous and heterogeneous catalysts for OER^[2-6]. To drive this reaction photochemically several steps analogous to photosynthesis are required: I) photon absorption to

generate excited charge carriers, II) separation of these excited charge carriers and their transport to the active site to III) drive the reaction. In nature, the processes are locally separated into different modules serving as antenna unit for absorption and a CaMn_4O_5 cluster as catalytic unit for the OER^[7]. Mimicking the natural blueprint, a device for photochemical watersplitting can therefore be separated into at least two modules according to the functionality: The absorber unit and the catalytic unit.

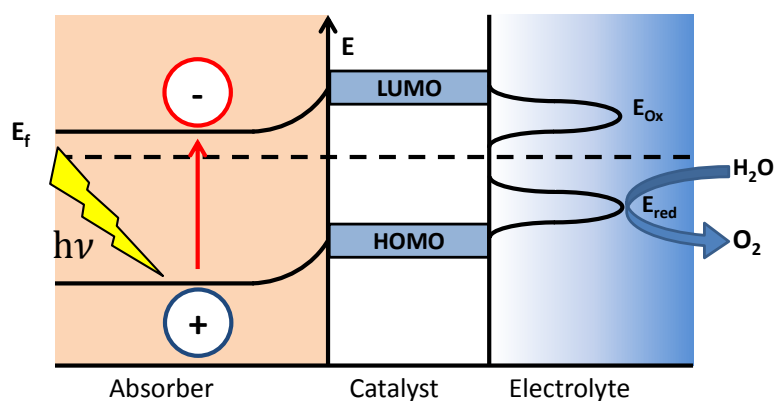


Figure 1.1: Schematic illustration showing the requirements on the electronic structure for a functional photoelectrochemical-cell involving an oxide absorber and a molecular catalyst

For targeted design of photocatalytic systems, one needs to consider the demands on the absorber and catalytic unit as well as their interplay allowing to chose and optimize the modules separately.

The essential parameters for a functional and efficient device are: The absorber should be able to harvest the energy of ideally the majority of the solar spectrum, which requires suitable absorption. While for an efficient absorption commonly the bandgap is optimized^[8], new results show that usable photon absorption is possible even without a bandgap^[9]. These new absorber materials are based on the employment of polaron quasiparticles arising from the strong electronic correlated properties of these materials. Here, electrons and the lattice phonons couple creating the polaron quasiparticle that give rise to the non-bandgap absorption properties. Regardless of the nature of the charge carriers, the absorption processes need to generate excited charges with a long life time. The long life times are required as the charges need to be transferred to the catalytically active site, therefore the transport properties within absorber, the catalyst and across the interface ought to be sufficient to enable the charge

transport.

The charge transport is directly related to the electronic structure and the band alignment between the catalyst and the absorber as schematically shown for an assembly of oxide absorber and molecular catalyst in Figure 1.1. As indicated, the band alignment relies on suitable band position for the absorber and catalyst to ensure efficient charge transfer. Moreover, a matching band position between the catalyst and the electrolyte is required in order to drive the water oxidation efficiently. In addition to the long life time of the excited charge carriers, the reaction rates of the catalyst need to be sufficiently fast to allow synchronization as well as to optimize the efficiency of the device. Lastly, both the absorber and the catalyst need to be stable for the realization of compatible photochemical devices. This includes both (i) the photostability i.e. stability throughout numerous absorption processes and chemical stability of the absorber as depending on the cell design the absorber is in contact to the working electrolyte/the working conditions and (ii) preservation of the active catalyst under reactive conditions.

Based on these requirements, different approaches have been made to realize photoelectrochemical devices for water splitting^[5,8,10–15]. The most simplistic design involves only one module - the photocatalyst directly absorbing the photon and driving the reaction^[8,16,17]. To date all photocatalysts face significant challenges such as stability and the synchronization between absorption and reaction time scales^[18–20]. To overcome these challenges the field of hybrid assemblies (dividing the device into modules according to the functionalities) use photoabsorbers, e.g. photosensitizers with various catalyst. Among the most prominent examples are purely molecular assemblies working under homogeneous conditions^[13,21,22] and the use of molecular sensitizers on oxide catalysts such as TiO₂^[12,23–25].

These approaches involve either the uncertainty of the electronic transport and intermediates or the slow reaction rates of heterogeneous catalysts. Starting from the developments of *T. J. Meyer* with the first molecular catalyst for water oxidation, the blue dimer^[26], extensive research gave rise to an ever growing zoo of molecular catalysts for the water oxidation. The high degree of structural flexibility offers unlimited tuning possibilities leading to reaction rates surpassing the reaction rates of the natural benchmark of PSII and the best heterogeneous catalyst by orders of magnitude^[27–29]. Note that among the most active catalysts, several are mononuclear complexes relying on cooperative effects. These cooperative effects make them incompatible to

serve as heterogeneous photoanode, e.g. as water splitting occurs through the coupling of two highly oxidized mononuclear ruthenium complexes^[28].

In order to serve as photoanode, the catalyst needs (i) to be equipped with the possibility to bind to the absorber to facilitate electron transfer (ET); (ii) preserve the reactivity upon immobilization; (iii) preserve the stability upon immobilization. Despite these challenging requirements, molecular catalysts are ideal candidates for photochemical cells by immobilization on the absorber combining the structural flexibility of a molecular complex with the advantages of reliable ET. Upon immobilization, the electron transfer would be facilitated and more reliable compared to homogenous systems through stable binding to the absorber. This reliable and stable ET is essential for the synchronization of reaction rates and life time of excited charge carriers. Despite the advantages, only few reports have been made on the implementation of said catalysts in a hybrid device to drive the reaction via photoexcitation.

The absorption via molecular photosensitizers (dyes) is limited by the low photostability of the dye and suffers from small accessible energy range of the absorption. Promising candidates for photostable absorbers are metal oxides as they are intrinsically stable against oxidative conditions (in alkaline media) as well as highly photostable. Moreover among these metal oxides the family of perovskites with the structure ABO_3 offers a broad range of properties. These properties arise from the strongly correlated electronic structure and involve optical absorption over a wide spectroscopical range that can be tuned via doping^[30–32]. Recent results showed that these excited polaronic charge carriers achieve life times on the nanosecond time scale^[9] making them promising candidates and alternatives to conventional semiconducting absorbers such as silicon.

In that context the presented thesis focuses on material system of the Ru based binuclear molecular catalyst developed by *F. Meyer* and the polaronic absorber $La_{0.6}Sr_{0.4}MnO_3$ (LSMO). The components were chosen (i) LSMO as absorber based on the tunable broad range absorption^[33] and (ii) a dinuclear ruthenium complex as catalyst as it is the chemically rugged (in acidic media), well characterized and the reaction takes place at one complex^[34–37]. The questions addressed in this thesis can be separated into two parts. The first part covers the properties of LSMO as substrate in the hybrid assembly both in respect to the background activity and the stability of the substrate under working conditions. The development of the rotating ring disk electrode (RRDE) setup as key experimental technique for epitaxial thin films allowed detailed analysis of

the reaction mechanism and corrosion pathways on stoichiometric LSMO (see chapter 3). Systematic studies of the role of defect chemistry were employed leading to the development of strategies to improve the stability of LSMO under working conditions (see chapter 4).

The second part focuses on the role of the molecular catalyst immobilized on solid support in collaboration with *J. Odrobina* and *F. Meyer*. The catalyst was immobilized on the model oxide electrode indium tin oxide (ITO) as proof of concept for the functional immobilization. In Chapter 5 the functionality upon immobilization including activity and stability is investigated. The central objective of chapter 6 is the interdependence of activity and stability with focus on the role of the interface. Systematic variation of the anchor group and thereby the interface led to a comprehensive understanding on the limitations of the stability under working conditions. The employed anchors showed the influence of the number of anchor groups with an increasing number of anchors not improving the binding as well as of the nature of the used anchor with the phosphonate anchor binding the strongest. Furthermore, the adaptation of the RRDE method allowed to evaluate the binding stability under operating conditions showing the competition between water oxidation and the oxidative anchor cleaving.

The presented results and methods open the door towards the combination of both modules to realize a photochemically driven device for water oxidation as well as the study of photon driven charge transfer dynamics in future work.

2 Scientific Background

The scientific background is separated into the two aspects of the chosen approaches: the evaluation of LSMO with respect to its function as a substrate and the evaluation of the immobilization of the molecular catalyst on an oxide model electrode. The use of manganites as the absorber and substrate for molecular catalysts implies that the primary function of the manganite will be photoabsorption. However, as the manganites are intended to serve as substrate, upon incomplete coverage the background activity for the OER and stability during the reactive conditions of the OER need to be evaluated. This is of particular interest as perovskites are among the most promising transition metal oxides for the OER within the focus of current research since they are made from abundant materials and show high activity^[38–42]. The following section highlights the biggest challenges in the understanding of activity and stability of these systems.

Molecular complexes immobilized on a solid support face significant challenges for the realization as an efficient hybrid device in the field of artificial photosynthesis: (i) the development of efficient and fast catalysts with high chemical stability and (ii) a stable binding/interface that allows fast electron transfer. The key objectives of this thesis is the characterization of the catalyst on the surface and the determination of the limitations of its stability. The determination both of the chemical stability and the stability of the binding between complex and solid support are central challenges within the community and will be introduced to elucidate the current understanding about the limitations.

2.1 Oxygen evolution reaction on perovskites

Research on metal oxides for oxygen catalysis pursued already more than a century ago, e.g. in^[43] and has gained more and more attention as they offer the perspective of cheap yet efficient catalyst in industrial applications. Along with simple metal oxides and oxide semiconductor the research of *Matsumoto*, *Trasatti*, *Bockris* and *Otagawa* focused in particular on perovskites^[39,44–46]. The family of perovskites with the general structure of ABO_3 offers a broad range of properties such as magnetic, absorption and electric properties that can be tuned via doping^[47]. The systematic research started attempting to identify the reaction mechanism and tailor the activity by control of the active site, which

sparked the fundamental experimental work on various perovskites.

In order to understand the challenge in the identification of the active sites and its limitations, one first needs to understand the desired reaction. The water oxidation can be summarized as a four step electron transfer reaction here exemplary shown for alkaline media (commonly used for oxide electrocatalysts): $4\text{OH}^- \rightarrow 2\text{H}_2\text{O} + \text{O}_2 + 4\text{e}^-$. The released electrons are typically used for hydrogen evolution, but due to the sluggish kinetics of the oxygen evolution, the improvement of the oxygen evolution remains the bottleneck for efficient water oxidation. This reaction proceeds through a four step reaction via the adsorption of hydroxide (OH^-) and different reaction intermediates to result in oxygen. The reaction and their intermediates are associated with energy barriers ideally lowered by the catalyst. However, upon unequal energy barriers, one reaction step will become rate limiting. This rate limiting step is experimentally accessible via Tafel analysis and the resulting Tafel slope can be modeled theoretically reflecting the reaction kinetics such as the rate limiting step^[48–50].

Additionally, the largest involved energy barrier will determine the required overpotential i.e. the potential that needs to be applied in addition to the standard *Nernstian* potential of 1.23 V (defined at pH 0) required to drive the reaction^[51]. The overpotential therefore relates to the overall activity of a catalyst and is assumed to mainly depend on the binding strength of the species involved in the reaction^[52]. Based on this assumption the highest activity requires an optimum between the adsorbates binding neither too strong nor too weak on the catalyst surface known as the *Sabatier* principle^[53]. Deviations from the optimum in binding strength of the adsorbates are one of the origins of the overpotential for the reaction (Figures 2.1A-B). Here, the respective energy barrier ΔG of each intermediate is depicted, which relates to the overpotential.

The procedure of the reaction depends on the reaction mechanism that itself is related to the nature of the active site. A detailed understanding of both mechanism and the active site is therefore posing one of the central challenges in today's catalyst research. First models for the reaction mechanism of the OER on perovskites have been proposed already by *Bockris*^[48] assuming the metal, specifically the B-site, as active site involving HO^* , HOO^* and O^* intermediates. Based on the assumption of a metal centered reaction mechanism, computational approaches using density functional theory (DFT) have been made. They model the reactions on systems ranging from simple metal oxides to perovskites^[52,54,55]. These calculations found fundamental scaling relations

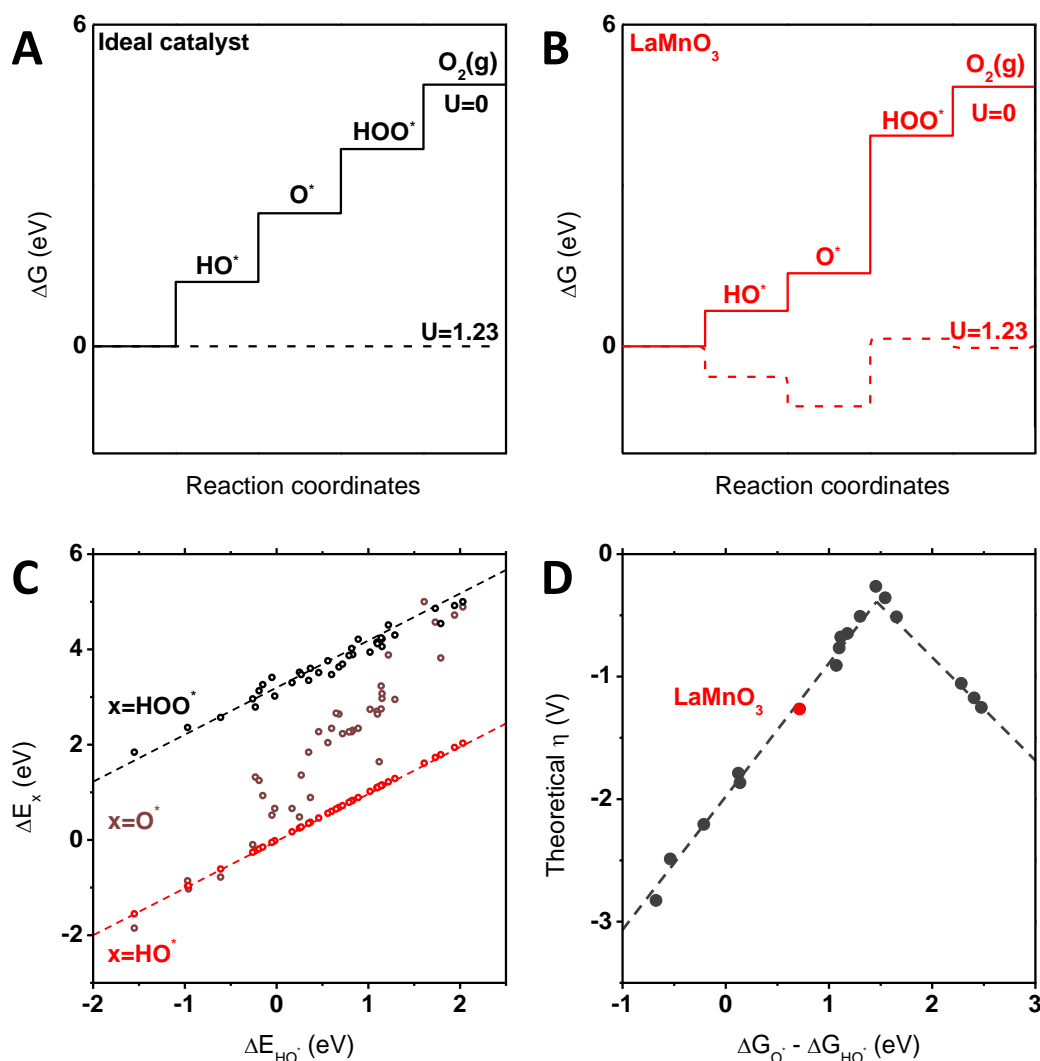


Figure 2.1: Schematic picture on the standard free energy of the four step reaction of the OER at zero potential on A) an ideal catalyst, B) on LaMnO_3 , C) Scaling relations of the free energy between the reaction intermediates on different perovskite surfaces, D) Theoretical overpotential based on the energy difference of the O^* and HO^* intermediates calculated by DFT on different perovskite surfaces. Figures based on data from [52].

for the aforementioned intermediates. The scaling relations define the difference in binding energy of $\Delta E_{O^*} - \Delta E_{HO^*}$ as an universal descriptor for the OER as *Rossmeisl* and coworkers found a linear scaling relation of 1:1 between the binding energy ΔE_{HO^*} and ΔE_{HOO^*} with an offset of $3.2 - 3.4 \text{ eV}^{[52]}$ and a 2:1 scaling relation between ΔE_{O^*} and $\Delta E_{HOO^*}^{[55]}$ shown in Figure 2.1C). The calculated energies for various oxides by *Man* et al.^[52] resulted in a volcano shape (commonly referred to as volcano plot) that can be seen in Figure 2.1D) illustrating the *Sabatier* principle. On the left hand side, the adsorbates are too strongly bound and on the right hand side too weakly bound. In correspondence to the overpotential, the scaling relation indicates the limitations of the reaction mechanism with the highest energy barrier corresponding to the potential determining step.

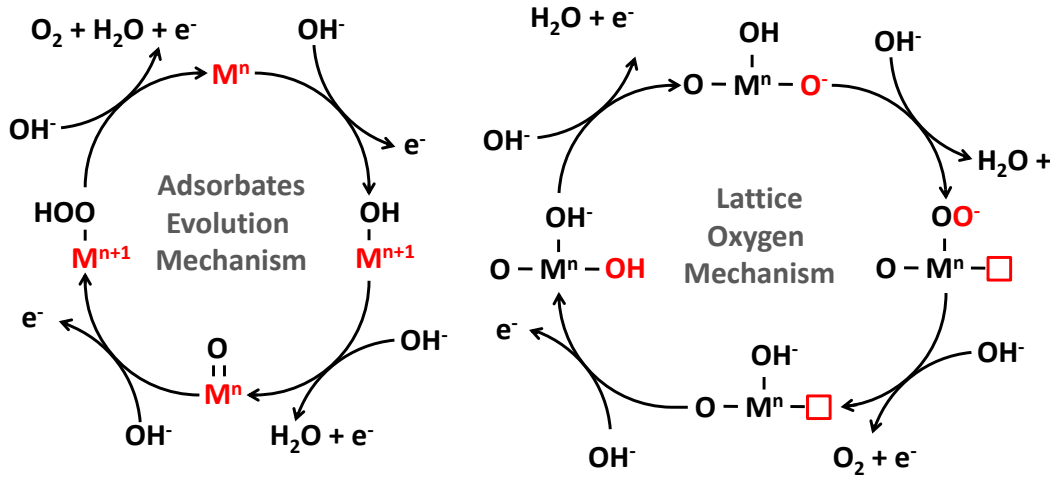


Figure 2.2: Schematic reaction schemes for the OER on perovskites based on the metal centered reaction mechanism^[52] and the redox active lattice oxygen mechanism^[56]. M denotes a transition metal and n its positive oxidation state.

The previously shown relations rely on the assumption of the reaction taking place on the B-site of the perovskite. Despite the frequently used assumption, experimental evidence for the B-site as active site for the OER has been scarce to date. The challenges in the determination of the active surface is reflected by simulations of *Rong* et al.^[57] suggesting that for $LaMnO_3$ the surface is changing throughout the reaction. The resulting active surface is formed regardless of the initial configuration as the surface reorganizes during catalysis including partial desolution^[57]. In addition in recent years an increasing number of reports indicate experimentally and theoretically that the lattice oxygen might participate as

active site in the OER on perovskites^[56,58–63]. Therefore the current understanding distinguishes at least between the two mechanisms for perovskites in alkaline media shown in Figure 2.2. Depicted are the metal centered reaction (adsorbates evolution mechanism) and the reaction involving lattice oxygen (lattice oxygen mechanism). Due to the redox active oxygen, the catalyst may become susceptible to corrosion as oxygen vacancy formation might destabilize the catalyst^[64–66]. With the objective to find universal scaling relations and descriptors for the catalytic activity starting with the first attempt for material specific descriptors by *Bockris*^[46] over numerous other studies^[41,56,59,67,68] led to the understanding that for the strongly correlated perovskites the complex interplay between the metal 3d and the oxygen 2p states modifies the reaction mechanism and thereby both the activity and stability (refer e.g. to^[63,67,69] for detailed discussion about the electron structure and their involvement in the reaction).

Stability of oxides during catalysis

Additional to high activity, the stability of a catalyst during catalysis is one of the major objectives and key challenges. Identification of limiting parameters and descriptors is particularly challenging as both the activity and stability depend on the configuration of the very surface. The nature of the present surface under the reactive conditions remains pivotal as the surface is prone to reconstruction^[57,70,71] and decomposition^[40,63,64,72–78]. The decomposition can proceed via partial dissolution, e.g. of the A-site limited to the surface or even extend throughout the bulk of the material, e.g. the formation of a new phase such as the superstructure shown in Figure 2.3. Irrespective of the length scale, even the partial dissolution on the surface can strongly affect the activity without bulk corrosion and might occur due to the surface reconstruction associated with the reaction^[57]. In other cases, the working conditions such as the electrolyte might be related to the bulk stability as neutral or even acidic pH is known to destabilize the perovskite structure^[40,63,72,74]. These trends might additionally be related to the chemical composition as the corrosion might be facilitated through the intrinsic differences in solubility^[79], phase separation^[63] or the formation of soluble species during the reaction^[64,73,75–78]. Furthermore, the active site and the corresponding reaction mechanism might be related to possible decomposition pathways and therefore reflect dependencies on the electronic structure, e.g. for the lattice oxygen mechanism^[56,59,63].

The redox active lattice oxygen mechanism involves the formation of oxygen vacancies (V_O) possibly destabilizing the catalyst upon incomplete recovery during the oxygen evolution. Depending on the reaction conditions and the material, the incomplete recovery of lattice oxygen might then proceed in the bulk and lead to amorphization frequently observed for materials with redox active oxygen^[59,63–65,74]. Recent studies suggest that the reaction mechanism is related to the relative position of the metal d states and the oxygen p states as well as their hybridization^[56,58–60,63,65] (schematically shown for perovskites Figure 2.3). Due to the involvement to the possible corrosion pathway, the position of the oxygen p states can serve as a measure for the stability with hybridized oxygen and metal states close to the *Fermi* level making the catalyst more susceptible for V_O formation (Figure 2.3).

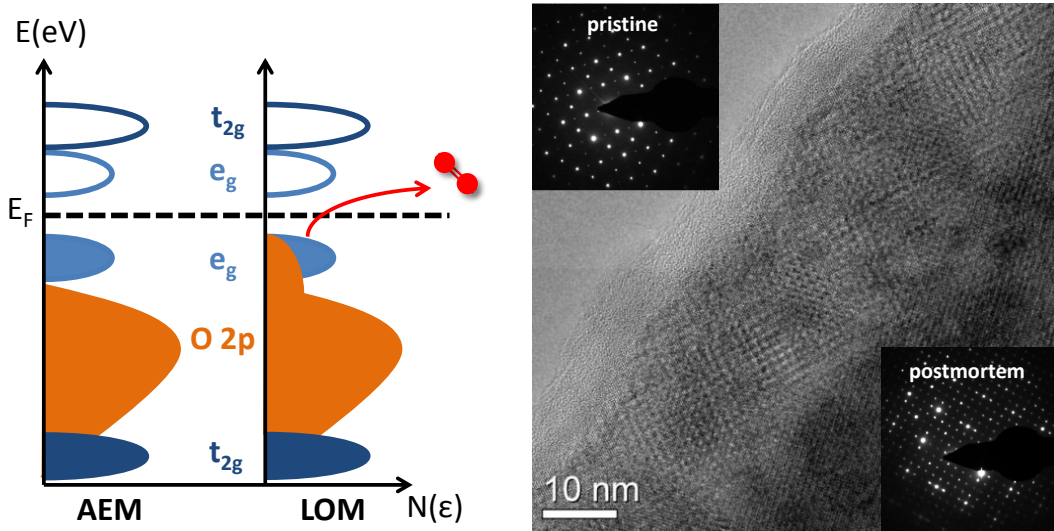


Figure 2.3: Left: Schematic representation of the configuration of the density of states for perovskites possibly resulting in either the metal centered reaction mechanism (AEM) or redox active lattice oxygen mechanism (LOM)^[58,59,62,63,69]. The formation of oxygen vacancies presumably as consequence of the LOM depends on hybridized metal e_g and oxygen 2p states near the *Fermi* energy. Right: High resolution TEM images showing a superstructure due to ordered oxygen vacancies in $\text{Pr}_{0.64}\text{Ca}_{0.36}\text{MnO}_3$. The oxygen vacancies were formed upon prolonged exposure to oxidizing conditions (details in^[62]). The superstructure of the vacancies can be seen in the insets showing selected area electron diffraction (SAED) images.

Despite the tremendous efforts and the importance in the elucidation of structural and electronic effects on the stability, these studies frequently consider ideal surfaces and catalysts. Due to preparation oxides commonly represent non-ideal

crystals as they experience structural defects such as impurities and vacancies which itself are known to affect the stability. These initially present defects and impurities may further influence the stability and activity in addition to the effects of reconstruction during water oxidation. Systematic studies on the effects induced by defects and impurities on stability and activity are limited to simple metals or metal oxides^[80–83]. The analysis of the defect structure alone in perovskites is complicated, as a broad variety of defect types such as interstitial, vacancies for all sites as well as substitutional defects are controversially discussed for perovskites^[84–87]. The defect types strongly depend not only on material system but also on the preparation method^[84–87] making the analysis of both the present defect types crucial for the analysis of the accompanying impact on the stability. The stability of the oxide surface is of particular interest with respect to the intended function as solid support for the molecular catalyst as the stability of the device directly relates to the stability of the substrate. Therefore, the analysis of both the reaction mechanism and the preparation induced defects for the material system at hand are essential for the deduction of universal descriptors that define the activity and the stability, but remain the paramount of the experimental challenges in catalysis research.

2.2 Stability of hybrid systems for artificial photosynthesis

For photoelectrochemical devices, hybrid systems with molecular catalysts immobilized on solid support represent promising model systems among the approaches. They offer the advantage of individual optimization, yet these hybrid systems face significant challenges. In addition to efficient and active molecular catalysts and a solid support with suitable absorption properties, the stability of the hybrid system remains the crucial task. For hybrid systems consisting of a solid support and a molecular catalyst one needs to distinguish the following factors contributing to the stability of the hybrid system:

- I. Stability of the substrate
- II. Stability of the catalyst
- III. Stability of the interface

The limitations of the components strongly depend on the material system as

well as the reaction conditions. In order to elucidate the role of each component they are addressed individually in the following.

The primary function of the substrate in terms of stability is to serve as support of the molecular catalysts providing reliable electron transfer. However, upon incomplete coverage of the support by the molecular catalyst, the substrate is in contact to the electrolyte. Thus the substrate is required to remain stable under the working conditions, i.e. strongly oxidizing or reducing conditions in addition to being chemically stable in the working electrolyte. These requirements complicate a suitable choice of the substrate as it strongly depends on the working conditions of the catalysts and the required properties of the substrate such as the absorption properties. Oxides are frequently used as substrates which are generally robust against oxidizing conditions but frequently unstable under acidic conditions^[40,88]. In addition to the bulk stability, the very surface of the oxide may undergo surface reconstruction as stated in the previous section which directly relates to the interface to the molecular complex and affects the stability on the surface. As the nature of the oxide surface was part of the previous section, only the aspects of the stability concerning the integrity of the molecular catalyst and the interface will be discussed in the following.

The harsh conditions of the electrolyte and the e.g. strongly oxidizing conditions of the desired reaction not only pose a significant challenge for the substrate but also for the molecular catalyst itself. For water oxidation, several reports illustrate the necessity for a chemically rugged ligand stable against oxidation, as the reaction pathway of the water oxidation involves high valent metal oxo species^[89]. These highly oxidized, highly reactive metal species, e.g. Ir and Ru, have the ability not only to drive the water oxidation but possibly also the oxidation of the backbone ligand^[89–92]. The oxidation or decomposition of the ligand leads to the formation of thermodynamically more stable metal oxide particles^[90–92]. These oxide particles itself can be very active as e.g. RuO₂ and IrO₂ are among the most active heterogeneous catalysts^[40,93–95]. Thus it is necessary to clarify the nature of the active catalyst as the molecular catalyst itself might only serve as precursor for the active catalyst^[90,96,97]. Additionally, the improvement the ligand design is a synthetic challenge in order to provide a high degree of chemical stability and therefore control over the active states of the catalyst.

One of the key descriptors commonly used to describe the stability of molecular catalysts is the turn over number (TON), i.e. the number of reaction cycles a catalyst can undergo before passivation or decomposition. Within the field of

molecular Ruthenium based catalyst recent progress led to activity exceeding and stability approaching the natural benchmark system of photosystem II^[98]. Note that the most active and stable molecular catalyst reported are homogeneous (in solution) catalyst and the properties of the immobilized catalysts might be altered due to competing processes such as formation of the surface bound species $\text{Ru-O}_{\text{surface}}$ thus passivating the active site during the reaction^[90]. The analysis of decomposition pathways and nature of the active catalysts is essential to determine stability defining parameters and provide objective benchmark parameters.

Once the stability of both the molecular catalyst and the substrate is achieved separately, the stability of the interface between the catalyst and the substrate still can be limiting for the activity of the hybrid system. Note that the activity of the anchored catalysts requires a reaction mechanism that does not rely on intermolecular interactions hence allowing the reaction solely on one molecular catalyst. Otherwise a sufficiently high degree of surface coverage would be required and the preservation of the reactivity might not be guaranteed. The stable link between catalyst and substrate is mandatory for efficient electron transfer determining the efficiency of (photo)-electrochemically active hybrid devices. Furthermore, the detailed configuration of the interface has significant consequences for the efficiency of the hybrid system as it strongly depends on the electronic structure of the interface^[99–101].

In order to establish a defined and stable interface, the complexes are frequently immobilized on the substrate via functional groups selected depending on the nature of the substrate (further addressed below)^[102]. For the employed oxide substrate, the stable anchoring under aqueous conditions is achieved most commonly by acid functional groups such as carboxylic and phosphonic acids^[103–107]. However, even for successful binding of complexes on substrates, the stability of the binding under reactive conditions is frequently suffering from desorption or decomposition of the anchor^[108–110], making the understanding of the possible degradation pathways essential.

The nature of the acid functional group implies that the binding strength is correlated to the pH value of the electrolyte as the H^+ and HO^- compete with the bonds of the oxide and the anchor group^[103]. The binding mode, e.g. three-fold covalently bound phosphonate anchor is not fixed but rather represents the equilibrium state between a broad range of possible configurations e.g. covalently bound to physisorbed and desorbing molecules. Therefore, a simplifying assumption could be that the more binding possibilities the anchor provides the

stability of the interface will increase^[103,111,112]. But besides the number of binding sites the number of acid functionalities relates to the solubility in aqueous conditions, which might facilitate leaching from the surface as the acid functionalities relate to the polarity of the molecule. The binding strength is also related to the resemblance of the used anchor and the substrate e.g. silane anchors will bind more stable on silicon based substrates such as SiO_2 than other substrates^[102]. The numerous dependencies illustrate the complications and experimental challenges defining the stability and the frequently uncovered role of the interface for hybrid systems. Therefore, the role of the interface in terms of stability is of utmost importance.

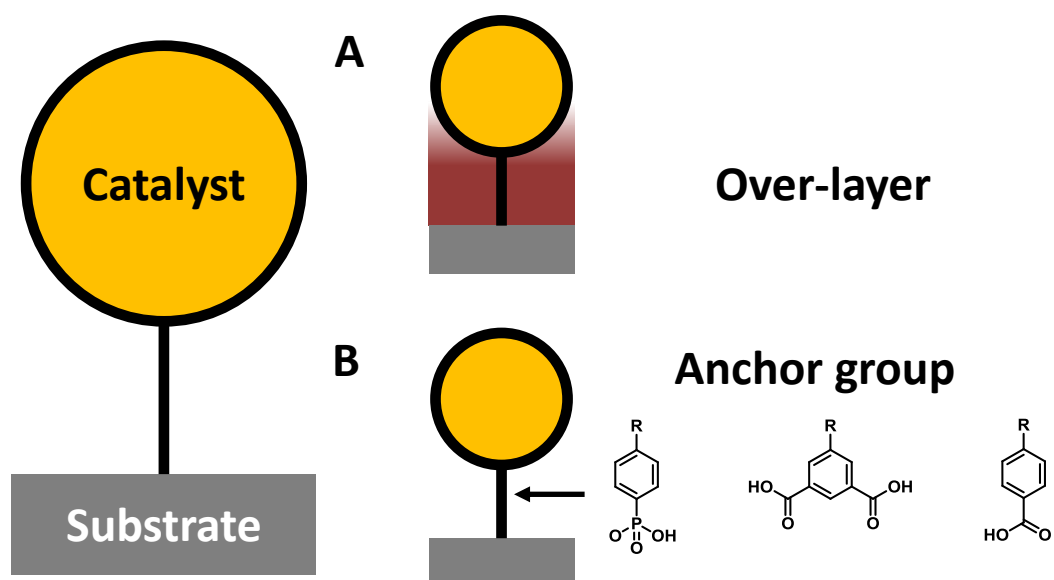


Figure 2.4: Illustration of strategies to improve the stability of hybrid assemblies targeting the interface; **A)** Use of over-layers such as TiO_2 and PMMA to avoid desorption, **B)** Modification of the binding mode by altering the anchoring groups of the molecular complex

Based on the displayed contributions to the stability of hybrid systems, several strategies have been published addressing specific limitations of the different systems. These strategies involve:

- I. Improve catalyst design to avoid decomposition of the ligand
- II. Hinder desorption by over-layers such as PMMA, TiO_2 , Al_2O_3
- III. Improve binding strength by altering the anchor and substrate

The strategies to improve catalyst design require in-depth understanding about the reaction mechanism and the corrosion pathways. The approaches besides

the synthetic approach are schematically depicted in Figure 2.4. The approach shown in Figure 2.4A) attempts to stabilize the anchored catalyst on the surface via additional stabilizing layers of polymers or oxides which cover the anchor groups. However, the increasing stability of the anchoring is accompanied with a drastic impact on the morphology of the hybrid making the resulting system structurally undefined and lead to a drop in WOC activity as the catalyst is covered as well^[113–115].

Directly targeting the stability of the interface, approaches involve variation of the substrate or the surface of the substrate and the use of different anchor groups. The benefit of the use of other anchor groups strongly depends on the used substrate and poses a synthetic challenge. For oxides, commonly acid functionalities^[102–107] provide the best binding, while for carbon based substrates non-covalent anchor groups binding via $\pi - \pi$ interaction provide stable binding^[116]. One of the benefits of the carbon based systems is the insoluble nature in aqueous solutions rendering dissolution negligible. Furthermore, both variation of the substrate and the variation of the anchor will also affect the activity as e.g. the electron transfer depends on the electronic interface^[99–101]. For example the commonly used phosphonate anchor is considered to bind more strongly on oxides than the carboxylate anchor but the ET might be faster for the latter^[103,112].

Finally, one strategy modifying the interface involves the variation of the substrate surface via pretreatment of the substrate by UV radiation, thermal treatment, and additives^[102,103]. These treatments might improve the stability but are not applicable to all material systems due to e.g. the limited thermal stability. Moreover, a detailed understanding on the effect of the treatment on stability is experimentally challenging and hardly addressed. In summary, the stability of hybrid systems consisting of molecular catalyst and solid support depends on various parameters and a detailed analysis is complicated as it involves the analysis of surface species ideally under operating conditions and represents the paramount of experimental objectives within the field.

Simplifying approaches are needed in order to obtain meaningful results. Here, the use of a highly defined and simple device design may help to overcome the experimental challenges. The options varying the oxide or the oxide surface are limited, e.g. by pretreatment based on the device design with the molecular catalyst being immobilized directly on the absorber. However, the interface can be studied by using a well known model system such as Indium-tin oxide (ITO) as solid support with established preparation tactics^[117–123] in combination with

the well characterized diruthenium molecular catalyst^[34–37]. Here, the interface can than be tuned with anchor groups established for the immobilization on oxides^[103–106,124] to make thorough analysis and the deduction of new guidelines possible.

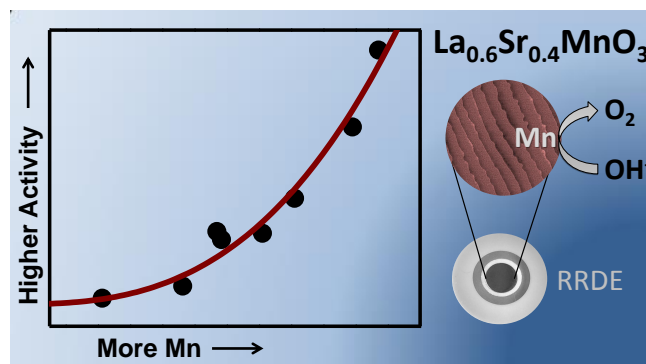
3 Rotating Ring-Disk Electrode Study of Oxygen Evolution at a Perovskite Surface: Correlating Activity to Manganese Concentration

J. Scholz, M. Risch, K. Stoerzinger, G. Wartner, Y. Shao-Horn, C. Jooss

Reproduced from journal of physical chemistry C **120**, 27746-27756, 2016

Abstract: Transition-metal oxides with the perovskite structure are promising catalysts to promote the kinetics of the oxygen evolution reaction (OER). To improve the activity and stability of these catalysts, a deeper understanding about the active site, the underlying reaction mechanism, and possible side reactions

is necessary. We chose smooth epitaxial (100)-oriented $\text{La}_{0.6}\text{Sr}_{0.4}\text{MnO}_3$ (LSMO) films grown on Nb:SrTiO_3 (STNO) as a model electrode to investigate OER activity and stability using the rotating ring-disk electrode (RRDE) method. Careful electrochemical characterization of various films in the thickness range between 10 and 200 nm yields an OER activity of the epitaxial LSMO surface of $100 \mu\text{A}/\text{cm}_{\text{ox}}^2$ at 1.65 V vs. RHE, which is among the highest reported for LSMO and close to (110)-oriented IrO_2 . Detailed post-mortem analysis using XPS, XRD, and AFM revealed the high structural and morphological stability of LSMO after OER. The observed correlation between activity and Mn vacancies on the surface suggested Mn as the active site for the OER in (100)-oriented LSMO, in contrast to similar perovskite manganites, such as $\text{Pr}_{1-x}\text{Ca}_x\text{MnO}_3$. The observed Tafel slope of about 60 mV/dec matches the theoretical prediction for a chemical rate-limiting step that follows an electrochemical pre-equilibrium, probably O-O bond formation. Our study established LSMO as an atomically flat oxide with high intrinsic activity and high stability.



3.1 Introduction

Water splitting represents a promising approach to use hydrogen bonds as energy carrier toward sustainable energy storage to replace the current use of fossil fuels. The water splitting reaction can be separated into two half-reactions, the

oxygen evolution reaction (OER), $2\text{H}_2\text{O} \rightarrow \text{O}_2 + 4\text{H}^+ + 4\text{e}^-$, and the hydrogen evolution reaction (HER), $4\text{H}^+ + 4\text{e}^- \rightarrow 2\text{H}_2$. Water splitting is mainly limited by the OER due to sluggish kinetics even for the most active materials^[3,4,40,125]. First-row transition-metal oxides are promising OER electrocatalysts^[38,39,41,42] because they can be made from relatively earth-abundant materials, such as Mn, Co, Fe, and Ni, with high OER activity comparable to those of the state-of-the-art catalysts based on precious metals, such as RuO_2 and IrO_2 ^[76,94,95,126]. In the perovskite structure ABO_3 , B-site transition-metal cations form a corner-sharing network of BO_6 octahedra. A-site doping allows for the control of B-site valence states as well of B-O bond length and tilt^[127,128]. The mechanism of OER on perovskite surfaces is not well understood and might differ from other OER catalysts, such as photosystem II or metal oxides with different crystal structure, as discussed in, for example, refs^[3] and^[129]. Much of the recent mechanistic insight is owed to DFT calculations^[52], which assume that the four-step electron-transfer reaction takes place at an active metal site (denoted by M in Scheme 3.1).

The free energy of each reaction step is determined by the binding energy

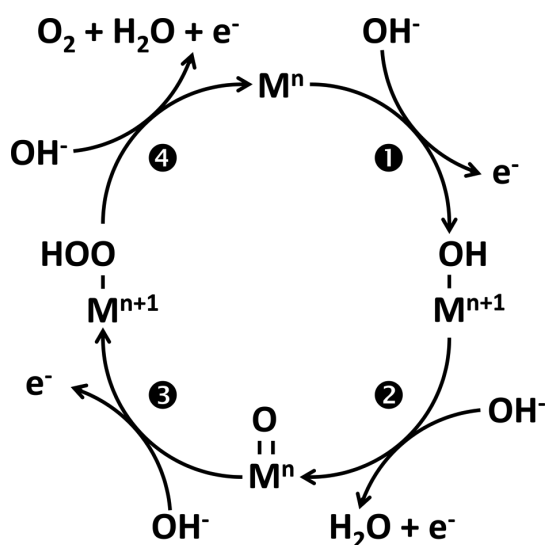


Figure 3.1: Hypothetical Reaction Mechanism of the OER on Perovskites written for Alkaline Media^[3,52]. M denotes a transition metal and n its (positive) oxidation state

between the metal-site atom and the oxygen atom of the M-OH, M-O, or M-OOH intermediates. For manganites, e.g., LaMnO_3 , such calculations predict that Mn oxidation followed by O-O bond formation (step 3) on a hypothetical M-O surface site is rate-determining^[52]. While not unambiguous, an experimental Tafel slope of ~ 60 mV/dec can be estimated for such a scenario.

However, the DFT calculations are based on a 'frozen surface' approximation, where electron-transfer-induced structure dynamics and formation of surface defects are disregarded. Yet, there also have been several recent reports for manganites and other oxides acknowledging the active role of lattice oxygen during OER^[56,58,59,61–63,130]. Participation of lattice oxygen results in a mechanism differing from that in Scheme 3.1, where redoxactive lattice oxygen or even surface oxygen vacancies may form alternative active sites for OER. Furthermore, experimental Tafel slopes larger than 60 mV/dec are frequently reported^[3,44,46,65,131,132], which indicates side reactions and/or a mechanism differing from that in Scheme 3.1. Therefore, a deeper understanding of the nature of the active site, the OER activity, and the OER mechanism of manganite electrodes is urgently required.

A detailed evaluation of both the activity and mechanisms requires the study of very well-defined model systems. For composite electrodes, where carbon additives are used to provide sufficient conductivity between the oxide and the support^[3,133], many carbon additives oxidize in typically investigated OER voltage ranges^[134], giving rise to background oxidation currents^[135]. Moreover, the OER activity and potentially the mechanism depend on the active surface facet of the oxide^[95,136], which is often unknown or undefined when catalyst powders are used. Electrodeposited oxide films avoid the problems of the carbon support (assuming complete coverage of the substrate), but the uncertainties of the electrochemically active surface area and crystallographic surface terminations persist. The investigation of well-defined flat epitaxial films with one single surface orientation allows for a reliable study of the activity of single facets^[95,137].

Furthermore, the implementation of epitaxial thin films in a rotating ring - disk - electrode (RRDE) setup gives insights into the correlation between electrochemical properties of the disk electrode and reaction products detected at the ring. This allows for discrimination between currents from catalysis and side reactions, for example, between electrochemical oxygen and peroxide formation, as demonstrated for Pt single crystals^[138,139]. While RRDE investigations of the OER kinetics for metal single crystals have been accessible, RRDE investigations on oxide materials have focused on ink-cast oxide particles or electrochemically deposited films on a conducting substrate^[40,56,94,126,140–142]. Hence, experiments with rotating epitaxial oxide films offer great opportunities to gain mechanistic insight into the activity of a single surface orientation under conditions of well-controlled surface chemistry.

In this study, we have chosen epitaxial $\text{La}_{0.6}\text{Sr}_{0.4}\text{MnO}_3$ (LSMO) grown on Nb:SrTiO_3 (STNO) to study the activity and mechanism of a model (100) perovskite surface with a RRDE. The semiconductor LSMO was selected because of its highly conductive nature and the well-established fabrication of atomically smooth epitaxial films^[143,144]. First, structural and chemical properties of as-grown LSMO thin films were characterized by X-ray diffraction, atomic force microscopy, and photoelectron spectroscopy. Second, the metal-like electrochemical behavior of the LSMO electrode with facile electron transfer was verified using the redox potentials of the ferri-/ferrocyanide redox reaction as a calibration standard. Third, the OER activity and stability of epitaxial LSMO was evaluated by cyclic voltammetry (CV) and chronoamperometry (CA). The comparison of the measured Tafel slopes of the LSMO disk and Pt ring electrodes in OER allowed us to evaluate the rate-limiting reaction step of the mechanism. No structural or morphological changes were found after chronoamperometry for 1 h. The post-mortem analysis of changes in the elemental composition of the surface revealed a change in the Mn surface concentration without formation of an amorphous surface phase. Our data implied Mn and not oxygen or oxygen vacancies as the active site for OER on LSMO.

3.2 Experimental section

Film Fabrication: $\text{La}_{0.6}\text{Sr}_{0.4}\text{MnO}_3$ (LSMO) electrodes used for electrochemical and electric measurements were prepared by ion-beam sputtering (IBS). Round 0.5 wt % Nb-doped SrTiO_3 (STNO) and rectangular undoped SrTiO_3 (STO) with (100) orientation (CrysTec GmbH) were used as substrates. The films were deposited at 800 °C in an oxygen atmosphere of 1.7×10^{-4} mbar. To reduce the amount of preparation-induced defects, the prepared films were kept under preparation conditions for 1 h and carefully cooled down to room temperature, including a resting point of 30 min at 500 °C. The film thickness was chosen to be between 10 and 200 nm in order to compare with previous reports in the literature, where either 15 nm^[131,145] or 200 nm films were used^[142]. The film thickness was measured by X-ray reflectometry (XRR).

Electrode Assembly: For the RRDE setup, epitaxial tetragonal^[143,146] (100)-oriented LSMO thin films were assembled as schematically indicated in Figure

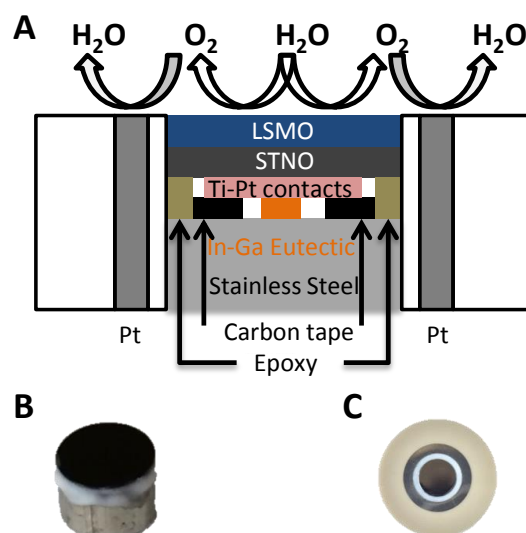


Figure 3.2: (A) Schematic view of the electrode made from LSMO thin films between 200 and 10 nm grown on a 0.5 mm thick STNO substrate. An ohmic back contact consists of 5 nm Ti and 100 nm Pt films. Photographs of (B) the assembled electrode (EEL setup, 5 mm disk diameter) and (C) the electrode in an RRDE assembly (IMP setup, 4 mm disk diameter). For detailed dimensions and the procedure for the electrode assembly, see Table 3.1 and the text.

3.2A. The backside contact consisting of 5 nm Ti and 100 nm Pt layers were prepared by IBS at room temperature. In order to produce reliable ohmic contacts between the prepared films and the stainless steel holder, sputtered Ti and Pt layers were applied, whereas carbon tape and InGa eutectic (Sigma-Aldrich, 99.99%) act as a flexible and adjustable conductive spacer. The side of the assembly was affixed and sealed with chemically stable, nonconductive epoxy (Omegabond 101), leaving only the thin film surface exposed to the electrolyte. To provide more protection against leakage of the electrolyte, a nonconductive, chemically resistant heat shrink tube was added for the IMP setup (see below) covering the whole stainless steel cylinder. The spacer units were necessary for alignment in the RRDE setup. The final electrode assembly can be seen in Figure 3.2B,C.

Electrochemical Measurements: Electrochemical measurements were performed independently in two laboratories using samples fabricated at the IMP. Details of the experimental setups can be found in Table 3.1. The 0.1 M KOH electrolyte was prepared either by diluting KOH stock solution with deionized water (Milli-Q, > 18.2 MΩ) or dissolving KOH pellets in deionized water (Milli-Q, > 18.2 MΩ). The electrolyte was saturated with Ar gas at

Table 3.1: Electrochemical Setups used at the Institute of Materials Physics (IMP) at University of Göttingen and used at the Electrochemical Energy Laboratory (EEL) at the Massachusetts Institute of Technology

setup	IMP	EEL
potentiostat	Interface 1000E (Gamry Instruments Inc.)	VSP-300 (Biologic SAS)
sampling mode	'noise-reject': current average over last 20% of step duration	current average over last 50% of 5 μ s step duration
cell volume (mL)	75	120
rotator	RRDE-3A (ALS Co. Ltd.)	MSR (Pine Research Instrumentation, Inc.)
electrode assembly	Pt ring (ALS Co. Ltd.)	Pt ring (Pine Research Instrumentation, Inc., E6 series)
disk diameter (mm)	4	5
inner ring diameter (mm)	5	6.5
outer ring diameter (mm)	7	7.5
height steel cylinder (mm)	3.5	3.5
reference electrode	Saturated calomel (ALS Co. Ltd.)	Saturated calomel (Pine Research Instrumentation, Inc.)
reference voltage	$E_{ref} = 0.997$ V measured *	$E_{ref} = 0.998$ V measured *
KOH supplier, purity	Sigma-Aldrich (1 M solution)	Alfa Aesar (pellets), 99.98%
Ar gas supplier, purity	Air Liquide, 99.999%	Airgas, 99.999%

* The electrode was calibrated to the RHE scale by CV measurement of hydrogen evolution in H₂-saturated 0.1 M KOH, where the average voltages of zero current from the positive- and negative-going CV scans were found at 0.998 V vs. RHE for the EEL setup and 0.997 V vs. RHE for the IMP setup.

least 30 min in advance of the measurement and continuously purged with Ar throughout the measurement. Electrode potentials were converted to the RHE scale using $E_{RHE} = E_{applied} + E_{ref}$. The low solubility of oxygen in water causes bubble formation at the disk^[141] and an accurate determination of the OER overpotential is further complicated by the increasing O₂ concentration in Ar-saturated electrolytes. For these reasons, we did not quantitatively analyze oxygen detected by ring electrodes.

Electrochemical Protocols: An identical measurement protocol was used to investigate OER kinetics for both setups. The double-layer capacitance was measured by cycling three times from 1.1 to 1.2 V vs. RHE with 10, 20, 50, 100, and 200 mV/s at 2500 rpm, and the capacitive current was extracted at the middle of the potential range according to the IUPAC recommendation^[147]. The OER activity was investigated by cycling three times from 1.1 to 1.75 V vs. RHE with 10 and 200 mV/s at 2500 rpm. Subsequently, the samples were held at 1.7 V vs. RHE for 1 h. The ring electrode was constantly held at 0.4 V vs. RHE to probe for O₂ [calibration data shown in Figure 8.1, Appendix A]. Before each measurement series, electrochemical impedance spectroscopy (EIS) was conducted with an amplitude of 10 mV at open circuit potential ($R=45\pm14\ \Omega$ for EEL setup and $R=48\pm5\ \Omega$ for the IMP setup). The potentials were referenced to the reversible hydrogen electrode (RHE) scale in 0.1 M KOH and corrected for the electrolyte resistance extracted from the high-frequency intercept of the real impedance. Additional experiments on the $[\text{Fe}(\text{CN})_6]^{3-/4-}$ reaction were performed using the EEL setup and LSMO films with thicknesses of 40 and 200 nm in Ar-saturated 0.1 M KOH, to which 5 mM each of $\text{K}_4\text{Fe}(\text{CN})_6 \cdot 3\ \text{H}_2\text{O}$ (Sigma-Aldrich, 98.5%) and $\text{K}_3\text{Fe}(\text{CN})_6$ (Sigma-Aldrich, 99%) were added. The disks were scanned from 0.65 to 1.65 V vs. RHE at a rate of 200 mV/s, while the ring potential was set to 1.55 V vs. RHE to probe for ferrocyanide to ferricyanide oxidation.

Structural Characterization: The films were characterized using extensive X-ray diffraction (XRD) measurements. XRD and XRR measurements were carried out with a Bruker D8 discover system with a Cu K α source. The surface morphology was characterized by atomic force microscopy (AFM) using a MFP-3D Classic (Asylum Research) in tapping mode. The root mean squared roughness (rms) was calculated using the Gwyddion software^[148] to quantify surface morphology (Tables 8.1 and 8.2, Appendix A). Additionally, an effective roughness factor was determined by dividing the three-dimensional surface area by the projected area^[131], where the former was obtained by a triangulation

method in Gwyddion^[148]. All films had terraced surfaces that reflect the terrace structure of the substrate surface. Such vicinal surfaces are generated by small deviations from the ideal low index surface due to imperfect polishing. In our samples, the deviation from (100) is up to 0.3° and the terrace width of the LSMO surface and structure of the terraces slightly varied even within one sample (Figures 8.2-8.4, Appendix A). Nevertheless, all epitaxial LSMO films exhibit a vicinal (100) surface, where the (100) surface facets of the terraces are separated by unit cell steps. Extensive post-mortem analysis of structural changes was applied to samples measured by the IMP setup.

Electric Transport Measurements: The in-plane resistivity was measured in a physical property measurement system (PPMS) using a four-point probe setup on the LSMO films grown on insulating STO.

Chemical Composition Characterization: The elemental composition was measured with XPS (Physical electronics PHI Versaprobe II) using an Al K_α source. The binding energy scale was calibrated by defining the fitted C 1s peak for adventitious carbon at 284.8 eV^[149]. Extensive postmortem analysis of chemical changes was only performed on samples measured by the EEL setup. Compositions were calculated by dividing the RSF-corrected spectral areas by the sum of the areas of La, Sr, Mn, and O. Subsequently, the fractions of La, Sr, and O were divided by that of Mn to obtain the atomic ratio. We note that the escape depths of electrons differ among the La, Sr, O, and Mn spectra. Samples for XPS were carefully rinsed with copious amounts of Milli-Q water after electrochemistry and subsequently stored under vacuum at 50 °C for less than 24 h.

3.3 Results and Discussion

In the following, a thorough study of OER activity and stability on epitaxial (100)-oriented LSMO thin films is presented. As epitaxial LSMO films are not an established electrode material, we first present the structural and electrical properties of the prepared LSMO thin films (section 3.3.1), followed by their careful electrochemical characterization via rotating ring - disk methods (section 3.3.2). We show that the semiconducting electrode behaves like a metallic electrode. The careful characterization of the electrode material allows us to relate changes in the physical properties to activity and stability during OER (section

3.3.3). Sections 3.3.1-3.3.3 jointly established the model character of our LSMO electrodes. Finally, we correlate OER activity to changes in atomic ratios of the LSMO surface, suggesting Mn as the active site (section 3.3.4).

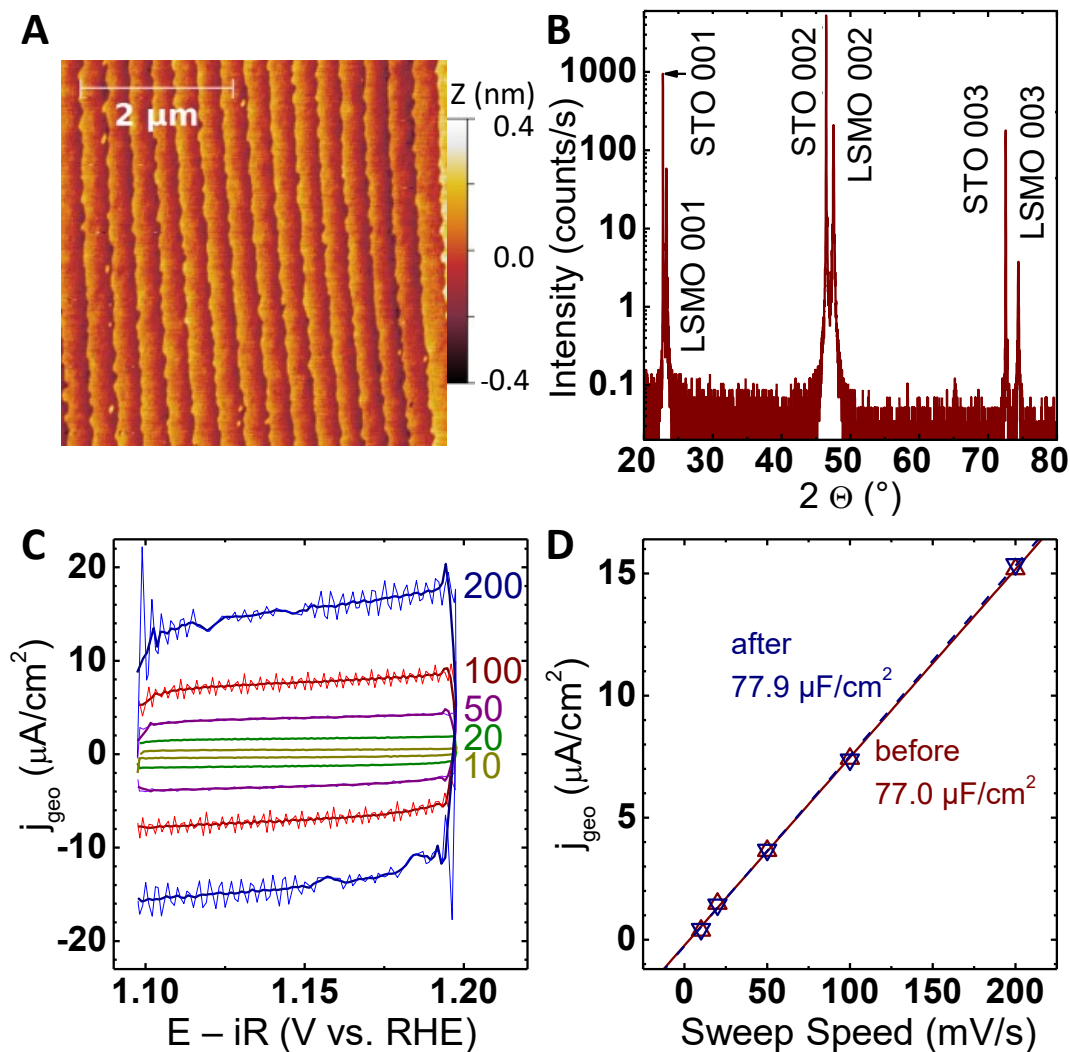


Figure 3.3: (A) Representative AFM image of a $\text{La}_{0.6}\text{Sr}_{0.4}\text{MnO}_3$ film of 80 nm grown on (100)-oriented STO. (B) wide-angle out-of-plane XRD scan on a representative $\text{La}_{0.6}\text{Sr}_{0.4}\text{MnO}_3$ film of 80 nm. (C) Double-layer capacitance of a $\text{La}_{0.6}\text{Sr}_{0.4}\text{MnO}_3$ film of 20 nm in Ar saturated 0.1 M KOH at the indicated scan rates (in units of mV/s) shows the rectangular shape where thick lines were smoothed by a second-order polynomial filter in EC Lab (seven point window)^[150]. (D) The specific capacitance of a $\text{La}_{0.6}\text{Sr}_{0.4}\text{MnO}_3$ film of 20 nm extracted from double-layer capacitance measurements using the EEL setup before (up triangles) and after storage in air for a week followed by OER measurements (down triangles). The capacitance was normalized by the geometric disk area and the roughness factor obtained from AFM (Figure 8.2).

3.3.1 Physical Properties of LSMO Films.

LSMO films were grown on single crystalline STNO substrates with atomically flat surfaces rivaling those of more commonly investigated metal surfaces, e.g., Pt^[151]. AFM images of the LSMO films (Figures 3.3A and 8.2-8.4, Appendix A) show terraced surfaces with an average root-mean square (RMS) of 0.12 ± 0.03 nm for samples used for the IMP setup (Table 8.1, Appendix A) and 0.13 ± 0.04 nm for samples used for the EEL setup (Table 8.2, Appendix A). Surface roughness was identical within experimental uncertainty (95% confidence interval), regardless of film thickness. The observed step heights of the terraces of about ~ 0.4 nm corresponds to single unit cells of the LSMO crystal (Figure 8.2, Appendix A)^[152]. Considering the ratio of $> 250 : 1$ between the terrace widths of 100-700 nm and the step height of 0.4 nm (Figure 8.4, Appendix A), the contribution of the edges to the surface area can be neglected.

The epitaxy of the grown films is shown by out-of-plane X-ray diffraction (Figure 3.3B) exhibiting only reflections from the substrate and LSMO that belong to the (100) orientation, which was supported by φ -scans, rocking curves, and detailed 2Θ scans (Figure 8.5, Appendix A). φ -Scans showed the identical 4-fold symmetry as the substrate supporting high epitaxy. Rocking curves indicated high epitaxy limited by the substrate quality. Detailed 2Θ scans on the (200) reflection showed an increased tensile out-of-plane strain (-0.8 to -1.2%) with increasing film thickness from 10 to 200 nm. A tetragonal distortion of the rhombohedral lattice (space group $R\bar{3}c$) on the order of 1% due to substrate misfit is often observed in LSMO films^[143,146]. We note that the magnitude of strain and its trend with thickness depend on the preparation method and conditions^[153,154]. The initial stress due to lattice misfit between the film (pseudocubic lattice parameter $a' = 3.88$ Å)^[152] and the substrate (cubic lattice parameter $a = 3.905$ Å)^[155] can be modified due to preparation induced defects. In summary, AFM and XRD showed epitaxial growth of smooth LSMO films, which allowed correlation of the electrochemical properties exclusively to (100)-oriented LSMO.

To bridge the structural properties and electrochemical application, the double-layer capacitance was measured, showing the expected response of a flat surface. The double-layer capacitive current (Figure 3.3C) follows the expected linear behavior of an ideal capacitor with scan rate ν given by $i_C = \nu C_{DL}$ ^[51] (Figure 3.3D), with a specific capacitance of $C_{LSMO} = 77 \pm 2$ $\mu\text{F}/\text{cm}^2$ in 0.1 M KOH for the thinnest (100)-oriented LSMO films with thicknesses of 20 nm. Moreover, the

good fit by linear regression in Figure 3.3D supported that the observed currents were exclusively due to physical adsorption in the double-layer (and not due to Mn redox). Although specific capacitances for perovskite oxide surface have not been available previously, the value is consistent with the specific capacitance of $60 \mu\text{F}/\text{cm}^2$, which is considered universal for oxide surfaces^[147]. Therefore, the obtained specific capacitance in this study could serve as a reference value for future estimations

3.3.2 Electrochemistry of Semiconducting LSMO.

The band structure of semiconductors and particularly band bending at internal interfaces and the surface can prevent current flow^[145,156,157], which is not observed for metal electrodes. Furthermore, the mechanism of electron conduction in oxide semiconductors differs from that of metals having delocalized electrons. Both can influence the apparent catalytic activity and might lead to a misinterpretation of catalytic rate-limiting steps. Our LSMO films had an in-plane resistivity of $< 10^{-3} \Omega\text{cm}$ at room temperature, which was lower than reported previously ($< 10^{-2} \Omega\text{cm}$)^[144] but higher than that of metals ($\sim 10^{-6} \Omega\text{cm}$)^[158]. The LSMO resistivity decreased with film thickness (Figure 8.6, Appendix A). This correlates with the observed reduction of tensile out-of-plane strain with thickness and may be due to an improved hopping of localized electrons via double-exchange, depending on the angles of manganese-oxygen bonds^[33,144,159]. These semiconducting properties of LSMO prompted us to investigate if its electron transfer is suitable for electrochemistry at OER voltages.

Electron transfer kinetics to the LSMO surface was shown to be facile using the ferri-/ferrocyanide redox couple (Figure 3.4). Both a 40 nm film and a 200 nm film showed the symmetric duckbill shape of a fast, reversible redox couple (Figure 3.4A), having similar amplitudes of the cathodic and anodic peaks (Table 8.3, Appendix A); i.e., electrochemical charge transfer did not correlate with bulk conductivity (Figure 8.6, Appendix A). Moreover, the reversible potential of the ferri-/ferrocyanide solution was 1.18 V vs. RHE, regardless of film thickness. The voltage difference between the cathodic and anodic peaks was 92 and 102 mV, for 40 and 200 nm thickness, which was slightly larger than the expected scan-rate-independent 56 mV for a fully reversible one-electron process with fast

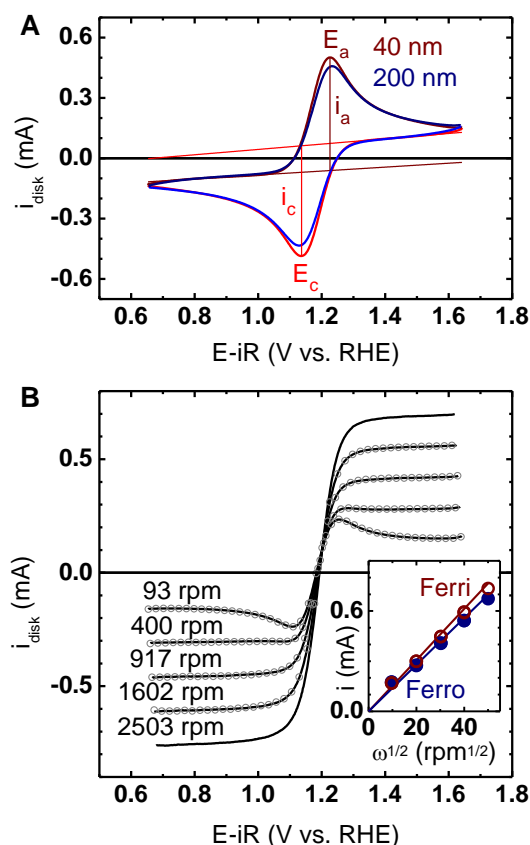


Figure 3.4: Disk currents of $\text{La}_{0.6}\text{Sr}_{0.4}\text{MnO}_3$ films of 40 and 200 nm in 5 mM of each ferro- and ferricyanide with 0.1 M KOH supporting electrolyte (Ar-purged) at 200 mV/s measured using the EEL setup. (A) Surface charge transfer kinetics at unrotated, quiescent electrodes. Thin lines indicate baselines for determination of current amplitudes i_a/i_c at peak potentials E_a/E_c . (B) Kinetics of ferri-/ferrocyanide redox. Rotation speeds were increased from 93 to 2503 rpm (lines) and subsequently decreased back to 93 rpm (circles), which was measured using a laser tachometer. The inset shows the Levich plot of ferrocyanide oxidation (solid circle), ferricyanide reduction (open circle), and currents calculated using eq 3.1 (solid lines). All disk currents were corrected for capacitive currents by averaging positive and negative-going scans of the second cycle.

kinetics^[40,160]. Peak separations of 104 mV for a 10 nm LaMnO₃ film^[145] and 115 mV for a 15 nm La_{0.67}Sr_{0.33}MnO₃ film^[156] were found at a sweep speed of 10 mV/s. Peak separations greater than 56 mV and spread greater than 10 mV are frequently reported for ferri-/ferrocyanide^[161–163] in various electrolytes on conventional metal and carbon electrodes due to the cleanliness of the electrode^[164], uncompensated resistances, and nonlinear diffusion^[165]. The similarity of the peak currents and low voltage difference between the cathodic and anodic peaks established the ability of the LSMO films to donate or accept electrons at voltages relevant to oxygen evolution.

In rotating disk electrode (RDE) experiments, our LSMO films also showed the response of a flat metal electrode using the ferri-/ferrocyanide redox couple in an electrolyte containing 5 mM each of ferricyanide and ferrocyanide in 0.1 M Ar saturated KOH (Figure 3.4B). The capacitance-corrected limiting currents showed the expected linear current increase for quadratic increase of the rotation speeds for both ferricyanide reduction (negative currents) and ferrocyanide oxidation (positive currents), which is in agreement with the Levich equation^[51] (Figure 3.4B, inset)

$$i_L = 0.201 n F A C D^{2/3} \gamma^{-1/6} \omega^{1/2} \quad (3.1)$$

where $n=1$ is the number of transferred electrons, $F=96\,485.33$ C/mol is the Faraday constant, $C=5$ mM is the concentration of the active species, $A=0.196$ cm² is the electrode area, D is the diffusion coefficient of ferrocyanide (6.32×10^{-6} cm²/s)^[166] or ferricyanide (7.28×10^{-6} cm²/s)^[166], $\gamma=1.02 \times 10^{-2}$ cm²/s is the kinematic viscosity^[166], and ω is the rotation speed in units of rpm. Literature values of D and γ could not be found for 0.1 M KOH, and we used the values for 5 mM each of ferricyanide and ferrocyanide in 0.504 M KOH at 26.6 °C instead; the temperature in our experiment was 24.4 °C. Both lead to a slight overestimation of the calculated limiting currents. Unlike previous RDE experiments^[142], our LSMO films show ferri-/ferrocyanide redox kinetics akin to that of metal surfaces, which establishes their suitability for RRDE investigation of the OER. This is further supported by the measurement of ring currents and linear correlation between ring and disk currents in Figure 8.9 (Appendix A).

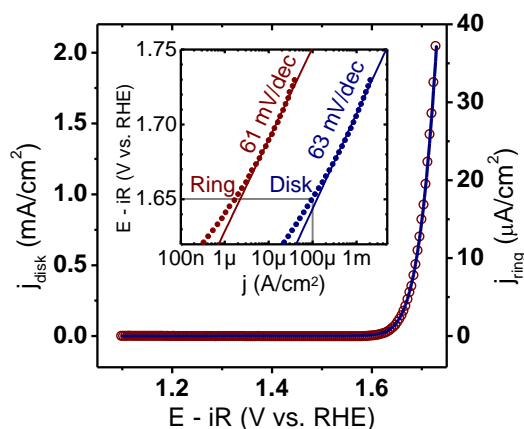


Figure 3.5: CV measurement of a 20 nm $\text{La}_{0.6}\text{Sr}_{0.4}\text{MnO}_3$ film (solid blue line) and the corresponding ring current (open red circles) obtained by CA at 0.4 V vs. RHE acquired using the EEL setup. The inset shows the Tafel analysis of the Pt ring (red circles) and the disk LSMO (blue circles) currents as a function of the disk voltage obtained from CV. All measurements were performed with Ar-purged 0.1 M KOH supporting electrolyte at 10 mV/s and 2503 rpm. The voltage was corrected for electrolyte resistance (47 Ω), and the positive-going direction of the second scan is shown.

3.3.3 Activity and Stability of LSMO during Oxygen Evolution.

The activity and stability of all epitaxial films was evaluated by CV. OER measurements of a LSMO film of 20 nm thickness are shown as an example in Figure 3.5, and other investigated films can be found in Figures 8.12 and 8.13 (Appendix A). In CV, no features except for the onset of oxygen evolution could be observed, as previously reported for quiescent measurements^[131]. The onset voltage of OER current occurred at voltages greater than 1.6 V vs. RHE, independent of film thicknesses between 10 and 200 nm, since the space charge layer in LSMO is less than 3 nm^[145,167]. We observed a disk current of $100 \mu\text{A}/\text{cm}_{\text{ox}}^2$ at 1.65 ± 0.01 V vs. RHE using the EEL setup and 1.67 ± 0.02 V using the IMP setup, which was identical within experimental uncertainty. Error bars (2σ , 95% confidence interval) were calculated from the experimental scatter of the measurements shown in Figures 8.12 and 8.13 (Appendix A). No change was found in the OER activity from cyclic voltammetry before and after voltage holding at 1.7 V vs. RHE for 1 h (Table 8.5, Appendix A). Moreover, the voltages required to obtain an OER current of $100 \mu\text{A}/\text{cm}_{\text{ox}}^2$ were consistent with previous results for both 15 nm of (100)-orientated $\text{La}_{0.8}\text{Sr}_{0.2}\text{MnO}_3$ (1.7 V vs. RHE)^[131] as well as 200 nm of $\text{La}_{0.8}\text{Sr}_{0.2}\text{MnO}_3$ on Pt^[142] (1.68 V vs. RHE) and were similar to those of powders^[131] considering the experimental uncertainty (Table 8.6, Ap-

pendix A). The intrinsic OER activity of (100)-oriented LSMO is similar to that of (110)-oriented IrO_2 but lower than that of (110)- and (100)-oriented RuO_2 , (100)-oriented $\text{Ba}_{0.5}\text{Sr}_{0.5}\text{Co}_{0.8}\text{Fe}_{0.2}\text{O}_{3-\delta}$ (on LSMO), or LaCoO_3 thin films (Table 8.6, Appendix A)^[3,95,131]. For our extremely flat LSMO films, the disk area equals the area of the active oxide (indicated by subscript 'ox'), while the oxide area (A_{ox}) is usually larger than the disk area (A_{disk}) for electrodeposited films and supported nanoparticles (e.g., $A_{\text{ox}}/A_{\text{disk}}=60$ for RuO_2 in ref^[94]). While other options for normalization exist^[3], the oxide area is most meaningful when discussing the effect of composition on activity, making it the most suitable choice for our purposes. Therefore, the comparably low disk currents in Figures 3.5 and 8.12 and 8.13 (Appendix A) translate into high intrinsic activity per oxide area. However, it should be noted that LSMO, having a high intrinsic activity, does not suggest applicability on a large scale, where high activity per geometric area is needed.

The onset of OER activity was further investigated by the RRDE method, where oxygen generated at the disk moved to the ring by forced convection. Oxygen was then reduced at the ring under mass-limiting conditions; i.e., the ring current only depends on the concentration of oxygen (Figure 8.1B, Appendix A). At a ring voltage of 0.4 V vs. RHE, reduction of species other than oxygen would be conceivable if they were present in the O_2 -saturated KOH electrolyte. For the LSMO electrodes, the formation of hydrogen peroxide under oxidative conditions was negligible (Figure 8.11, Appendix A). The electrochemical formation of soluble permanganate is thermodynamically possible at disk voltages above ~ 1.5 V vs. RHE^[73,79] and was reported as a side reaction for reactively sputtered MnO_x ^[76]. However, after chronoamperometry at 1.7 V vs. RHE, no evidence of structural changes or loss of material could be found, as discussed in the following section, hence indicating that permanganate formation was negligible. Due to the lack of evidence for other reducible species in the electrolyte, we conclude that ring currents respond solely to dissolved oxygen and, together with the observed correlation of ring currents with the disk currents (Figure 3.5), thus suggested that the onset of disk currents corresponded to the onset of the OER. Furthermore, ring currents can be used for mechanistic discussion (e.g., Tafel analysis) as they represent exclusively the catalytic current due to the OER.

Tafel slopes of disk current densities in the range from ~ 0.02 to 2 mA/cm^2 were found to be independent of film thickness and measurement setup. We identified two distinct Tafel slopes, one at low current densities of 0.02 - 0.2 mA/cm^2 and one at higher current densities of 0.2 - 2 mA/cm^2 (Table 8.4, Appendix A). We

will focus on the latter Tafel slope (lines in inset of Figure 3.5) because it was observed at overpotentials commonly compared in the literature^[3,38,39,65,131]. The Tafel slopes had values of 65 ± 5 mV/dec at the disk and 66 ± 6 mV/dec at the ring using the IMP setup (Table 8.4, Appendix A) and 63 ± 3 mV/dec at the disk and 62 ± 5 mV/dec at the ring using the EEL setup (Table 8.5, Appendix A). In addition, Tafel slopes of both disk and ring were unchanged after holding for 1 h at 1.7 V vs. RHE (Table 8.5, Appendix A). Having no difference in the disk and ring Tafel slopes over ~ 2 decades of disk current suggested that neither capacitance nor corrosion affected the disk currents of our LSMO disk.

Tafel slopes can be predicted on the basis of the sequence of elementary reaction steps and the rate-determining step of the mechanism^[48–50]. Our Tafel slopes are consistent with the Tafel slope of 59 mV/dec expected for OER at 25 °C, having an electrochemical pre-equilibrium followed by a chemical rate determining step, such as O-O bond formation between OH_{aq} and a hypothetical $\text{Mn}=\text{O}$ surface site, as predicted for LaMnO_3 and shown in Scheme 3.1^[52]. Prior to O-O bond formation, most proposed OER mechanisms require Mn oxidation, which is a probable electrochemical pre-equilibrium step for Mn as the active site^[3]. Chemically limited reaction mechanisms without a highly oxidized $\text{M}=\text{O}$ intermediate, e.g., those involving lattice oxygen, have smaller Tafel slopes of ~ 30 mV/dec^[56]. Larger Tafel slopes of ~ 120 mV/dec are indicative of mechanisms where an electrochemical step is rate-limiting^[50]. All of these Tafel slopes were derived under the assumption that the active site is not blocked by adsorbates (i.e., low surface coverage limit).

The OER Tafel slope of our LSMO disks was lower than previously reported for a 15 nm $\text{La}_{0.8}\text{Sr}_{0.2}\text{MnO}_3$ film with (100) orientation (70 mV/dec)^[131] and $\text{La}_{0.6}\text{Sr}_{0.4}\text{MnO}_3$ powder (125 mV/dec)^[46] as well as other manganese-based electrocatalysts with Tafel slopes between ~ 90 and 160 mV/dec^[3,44,65,132]. In addition to the mechanism, Tafel slopes are also sensitive to differences in conductivity^[156] and surface roughness^[168]. The relation between roughness and the Tafel slope is not straightforward^[169], and the determination of accurate catalytic currents becomes challenging for very rough surfaces, e.g., due to high capacitive currents. Low electric conductivity previously led to Tafel slopes above 60 mV/dec (for ORR of LSMO)^[156], and in the most extreme cases, where electron transfer becomes limiting, 120 mV/dec should be expected. The high conductivity and the extremely low roughness of our films, as well as the agreement of the disk and ring Tafel slopes, support that the obtained Tafel slopes of ~ 60 mV/dec are representative for (100)-oriented LSMO electrodes.

To evaluate the long-term stability during OER, all LSMO films were charac-

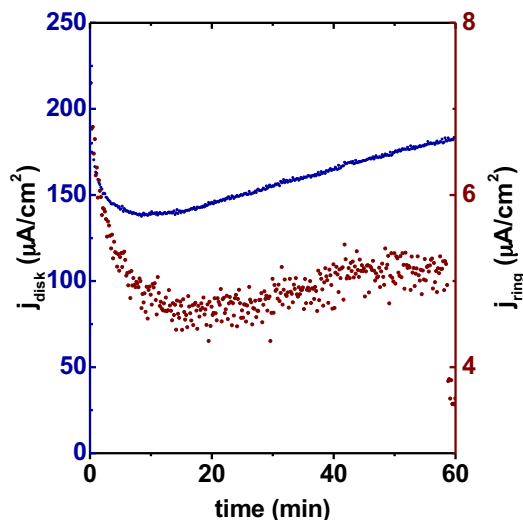


Figure 3.6: Chronoamperometry (CA) of a 10 nm $\text{La}_{0.6}\text{Sr}_{0.4}\text{MnO}_3$ disk at 1.7 V vs. RHE using the IMP setup. The blue line shows the disk current and red dots the corresponding ring current obtained by CA at 0.4 V vs. RHE. The measurement was performed with Ar-purged 0.1 M KOH at 2500 rpm.

terized using chronoamperometry (CA) for 1 h at 1.7 V vs. RHE following the CV measurements. An example for a 10 nm LSMO electrode is shown in Figure 3.6, and the data for the other films can be found in Figures 8.14 and 8.15 (Appendix A). The majority (70%) of LSMO electrodes showed that the disk current dropped within the first 10 min and then increased until the end of the measurement, which correlated with small or no increases in the ring current due to bubble formation and O_2 -saturation of the electrolyte. Selected electrodes were stored in air for up to 1 week and then evaluated again by CV (Figure 8.13F-H, Appendix A) and CA (Figure 8.15F-H, Appendix A). During the latter CA measurement, the disk current dropped again initially but then rose above the value it had in the first measurement.

Similar activation during OER was previously observed for $\text{La}_{0.8}\text{Sr}_{0.2}\text{MnO}_3$ during CV after ~ 10 cycles (~ 20 min)^[131] in O_2 -saturated 0.1 M KOH, which was attributed to manganese oxidation on the surface. Increasing currents during OER CA due to corrosion, phase change, or electrolyte saturation with oxygen can be neglected because (i) the calculated amount of soluble $\text{Mn}^{\text{VII}}\text{O}_4^-$ exceeded the number of Mn atoms in the film by more than 1 order of magnitude (calculation detailed in the Appendix A), (ii) the obtained charge is too large to be explained by a phase change, e.g., from a perovskite to a Ruddlesden-Popper phase, and (iii) the electrolyte in the diffusion layer would be saturated with

oxygen in ~ 4 s for the estimated OER currents (calculation described in the Appendix A) so that this effect cannot explain rising currents over the duration of ~ 50 min. Therefore, we propose that the formation of a more active surface phase on LSMO might contribute to the observed current enhancement in this study.

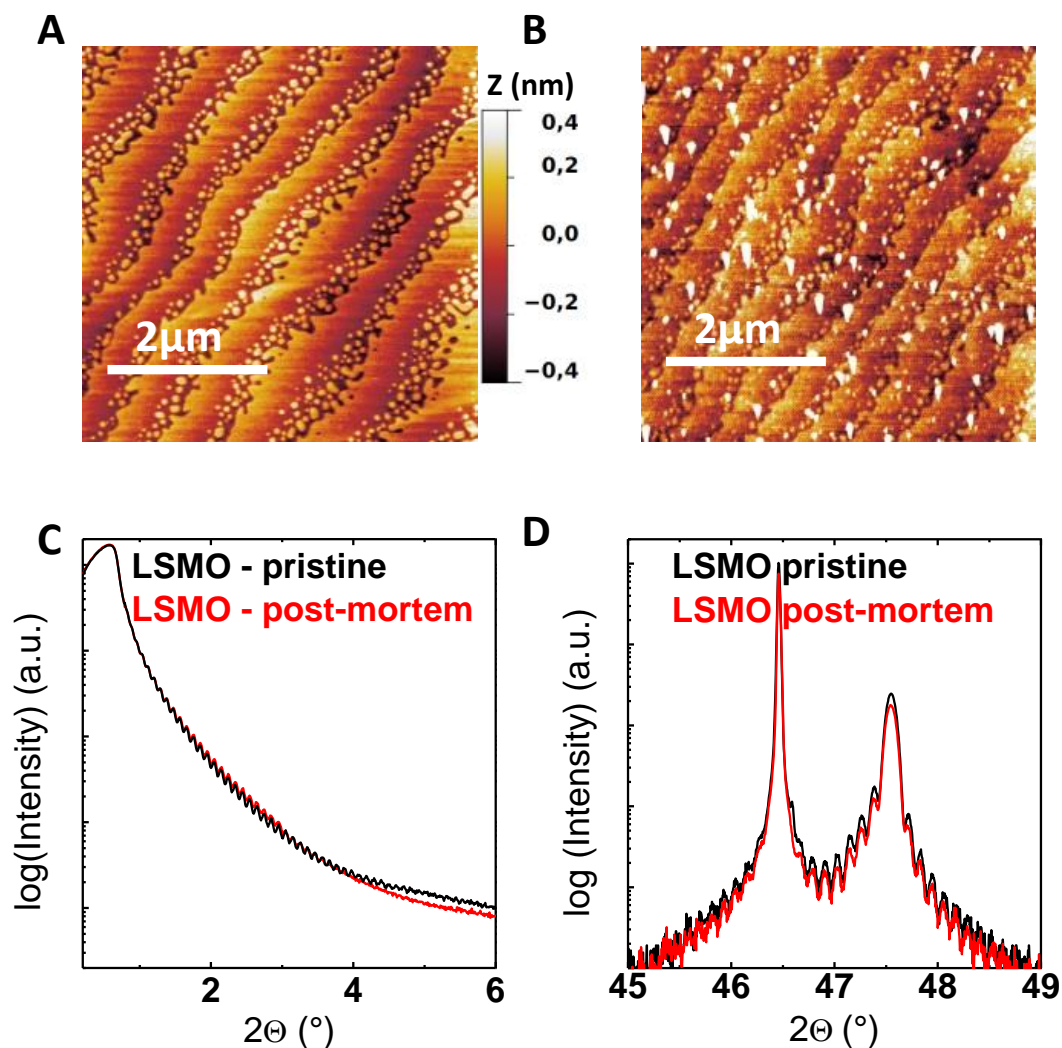


Figure 3.7: Post-mortem analysis on a 80 nm $\text{La}_{0.6}\text{Sr}_{0.4}\text{MnO}_3$ film using AFM and XRD: (A) the surface of the as-grown sample, (B) the surface after CV (three cycles between 1.1 and 1.75 V vs. RHE with 10 and 200 mV/s at 2500 rpm) and CA at 1.7 V vs. RHE for 1 h (data in Figures 8.12B and 8.14B, Appendix A), (C) the lack of notable changes in XRR patterns, and (D) the lack of notable changes in XRD due to CA using the IMP setup. Small changes of the high-angle part of the diffractogram might originate from minor changes in surface density.

3.3.4 Correlating Trends in OER Activity to Surface Composition of the Electrode.

The increase in the OER current density in Figure 3.6 is most likely not resulting from surface roughening. Representative AFM images of an LSMO film of 80 nm before (Figure 3.7A) and after 1 h of OER at 1.7 V vs. RHE in 0.1 M KOH (Figure 3.7B) showed comparable terraces and island-like structures near the terrace edges. The preservation of the surface terraces corresponding to perovskite unit cell steps can therefore rule out severe surface degradation or more specifically the formation of an amorphous surface layer. Moreover, the presence of minuscule features such as the islands after CA can rule out significant film dissolution, because we expect that such features with high surface energy dissolve first. The stability of the LSMO under catalytic conditions was supported by TEM measurements showing no significant changes in structure even at the surface (Figure 8.16). Similar observations were made for films of other thicknesses having varied terrace width associated with different miscuts in the Nb:SrTiO₃ substrate (Figure 8.3, Appendix A). The presence of white spots in Figure 3.7B with heights of up to 10 nm (see Figure 8.17, Appendix A) might be related to electrolyte residue. In addition, XRR analysis shows no noticeable changes before and after the CA OER measurement, reflecting that the bulk thickness as well as the roughness remained unchanged (Figure 3.7C). Moreover, out-of-plane XRD measurements revealed small changes in strain, which did not correlate with the strain in the as-grown film nor the currents during CA (Figure 8.5B, Appendix A), further corroborating the preservation of the perovskite structure for all film thicknesses. In summary, AFM, XRR, and XRD, analyses performed after the CA OER measurement showed no noticeable changes in the surface structure or the bulk structure, which supports that the increase in the OER current cannot be attributed to surface roughening, surface amorphization, or Mn dissolution.

XPS spectra taken of the pristine samples and after 1 h of CA at 1.7 V vs. RHE supported unchanged manganese valence and revealed changes in the surface chemical composition of LSMO during OER activity. A survey scan showed no additional core level features due to contamination, except trace amounts of lead (Pb) after the CA OER measurement (Figure 8.18, Appendix A), which presumably came from the electrochemical cell made from glass. The La 4d

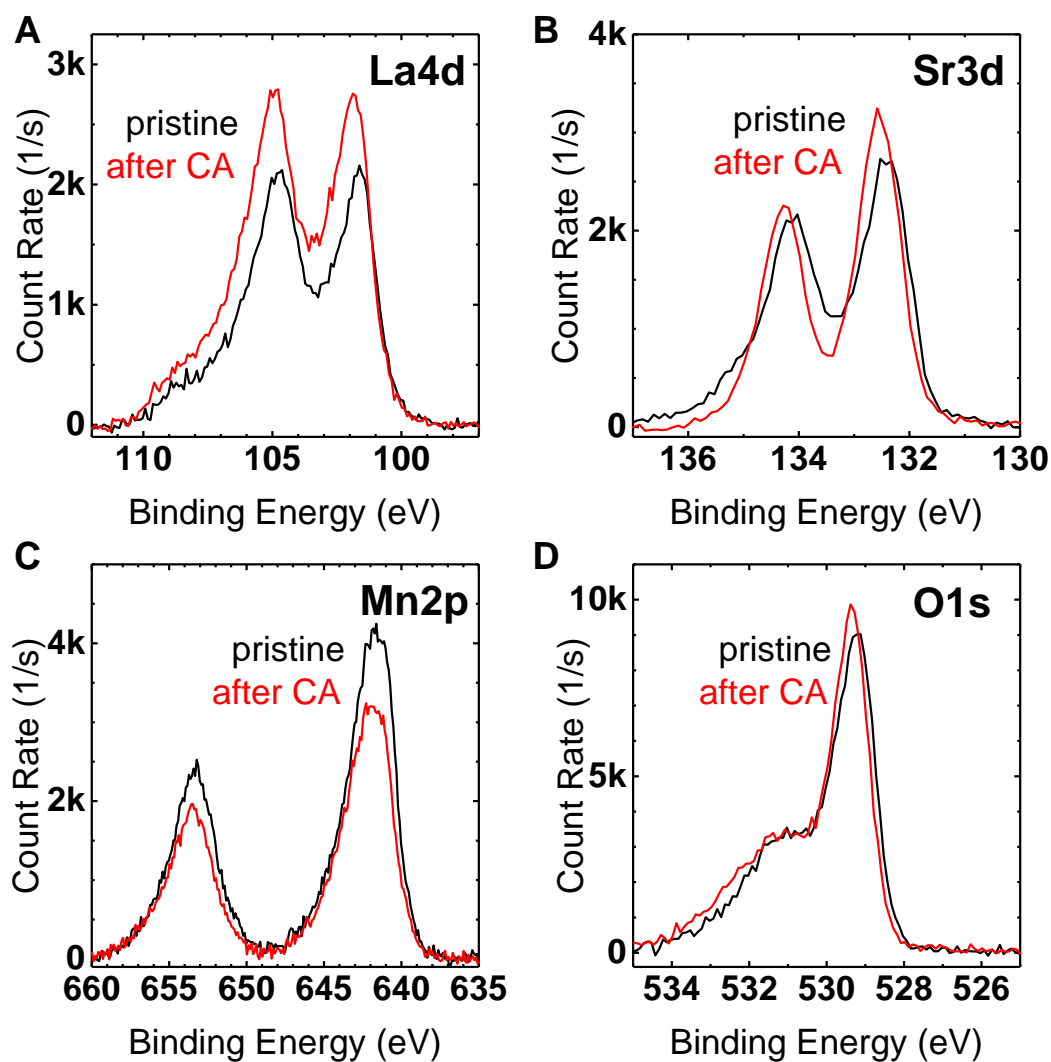


Figure 3.8: Representative XPS spectra of a 20 nm thin $\text{La}_{0.6}\text{Sr}_{0.4}\text{MnO}_3$ film showing the (A) La 4d, (B) Sr 3d, (C) Mn 2p, and (D) O 1s core levels for the pristine sample (black) and the same sample after CV (three cycles between 1.1 and 1.75 V vs. RHE with 10 and 200 mV/s at 2500 rpm) and CA at 1.7 V vs. RHE for 1 h (red) using the EEL setup.

spectrum of the pristine sample exhibits the $d_{5/2}$ and $d_{3/2}$ doublet at binding energies of 101.6 and 104.8 eV (Figure 3.8A). The pristine Sr 3d spectrum shows the $d_{5/2}$ and $d_{3/2}$ doublet at binding energies of 132.4 and 134.1 eV for the pristine sample (Figure 3.8B). The pristine Mn 2p spectrum shows two broad $p_{3/2}$ and $p_{1/2}$ doublets at 641.7 and 653.3 eV (Figure 3.8C). While determination of the Mn oxidation state is challenging due to the multiplet emission lines of various Mn valences, the unchanged peak position and width suggest an unchanged valence state before and after the CA OER measurement. It is conceivable that Mn^{IV} ions that may have formed during OER react with water during cleaning or with oxygen in air. Thus, resolving valence changes in active states requires in situ experiments, which are outside the scope of this study. The main emission line of the pristine O 1s spectrum shows a peak at 529.2 eV with a broad energy shoulder around 531.2 eV, where the peak is assigned to bulk oxygen and the shoulder to surface oxygen (Figure 3.8D)^[170].

The average atomic ratios of LSMO film surface were close to the nominal composition $\text{La}_{0.6}\text{Sr}_{0.4}\text{MnO}_3$ for pristine samples but not after oxygen evolution for 1 h. We found 0.68 ± 0.16 lanthanum atoms, 0.50 ± 0.12 strontium atoms, and 3.69 ± 0.76 oxygen atoms per manganese for the pristine samples (Figure 3.9A), which agrees well with the expected atomic ratios. There were no noticeable differences in the La/Mn, Sr/Mn, and O/Mn atomic ratio with thickness in five pristine samples having thicknesses between 10 and 200 nm (Figure 8.19, Appendix A). After cyclic voltammetry and the CA OER measurement at 1.7 V vs. RHE for 1 h, the average of all elemental ratios relative to manganese increased, but only the increase of La was significant considering experimental uncertainty (Figure 3.9A). Changes in the atomic ratios (X_e/X_p) before and after OER CA corroborated that the film surfaces were significantly enriched in lanthanum, while the ratios of strontium and oxygen remained unchanged within error and that of manganese was reduced after OER (Figure 3.9B). The film composition after OER is changed as a result of the surface dissolution of Mn atoms and potentially Sr, as its average ratio is below unity. Both SrO as well as Sr-OH species show a significant solubility in water^[171,172]; thus, surface dissolution of Sr in water is conceivable for various perovskites^[173,174]. Dissolution of Mn atoms from tri- or tetravalent binary MnO_x compounds can only evolve under alkaline conditions under strongly oxidizing conditions^[175]. However, Mn dissolution is less understood for perovskites, having higher formation enthalpy than binary oxides. Normally, the formation of cation vacancies should be coupled to anion vacancy creation in order to keep the

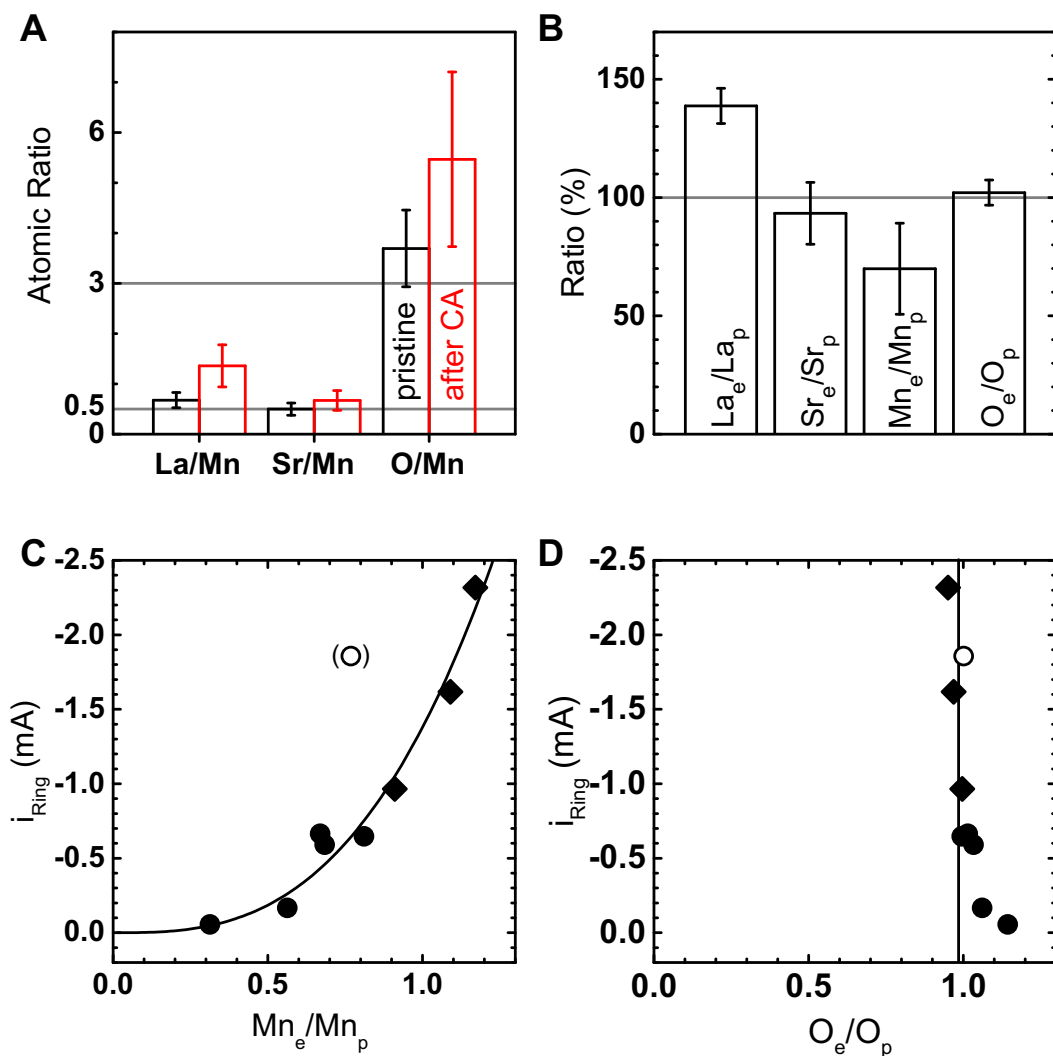


Figure 3.9: (A) Average atomic ratio relative to Mn of five pristine $\text{La}_x\text{Sr}_y\text{MnO}_z$ (nominally $\text{La}_{0.6}\text{Sr}_{0.4}\text{MnO}_3$) films before (black, 'pristine') and after 1 h of CA at 1.7 V vs. RHE (red, 'after CA') determined by XPS. (B) Ratio of electrolyzed (X_e , i.e., after CA) to pristine stoichiometry (X_p) of O, Sr, La, and Mn. Correlation between OER activity and the change in the surface atomic ratio of electrolyzed to pristine (C) manganese (Mn_e/Mn_p) and (D) oxygen (O_e/O_p). OER activity is monitored via the background-corrected ring current at 1 h CA obtained either from electrochemistry on pristine surfaces (circles) or repeated measurements (diamonds) using the EEL setup. An outlier (open circle) was not considered in the trend (see the text). Error bars in panels A and B denote the 95% confidence interval (2σ) of five films. For the observation of the increase of $\text{Mn}_e/\text{Mn}_p > 1$ after repeated CA, see the text.

charge balance in Schottky-type defects.

Notably, the surface oxygen ratio after CA to pristine samples is not changed. This indicates that under strongly oxidizing conditions Mn under-stoichiometry may evolve by a defect reaction, where the charge imbalance induced during Sr^{2+} dissolution and La^{3+} enrichment is compensated via Mn^{3+} vacancies in a $V_{\text{Mn}}''' / D_{\text{La}}'''$ defect couple (Kröger - Vink notation)^[176] as corroborated by the proportionality of $\text{Mn}_e / \text{Mn}_p$ to $\text{La}_e / \text{La}_p$ (Figure 8.20, Appendix A). Apparently, the formation of anion/cation pair Schottky-type defects $V_{\text{Sr}}'' / V_{\text{O}}''$ was avoided. Preservation of perovskite structure for large Mn vacancy concentrations with La/Mn ratio up to 1.09 was proven in LaMnO_3 ^[85] and is verified for our LSMO films via high-resolution TEM studies (Figure 8.16A, Appendix A). Interestingly, the ratio of manganese in the pristine sample relative to that after OER CA increased above 100% when the protocol was repeated (diamonds in Figure 3.9C). As expected from the defect couple described above, Mn over-stoichiometry correlates to a drop of surface La and vice versa (Figure 8.20, Appendix A). Moreover, EDX line scans showed that the surface is enriched in La within 2 nm below the surface (Figure 8.16B,C, Appendix A), which reduces the escape depth of Mn 2p electrons. In stoichiometric LSMO, the escape depth of these electrons is 2 nm (ca. five unit cells)^[177]. Thus, the magnitude of the atomic ratio $\text{Mn}_e / \text{Mn}_p$ can be explained by a combination of electron escape depths, a La terminated surface, and Mn vacancies after OER.

Having established that detected currents are predominantly of catalytic nature, we studied their dependence on chemical changes. The ring current at 1 h of OER at 1.7 V vs. RHE as a proxy for oxygen evolution increased monotonously with the atomic ratio of Mn ($\text{Mn}_e / \text{Mn}_p$); that is, the more Mn that was retained, the higher the observed activity. This correlation suggests that Mn is the active site for the OER on LSMO (Figure 3.9C). While the transition metal is frequently proposed as the active site^[3,172], direct correlation between $\text{Mn}_e / \text{Mn}_p$ and OER activity has not been reported in perovskite oxides to the best of our knowledge. Finally, the lack of changing oxygen atomic ratio (O_e / O_p) during OER (Figure 3.9B) and the absent correlation between surface oxygen and OER activity supported electrocatalysis involving manganese without participation of lattice oxygen. In contrast, recent findings on other perovskite systems propose the involvement of oxygen vacancies^[56,58,59,61–63]. This is even the case for the structurally similar manganite compound $\text{Pr}_{1-x}\text{Ca}_x\text{MnO}_3$ ($x = 0.0-0.8$)^[61–63], probably due to different contributions of the O 2p states compared to LSMO^[32,59,63]. An increase of OER activity correlates with a drop

of surface La concentration (La_e/La_p in Figure 8.21C, Appendix A) as a result of the $V_{\text{Mn}}'''/D_{\text{La}}'''$ defect couple. Involvement of La as an active site can be excluded on the basis of the LaMnO_3 band structure, where La 4f states are not involved in bonding and 5d states have energies far above the Fermi level^[178]. Future efforts will include in situ studies of the active state of the LSMO (100) surface and further understanding the mechanism of Mn vacancy formation to bolster the stability of LSMO.

3.4 Conclusions

We have successfully extended the RRDE method for the study of epitaxial LSMO thin films with a (100) surface. Using the facile ferri-/ferrocyanide reaction, we demonstrated that such LSMO electrodes exhibit the response of a flat metal electrode. Subsequently, we used these electrodes to study the OER in two laboratories, where we found identical results within error. CV measurements showed high OER activity and identical onset of LSMO disk and Pt ring currents, thereby establishing the detection of oxygen at the ring. Moreover, the same Tafel slopes of about 60 mV/dec within error were found for both the disk and ring currents, indicating a high efficiency for the OER and that the obtained value of the Tafel slope is not hampered by a parasitic process. The obtained value of the Tafel slope indicates that the reaction sequence is characterized by an electrochemical pre-equilibrium followed by a chemical rate-determining step. DFT calculations based on a frozen surface, which assume the B-site as the active site, suggest that the rate-limiting step is the chemisorption of an OH species at an oxidized Mn=O site, i.e., O-O bond formation^[52].

The long-term measurements showed either stable disk currents or in some cases even increasing currents. Extensive post-mortem analysis demonstrated the structural and morphological stability of LSMO during CA, which is highly desirable for practical OER electrocatalysts and model surfaces. OER activity did not correlate with film thickness, conductivity, or strain. Yet, the chemical composition was modified during CA, where La content increased, while surface Mn decreased. The concentration of retained surface Mn correlates with the activity, allowing us to identify Mn as the active site of (100)- oriented LSMO. Although a metal-centered active site is theoretically predicted for OER at perovskite surfaces, clear experimental evidence has been scarce to date. Our finding that

3.4 Conclusions

surface oxygen was maintained after OER is in contrast to observations for other perovskite oxides, where active surface oxygen gives rise to the formation of oxygen vacancies in the active state during OER^[56,58,59,61–63].

Our study established LSMO as an atomically flat oxide with ideal electrochemical properties, high intrinsic activity, and high stability. Moreover, Mn as the active site and the rate-limiting step from Tafel analysis agree well with the mechanism commonly assumed in DFT calculations (Scheme 3.1). Therefore, LSMO thin films can serve as model electrodes to test theoretical predictions regarding the OER mechanism using in situ experiments.

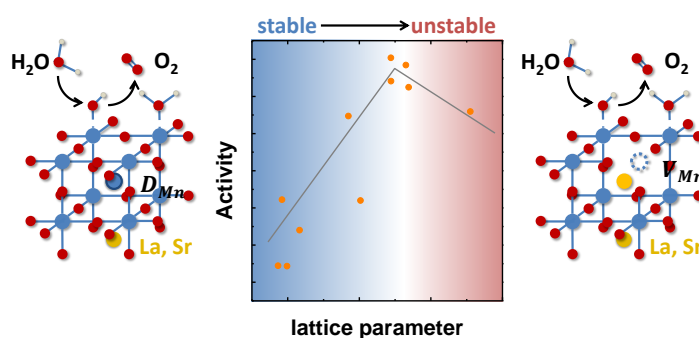
4 Tailoring the oxygen evolution activity and stability using defect chemistry

J. Scholz, M. Risch, G. Wartner, C. Luderer, V. Roddatis, C. Jooss

Reproduced from MDPI Catalysts 7, 139, 2017

Abstract: Improving the activity of catalysts for the oxygen evolution reaction (OER) requires a detailed understanding of the surface chemistry and structure to deduce structure-function relationships (descriptors) for fundamental insight. We chose epitaxial

(100) oriented $\text{La}_{0.6}\text{Sr}_{0.4}\text{Mn}_{1-\delta}\text{O}_3$ (LSMO) thin films as a model system with high electrochemical activity comparable to (110)-oriented IrO_2 to investigate the effect of Mn off-stoichiometry on both catalytic activity and stability. Extensive structural characterization was performed by microscopic and spectroscopic methods before and after electrochemical characterization using rotating ring-disk studies. Stoichiometric LSMO had the highest activity, while both Mn deficiency and excess reduced the catalytic activity. Furthermore, all samples preserved the crystal structure up to the very surface. Mn excess improved the long-term activity and we hypothesize that excess Mn stabilizes the surface chemistry during catalysis. Our data shows that the defect chemistry should be considered when designing catalysts with enhanced activity and rugged stability.



4.1 Introduction

With the world facing limited supply of fossil fuels, the water splitting reaction poses an alternative and promising approach towards sustainable energy. The efficiency of the water splitting reaction is limited by the half reaction of the oxygen evolution reaction (OER) even for the most active materials due to the sluggish kinetics of the four-step electron/proton transfer reaction^[3,4,40,125]. Promising candidates for OER catalysts are first-row transition metal oxides^[38,39,41,42,77,179] as they consist of earth abundant elements, such as Mn, Fe,

Co, and Ni, which can show activities per catalyst area comparable to state-of-the-art catalysts, such as RuO₂ and IrO₂^[76,94,95,126]. Among these catalysts are frequently perovskites with the ABO₃ structure, which show a broad range of properties that arise from tuning of the valence states of the B-site, B-O bonding length and angle by varying the A-site doping, thereby also affecting the catalytic activity for the OER. However, the requirement for deriving design principles for more efficient catalysts is a detailed understanding of the surface chemistry and structure including modifications due to possible side reactions such as corrosion or passivation.

The interplay between structural and electronic properties has gathered broad attention in the search for simple universal descriptors of catalytic activity^[3,39,41,52,67,68,180,181]. Yet, the complex entanglement of structural and electronic properties represents a key-challenge in the experimental deduction of descriptors and the complex dependency of both mechanism and active site on structural and electronic properties. This can be seen for, e.g., chemically similar manganites such as Pr_{0.66}Ca_{0.33}MnO₃ (PCMO) with lattice oxygen proposed as active sites^[61,63] and La_{0.6}Sr_{0.4}MnO₃ (LSMO) with Mn as active site^[179]. These interdependencies complicate the design strategies to tailor the catalytic activity at the atomic level. Nonetheless, structural approaches have been successful in modifying the activity such as variation of strain in LaCoO₃^[130,137,182] and LaNiO₃^[183]. Despite the success of structural approaches tuning the activity, the understanding and detailed control of the active site and the reaction mechanism involves disentangling the effects of strain on catalytic activity either caused by misfit strain or caused by change of lattice parameter due to preparation-induced point defects. These intrinsically different effects cannot be separated out by x-ray diffraction measurements of the lattice parameter alone, but need careful correlation to stoichiometric and off-stoichiometric point defect structure of the samples. The arising impact on the electronic structure will be very different. Direct experimental access to the defect structure is of particular interest as it not only affects the catalytic activity but has strong implications for the stability of the catalyst.

While the implications of defects for the OER, such as impurities and vacancies on activity and stability are frequently discussed^[184–188], detailed studies elucidating the interplay have mainly focused on metals and simple metal oxides so far^[80–83]. In our previous work, we proposed LSMO as model system for a transition metal oxide with a high degree of structural control^[179] allowing to investigate the effects of defects on the stability and activity. By

changing the A-site to B-site ratio resulting in different Mn off-stoichiometries of LSMO under preservation of the epitaxial LSMO structure, it is possible to further elucidate the influence of the electronic structure on the activity and the reaction mechanism for a given defect structure. While the effects on the defect structure and changes in electronic structure by preparation of off-stoichiometric manganites were reported^[85–87], the effects on the catalytic activity have not been addressed to date. Therefore, LSMO represents a model system to evaluate the effects of the point defect structure on catalytic activity. In this study, we prepared $\text{La}_{0.6}\text{Sr}_{0.4}\text{Mn}_{1-\delta}\text{O}_3$ with various off-stoichiometric compositions from Mn excess ($\delta > -0.07$) to Mn deficiency ($\delta < 0.04$) under preservation of the LSMO structure. Extensive characterization involving XRD, AFM, and TEM was employed to firstly ensure structural control and secondly to deduct the influence of the off-stoichiometry on the defect structure. The effects of the Mn off-stoichiometry on both the activity and the stability in terms of defect structure were studied using rotating ring-disk electrode (RRDE) measurements in combination with postmortem analysis. The RRDE setup allows the distinction of the LSMO disk currents corresponding to O_2 evolution from possible side reactions^[141,179], which provides an in-depth analysis on the electrochemical activity and stability. The electrochemical activity and stability showed dependence on the defect structure without affecting the reaction mechanism. Thus, LSMO can serve model system to study the effects of the point defect structure on the activity for more complex oxide catalysts. Furthermore, strategies to tailor the stability of catalyst can be deduced since the defect structure strongly influences the stability.

4.2 Results

In the following, the investigations on off-stoichiometric LSMO are connected by thorough structural characterization (section 4.2.1), followed by electrochemical investigations via RRDE measurements establishing the OER activity (section 4.2.2) and the stability under catalytic conditions involving extensive structural post-mortem characterization (section 4.2.3).

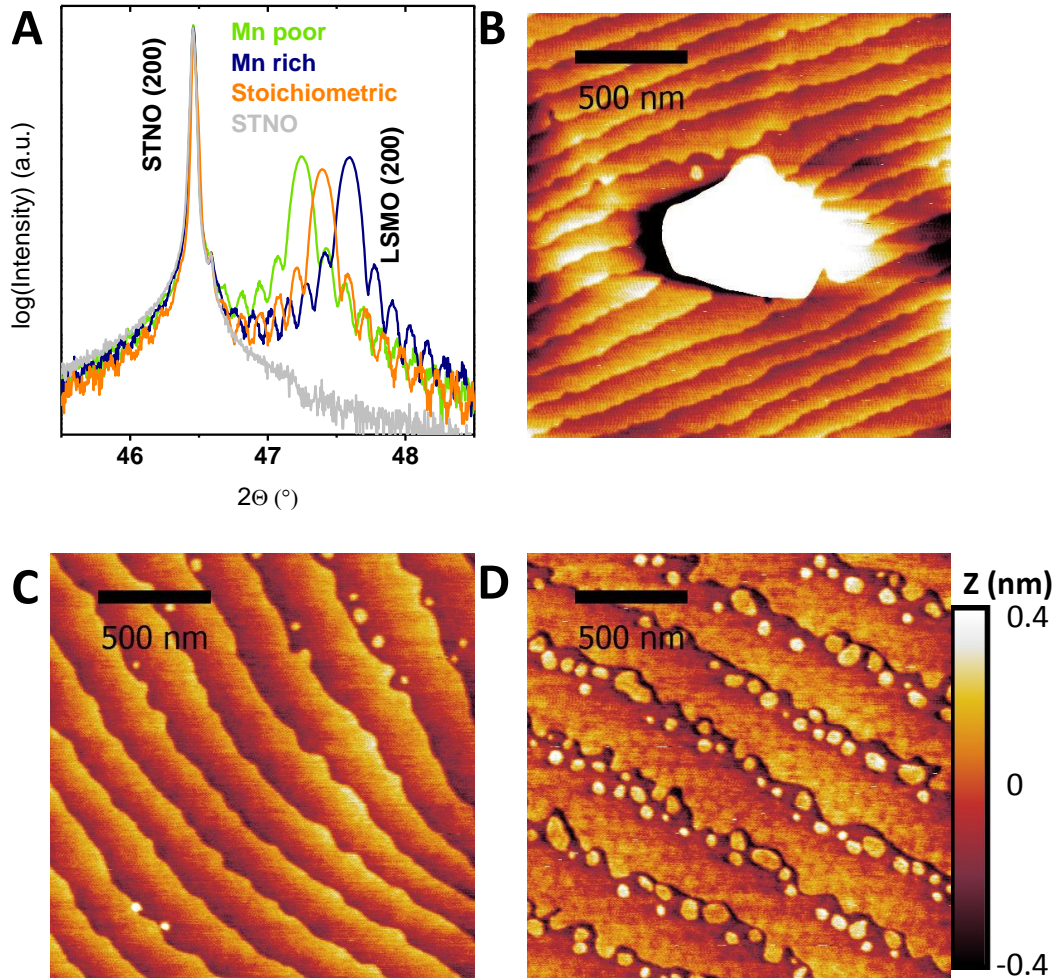


Figure 4.1: (A) Out-of-plane X-ray diffraction on representative samples of all investigated $\text{La}_{0.6}\text{Sr}_{0.4}\text{Mn}_{1-\delta}\text{O}_3$ off-stoichiometries showing only the (200) STNO substrate and the (200) LSMO reflex. (B) - (D) Representative AFM images of (B) a $\text{La}_{0.6}\text{Sr}_{0.4}\text{Mn}_{1-\delta}\text{O}_3$ film with Mn excess showing a typical Mn_3O_4 precipitate, (C) a stoichiometric $\text{La}_{0.6}\text{Sr}_{0.4}\text{MnO}_3$ film, and (D) a Mn-deficient $\text{La}_{0.6}\text{Sr}_{0.4}\text{Mn}_{1-\delta}\text{O}_3$ film. Note the height scale in (D) corresponds to the unit cell step height and is identical for all AFM images. The imaging of the precipitate in (B) requires a larger height scale (see Figure 8.25).

4.2.1 Structural and electronic characterization

Epitaxial (100)-oriented $\text{La}_{0.6}\text{Sr}_{0.4}\text{Mn}_{1-\delta}\text{O}_3$ films with different Mn off-stoichiometry were prepared on (100)-oriented STNO by ion beam sputtering (IBS). Due to different sputter yields of the used elements particularly Mn and La/Sr the off-stoichiometry could be adjusted by choosing different deposition position relative to the target resulting in a variation of Mn content between +7.2 % and -4.1 % with respect to the ideal stoichiometry of $\text{La}_{0.6}\text{Sr}_{0.4}\text{MnO}_3$. The ratio of Sr to La for the chosen Mn off-stoichiometries varied less than 1.5%. The ratio of all components was determined by energy dispersive X-ray spectroscopy (EDX). The epitaxy of all films is indicated by out-of-plane X-ray diffraction measurements (Figure 4.1A) with only the (hoo) reflections of the substrate and LSMO present. The epitaxial growth was confirmed by φ -scans, rocking curves, detailed 2Θ scans, and pole Figures at the (200) reflex (Figures 8.23 and 8.24). The latter exhibit a perfect orientation in-plane with the substrate respectively, while the φ -scans show a four-fold symmetry exhibiting equivalent 'cross-directions' of substrate and film. Both together give evidence for the high epitaxy within the accuracy of measurement setup. The resemblance of LSMO film and corresponding substrate rocking curves indicate epitaxy limited by the substrate quality.

While not affecting the epitaxy, the Mn off-stoichiometry influences both the strain state of the films as well as the surface morphology. Detailed scans on the (200) reflection (Figure 4.1A) show a dependence of the strain state on the Mn off-stoichiometry of the LSMO film and thickness fringes (Laue-oscillations) whose periods are inversely proportional to the film thickness. The lattice parameter decreased with increasing Mn content (Figure 4.3A).

In addition to the variation of the lattice parameter, the surface morphology reveals pronounced effects of Mn excess. All LSMO films deposited at sufficiently high temperatures show atomically flat surface as reported previously^[179]. Atomic force microscopy (AFM) images (Figure 4.1C-D and 8.25) show terraced surfaces with root-mean square (RMS) of 0.12 ± 0.03 nm with only minor differences with stoichiometry (table 8.7). The difference of the terrace width and the unit cell height steps of 0.4 nm is more than two orders of magnitude, the contribution of the terrace edges to the total surface area is negligible. The increased roughness for samples with Mn excess is due to formation of Hausmannite, i.e., Mn_3O_4 (Figure 4.1B) with the surface of the surrounding film being identical to the stoichiometric and Mn deficient films. The formation of related MnO or

MnO₂ precipitates was previously reported for Pr_{0.66}Ca_{0.33}MnO₃^[189] and was predicted by Grundy et al for La_{0.6}Sr_{0.4}MnO₃^[190] to occur for Mn excess of more than 0.4 %. The identification of the precipitates in our LSMO films as Mn₃O₄ is based on EDX and electron energy loss spectroscopy (EELS) analysis (for details see Figures 8.26, 8.27). The density of precipitates scaled with the Mn excess and was evaluated using scanning electron microscope (SEM) images (Figures 8.28, 8.29). However, even for a Mn excess of 7.2 % the estimated contribution of the surface of the precipitates to the overall surface area was with a maximum of 1.6 % negligible.

Furthermore, detailed TEM analysis revealed no grain boundaries or other defects as can be seen in Figure 4.2A and no differences in the crystal structure of the LSMO film besides the formation of precipitates as can be seen in Figure 4.2B. Based on the models in refs.^[85,86,191], Mn off-stoichiometry is assumed to be compensated by generation of point defects, which are either accompanied by changes in Mn valence and/or the presence of vacancies. The Mn valence can be determined using the energy difference between the pre-edge of the O K-edge and the onset of the Mn L-edge in EELS^[192,193]. This method was used since it does not depend on the intensity of the Mn L-edge or O K-edge in contrast to other methods^[61,87,194–196], which can be corrupted by C surface layers. In LSMO films with Mn excess at areas far from the Mn₃O₄ precipitates, the Mn valence appears to remain unchanged within error compared to the stoichiometric LSMO (Figure 8.31). For the pristine samples, the observed decrease in Mn valence towards the surface (Figure 8.32) can be attributed to preparation induced oxygen deficient regions less than 2 nm or surface damage related oxygen deficiency due to ion milling required for the TEM lamella preparation.

While it is challenging to directly relate changes in the electronic structure to the effects of vacancies, sufficiently high electron doping by oxygen vacancies induces a shift of the onset of the EELS O K-edge feature^[197]. However, no differences in the O K-edge within measurement accuracy were observed between stoichiometric LSMO and LSMO with Mn excess as can be seen in Figure 4.2C. The dependence of the O K-edge on the local electronic structure is shown by EELS scans across the interface between STNO substrate and LSMO film (Figure 4.2C and 8.33), where particularly the pre-edge changes. Supported by the lack of apparent changes in both O K-edge and Mn L-edge (Figure 4.2C,

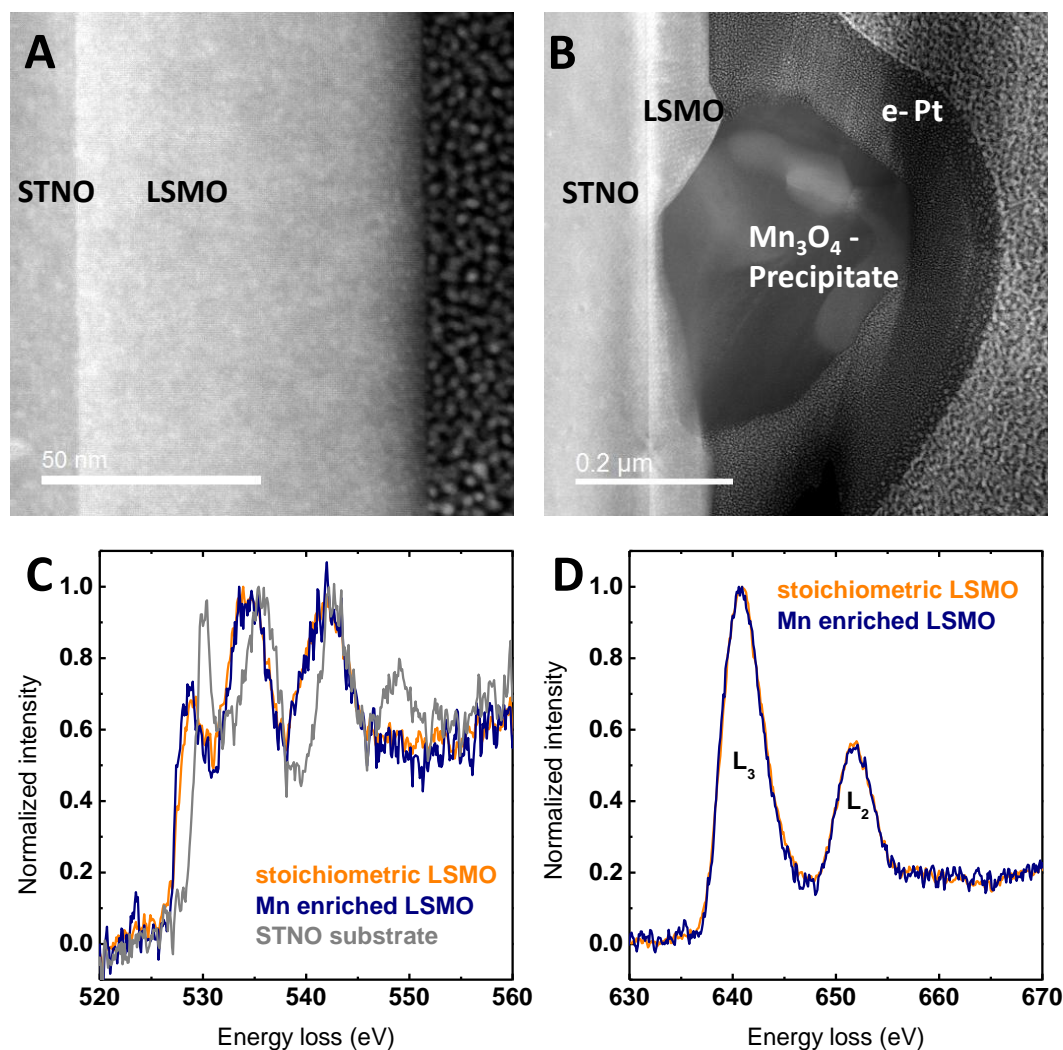


Figure 4.2: (A) HR-STEM image showing the defect-free film from the STNO substrate to the surface of $\text{La}_{0.6}\text{Sr}_{0.4}\text{Mn}_{1-\delta}\text{O}_3$ film with Mn excess. (B) TEM image showing cross section of typical precipitate on a $\text{La}_{0.6}\text{Sr}_{0.4}\text{Mn}_{1-\delta}\text{O}_3$ film with Mn excess. (C) Oxygen K-edge EELS comparing a $\text{La}_{0.6}\text{Sr}_{0.4}\text{Mn}_{1-\delta}\text{O}_3$ film with Mn excess, stoichiometric $\text{La}_{0.6}\text{Sr}_{0.4}\text{MnO}_3$ film, and the STNO substrate. (D) Mn L-edge EELS comparing films of $\text{La}_{0.6}\text{Sr}_{0.4}\text{Mn}_{1-\delta}\text{O}_3$ with Mn excess and stoichiometric $\text{La}_{0.6}\text{Sr}_{0.4}\text{MnO}_3$. The resolution of the EELS measurements is evaluated in Figure 8.30.

D), no indications could be found for the presence of bulk oxygen vacancies assumed for a Schottky defect couple (anion and cation vacancies preserving charge neutrality).

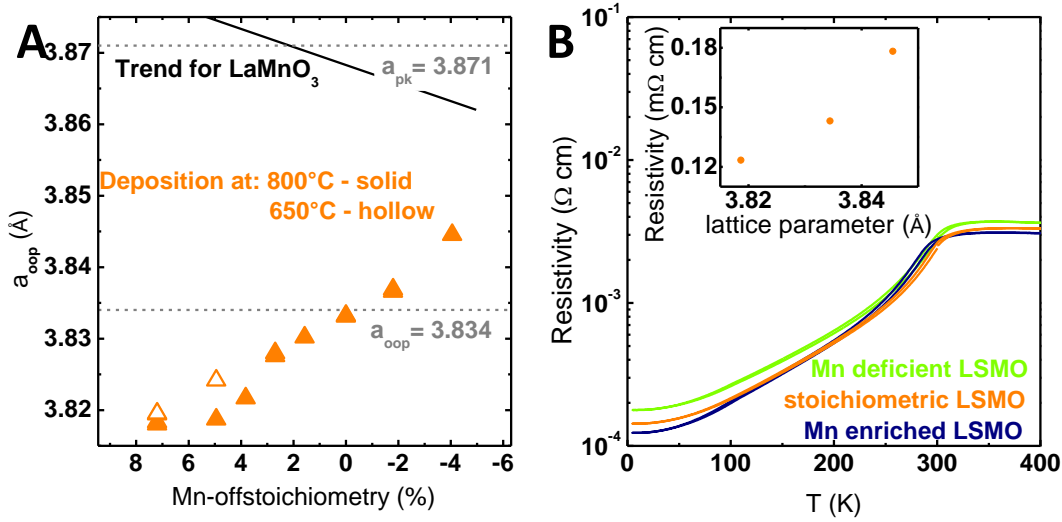


Figure 4.3: (A) Out-of-plane lattice parameter correlated with the total Mn off-stoichiometry. The lattice parameter was calculated based on wide angle out-of-plane X-ray diffraction measurements using a monochromator. The shown trend of the lattice parameter with changing Mn content (black line) for LaMnO_3 is based on Marozau et al.^[85]. (B) Bulk conductivity of $\text{La}_{0.6}\text{Sr}_{0.4}\text{Mn}_{1-\delta}\text{O}_3$ films with different Mn off-stoichiometries and identical thickness measured by PPMS. The inset shows the extracted remanent resistance at 4 K correlated with the respective lattice parameter.

The observed shift of the XRD peak position was used to evaluate the structural effect of Mn off-stoichiometry and to gain further insight into the present defects. The calculated out-of-plane lattice parameter decreased continuously with increasing Mn content (Figure 4.3A). The stoichiometric lattice parameter did not match the bulk values reported in literature (pseudo cubic lattice parameter $a' = 3.871$ Å)^[152] but matched the out-of-plane lattice parameter calculated assuming a tetragonally strained LSMO film (see refs.^[143,146]) with an identical in-plane lattice parameter of the substrate ($a = 3.905$ Å)^[155] and LSMO film with preservation of the cell volume and the resulting out-of-plane lattice parameter of $a'' = 3.833$ Å. As the strain state of LSMO films and thereby the lattice parameter depend on the preparation methods and conditions^[153,154], the observed trend might be due to preparation-induced defects. A spatial variation of preparation induced defect is reflected exemplarily by the gradient of incorporated Xe atoms (Figure 8.34). Since the incorporated Xe atoms

correspond to transferred additional momentum during the growth process an influence on the defect formation is conceivable.

In addition to the influence of the preparation, the trend of the lattice parameter with the Mn off-stoichiometry is discussed to reflect the defect structure introduced by the Mn off-stoichiometry. For the closely related LaMnO_3 ^[85,86] and SrMnO_3 ^[87], an increasing lattice parameter with increasing Mn content was observed and explained by the formation of A-site vacancies for Mn excess and Mn vacancies for Mn deficiency. Marozau^[85] proposed that the formation of A-site vacancies was accompanied with oxygen vacancies (Schottky defects) for Mn excess that should induce changes in the EELS structure as well as result in increasing lattice parameters. The increasing lattice parameter (Figure 4.3A) in addition to the lack of evidence for oxygen vacancies in EELS indicate that the detailed defect structure in our samples might differ from that in the study of Marozau^[85]. The implications of the observed defect structure for catalytic activity and stability will be discussed in section 4.3.

To further investigate the influence of Mn off-stoichiometry, temperature dependent electric transport measurements were conducted on all samples, which showed nearly identical highly conductive behavior and only minor differences in resistivity (see Figure 4.3B). Note that the residual resistivity at 4 K scaled with the Mn off-stoichiometry. The increased resistivity of the Mn deficient LSMO film points to defect scattering and thus to the presence of Mn vacancies. In contrast, the reduced resistivity both above T_c and at low T for the Mn-rich LSMO film indicated changes of the electronic structure such as bandwidth, induced by lattice strain. Therefore, the residual resistivity at 4 K scaled with the out of plane lattice parameter (inset of Figure 4.3B), but has a different mechanistic origin. In summary, despite of Mn excess induced formation of precipitates, the main fingerprint of Mn off-stoichiometry in LSMO is a change of the out-of-plane lattice parameter. It reflects a change in point defect concentration which is both due to a spatial variation of the stoichiometry superimposed by spatial variation of preparation induced defects as indicated by the gradient in incorporated Xe. Having established the structural properties and the highly conductive nature of all LSMO off-stoichiometries, we can evaluate the influence of Mn off-stoichiometry on catalytic activity.

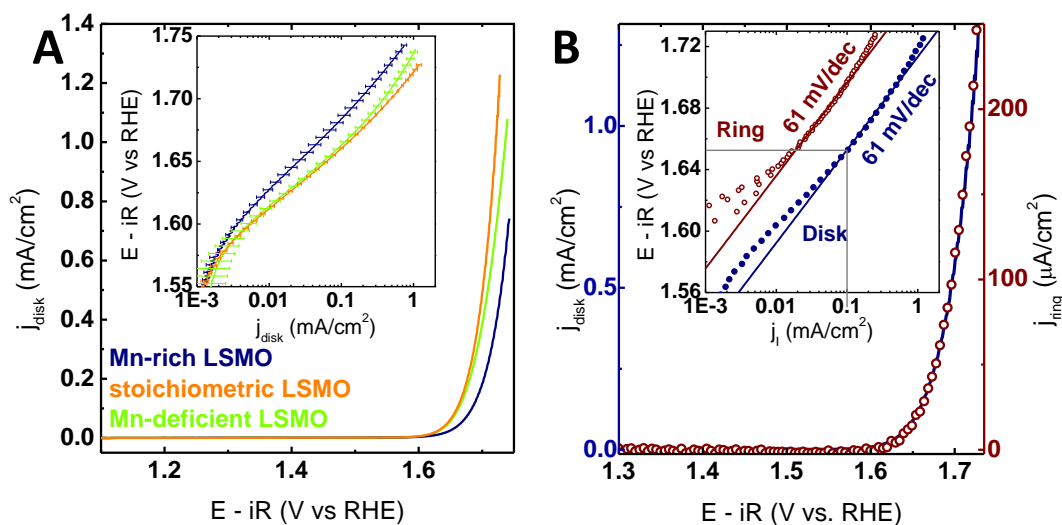


Figure 4.4: (A) Linear sweep voltammograms (LSV) of all investigated off-stoichiometries averaged over the positive scan direction (table 8.8). The inset shows the Tafel analysis for the averaged positive scans for each sample of the respective stoichiometry. The error bars are based on the mean deviation. (B) LSV measurement in positive scan direction of a stoichiometric $\text{La}_{0.6}\text{Sr}_{0.4}\text{MnO}_3$ film (solid blue line) and the corresponding ring current (open red circles) obtained by chronoamperometry (CA) at 0.4 V vs. RHE. The inset shows the Tafel analysis of the Pt ring (red circles) and the disk LSMO (blue circles) currents as a function of disk voltage obtained from LSV. All measurements were performed with Ar-purged 0.1 M KOH supporting electrolyte at 10 mV/s and 1600 rpm. The voltage was corrected for electrolyte resistance (47Ω)

4.2.2 Electrochemical characterization

In order to evaluate the effects of the Mn off-stoichiometry on the catalytic activity, all samples were characterized electrochemically where both the activity and stability was probed by cyclic voltammetry (CV). With the suitability of LSMO for electrochemical measurements previously established and CV measurements allowed direct analysis of OER activities^[179]. The effect of the Mn off-stoichiometry on the catalytic activity was studied by linear sweep voltammograms (LSV) extracted from CV for measurements averaged over all samples of each respective Mn off-stoichiometry (Figure 4.4A). The stoichiometric samples are the most active ones and the activity of LSMO with Mn deficiency is only marginally smaller considering the error. Samples with Mn excess exhibited a significantly lower activity, where higher excess further decreased the activity (Figure 8.35). These differences are shown both in the overpotential required to reach $100 \mu\text{A}/\text{cm}^2$ and the current densities at a fixed potential of 1.7 V vs. RHE (see table 4.1). In contrast to electrodeposited films or supported nano-particles reported in literature^[40,94,126,140,141], for all samples investigated here, the geometric surface equals the oxide surface area due to the low surface roughness (table 8.7). Moreover, the observed current densities of $100 \mu\text{A}/\text{cm}^2$ at potentials of 1.66 V vs. RHE for the stoichiometric samples are consistent with our previous findings, further supporting the fairly high intrinsic activity of stoichiometric (100) LSMO films, which is comparable to, e.g., (110) IrO_2 films with an overpotential of 460 mV (1.69 V vs. RHE) at $100 \mu\text{A}/\text{cm}^2$ ^[95] and to the similar (100) oriented $\text{La}_{0.8}\text{Sr}_{0.2}\text{MnO}_3$ with an overpotential of 470 mV (1.70 V vs. RHE) at $100 \mu\text{A}/\text{cm}^2$ ^[131]. However, LSMO showed lower activity compared to the benchmark catalyst (100) RuO_2 films with an overpotential of 290 mV (1.52 V vs. RHE) at $100 \mu\text{A}/\text{cm}^2$ ^[95] and LaCoO_3 with an overpotential of 360 mV (1.59 V vs. RHE) at $100 \mu\text{A}/\text{cm}^2$ ^[3] (additional comparison in table 8.6). We compared epitaxial thin films to provide an unbiased comparison of these low surface area materials which allow for fundamental mechanistic studies of single surface orientations.

For the samples with Mn excess, the contribution of the Mn_3O_4 precipitates to the catalytic activity needs to be considered because Mn_3O_4 was reported as having a significant activity for the OER with a 290 mV overpotential at a current density of $0.1 \text{ mA}/\text{cm}_{\text{geo}}^2$ ^[198]. However, a direct comparison to the observed

4.2 Results

Sample	Mn-off stoichiometry (%)	Overpotential at $100 \mu\text{A}/\text{cm}^2$ (mV)	j_l at 1.7 V vs. RHE ($\mu\text{A}/\text{cm}^2$)	Tafel slope disk (mV/dec)	Tafel slope ring (mV/dec)
LSM-2	-2.0	434	385	61	62
LSM-4	-4.1	437	341	58	59
LSM-2	-2.0	431	460	59	62
LSM	~ 0.0	430	502	60	59
LSM	~ 0.0	433	588	61	61
LSM+2 ^a	+1.6	453	217	63	64
LSM+4 ^a	+3.8	449	218	63	63
LSM+7	+7.2	458	162	61	63
LSM+5	+5.4	449	226	57	61
LSM+7	+7.2	458	167	59	62

Table 4.1: Catalytic parameters for all investigated samples. Mn off-stoichiometry is based on the Mn gradient of the total Mn concentration. Note that the amount of Mn dissolved in the LSMO matrix might differ (for details see Figure 8.36). ^a samples of ref.^[179]. These samples showed no precipitates.

highly crystalline precipitates is complicated by the fact that ref.^[198] considers electrodeposited films with undefined geometric surface. Nonetheless, a change of activity with increasing Mn_3O_4 contribution as well as change of Tafel slope due to changing mechanism could be expected. The observed decrease in activity with increasing density of precipitates (Figure 8.35) suggests inferior activity of the precipitates as compared to LSMO. Furthermore, no change in Tafel slope was observed, which indicated that the mechanism of OER on LSMO was not affected by the precipitates. Note that for LSMO films with Mn excess, but without Mn_3O_4 precipitates the activity also was reduced (Figure 8.35B). This indicates a predominant effect of Mn excess on the LSMO activity rather than an effect of the precipitates.

The onset of the OER was investigated by RRDE measurements. By rotation of the RRDE, the O_2 produced during OER at the disk electrode is transported outwards by forced convection to a Pt ring electrode. At the Pt ring electrode, the O_2 is reduced under mass limiting condition, i.e. the ring currents depend only on the concentration of O_2 (see calibration measurements in Figure 8.1). The reduction of species other than O_2 is possible at 0.4 V vs. RHE at the ring electrode. However, as discussed in ref.^[179] for LSMO, no indication was found for possible side reactions such as formation of permanganate or peroxide (Figure 8.11). Thus, it was concluded that the observed ring currents

solely correspond to dissolved oxygen, which allows the correlation of disk currents to ring currents corresponding to evolved oxygen. For all samples, the observed exponential increase in disk currents corresponded to an increase in ring currents (exemplarily shown for stoichiometric LSMO in Figure 4.4B, all other samples in Figure 8.37), suggesting that the onset observed for LSMO is in fact the onset of OER.

Moreover, the ring currents under these conditions can be used for mechanistic insight by Tafel analysis as proposed in our previous work. Despite the observed differences in activity for the different Mn off-stoichiometries, the Tafel analysis for all samples showed Tafel slopes of 60 ± 2 mV/dec and 62 ± 2 mV/dec for the ring electrodes (table 4.1, Figure 4.7A). Identical Tafel slopes at ring and disk electrodes suggest that neither capacitance nor corrosion affected the disk currents representing high efficiency for the OER. Additionally, the Tafel slope can be theoretically modelled based on a sequence of elementary reaction steps, having a rate limiting step and pre-equilibria^[48–50]. The observed Tafel slopes fit the theoretical determined slope of 59 mV/dec for the OER at 25 °C corresponding to an electrochemical pre-equilibrium followed by a chemical rate- determining step, such as O-O bond formation. Hence, we conclude the mechanism of the OER was not affected by Mn off-stoichiometry (further discussed below).

4.2.3 Stability characterization

In order to evaluate the effects of the Mn off-stoichiometry on the stability under catalytic conditions, all samples were characterized using prolonged electrochemical cycling following the initial characterization. By comparing the overpotential required to obtain a current density of $100 \mu\text{A}/\text{cm}^2$ throughout 100 consecutive cycles between 1.1 and 1.75 V vs. RHE (corresponding to a total measurement time of $\sim 3:40$ h), we observed no pronounced activation or decrease in overpotential (Figure 4.5). The overpotential of the Mn-deficient sample increased by ~ 25 mV, while the change in overpotential for the stoichiometric sample increased only by 10 mV. Notably the sample with Mn excess showed an increase in overpotential of less than 2 mV during 100 cycles leading to the highest long-term stability as well as an activity surpassing that of the Mn-deficient samples and approaching that of the degrading stoichiometric

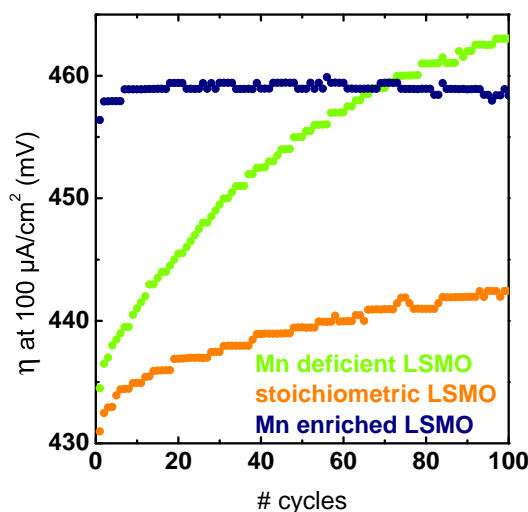


Figure 4.5: Overpotential required to obtain $100 \mu\text{A}/\text{cm}^2$ extracted from the positive scan direction of 100 consecutive CV measurements. The measurement protocol applied to the samples prior to extensive CV measurements was identical for all samples. All electrochemical measurements were performed in Ar-saturated 0.1 M KOH supporting electrolyte and 1600 rpm.

sample. Additional chronoamperometric measurements showed comparable stability trends (Figure 8.38). Hence, we conclude that high long-term stability and activity strongly depends on the Mn off-stoichiometry. In addition to the changes in activity during long-term measurements, the effect on the reaction mechanism was evaluated by comparing the initial to the final LSV measurements (Figure 8.39). The comparison reveals only small changes in the Tafel slope of less than 8 mV/dec, indicating no significant change in the dominant reaction mechanism so that the observed changes can be compared directly. Thereby we can state that the Mn-deficient samples were the most unstable ones and despite the lowest initial overpotential, the activity of the stoichiometric samples degraded less than that of the Mn-deficient samples but still noticeably. Moreover, LSMO with Mn excess has the lowest activity and showed the highest stability to the effect that it surpassed LSMO with Mn deficiency after ~ 60 cycles.

As the electrochemical measurements showed differing long-term behavior, extensive post-mortem analysis using AFM, XRD, XRR, REM, and TEM was employed to elucidate the observed behavior. AFM images as exemplarily shown in Figure 4.6A revealed no significant roughening even for the Mn-deficient sample with the most extreme changes during extensive cycling.

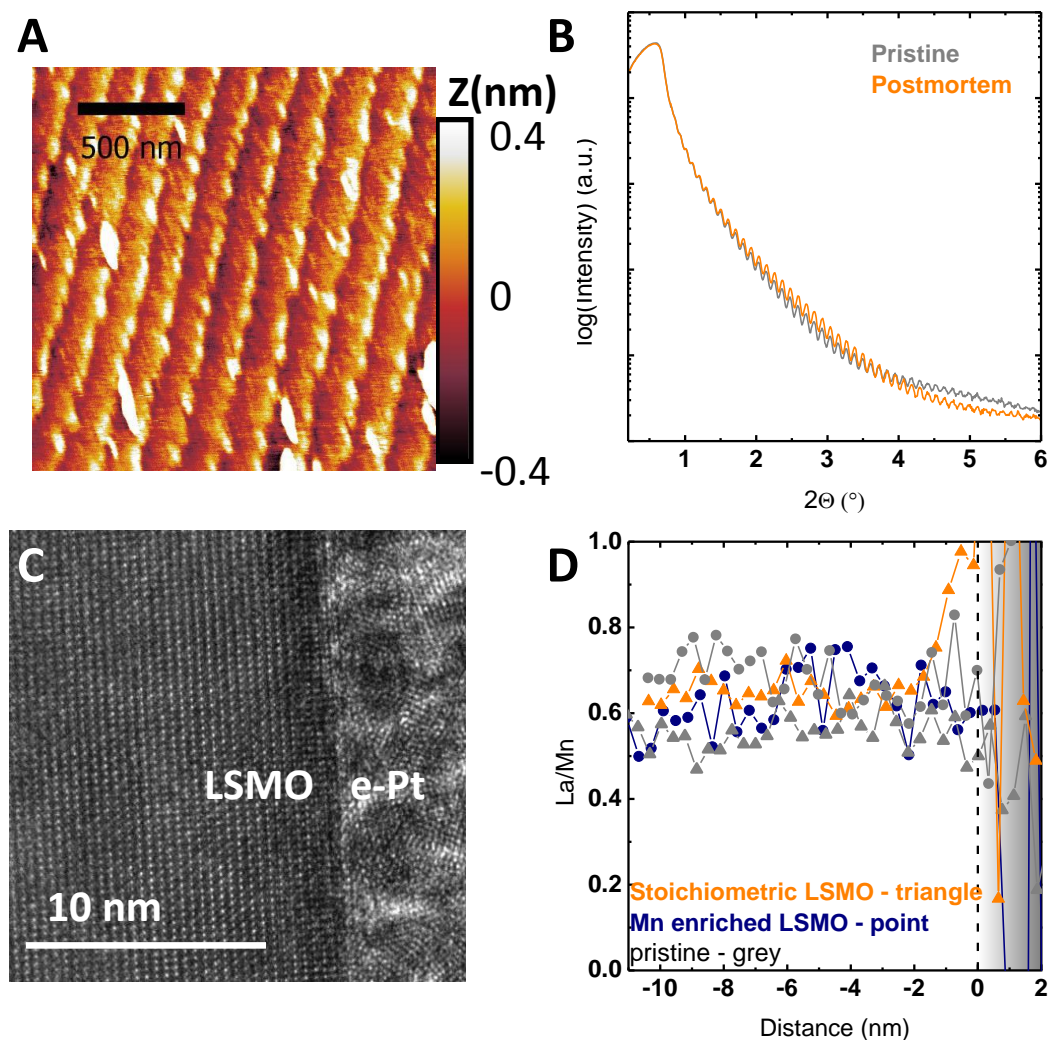


Figure 4.6: (A) Representative AFM image of a Mn-deficient sample after extensive cycling. (B) XRR patterns of the same Mn-deficient sample shown in (A). (C)-(D) Post-mortem TEM characterization of a stoichiometric LSMO sample after chronoamperometric measurement. (C) HR-TEM image of the surface of the stoichiometric LSMO sample showing the preservation of the crystallinity at the interface to the electron-beam deposited Pt. (D) Correlation between the EELS data across the interface and the electrochemical treatment for different samples obtained by STEM mode. The ratio was determined for the concentration normalized to the respective bulk concentration to allow comparison of relative changes across the interface (for details of EELS analysis see Figure 8.30-8.33). The interface to the electron deposited Pt is indicated by the dashed line at 0 nm

Moreover, the surface morphology remained intact during extensive cycling preserving the unit cell step height and suggesting the preservation of the crystal structure. Additionally, only changes of the lattice parameter of less than 0.03 % after electrochemical treatment were measured by XRD. Note that adjustment accuracy can result in differences in lattice parameter within the observed range. Furthermore, these subtle changes did not correlate with the Mn content (Figure 8.40). The loss of material would be conceivable, e.g. by the formation of the soluble $\text{Mn}^{\text{VII}}\text{O}_4$ according to the Pourbaix diagram^[73,79]. However, XRR measurements Figure 4.6B did not support significant structural changes due to corrosion or roughening by showing changes in film thickness of less than 0.5 nm (with only one exception of a Mn enriched sample; see table 8.8) and only small changes in the high angle part of the diffractogram. The changes in the high angle part can be attributed to variation in density and roughness at the surface or the internal interface.

The absence of significant changes applies to all samples, but as AFM, XRD, and XRR are not sensitive to the changes of the precipitates, statistical analysis using REM was used to evaluate the role of Mn_3O_4 precipitates. Here the evaluated parameters were the density of precipitates per area and the mean diameter of the precipitates. Despite the considerable error due to the statistical deviations over the whole sample area, we note the tendency of decreasing particle densities and increasing mean diameter shown in Figure 8.29. The detachment of precipitates can be understood considering the interface between the precipitates and the LSMO as a possible weak link. By the formation of soluble species, the effect of an unstable interface is more pronounced for smaller precipitates with higher surface to volume ratio. Thereby smaller precipitates might detach before big precipitates leading to an increase in the mean diameter and decreasing particle densities. Additional indications can be found in Figures 8.28B and D, showing remaining holes after electrochemical treatment.

The observed stability of the film was further supported by HR-TEM analysis (Figure 4.6C) showing the preservation of the crystal structure up to the very surface and stability down to the atomic scale. In addition, EELS allows evaluating chemical changes due to electrochemical treatment at the atomic scale. As reported for nearly stoichiometric LSMO^[179], the long-time performance under catalytic conditions at 1.7 V vs. RHE led to enrichment of La within a region of 2 nm, which is close to the resolution limit of 1.5 nm of the used setup (Figure 8.30). This enrichment in La can be seen by the increase in La to Mn ratio

towards the surface (Figure 4.6D) and presumably partial dissolution of Mn within the first unit cells was explained by the defect couple of V_{Mn}''' / D_{La}''' . The La to Mn ratio determined by EELS analysis was compared for stoichiometric and samples with Mn excess (Figure 4.6D). While the stoichiometric sample showed the same trend as observed by XPS in ref.^[179], no enrichment of La was found for samples with Mn excess after electrochemical treatment. Additionally, no significant change was found in the bulk stoichiometry after the electrochemical stability measurements (Figure 4.6D). To elucidate subtle changes in the electronic structure due to electrochemical treatment, the fine structure of the Mn L-edge was analyzed. The oxidation of Mn would result in changes in the O K-edge and the Mn valence accessible by EELS. Direct comparison between both the initial Mn L-edges as well as the post-mortem Mn L-edges revealed an increase in Mn valence in the vicinity of the surface presumably due to healing of oxygen deficiency by the electrochemical treatment. Thereby, we found indications for subtle changes in the surface chemistry in addition to the exclusion of surface roughening and exclusion of significant loss of material. Nevertheless, the Mn off-stoichiometry affected the stability as the samples with Mn excess are the most stable samples in terms of activity as well as absence of structural and chemical changes. It appears that the Mn excess poses as a stabilizing mechanism against Mn dissolution (further discussed below).

4.3 Discussion

In order to disentangle the effects of the Mn off-stoichiometry, one needs to distinguish between its effect on activity and stability. The initial assumption based on our previous work^[179] is that the activity is expected to depend on the Mn concentration in the near surface region as Mn is considered to be the active site. The Mn deficiency does influence the activity, which could be understood in terms of a reduction in number of active sites. Before considering the effects of Mn excess, it should be noted that one needs to distinguish between the nominal Mn off-stoichiometry including the precipitates and the Mn incorporated in the LSMO film without the precipitates. This distinction is necessary since the formation of Mn_3O_4 precipitates effectively removes excess Mn from the LSMO film. Furthermore, as Mn excess influences the activity even for negligible densities of precipitates (Figure 8.35B and Figure 8.36C),

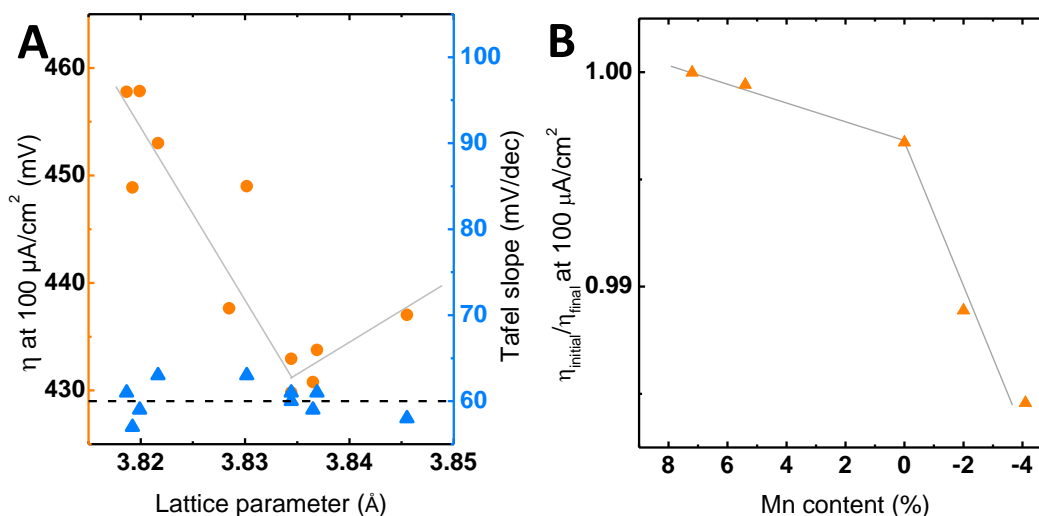


Figure 4.7: (A) The overpotential to obtain $100 \mu\text{A}/\text{cm}^2$ and the Tafel slope determined under identical conditions (see experimental section) correlated with the lattice parameter based on the forward direction of the 3rd initial CV measurement. (B) Relative changes of the overpotential to obtain $100 \mu\text{A}/\text{cm}^2$ of the 1st cycle compared to the 100th cycle with respect to the total Mn off-stoichiometry. All electrochemical measurements were performed in 0.1 M KOH supporting electrolyte (Ar) and 1600 rpm. The indicated lines are only to guide the eye.

we conclude that the activity strongly depends on excess Mn dissolved in the LSMO film.

Next, we correlate the observed effects of the Mn off-stoichiometry on the activity to the observed structural changes. The structural changes are reflected by a point defect induced change in LSMO out-of-plane lattice parameter (Figure 4.3A), which decreases with increasing Mn content. Comparing the lattice parameter to the electrochemical activity in terms of overpotential (Figure 4.7A), we observe that the activity scales with the lattice parameter and has a clear overpotential minimum for stoichiometric LSMO, i.e. in the absence of both Mn defects and vacancies. Here, the highest activity evolves at an out-of-plane lattice parameter that corresponds to the relaxed out-of-plane lattice parameter assuming identical in-plane parameters of LSMO film and the substrate as well as volume preservation. The correlation to the activity thereby indicates a maximum of the activity at a minimum of structural distortion as we have also argued for related perovskites^[67]. Effects of strain on the catalytic activity were reported previously for LaCoO_3 , SrCoO_3 ^[130,137] and LaNiO_3 ^[183], where the origin of the influence of strain on the activity was explained by strain induced changes in the electronic configuration^[183] via differences in the

charge transfer resistance^[137] or the amount of oxygen vacancies introduced by strain^[130]. These examples illustrate the complex interplay and dependencies of electronic structure on the structural parameters and possible experimental approaches to evaluate the dependencies.

To understand the implications of structural changes, such as strain, we need to consider the effects of the Mn off-stoichiometry. The changes of strain alone do not account for the complete effect of the Mn off-stoichiometry. Comparing the changes in activity resulting from the Mn off-stoichiometry to the introduced variation of the lattice parameter (caused by variations in film thickness) showed a dominant effect of the Mn off-stoichiometry (Figure 8.41). The significance of the impact of the Mn off-stoichiometry indicates that the role of the Mn off-stoichiometry on the defect structure has to be elucidated in more detail. Some reports have attributed the change of lattice parameter to the characteristics of defect chemistry. As reported for LaMnO_3 ^[85,86] and SrMnO_3 ^[87], a systematic variation of A-site to Mn ratio resulted in Mn vacancies for Mn-deficient samples and La vacancies for samples with Mn excess accompanied by the formation of oxygen vacancies and preservation of the charge neutrality by changing Mn valence states.

The nature of the defects in the presented samples needs to be evaluated as the trend of the lattice parameter is opposite to the previously reported trends^[85–87] (Figure 4.3A). In order to unravel the underlying defect chemistry, we consider two scenarios for LSMO with Mn excess: the previously proposed formation of A-site vacancies coupled to formation of oxygen vacancies (scenario A) and formation of Mn defects located at the A-site (scenario B).

In scenario A, the assumption of Mn excess leads to the formation of Schottky defects, which would result in an increase in lattice parameter as well as indications for oxygen vacancies in the fine structure of the O K-edge (Figure 4.2C). Electrochemical treatment might then decrease the number of oxygen vacancies by electrochemical oxidation. As stated above, we observed a decrease in lattice parameter and found no evidence for oxygen vacancies in the bulk. Note that the increase in valence subsequently to the electrochemical treatment is present for stoichiometric LSMO and LSMO with Mn excess (Figure 8.31), presumably due to a small oxygen deficient region within the outmost 2 nm of the surface. Therefore, we conclude that the formation of Schottky defects for samples with Mn excess is negligible.

In scenario B; Mn excess might lead to the formation of substitutional Mn defects at the A-site, which would result in a reduced lattice parameter as the

ion radius of Mn^{3+} (0.58 Å) is significantly smaller than both La (1.36 Å) and Sr (1.44 Å)^[199] in a simplistic geometric model. Furthermore, a substitutional Mn defect would result in a small decrease in Mn valence as the charge of 2.6+ at the A-site needs to be compensated by Mn ($\text{Mn}^{3.4+}$ in LSMO), thereby reducing the Mn oxidation state towards Mn^{3+} . We observed a small but insignificant decrease in Mn valence between stoichiometric LSMO and LSMO with Mn excess (Figure 8.31). The oxidation of Mn following the electrochemical protocol is not expected as no oxygen vacancies should be present. However, as the effect is limited to the very surface, we cannot exclude that surface regions were damaged by film preparation. Mainly supported by trend of decreasing lattice constants, we hypothesize that the excess Mn in the LSMO might be located at the A-site and compensate for the changes in charge. The reduced activity of LSMO with Mn excess suggests that Mn located at the A-site would not participate as active site.

For Mn-deficient manganites, the formation of Mn vacancies was previously reported^[85,87]. With the assumption of the formation of Mn vacancies for Mn deficient LSMO, the increase in resistivity observed in transport measurements (Figure 4.3B) as well as the differences in activity (Figure 4.7A) can be understood. The formation of Mn vacancies will affect the conductivity depending on the Mn-O-Mn bonds resulting in increasing resistance. Moreover, the formation of Mn vacancies might limit the activity due to fewer Mn participating as active sites in Mn deficient LSMO.

In addition to the effects on the catalytic activity, the defect chemistry will presumably also affect the chemical stability by facilitating different corrosion pathways. Figure 4.7B shows the ratio of the overpotential in cycle 1 to cycle 100 as a measure of long-term behavior for the investigated Mn off-stoichiometries. Here despite having a limiting effect on the activity, the excess Mn appears to stabilize the LSMO as the change in overpotential ratio is negligible for LSMO with Mn excess but significant for LSMO with Mn deficiency. In our previous work^[179], we proposed that the changes in surface chemistry observed by XPS during the long-term stability measurements are triggered by the charge imbalance introduced during Sr^{2+} dissolution. This charge imbalance was proposed to lead to the formation of a $V_{\text{Mn}}''' / D_{\text{La}}'''$ defect couple that we monitored here (Figure 4.6D). The formation of the $V_{\text{Mn}}''' / D_{\text{La}}'''$ defect couple was previously associated with a decrease in activity^[179]. Modifying the generation of this defect couple by Mn off-stoichiometry thus represents a possible pathway for tuning the long term activity. The La enrichment measured only in case of the

stoichiometric sample by chemical analysis with EELS (Figure 4.6B) supports the assumption of differences in the surface chemistry stated in scenario B.

Considering the defect chemistry for LSMO with Mn excess, the effect of Mn off-stoichiometry on the electrochemical stability can be understood. Under the assumption of the proposed corrosion pathway, Mn located the A-site as substitutional defects might hinder pronounced formation of the V_{Mn}''' / D_{La}''' defect couple. Thereby the lack of change in surface composition will preserve the initial Mn excess with its original activity or serve as internal reservoir replacing the fraction of dissolved B-site Mn. Therefore, we assume that the preservation of the catalytic activity as can be seen in Figure 4.7B and Figure 8.39A can be obtained by stabilization of the BO_3 network. Accordingly, for Mn deficient samples, the formation of the V_{Mn}''' / D_{La}''' defect couple might not be hindered leading to a more pronounced corrosion compared to stoichiometric LSMO as even less Mn is available in the bulk to replace potential vacancies at the surface. Based on these assumptions, the trend of LSMO with Mn excess being the most stable and Mn deficient LSMO being the most unstable (Figure 4.7B) can be understood.

4.4 Materials and Methods

Film fabrication: $La_{0.6}Sr_{0.4}MnO_3$ (LSMO) electrodes used for electrochemical and electric measurements were prepared by ion-beam sputtering (IBS). Round 0.5 wt% Nb-doped $SrTiO_3$ (STNO) and rectangular undoped $SrTiO_3$ (STO) with (100)-orientation (CrysTec GmbH) were used as substrates. The stoichiometry of the prepared films depends on the deposition position due to element specific sputter yield and was determined based on the position where MnO_x precipitates begin to form as described in ref^[189]. The stoichiometry gradients were measured by EDX on samples with 2 μm thickness to avoid superposition of Sr and O X-ray emission lines by contribution of the STO substrate. The films were deposited at 800 °C or 650 °C in an oxygen atmosphere of 1.7×10^{-4} mbar. To reduce the amount of preparation-induced defects, the prepared films were kept under preparation conditions for 1 h, and carefully cooled down to room temperature including a resting point of 30 min at 500 °C. To suppress the formation of MnO_x precipitates reference samples were prepared at a deposition temperature of 650 °C. These samples were only used for

structural analysis. The film thickness of 80 nm was chosen and controlled by X-ray reflectometry (XRR). The assembly of the RRDE electrodes is described in detail in ref [9]. In short, backside contacts for the STNO substrate consisted of 5 nm Ti and 100 nm Pt layers prepared by IBS at room temperature to ensure a reliable ohmic contact. Carbon tape and InGa eutectic (Sigma-Aldrich, 99.99%) served as flexible and adjustable conductive spacer. In the final assembly only the thin film surface is exposed to the electrolyte after fixation with chemically stable, nonconductive epoxy (Omegabond 101).

Electrochemistry: The electrochemical measurements were carried out with two Interface 1000E (Gamry Instruments Inc.) in a bipotentiostat setup and a RRDE-3A rotator (ALS Co. Ltd.). The rotating ring electrode consists of a disk electrode of the assembled LSMO electrode with a diameter of 4 mm and a Pt ring electrode with an inner diameter of 5 mm and an outer diameter of 7 mm. All electrochemical measurements were performed in 0.1 M KOH electrolyte prepared by diluting KOH stock solution (Sigma Aldrich) with deionized water (MilliQ, > 18.2 MΩ). The electrolyte was saturated with Ar gas at least 30 min in advance of the measurement and continuously purged with Ar throughout the measurement. Electrode potentials were converted to the RHE scale using $E_{RHE} = E_{applied} + E_{ref}$. The low solubility of oxygen in water causes bubble formation at the disk^[141] and an accurate determination of the OER overpotential is further complicated by increasing O₂ concentration in Ar-saturated electrolytes. For these reasons, we did not quantitatively analyze oxygen detected by ring electrodes.

Electrochemical protocols: For all samples, an identical measurement protocol was used. The OER activity was investigated by cycling three times from 1.1 V vs. RHE to 1.75 V vs. RHE with 10 mV/s at 1600 rpm followed by short chronoamperometric (CA) measurements for 60 s at 1.59, 1.615, 1.64, 1.665, 1.69, and 1.715 V vs. RHE separated by 60 s conditioning steps at 1.1 V vs. RHE. The ring electrode was constantly held at 0.4 V vs. RHE to probe for O₂ (calibration data shown in Figure 8.1). As only the positive going scan direction is shown in Figure 4.4, the measurements are referred to as linear sweep voltammograms (LSV). Before each measurement series, electrochemical impedance spectroscopy (EIS) was conducted with an amplitude of 10 mV at open circuit potential ($R = 48 \pm 5 \Omega$). The potentials were referenced to the reversible hydrogen electrode (RHE) scale in 0.1 M KOH and corrected for the electrolyte resistance extracted from the high frequency intercept of the real impedance. Subsequently the long-term stability was measured by cycling 100

times from 1.1 V vs. RHE to 1.75 V vs. RHE with 10 mV/s at 1600 rpm. For the LSMO with Mn excess and the Mn deficient LSMO three samples were measured, while for the stoichiometric LSMO two samples were measured. The individual RRDE CV measurements can be seen in Figure 8.37 and the averaged values for the initial CVs of the respective off-stoichiometry can be seen Figure 4.4A.

Structural characterization: The films were characterized using extensive X-ray diffraction (XRD) measurements. XRD and XRR measurements were carried out with a Bruker D8 discover system with a Cu K_α source. The surface morphology was characterized by atomic force microscopy (AFM) using a MFP-3D Classic (Asylum Research) in tapping mode. The root mean squared roughness (rms) was calculated using the Gwyddion software^[148] to quantify surface morphology (table 8.7). Additionally, an effective roughness factor was determined by dividing the three-dimensional surface area by the projected area^[131], where the former was obtained by a triangulation method in Gwyddion^[148]. All films had terraced surfaces, which reflect the terrace structure of the substrate surface. Such vicinal surfaces are generated by small deviations from the ideal low index surface due to imperfect polishing. In our samples the deviation from (100) is up to 0.3 ° and the terrace width of the LSMO surface and structure of the terraces slightly varied (Figures 8.23; more detail in ref.^[179]). Nevertheless, all epitaxial LSMO films exhibit a vicinal (100) surface, where the (100) surface facets of the terraces are separated by unit cell steps. An extensive post-mortem analysis of structural changes was applied to samples measured directly after completion of the electrochemical measurement.

Electric transport measurements: The in-plane resistivity was measured in a physical property measurement system (PPMS) using a 4-point probe setup on the LSMO films grown on insulating STO.

TEM analysis: The TEM analysis was performed on electron transparent lamella cut from different LSMO samples by focused ion beam (FIB, FEI Nova Nanolab 600) in a cross section geometry. These sections were mounted on a copper grid to allow the careful thinning process using a precision ion polishing system (PIPS) by low energy Ar ions. In order to minimize redeposition of the sputtered material a S-shaped geometry was used allowing ion milling under angles below 30° in-plane and an Ar-beam with 10° and energies between 2 and 0.5 kV to obtain highly crystalline samples. HR-TEM imaging and EEL spectroscopy were performed with an aberration corrected FEI Titan electron microscope using 300 keV electrons. The energy dispersive X-ray

(EDX) spectroscopy to map the elemental distribution in the Mn rich samples was performed in a Philips CM12 electron microscope with scanning (STEM) capabilities using 120 keV electrons.

4.5 Conclusion

We prepared LSMO samples with Mn off-stoichiometric between +7.2 % and -4.1 %. Variation of the Mn content preserved the LSMO structure but altered the defect chemistry and the induced strain. Based on TEM analysis, we identified Mn defects for LSMO with Mn excess and assumed Mn vacancies for LSMO with Mn deficiency. The high structural control of LSMO allowed extensive electrochemical analysis using an RRDE setup. The electrochemical evaluation showed a strong impact of the Mn excess/deficiency on the activity with the highest activity for the stoichiometric samples without changing the reaction mechanism as Tafel slopes remained unchanged for all investigated Mn off-stoichiometries. In addition to activity, the Mn off-stoichiometry also influenced the electrochemical stability, despite absence of corrosion in terms of change in film thickness or morphology for all samples. Changes in surface composition were limited to the length scale of a few unit cells depending on the Mn off-stoichiometry with no measurable changes for LSMO with Mn excess.

The lattice parameter as proxy of the defect structure correlated with activity, where stoichiometric LSMO had the highest activity. For Mn deficient LSMO, the presence of Mn vacancies is assumed to limit the activity due to decreasing number of active sites and further destabilizes the surface chemistry by formation of the V_{Mn}''' / D_{La}''' defect couple. The excess Mn on the other hand is assumed to form Mn defects located at the A-site. This assumption is supported by the observed reduction of the lattice parameter with increasing Mn over-stoichiometry as well as from the measured Mn valence state. These Mn defects would effectively hamper the formation of the V_{Mn}''' / D_{La}''' defect couple leading to improved stability at the cost of slightly reduced activity as compared to stoichiometric LSMO. Tuning the defect structure to find the optimum in the stabilizing effect of Mn defects and the limitation of the defects on the activity therefore poses a pathway to tailor both the activity and stability.

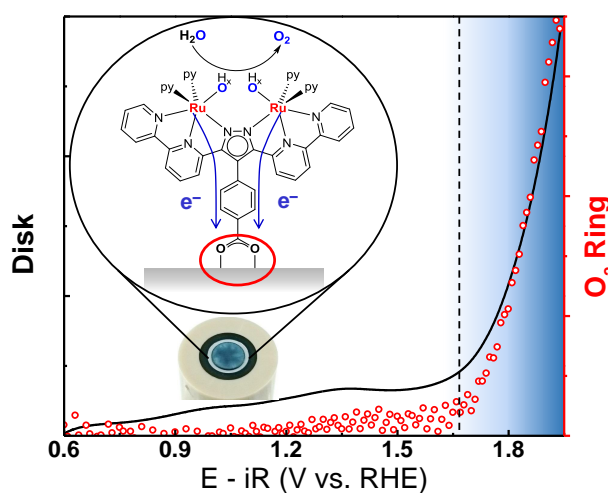
5 Backbone Immobilization of the Bis(bipyridyl)pyrazolate Diruthenium Catalyst for Electrochemical Water Oxidation

J. Odrobina, J. Scholz, A. Pannwitz, L. Francàs, S. Dechert, A. Llobet, C. Jooss, and F. Meyer

Reproduced from ACS catalysis 7, 2116-2125, 2017

Abstract: Efficient catalysts for water oxidation are key to all scenarios for artificial solar water splitting, and, in the case of molecular catalysts, their immobilization on conductive solid supports is considered essential for the construction of a photoelectrochemical cell. In this work, derivatives of the rugged 3,5-bis(bipyridyl)pyrazolate (bbp)-based diruthenium water oxidation precatalyst $[(\mu\text{-bbp})\{\text{Ru}(\text{py})_2\}_2(\mu\text{-X})]^{2+}$ ($\text{X} = \text{OAc}, \text{CO}_3\text{H}$) have been synthesized that are equipped

with a carboxylate anchor at the ligand backbone. The para- $\text{C}_6\text{H}_4\text{COOR}$ ($\text{R} = \text{Et}, \text{H}$) substituent at the pyrazolate- C^4 is shown to not have any significant effect on the electronic properties of the bbp-based diruthenium core, or on the catalytic performance when using Ce^{IV} as a chemical oxidant. The bbp-based complex with labile exogenous bicarbonate bridge (**4**) has been successfully anchored on mesoporous ITO (mesoITO), and the hybrid ITO|mesoITO|**4** shows electrochemical signatures similar to those of the homogeneous system. Its electrocatalytic water oxidation performance at pH 1 has been investigated by rotating ring disk electrode (RRDE) measurements, and high faradaic efficiency is evidenced by the agreement of Tafel slopes for the disk and ring currents. X-ray photoelectron spectroscopy (XPS) data before and after electrochemical measurements were compared to evaluate the chemical stability of the immobilized complex **4** during catalysis, showing that the surface-bound complex species remains intact without any decomposition to RuO_2 . However, gradual leaching of the complex leads to decreasing catalyst concentration and decreasing activity during electrocatalysis, reflecting weak attachment of the carboxylate anchor to the oxide substrate and emphasizing the need for improved anchoring strategies.



5.1 Introduction

Facing the world's increasing energy demand and the urgent need for sustainable energy conversion schemes, the scientific community is devoting immense effort on the construction of systems for artificial solar water splitting^[2,5,10,200–213]. One of the main challenges in this context is the development of catalysts for the water oxidation half-reaction. This reaction, which requires orchestrating the transfer of four electrons and four protons, is demanding both thermodynamically and kinetically. An increasing number of homogeneous and heterogeneous catalyst systems capable of mediating water oxidation has been reported in recent years, many of them using ruthenium as the metal ion of choice^[6,27,214–224]. A key advance has been the use of dinucleating bridging ligands such as the 3,5-bis(pyridyl)pyrazolate that positions two metal ions in close proximity^[225,226]. More recently, we contributed to this field by introducing a family of highly preorganized and rugged diruthenium water oxidation catalysts (WOCs) based on the compartmental monoanionic 3,5-bis(bipyridyl)pyrazolate (bbp^-) ligand and related scaffolds that provide two tridentate binding pockets linked by a central pyrazolate bridge^[21,34,35,227]. These bbp -based diruthenium complexes, when furnished with axial pyridine coligands, feature two accessible coordination sites for water binding, both directed into the bimetallic pocket (*in, in*-position). Sequential oxidation of the diruthenium diaqua starting complex via a series of proton-coupled electron transfer steps leads to the active $\text{Ru}^{\text{IV}}(\text{=O})\text{Ru}^{\text{V}}(\text{=O})$ species, and ^{18}O labeling experiments using a highly water-soluble representative of this catalyst family evidenced that O-O bond formation proceeds via water nucleophilic attack (WNA) on one of the $\text{Ru}=\text{O}$ units of the high-valency intermediate^[34]. While initial screening of catalyst efficiency and mechanistic studies for molecular WOCs in homogeneous solution are often conducted using sacrificial chemical oxidants such as cerium ammonium nitrate (CAN)^[228,229], further applications require anchoring of the complexes on conductive solid supports for driving the water oxidation reaction electrochemically, and eventually for the construction of a photoelectrochemical cell^[25,106,114,230–238]. Such strategy exploits the beneficial atomic-scale tunability and design flexibility of well-defined molecular catalysts, in combination with the favorable properties of a heterogeneous oxide electrode for charge injection and device fabrication^[239]. In this work, we set out to furnish the bbp -based diruthenium WOC with an anchoring group for

immobilization on conductive oxides such as indium tin oxide (ITO), and we evaluate the electrocatalytic performance of the hybrid system. ITO is used as a model system and serves as a platform to understand and investigate the anchoring process and the properties of the hybrid systems, providing benchmark data, in light of recent findings for this electrode material^[104,110,240–242].

One of the common approaches for the immobilization of molecular complexes on solid supports includes the decoration of the molecular complex with suitable anchoring groups, such as carboxylates or phosphonates for surface derivatization^[229,243,244]. The chosen group must be appropriate for rapid interfacial electron transfer between the catalyst and the electrode and for dense and stable coverage of large surface areas in order to allow high catalyst loadings. However, limited stability of the anchor-surface binding under certain pH conditions, as well as decomposition under catalytic conditions, are common issues that must be thoroughly evaluated for each system^[90,109]. Herein, we present a hybrid system consisting of a modified bbp^- -based dinuclear ruthenium catalyst immobilized on mesoporous indium tin oxide (*meso*ITO), which is often used as electrode material, because it has a high surface area, is optically transparent, and is highly conductive^[241]. Furthermore, we show preliminary anchoring studies on more-complex oxides such as lanthanum strontium manganite (LSMO) in order to demonstrate the applicability to other oxide substrates with tunable electronic properties and excellent electronic conductivity. To that end, the bbp^- -based dinuclear ruthenium complex has been equipped with a carboxylate anchoring group at a backside position that does not interfere with the bimetallic active site (Figure 5.1). Note that preorganized dinuclear catalysts offer the advantage of supporting both relevant mechanisms for water oxidation that are known to potentially operate under different conditions (pH, etc.), viz, the water nucleophilic attack (WNA) as well as the coupling of two metal-oxo units (I₂M). The latter requires close proximity of two Ru=O units, which is not possible for common monometallic catalysts under restricted mobility conditions when anchored on solid supports. Thereby, the dinuclear ruthenium complex used here (Figure 5.1) is expected to preserve its catalytic activity evaluated under homogeneous conditions.

Two options appear most suited for decorating the bbp -type diruthenium complex with a carboxylate group for surface binding: using exogenous pyridine ligands with the anchoring group in *para*-position or functionalization of the

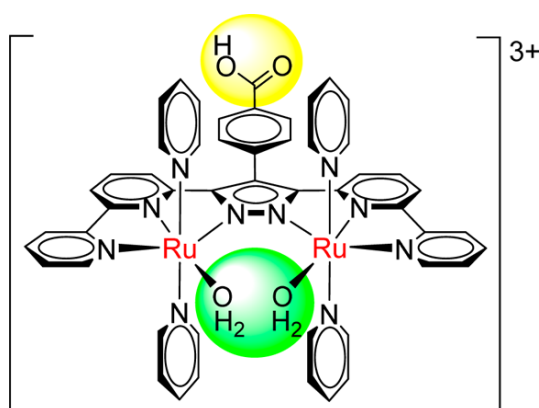


Figure 5.1: Catalyst design for the present work: bbp-type diruthenium complex with active site pocket (green) and carboxylate anchor attached at the ligand backside (yellow).

bbp[−] ligand backbone at the pyrazole-C⁴ position. While the former strategy may be synthetically simpler and the presence of four anchoring groups may be beneficial for stable surface binding, systems with covalent ligand modification at the pyrazole-C⁴ will not be impaired by pyridine dissociation during catalysis, and the active site pocket will likely be oriented away from the oxide surface. Therefore, the latter approach has been pursued in this work.

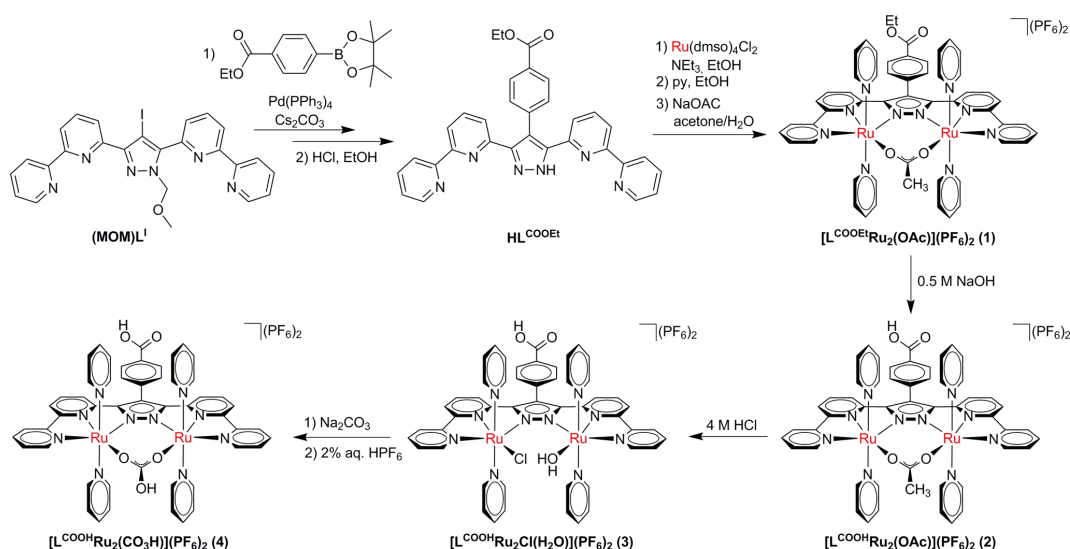


Figure 5.2: Synthetic Route for the Synthesis of the New Proligand HL^{COOEt} and Its Diruthenium Complexes Reported in This Work

5.2 Results and Discussion

Synthesis and Characterization of the Ligand and Diruthenium Complexes.

A multistep synthetic route to the bbp-based diruthenium precatalyst that is equipped with a carboxylate anchor at the pyrazolate backbone has been developed and is shown in Scheme 5.2. It starts from the MOM-protected iodo-derivative of Hbbp, (MOM)L^I[²⁴⁵]. Palladium-catalyzed Suzuki-Miyaura cross-coupling with 4-ethoxycarbonylphenylboronic acid pinacol ester, followed by acid removal of the MOM group, furnishes the new proligand (MOM)L^{COOEt}, in which the carboxylate group (protected as the ethyl ester) is linked to the pyrazolate-C⁴ via a phenylene spacer (see the Appendix B and [²⁴⁶] for experimental details and characterization of all new compounds). Protocols for the synthesis of the diruthenium complex [L^{COOEt}Ru₂(OAc)](PF₆)₂ (**1**) and subsequent exchange of the bridging coligand within the bimetallic pocket are adapted from procedures optimized previously for other Hbbp derivatives [³⁶]. Screening of possible reaction sequences showed that it is advisable to first deprotect the backbone carboxylate anchor, followed by removal of the relatively inert acetate bridge under strongly acidic conditions and final installment of the acid-labile bicarbonate coligand in the reactive precatalyst complex [L^{COOEt}Ru₂(CO₃H)](PF₆)₂ (synthetic sequence [L^{COOEt}Ru₂(OAc)](PF₆)₂ (**1**) → [L^{COOH}Ru₂(OAc)](PF₆)₂ (**2**) → [L^{COOH}Ru₂ CL(H₂O)](PF₆)₂ (**3**) → [L^{COOEt}Ru₂(CO₃H)](PF₆)₂ (**4**); see Scheme 5.2).

All compounds have been characterized by electrospray ionization (ESI) mass spectrometry, as well as one-dimensional (1D) and two-dimensional (2D) nuclear magnetic resonance (NMR) spectroscopy (¹H and ¹³C). Importantly, NMR spectra of the intermediate [L^{COOH}Ru₂ CL(H₂O)](PF₆)₂ (**3**) show a doubling of signals of the bbp scaffold and axial py ligands, compared to [L^{COOH}Ru₂(OAc)](PF₆)₂ (**2**), because of the reduced symmetry C_s. The apparent C_{2v} symmetry of the bimetallic core is restored after installment of the bicarbonate bridge in [L^{COOEt}Ru₂(CO₃H)](PF₆)₂ (**4**). Exchange of the coligands within the bimetallic pocket is further reflected by characteristic shifts of the *ortho* protons of the peripheral pyridine rings of L^{COOR} in the ¹H NMR spectra (9.49 ppm (**2**), 9.47 and 9.63 ppm (**3**), 9.54 ppm (**4**)). Both acetate-bridged complexes (**1**) and (**2**) could be isolated in crystalline form, and their structures were confirmed by X-ray diffraction (XRD). The molecular structures of the cations

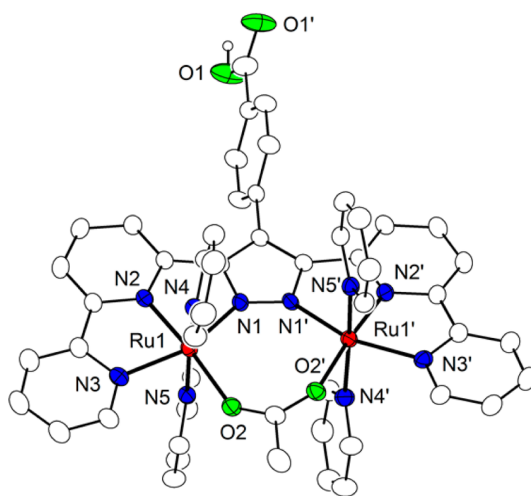


Figure 5.3: Molecular structure of the cation of $[L^{COOH}Ru_2(OAc)]^-(PF_6)_2$. 30% probability ellipsoids, solvent molecules, disorder and most hydrogen atoms are omitted for clarity. Selected atom distances: Ru1-N1, 2.012(3) Å; Ru1-N2, 1.950(3) Å; Ru1-N3, 2.067(3) Å; Ru1-N4, 2.092(3) Å; Ru1-N5, 2.093(3) Å; Ru1-O2, 2.122(2) Å; Ru1...Ru2, 4.2050(5) Å. Selected bond angles: N2-Ru1-N1, 78.64(11)°; N2-Ru1-N3, 80.39(11)°; N1-Ru1-N3, 159.03(11)°; N2-Ru1-N4, 94.40(11)°; N1-Ru1-N4, 91.42(12)°; N3-Ru1-N4, 90.18(11)°; N2-Ru1-N5, 91.72(11)°; N1-Ru1-N5, 90.81(11)°; N3-Ru1-N5, 89.80(11)°; N4-Ru1-N5, 173.79(11)°; N2-Ru1-O2, 174.83(10)°; N1-Ru1-O2, 106.46(10)°; N3-Ru1-O2, 94.50(10)°; N4-Ru1-O2, 86.33(11)°; N5-Ru1-O2, 87.48(10)°. Symmetry transformation used to generate equivalent atoms: (') 1-x, y, 3/2-z.

$[\text{L}^{\text{COOEt}}\text{Ru}_2(\text{OAc})]^{2+}$ and $[\text{L}^{\text{COOH}}\text{Ru}_2(\text{OAc})]^{2+}$ in^[246] and Figure 5.3, respectively. In essence, the backbone *para*-C₆H₄COOR (R = Et, H) substituent does not influence the metrical parameters of the bimetallic $[(\text{bbp})\text{Ru}_2(\text{OAc})]^{2+}$ -type core, which are essentially identical to those of the related complexes with H, Me, or Br substituents at the pyrazole- C^4 position^[34,35]. The pyrazole moiety (pyz) of the ligand $[\text{L}^{\text{COOEt}}]^-$, the two Ru ions, and the acetate-bridge (OAc) in the *in,in*-position are more or less inplane, as reflected by the small differences of the torsion angles Ru1-N1-N1'-Ru1' (5.6°) and Ru1-O2...O2'-Ru1' (7.9°) and the angle of the two planes pyz-OAc of 5.5°. In case of the ligand $[\text{L}^{\text{COOH}}]^-$, the torsion angles Ru1-N1-N1'-Ru1' (12.7°) and Ru1-O2...O2'-Ru1' (24.4°) show that the acetate bridge is more tilted, with respect to the pyrazole moiety, which is also reflected in the larger pyz-OAc interplanar angle of 15.5°. The phenyl groups attached to the pyrazole backsides are oriented in an orthogonal fashion to the pyrazolate plane, with interplanar angles of 55.7° and 75.0° for $[\text{L}^{\text{COOEt}}]^-$ and $[\text{L}^{\text{COOH}}]^-$, respectively.

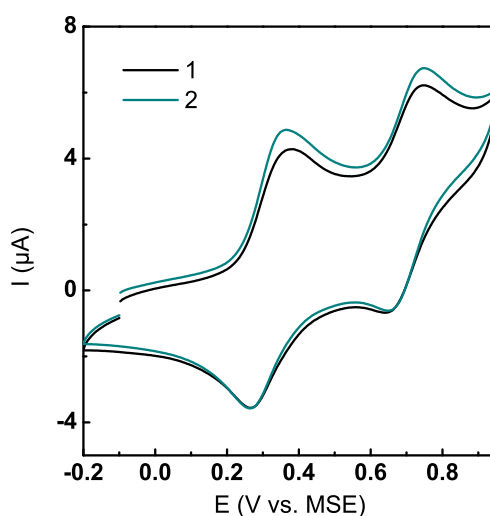


Figure 5.4: Cyclic voltammograms of **1** (black) and **2** (cyan) in PC with $t\text{Bu}_4\text{NPF}_6$ (0.1 M) measured at 100 mV/s with glassy carbon (GC) as the working electrode, platinum as the counter electrode, and a mercury/mercury sulfate electrode (MSE) as the reference electrode

Electrochemical Properties and Homogeneous Water Oxidation Catalysis. To assess the effect of the backbone anchor on the electrochemical properties, cyclic voltammograms of (**1**) and (**2**) were recorded in propylene carbonate (PC) solution. Redox potentials for the first two oxidations that sequentially give the $\text{Ru}^{\text{II}}\text{Ru}^{\text{III}}$ and $\text{Ru}^{\text{III}}\text{Ru}^{\text{III}}$ species (for (**1**): $E_{1/2}=0.27$ and 0.67 V; for (**2**): $E_{1/2}=0.28$

and 0.68 V vs MSE; see Figure 5.4) are very similar to the corresponding potentials of the diruthenium complex $[(^Me\text{bbp})\text{Ru}_2(\text{OAc})]^{2+}$ having a Me substituent at the pyrazolate- C^4 (Me: $E_{1/2}=0.24$ and 0.64 V vs MSE)^[34,35]. The performance of (**1**) and (**2**) in homogeneous water oxidation catalysis was first probed using Ce^{IV} species (in the form of cerium ammonium nitrate, CAN) as sacrificial chemical oxidant under conditions identical to those previously employed for the family of $[(^R\text{bbp})\text{Ru}_2(\text{OAc})]^{2+}$ precatalysts (**1**) and (**2**). Thus, 100 equiv of CAN were added to solutions of the complexes (**1**) and (**2**) in aqueous triflic acid at pH 1 (10^{-3} M complex in 0.1 M triflic acid). Under those conditions, the acetate bridge has been shown to hydrolyze to give the corresponding active di-aqua species with two water ligands in the *in,in*-positions (viz, pointing into the bimetallic pocket)^[36]. The formation of dioxygen was monitored by manometry and simultaneously by a Clarke electrode, showing a turnover number (TON) of ~ 23 , which is close to the maximum value of 25 and similar to what has been observed for $[(^Me\text{bbp})\text{Ru}_2(\text{OAc})]^{2+}$ ^[35]. Also, the initial turnover frequency (TOF_i) under these conditions ($\sim 3.5 \times 10^{-2} \text{ s}^{-1}$) is of the same order of magnitude as that of the bbp-based diruthenium complex lacking the backbone anchor, as reported in the literature ($6.8 \times 10^{-2} \text{ s}^{-1}$; see Table 9.1 in the Appendix B). All these findings confirm that the para- $\text{C}_6\text{H}_4\text{COOR}$ (R=Et, H) substituent at the pyrazolate- C^4 does not have any significant effect on the electronic properties or catalytic performance of the bbp-based diruthenium core.

Anchoring the Diruthenium Complex on ITO. For catalyst anchoring on the metal oxide surface, the bicarbonatebridged complex **4** was prepared for two reasons:

- (i) Having an exogenous bridging unit within the bimetallic pocket (instead of the diaqua species) should prevent potential direct interaction of the diruthenium active site with the metal oxide surface.
- (ii) The acid labile bicarbonate bridge is advantageous for ensuring fast dissociation of the exogenous bridge when generating the active diaqua species of the anchored catalyst under acidic conditions (exchange is usually slow for an acetate bridge).

To achieve a high loading of the diruthenium catalyst on the working electrode, ITO-laminated glass plates were first coated with mesoporous ITO (*mesoITO*), following protocols reported in the literature^[241,242], with slight modifications (see the Appendix B). Anchoring of **4** on the metal oxide surface was then performed by soaking the ITO|*mesoITO* electrodes for 1 day at room temper-

ature in a 0.1×10^{-3} M solution of **4** in methanol. The electrodes were then rinsed with methanol, to remove all of the complex that was not anchored to the surface. To demonstrate the model character of ITO as a solid support, we also immobilized **4** on lanthanum strontium manganite ($\text{La}_{0.6}\text{Sr}_{0.4}\text{MnO}_3$, LSMO) as an example of a more complex oxide with low surface area and a well-defined crystallographic surface. Successful surface deposition of **4** on LSMO is supported by X-ray photoelectron spectroscopy (XPS) and atomic force microscopy (AFM) measurements, as shown in Figure 9.18 in the Appendix B.

Thus prepared ITO|*meso*ITO|**4** electrodes were characterized by electrochemical measurements. This analytic method was chosen because *bbp*-based diruthenium complexes have diagnostic electrochemical signatures. In the following, we use two different reference scales, namely, potentials versus MSE for measurements in organic environments and RHE (reversible hydrogen electrode) for measurements in aqueous environments. Two reversible oxidation processes are accessible in organic solvents such as PC to give the respective $\text{Ru}^{\text{II}}\text{Ru}^{\text{III}}$ and $\text{Ru}^{\text{III}}\text{Ru}^{\text{III}}$ complexes, with potentials that are dependent on the type of exogenous bridge within the bimetallic pocket. The CV of **4** in homogeneous PC solution containing ${}^n\text{Bu}_4\text{NPF}_6$ (0.1 M) shows the first oxidation at $E_{1/2}=0.37$ V and the second oxidation at $E_{1/2}=0.74$ V vs MSE (scan rate = 100 mV/s; see Figure 5.5). The ITO|*meso*ITO electrode with anchored **4** was measured in a three-electrode setup, with the ITO|*meso*ITO|**4** electrode serving as the working electrode. The modified electrode shows two oxidation processes at potentials ($E_{1/2}=0.36$ and 0.77 V vs MSE) essentially identical to those of molecular **4** in PC solution, confirming successful anchoring of intact **4** onto the electrode (see Figure 5.5). As expected, the homogeneous system (**4** dissolved in PC) shows a linear dependence of the peak current on the square root of the scan rate, whereas for the immobilized catalyst (ITO|*meso*ITO|**4**), the peak current increases linearly with the scan rate (see lower part of Figure 5.5; CVs at different scan rates are shown in Figure 9.3 in the Appendix B).

The catalytic properties were investigated at pH 1 in 0.1 M triflic acid, because water oxidation mediated by complexes with the ${}^R\text{bbp}$ Ru_2 core is mechanistically fairly well understood at this pH^[34]. In addition, the chemical bond between the carboxylic acid anchoring group and a metal oxide is known to be more stable at low pH^[247]. The catalytically active species has been shown to be a diaqua- or a $(\text{H})\text{O} \cdots \text{HO}(\text{H})$ bridged complex, depending on the pH of the

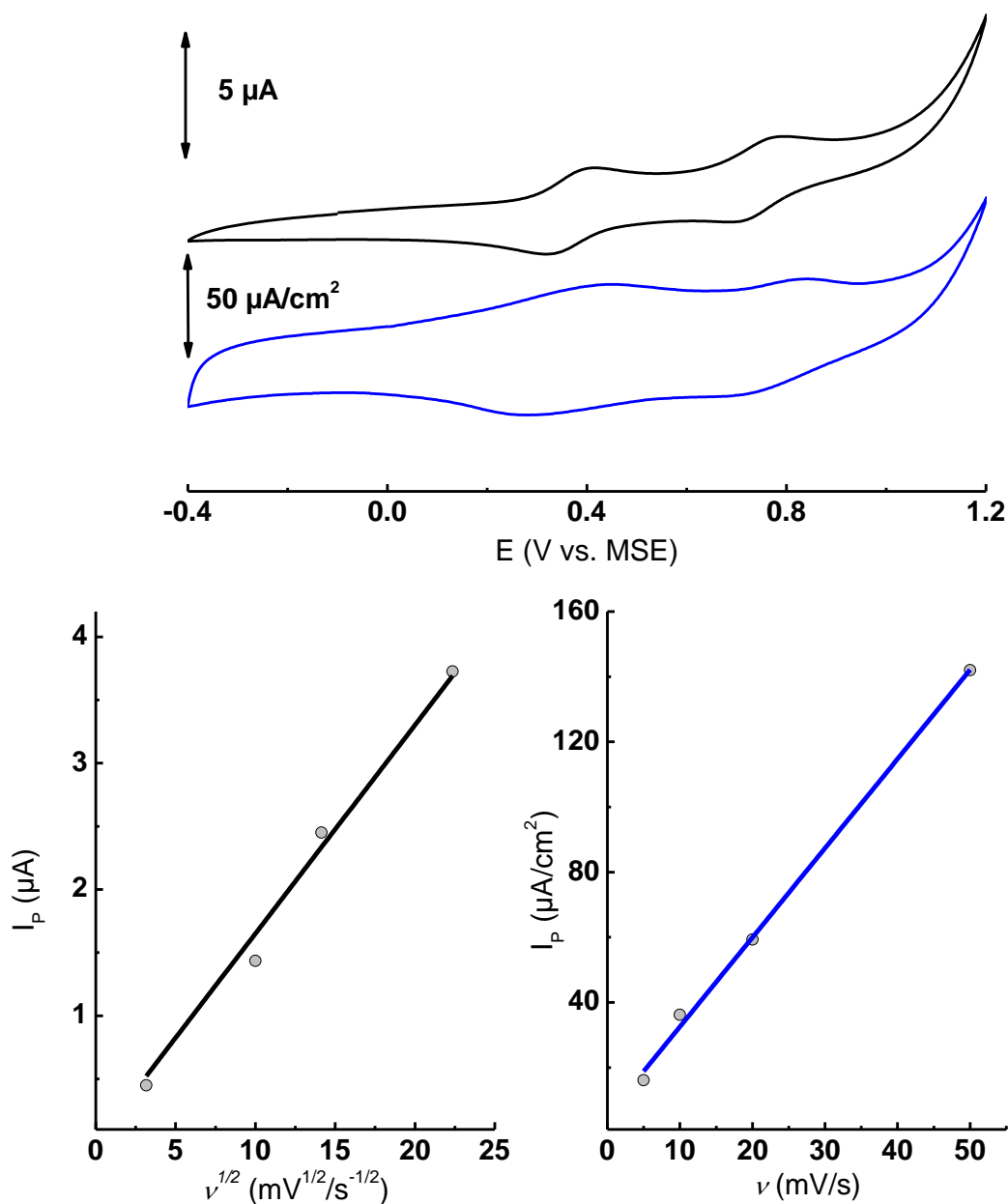


Figure 5.5: (Top) Cyclic voltammograms of (black curve) complex **4** in PC solution with Bu_4NPF_6 (0.1 M), measured at 100 mV/s with GC as the WE, platinum as the CE, and MSE as the ref, and (blue curve) complex **4** anchored onto ITO|*meso*ITO glass slides measured at 10 mV/s with ITO|*meso*ITO|**4** as the WE, platinum as the CE, and MSE as the ref. Bottom left graph shows the linear dependence of peak current I_p on the square root of the scan rate for complex **4** in PC. Bottom right graph shows the linear dependence of peak current I_p on the scan rate for complex **4** immobilized on ITO|*meso*ITO.

solution^[34,36].

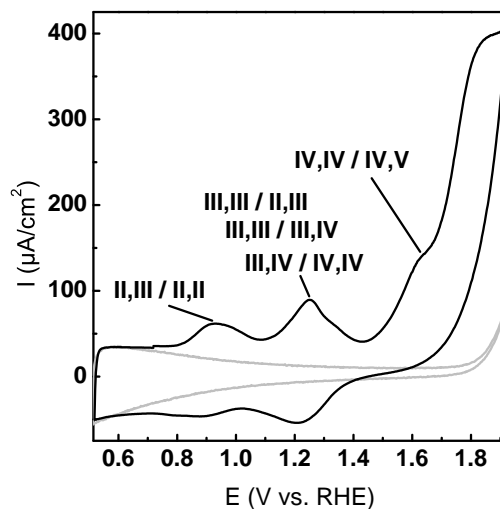


Figure 5.6: Cyclic voltammogram of **4** anchored onto ITO|*meso*ITO recorded at a scan rate of 10 mV/s (black) in 0.1 M triflic acid (pH 1); the background current density of the blank ITO|*meso*ITO electrode is shown in gray. WE, ITO|*meso*ITO; CE, Pt disk; and ref, MSE calculated to the RHE scale.

To further investigate the rapid exchange of the bicarbonate bridge in **4** by water, a CV of the modified ITO|*meso*ITO|**4** electrode was measured at pH 1 in 0.1 M triflic acid (Figure 5.6). It shows a reversible one-electron oxidation for the $\text{Ru}^{\text{III}}\text{Ru}^{\text{II}}/\text{Ru}^{\text{II}}\text{Ru}^{\text{II}}$ couple at $E_{1/2}=0.90$ V and three subsequent quasireversible oxidations at $E_{1/2}=1.23$ V ($\text{Ru}^{\text{III}}\text{Ru}^{\text{III}}/\text{Ru}^{\text{III}}\text{Ru}^{\text{II}}$), $E_{1/2}=1.27$ V ($\text{Ru}^{\text{III}}\text{Ru}^{\text{IV}}/\text{Ru}^{\text{III}}\text{Ru}^{\text{III}}$), and $E_{1/2}=1.31$ V ($\text{Ru}^{\text{IV}}\text{Ru}^{\text{IV}}/\text{Ru}^{\text{III}}\text{Ru}^{\text{IV}}$) vs RHE. These values compare well with the measured redox potentials of the water-soluble derivative $[(\mu\text{-bbp})\{\text{Ru}(\text{OH}_2)(4\text{-SO}_3\text{-py})_2\}_2]^-$ (where 4-SO₃-py is pyridine-4-sulfonate; see Figure 9.4 in the Appendix B)^[34]. At 1.44 V vs RHE, the cyclic voltammogram shows an increase in the oxidative current, which can be attributed to the formation of the $\text{Ru}^{\text{IV}}\text{Ru}^{\text{V}}$ species and the onset of catalytic water oxidation, corresponding to an overpotential of $\eta \approx 200$ mV. Following the small plateau at 1.62 V the complex is further oxidized to the $\text{Ru}^{\text{V}}\text{Ru}^{\text{V}}$ state, which is accompanied by a large electrocatalytic wave.

The stability of the catalyst complex, especially of its anchoring connection to the oxide surface, is strongly dependent on the applied bias. If repetitive cyclic voltammetry (CV) scans are measured for the hybrid system ITO|*meso*ITO|**4** at potentials up to 1.1 V vs. RHE, the loss of complex is only minor and the peak currents tend toward a stable situation (see Figure 9.4A in the Appendix B),

indicating that only some loosely bound or physisorbed complex is lost under those conditions. If the applied bias is higher, leaching is more pronounced (see Figure 9.4B in the Appendix B). In both cases, the positions of the oxidative and reductive waves for the $\text{Ru}^{\text{III}}\text{Ru}^{\text{II}}/\text{Ru}^{\text{II}}\text{Ru}^{\text{II}}$ couple of the immobilized complex hardly change, indicating that the complex itself remains intact but that it gradually detaches from the surface under oxidative conditions. When measuring repetitive CVs far into the catalytic region (up to 1.9 V vs. RHE), a significant loss of catalyst from the electrode surface can be observed, reflected by decreasing peak currents for the sequential oxidations of the RuRu complex and a concomitant drop of the electrocatalytic wave (see Figures 9.4C and 9.4D in the Appendix B). The issues of catalyst leaching and characterization of the ITO-bound species are addressed in more detail below.

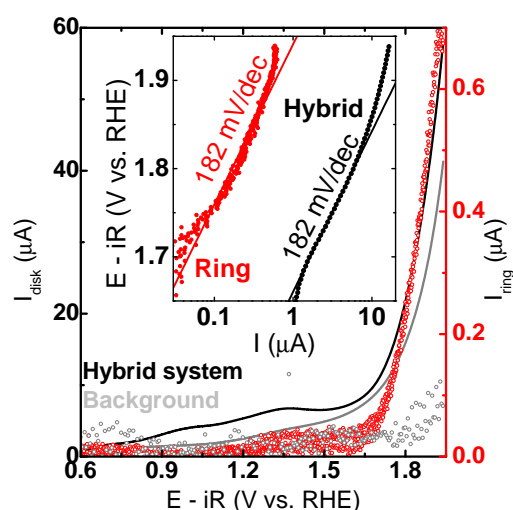


Figure 5.7: Rotating ring disk CV measurements of surface-anchored complex **4** (GC|*meso*ITO|**4**, solid black line) and the blank GC|*meso*ITO| electrode (solid gray line). The corresponding ring currents are shown as red and gray dots. The inset shows the Tafel analysis of both ring ($V_{\text{ring}}=0.2$ V vs. RHE) and hybrid current density, as a function of disk voltage after subtraction of the background currents of the blank electrodes. All measurements were performed with 0.1 M triflic acid as the supporting electrolyte (argon-purged) at 10 mV/s and 1600 rpm. The voltage was corrected for uncompensated resistance. The positive-going direction of the third scan is shown.

RRDE Characterization of the Hybrid Electrode. To further elucidate the catalytic activity of the anchored complex **4** and directly measure the correlation between the catalytic current and O_2 evolution, we applied rotating ring disk electrode (RRDE) measurements to the *meso*ITO|**4** system^[110]. Here, a potential

that was sufficient to drive the oxygen reduction reaction (ORR) on Pt in a diffusion-limited regime was applied on the Pt-ring electrode (see the ORR measurements on Pt in Figure 9.10 in the Appendix B). For the RRDE experiments, a polished GC disk was modified with mesoporous ITO (GC|*meso*ITO); the disks for the RRDE measurements were prepared as reported in the literature^[110]. Complex **4** was anchored onto the GC|*meso*ITO electrode, following a procedure similar to that used for modifying the ITO|*meso*ITO slides. All measurements were performed in argon-saturated 0.1 M triflic acid (pH 1), to reduce the O₂ background for the ring measurement. Examples of CV measurements using the RRDE setup are shown in Figure 5.7 for the oxidative scan direction. The GC|*meso*ITO disk electrode modified with complex **4** showed significant improvement of the catalytic currents, compared to the unmodified GC|*meso*ITO electrode and largely enhanced ring currents. The quiescent measurements on ITO|*meso*ITO electrodes revealed an exponential increase in currents above 1.55 V vs. RHE, following the initial oxidations of the catalyst from Ru^{II}Ru^{II} up to Ru^{IV}Ru^{IV} and then further to Ru^{IV}Ru^V, suggesting the onset of WOC above 1.55 V vs. RHE. A direct correlation between the Pt-ring currents and the GC|*meso*ITO electrode confirmed that the currents above ~ 1.69 V vs. RHE (and, thus, beyond the Ru^{IV}Ru^{IV} state) correspond to WOC. However, the differences in the observed overpotential might originate from the superposition of the oxidation beyond Ru^{IV}Ru^{IV} and the onset of the WOC. For the RRDE method, the dense particle layer of the *meso*ITO hampers the diffusion of O₂ to the ring electrode and might influence the observed onset of WOC, because of the imposed time delay. Despite the limited time resolution, the correlation between the disk currents and the measured O₂ allows a more defined onset of the WOC. These findings are in good agreement with the results reported for homogeneous bbp-based diruthenium catalyst systems, namely that the WOC only occurs at oxidation states above Ru^{IV}Ru^{IV}.

Quantification of the O₂ reduction at the ring electrode, even for known collection efficiencies using the ferri-/ferrocyanide redox reaction and flat electrodes, is limited by the low solubility of O₂ in water, which causes bubble formation at the disk (see, e.g., the discussion in ref^[141]). Furthermore, quantification of the faradaic efficiency is dependent on knowledge of the exact number of electrons transferred during the ORR at the ring electrode (for a detailed discussion, see the Appendix B). ORR is often assumed to be an exactly four-electron process; however, incomplete ORR can reduce this number under certain conditions. Using the number of electrons determined experimentally from ORR studies

under the same conditions (Figure 9.10 in the Appendix B), we calculated the faradaic efficiency (see Figure 9.11 in the Appendix B). However, there is a fundamental limitation of the accuracy for the faradaic efficiency for porous electrodes because the time delay observed in CA measurements (Figure 5.8) strongly influences the faradaic efficiency. Although the details of the diffusion limitation and thus the time scale for the O₂ transport from the disk to the ring may differ between chronoamperometry (CA) and CV experiments, the observed time delay of ~ 10 s in the CA measurement can serve as a rough estimate for the relevant time scale. Because of the large Tafel slope of 182 mV/dec for both the ring and disk currents (see inset in Figure 5.7), a time delay of 10 s results in a significant shift of the observed response at the ring electrode, even at the slow scan rate of 10 mV/s. Therefore, only a lower limit for the faradaic efficiency can be given for porous electrodes. Other methods that provide access to the efficiency, such as online gas mass spectrometry, rely on sufficiently long-term stability of the anchored complex, in order to provide measurable amounts of O₂.

Despite these limitations for the quantification of the faradaic efficiency, differential currents as used in the calculation of the Tafel slope can be evaluated, even without knowledge of the correct collection efficiency. As we have shown previously^[179], the ring Tafel slope is a measure of the catalytic Tafel slope superior to the disk Tafel slope, because it is not affected by capacitive currents or disk corrosion. Even the presence of a time delay between ring and disk currents does not affect the efficiency evaluation by Tafel slopes, if done for slow scan rates and in an appropriate voltage range. The inset of Figure 5.7 indeed shows an approximate agreement of the ring and disk Tafel slopes in a voltage range between 1.7 V and 1.9 V. Here, the background currents of the unmodified electrode for both the ring and the disk currents have been subtracted. The finding that disk and ring Tafel slopes are identical within error indicates that the disk current is dominated by the OER reaction and parasitic side reactions can be disregarded. This indeed supports a high faradaic efficiency, as discussed in the literature^[179]. Furthermore, the increase in the Tafel slope above ~ 1.8 V vs. RHE suggests that the reaction mechanism is changing, depending on the applied potential.

In order to obtain more-detailed information on the activity close to equilibrium, the samples were characterized using CA at increasing potentials following

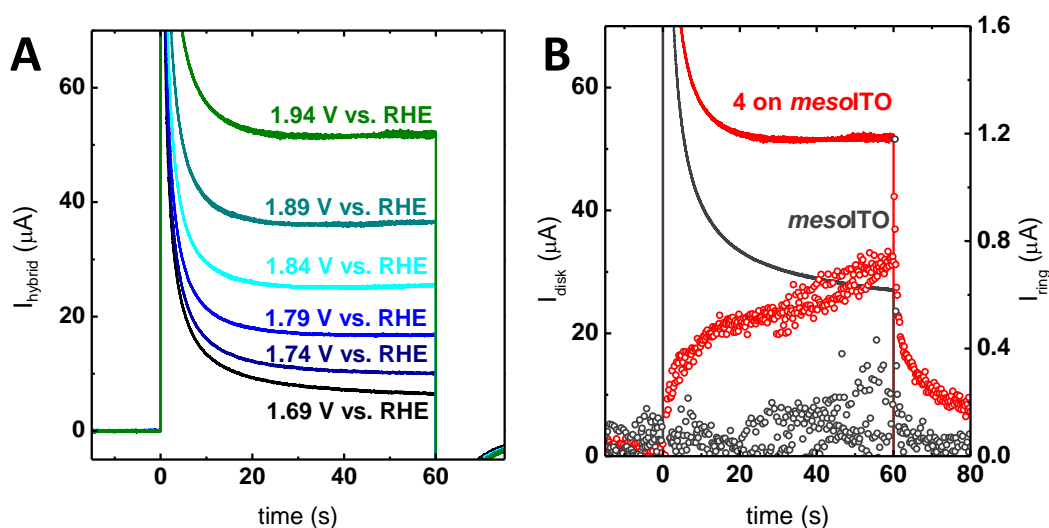


Figure 5.8: (A) Chronoamperometry (CA) measurements of GC supported *meso*ITO film with surface bound complex **4** at increasing potentials. (B) Exemplary CA measurement at 1.94 V vs. RHE for the blank GC|*meso*ITO electrode (gray trace) and for the GC|*meso*ITO with surface-bound complex **4** (GC|*meso*ITO|**4**, red trace), showing both the disk and ring currents. All measurements were performed in 0.1 M triflic acid supporting electrolyte (argon-purged) with 1600 rpm. Before and after the respective applied potential step, a potential of 0.5 V vs. RHE was applied for 60 s.

initial CV measurements. A typical measurement can be seen in Figure 5.8A, showing higher currents in response to increasing potentials. However, the increase is smaller than expected from the CV measurements, because of a decrease in catalyst surface coverage over time, as mentioned above and confirmed by XPS measurements (see below), as well as by the different time response of the blank and surface-functionalized *meso*ITO: while the functionalized electrodes reach constant currents above a potential of 1.79 V vs. RHE after ~ 20 s, the current of the blank *meso*ITO electrodes continues to decrease throughout the measured time period, as can be seen in Figure 5.8B. The differences in behavior can be caused by changing overpotentials due to oxygen saturation of the electrolyte within the diffusion layer (see discussion in the Appendix B for details) or the altered surface properties of the *meso*ITO upon anchoring of **4**. The ring currents of the functionalized electrode increase throughout each potential step and decrease slowly after applying the open circuit potential. The delay in the response indicates that the diffusion of the evolved O_2 out of the mesoporous ITO layer limits the time resolution, as observed also in the literature^[248].

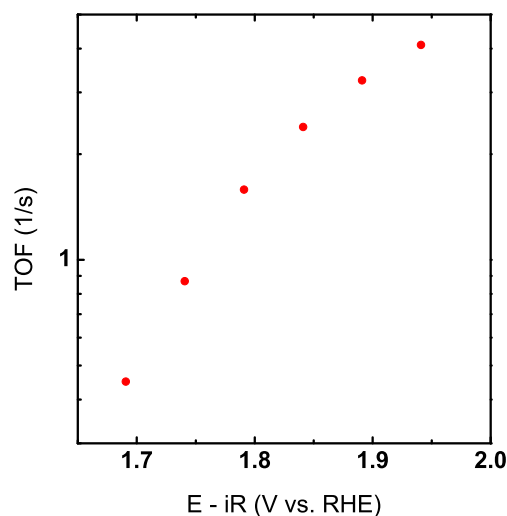


Figure 5.9: TOF values for GC|*meso*ITO|**4** obtained using multistep CA (Figure 5.8A) of the modified RRD electrode at increasing potentials. TOF values were calculated assuming a constant concentration of complex **4**. All measurements were performed in 0.1 M triflic acid supporting electrolyte (argon-purged) at 1600 rpm. The solid line is present only as a guide for the eye.

The change in turnover frequency (TOF) as a figure of merit of the hybrid system is shown in Figure 5.9. It can be determined by estimating the surface concentration of the anchored complex **4** by integrating the charge of the reversible one electron oxidation step $\text{Ru}^{\text{III}}\text{Ru}^{\text{II}}/\text{Ru}^{\text{II}}\text{Ru}^{\text{II}}$ at $E_{1/2} = 0.90$ V. The concentration was determined based on CV measurements prior to the CA measurements and was assumed to remain constant throughout the CA measurements. The TOF then was determined by using the integrated charge of the last 10 s of each CA step after subtracting the respective background currents (Figure 5.8).

The results for the anchored complex show a strong increase in TOF with increasing applied potential (Figure 5.9), reaching from 0.45 s^{-1} at an overpotential of $\eta = 0.52$ V to 4.1 s^{-1} at an overpotential of $\eta = 0.77$ V. The closely related water-soluble complex $[(\mu\text{-bbp})\{\text{Ru}(\text{OH}_2)(4\text{-SO}_3\text{-py})_2\}_2]^-$, under homogeneous conditions, shows TOF values that seem to be 1-2 orders of magnitude higher (15.7 s^{-1} at $\eta = 0.52$ V or $\sim 50 \text{ s}^{-1}$ at $\eta = 0.77$ V)^[37]. However, it is difficult to compare these values because the latter have been determined under highly optimized CV conditions in homogeneous phase, using the foot-of-the-wave analysis (FOWA), while TOF values for the *meso*ITO|**4** hybrid have been derived from nonoptimized bulk CA experiments. The lower TOF for anchored *meso*ITO|**4** and the decrease in activity during prolonged CV and during the

CA measurements likely reflect catalyst leaching and a decreasing surface concentration of the active complex. Consequently, the calculated TOFs for the *meso*ITO|4 hybrid material are an estimate on the lower limit of the true TOF. The electrochemical response of the complex, and, hence, also the catalytic activity, are diminishing significantly with higher applied potential during the CV experiments (see Figure 9.5).

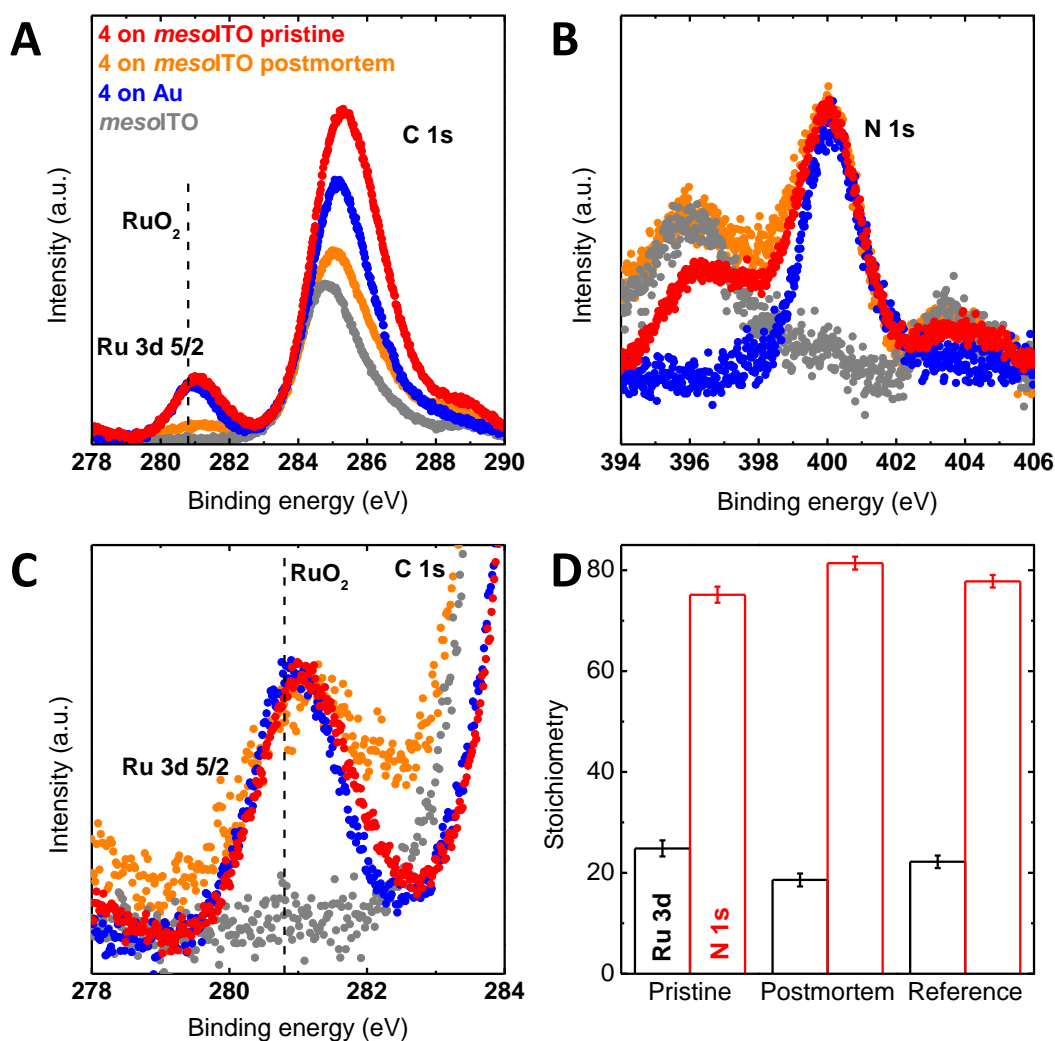


Figure 5.10: (A) XPS spectra of the C 1s core level, (B) XPS spectra of the N 1s spectra normalized on the same value, (C) XPS spectra of the Ru 3d level normalized on the same value, and (D) stoichiometry obtained by Ru 3d and N 1s spectra. All measurements were performed on a dropcast sample of complex 4 on Au, a hybrid electrode before (pristine) and after CV measurements and 5 min CA at 1.9 V vs. RHE (post mortem), and a blank electrode after exposure to the supporting electrolyte. The color code is identical for panels (A)-(C).

Stability of the Hybrid System during WOC. In order to evaluate the chemical stability of the immobilized complex **4** during catalysis, XPS was employed. XPS spectra of the modified electrodes show the expected species of the reference sample without significant chemical changes during WOC (Figures 5.10A-C). The survey scans showed the underlying Sn, In, and O core levels from the substrate and Au from the sample holder used for energy calibration (see Figure 9.15 in the Appendix B). The Ru 3d level signal is only present for the functionalized system. Its intensity decreased significantly after the electrochemical measurements, with respect to both the pristine sample, the electrolyzed sample, and the reference sample of complex **4** without the oxide substrate (Figure 5.10A). The reference sample was prepared by dropcasting the complex, dissolved in MeOH, on a sputtered Au holder. To compare the chemical shift, Figure 5.10C shows the Ru 3d level adjusted to the same intensity. The binding energies of the Ru 3d_{5/2} states are 281.1 eV for the pristine sample, 281.2 eV after the electrochemical measurement, and 280.9 eV for the reference. While no shift is observed within error when measuring before and after the electrochemical experiment, this cannot rule out the formation of RuO₂ that has a binding energy of 280.8 eV (measured on RuO₂ nanoparticles, 99.9% purity, Sigma-Aldrich). Note that the Ru 3d level has not changed due to the electrochemical treatment. Decomposition of Ru-based molecular catalysts under turnover conditions to finally yield RuO₂ is a commonly discussed mechanism that potentially compromises the catalytic activity^[90]. While the Ru 3d level is not an unambiguous descriptor for the decomposition to RuO₂, the N 1s core level can serve as an additional marker for the integrity of the molecular catalyst on the surface. Consistent with the observation for Ru 3d states, no significant shift of the binding energy could be found for the N 1s states (Figure 5.10B). To evaluate the stability of the complexes, the stoichiometry was determined using the unmodified intensities of the N 1s and Ru 3d spectra. Because of overlap of the Ru 3d_{3/2} species with the C 1s core level, the energy splitting between the Ru 3d_{5/2} and Ru 3d_{3/2} states could not be measured. It was fixed at 4.1 eV, according to the literature^[249], with an intensity ratio of 3/5. The obtained ratios of $c_{Ru}=21.9\%\pm 3.1\%$ and $c_N=78.1\%\pm 3.1\%$ are displayed in Figure 5.10D and are, within error, close to the expected 2:10 ratio for the molecular structure. Note that the error of $\pm 3.1\%$ is due to the overlap of Ru 3d and C 1s states, which causes increasing fitting errors with decreasing peak intensities. The absence of significant changes in the binding energies and the stable stoichiometry of the complex species suggest a

stable complex and rule out any decomposition to RuO_2 , as has been reported for related molecular systems^[90], since the formation of RuO_2 would either result in a loss of the pyridine units or complete decomposition of the ligand. The latter would be visible in a strong increase of the Ru:N ratio, which is not observed. The decreasing catalytic activity is hence due to a decreasing catalyst concentration, because of gradual leaching of complex **4** during the electrochemical measurement, which is likely caused by weak attachment of the carboxylate anchor to the oxide substrate.

To put the present system into perspective and to compare with other ruthenium catalysts anchored on oxide solid supports, Table 9.3 in the Appendix B lists the electrochemical TOF values of relevant systems (note that all are mononuclear ruthenium catalysts, and some of them are linked to a $[\text{Ru}(\text{bipy})_3]^{2+}$ unit)^[6,106,110,243]. Data for dinuclear **4** shown in Figure 5.9 are comparable to, or even slightly above, those of other high-performance catalysts. Table 9.3 also provides some stability information for the various systems. In contrast to complexes that decompose to RuO_2 ^[90], the performance of complex **4** anchored on ITO is only limited by the stability of the anchoring group. Note that Llobet et al.^[250–252], Meyer et al.^[253,254], and Sun et al.^[116,230,231,236,255–258] have reported other highly active mononuclear and dinuclear ruthenium-based WOC systems, that were either anchored on different solid supports (e.g., carbon nanotubes) or evaluated under different oxidative conditions, in the form of photoanodes.

5.3 Conclusions

We demonstrate the anchoring of a well-understood and robust diruthenium-based water oxidation catalyst $[(\mu\text{-bbp})\{\text{Ru}(\text{py})_2\}_2(\mu\text{-X})]^{2+}$ ($\text{X} = \text{OAc}, \text{CO}_3\text{H}$) onto an oxide support using a carboxylate anchor at the ligand backbone. For the oxide support, we have chosen an indium tin oxide film covered by mesoporous ITO suitable for high complex loadings, and preliminary tests have also evidenced successful anchoring on single crystalline perovskite oxide surface facets. The hybrid system was characterized by advanced electrochemical methods, including rotating ring disk electrode studies, and by X-ray photoelectron spectroscopy to evidence that the structural integrity of the WOC is preserved, even under catalytic conditions. The anchoring group, i.e., *para*- $\text{C}_6\text{H}_4\text{COOR}$ ($\text{R} = \text{Et}, \text{H}$) at the pyrazolate- C^4 is shown not to have any significant effect

on the catalytic performance nor on the oxidative and reductive waves of the $\text{Ru}^{\text{III}}\text{Ru}^{\text{II}}/\text{Ru}^{\text{II}}\text{Ru}^{\text{II}}$ couples under homogeneous conditions. TOF values for the anchored complex determined by bulk chronoamperometry increase with increasing applied potential and reach 4.1 s^{-1} at an overpotential of 0.77 V. The gradual decrease in activity during prolonged CV and during CA measurements likely reflects catalyst leaching and the resulting decreasing surface concentration of the active complex. Consequently, the calculated TOFs for the mesoporous ITO hybrid material are an estimate of the lower limit of the true TOF. For potentials up to 1.1 V vs. RHE, the loss of complex is only minor and the peak currents tend toward a stable situation, indicating that only some loosely bound complex is detached. At higher applied potentials, leaching is more pronounced, leading to the conclusion that the single carboxylate is a rather stable anchor close to equilibrium conditions but its bonding to the oxide substrate is the limiting factor during oxygen evolution under turnover conditions and needs to be modified and improved. This also is a key issue for catalyst anchoring on alternative oxide supports. Nevertheless, it could be shown that the bbp-type dinuclear ruthenium WOCs are promising candidates for highly active photoanodes, because of their high turnover frequencies and their oxidative robustness. The mayor limiting factor for this new generation of stable ruthenium-based WOC is the anchoring group, which will be optimized in future work.

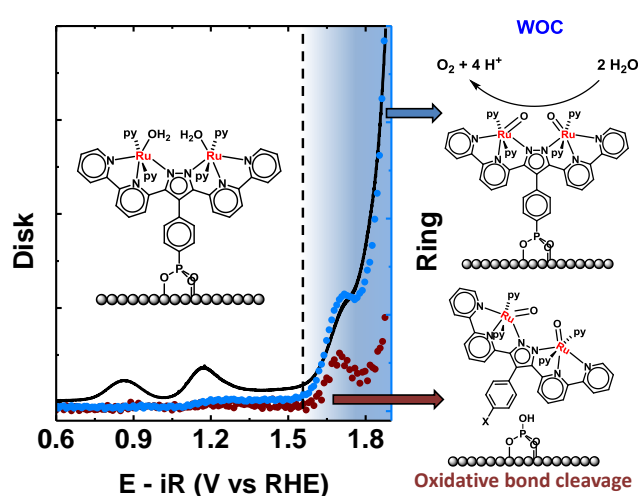
6 Chasing the Achilles' Heel in Hybrid Systems of Diruthenium Water Oxidation Catalysts Anchored on Indium Tin Oxide: the Stability of the Anchor

J. Odrobina, J. Scholz, M. Risch, S. Dechert, C. Jooss, and F. Meyer

Reproduced from ACS catalysis 7, 6235-6244, 2017

Abstract: The development of hybrid devices for photo-driven water oxidation with dinuclear molecular ruthenium catalysts on solid supports aims both at high efficiencies of the catalyst and at high stability of the linking to the surface. We herein report a systematic study regarding the stability of catalysts anchored on an indium tin oxide (ITO) support via different acid functional groups at the ligand backbone: viz., a single carboxylate anchor, two carboxylate anchors, and a phosphonate anchor.

The integrity of the hybrid electrodes ITO|*meso*-ITO|catalyst was evaluated under acidic aqueous conditions as a function of the applied electric potential below and above the onset of the oxygen evolution reaction (OER). Rotating ring disk electrode (RRDE) experiments allowed us to distinguish between the water oxidation and the desorption processes. X-ray photoemission (XPS) and X-ray absorption spectroscopy (XAS) after electrochemical treatment showed high chemical stability of the catalyst core structure but pronounced dependence of the hybrid stability on the oxidation state of the ruthenium center. A combination of these different spectroscopic techniques shed light on the mechanisms underlying catalyst desorption. Specifically, catalysts equipped with carboxylate anchors are found to continuously desorb already at low applied potentials below the OER onset, while for the more rugged phosphonate-based hybrid oxidative P-C(aryl) bond cleavage is proposed to occur, but only after reaching the high-valent Ru^VRu^{IV} state. These findings reveal specific challenges for anchoring strategies in molecular water oxidation catalysis.



6.1 Introduction

Exploiting renewable energy sources has become one of the most significant scientific topics in the first decades of the 21st century. In that context, artificial photosynthesis is an attractive approach to store solar energy in chemical bonds^[200]. The progress and increased attention in recent years is reflected by the increasing number of articles and reviews highlighting challenges of light harvesting and advances in catalytic performance^[8,11,13,112,202,205,208,259–262]. Water oxidation catalysis is one of the most critical steps in artificial photosynthesis. The reaction is a four-electron-four-proton coupled process which is energetically and kinetically very demanding. Overpotentials and catalyst stabilities must be improved to reach decent economically viable values. To rationally improve these properties, the catalysts should be well understood in terms of reaction mechanism as well as stability-limiting factors such as decomposition pathways. Molecular catalysts are spectroscopically easy to address and can be modified in a targeted and defined fashion. Especially in the field of ruthenium-based water oxidation catalysts (WOCs), it has been possible to gain thorough mechanistic insight into a number of systems^[6,21,34,201,228,263,264]. By intelligent ligand design, the efficiency of ruthenium WOCs has been drastically enhanced in the last 30 years^[34,222,225,227,229,265].

Some of these molecular ruthenium catalysts have been successfully grafted on solid supports, which is mandatory for solar-fuel devices^[232,234,251,252,258,266,267]. A convenient immobilization method is to anchor the molecules via acid functional groups to oxide substrates^[102]. Carboxylic and phosphonic acids are commonly used anchoring groups that achieve immobilization of catalysts under aqueous conditions^[103–106,124]. Despite the successful binding of complexes on substrates, the stability of the surface binding under reactive conditions is crucial for the total performance, and known systems are frequently suffering from degradation^[108–110]. A strategy to stabilize the anchored WOC on the surface is the use of additional stabilizing layers of polymers or oxides which cover the anchoring groups. However, the overlayer has a drastic effect on the morphology of the hybrid, leading to a drop in WOC activity^[113–115].

In order to optimize the binding between the solid support and the catalyst by chemically designed anchor groups, it is essential to understand the factors which determine the stability of the linkages. As the anchor represents the interface between the oxide substrate and the WOC, both parts contribute to the

stability and need to be understood. Indium tin oxide (ITO) is a promising candidate as an oxide substrate. It is conductive and optically transparent in a broad wavelength region, its physicochemical properties are well-known, and numerous studies of surface immobilization of molecular chromophores and catalysts on ITO have been reported in the literature^[117–123,268]. In addition to these favorable properties, the high surface area of mesoporous ITO (*meso*-ITO) is beneficial for understanding the hybrid systems in detail, due to higher surface concentration and enhanced detectability of electronic and spectroscopic fingerprints of the anchored complexes^[104,106,110,241,269].

The WOC used in the present investigation is based on a binucleating ligand which positions two ruthenium centers in close proximity. A family of diruthenium complexes based on the monoanionic bis(bipyridyl)pyrazolate (bbp^-) ligand was recently established as rugged and efficient WOCs^[21,34,35,37]. Each of the ruthenium ions is nested in a tridentate meridional binding pocket of the bbp^- ligand and coordinated by pyridine in the two axial positions. The resulting bimetallic pocket offers two possible binding sites for water coordination. The mechanism of water oxidation for a highly water soluble derivative under homogeneous conditions was shown to proceed via sequential proton-coupled electron transfer steps followed by water nucleophilic attack (WNA) in the formal $\text{Ru}^V(=\text{O})\text{Ru}^{IV}(=\text{O})$ state^{[34]1}. In recent work we reported the modification of the $\text{Ru}_2\text{-bbp}$ WOC **1** with a carboxylate anchoring group at the pyrazole- C^4 position in the ligand backbone^[270]. The modified complex **1** was successfully anchored to a *meso*-ITO support and showed high activity for water oxidation under pH 1 conditions without decomposition of the complex into RuO_2 . However, the binding between the oxide and the carboxylic acid functionality was identified as a weak link needing further improvement.

In this work, we present a set of ruthenium bbp complexes modified in a modular synthetic approach with three different anchoring functionalities, in order to interrogate and optimize the binding stability to the solid support: a single carboxylate anchor, two carboxylate anchors, and a phosphonate anchor. With the resulting stability improvement of the hybrid, we studied the most stable system to evaluate the activity and stability under reactive conditions using cyclic voltammetry (CV) and rotating ring disk electrode (RRDE) measurements. CV is employed to study the evolution of the hybrid surface coverage upon reversible electron transfer processes between the oxide surface and the anchored catalyst.

¹Contributions from ligand-based oxidation cannot be safely excluded beyond the $\text{Ru}^{IV}\text{Ru}^{IV}$ state

The adaptation of the RRDE method allowed probing the desorbed species *in situ* under reactive conditions by suitable setting of the ring potential. In addition, we applied XPS and XAS to investigate the chemical integrity of the anchored catalysts. On the basis of such detailed characterization of the immobilized complexes and the differences in stability and activity associated with the respective anchoring moieties, we can develop a comprehensive picture of the behavior of these molecular WOC hybrid systems.

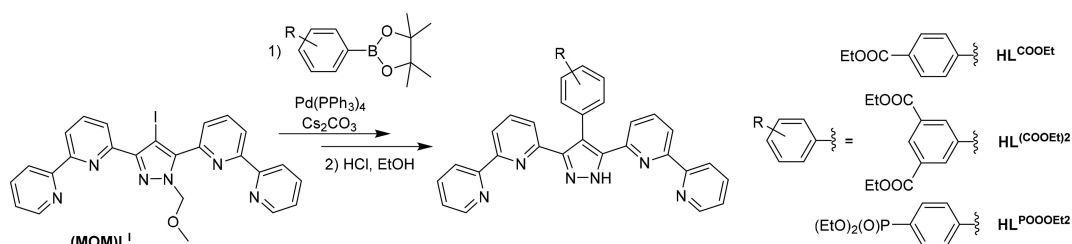


Figure 6.1: Synthetic Route for Introducing Different Anchoring Groups at the bbp Backbone, Giving Ether-Protected Proligands HL^{COOEt} , $\text{HL}^{(\text{COOEt})_2}$, and $\text{HL}_2^{\text{POOOEt}}$

6.2 Results and discussion

Synthesis and Characterization of the Complexes A modular synthetic protocol was developed that allows introducing different anchoring groups at the pyrazole- C^4 position. The synthesis of the new ligand derivatives has been adapted from previously reported procedures (details are given in the Supporting Information)^[34–36,270]. A palladium-catalyzed Suzuki-Miyaura cross-coupling reaction connects the ester variants of the anchoring groups with the methoxymethyl (MOM) protected iodo derivative of Hbbp, $(\text{MOM})\text{L}^{\text{I}}$ (Scheme 6.1), and pyrazole deprotection then occurs during acidic workup. To improve the binding stability of the complex to the oxide surface, taking HL^{COOH} as the starting point, we followed two strategies. In the first approach, we varied the number of possible anchoring sites by introducing a second carboxylic acid functional group in the ligand backbone. The resulting proligand $\text{HL}^{(\text{COOEt})_2}$ has two carboxylic acid groups in 3,5-positions at the peripheral phenyl group attached to the pyrazole- C^4 . In the second approach the carboxylic acid group in HL^{COOH} was replaced by a phosphonic acid group ($\text{HL}^{\text{POOOEt}_2}$), which is usually assumed to have a much higher binding constant to oxide

surfaces in comparison to the carboxylate anchor^[111]. The new complexes $[L^{(COOEt)_2}Ru_2(OAc)(py)_4](PF_6)_2$ and $[L^{(POOOEt)_2}Ru_2(OAc)(py)_4](PF_6)_2$, both containing an exogenous acetate bridge, could be synthesized following established procedures with only small optimizations of the protocols (see^[246])^[270]. The complexes have been fully characterized by electrospray ionization mass spectrometry (ESI-MS) and elemental analysis, as well as one-dimensional (1D) and two-dimensional (2D) nuclear magnetic resonance (NMR) spectroscopy (¹H, ¹³C, ³¹P); the molecular structure of $[L^{(POOOEt)}Ru_2(OAc)(py)_4](PF_6)_2$ was further authenticated by single-crystal X-ray diffraction (XRD)^[246]. For experimental details and spectroscopic signatures of all new compounds please refer to^[246].

To ensure rapid release of the exogeneous bridge and formation of catalytically active diaqua species $[L^xRu_2(OH_2)(py)_4]^{3+}$ upon acidification, the relatively inert acetate bridge in $[L^{(COOEt)_2}Ru_2(OAc)(py)_4](PF_6)_2$ and $[L^{(POOOEt)_2}Ru_2(OAc)(py)_4](PF_6)_2$ was replaced by acid-labile bicarbonate and, in the same one-pot reaction sequence, the backbone carboxylic or phosphonic esters were hydrolyzed to give the precatalyst complexes $[L^{COOH}Ru_2(CO_3H)(py)_4](PF_6)_2$ (**1**)^[111], $[L^{(COOH)_2}Ru_2(CO_3H)(py)_4](PF_6)_2$ (**2**), and $[L^{POOOH}Ru_2(CO_3H)(py)_4](PF_6)$ (**3**) (Figure 6.2). In the last case, acetate to bicarbonate exchange was best achieved via the intermediate bromo-bridged complex according to the sequence $[L^{(POOOEt)_2}Ru_2(OAc)(py)_4](PF_6)_2 \rightarrow [L^{POOOH}Ru_2Br(py)_4](PF_6) \rightarrow \mathbf{3}$. Details for the synthetic procedures and for the characterization of all new complexes are provided in^[246].

Several methods were applied to assess the influence of the different backbone anchoring groups on the electronic properties of the bbp-Ru₂ core. NMR shifts of the bicarbonate-bridged precatalysts **2** and **3** differ only slightly from the values reported for the parent **1**, which is equipped with a single carboxylate anchor (Figure 6.2)^[270]. Comparison of the structurally characterized acetate-bridged precursors **1a-3a** (Figure 6.2) reveals only minor differences in bond lengths and angles among the series of complexes (see^[246] for metric parameters). Furthermore, electrochemical fingerprints, determined by cyclic voltammetry for the Ru^{III}Ru^{II}/Ru^{II}Ru^{II} and Ru^{III}Ru^{III}/Ru^{III}Ru^{II} couples in propylene carbonate (PC) solution, do not differ significantly for **1-3**. The turnover numbers (TON) and initial turnover frequencies (TOF_i) in homogeneous chemically driven water oxidation catalysis under benchmark conditions, using 100 equiv of Ce^{IV} (cerium ammonium nitrate, CAN) as a sacrificial chemical oxidant in 0.1 M triflic acid solution, are very similar for

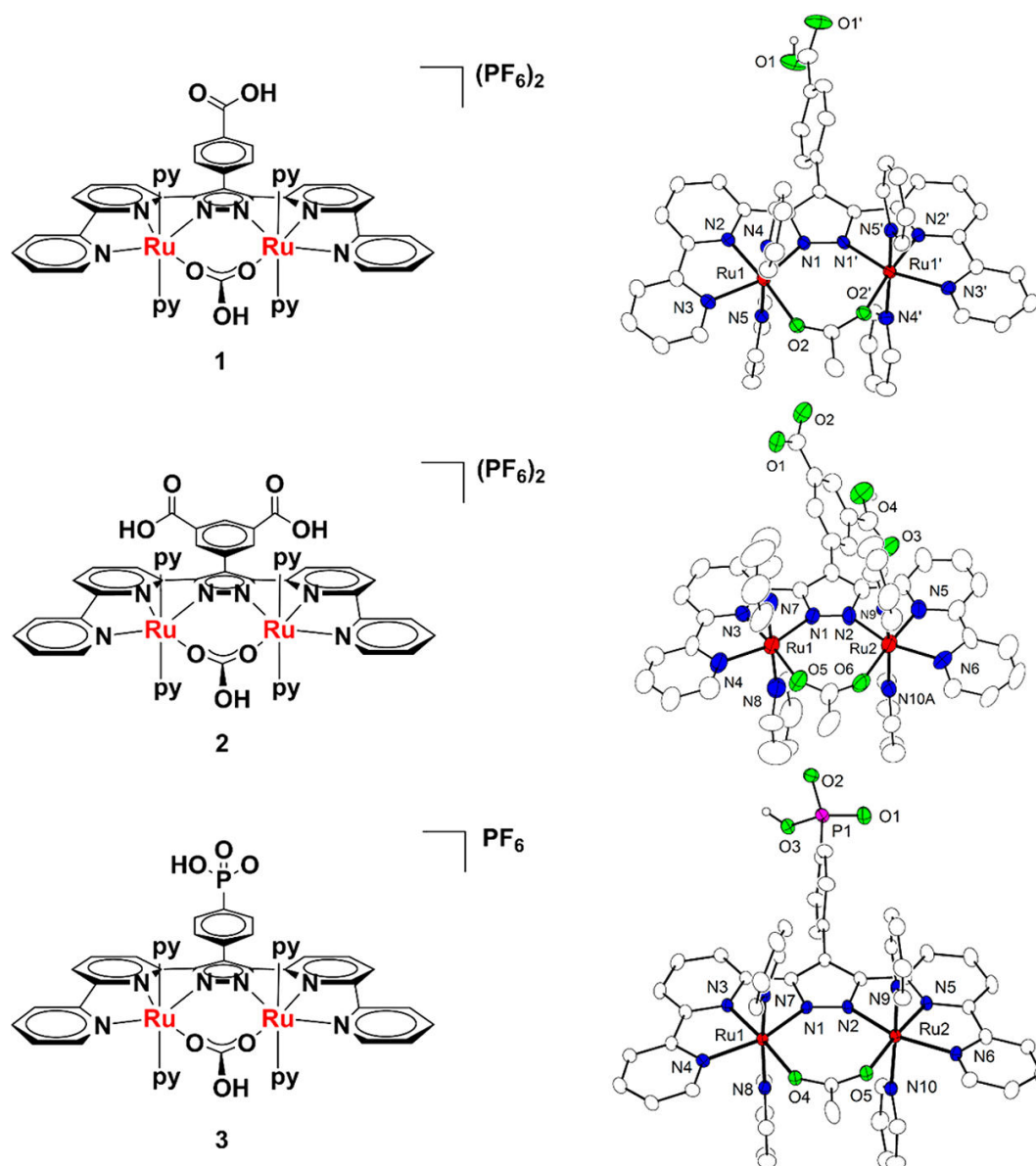


Figure 6.2: Molecular structures of (left) bicarbonate-bridged catalyst precursors **1**^[270], **2**, and **3**, which were anchored to the solid support, and (right) the corresponding acetate-bridged complexes **1a**^[270], **2a**, and **3a** determined with XRD

the set of catalysts and are similar to the values for the parent complex lacking any backbone anchor (see Table 9.2 in the Supporting Information). Taken together, we conclude that introducing and varying the anchoring groups at the pyrazole-C⁴ position has only minor effects on the electronic structure of the bbp-Ru₂ core.

Stability of the Hybrid below the OER Threshold. The general approach to immobilize the complexes is chemisorption of the ligand backbone carboxylic or phosphonic acid functionality to the ITO surface. To reach high surface loadings, the ITO glass slides were covered with a meso-ITO layer (ITO|*meso*-ITO) followed by an established annealing procedure^[104,239,241,242]. The catalyst precursor was immobilized by soaking the ITO|*meso*-ITO slides in a 0.1 mM complex solution in methanol. The growing process was monitored by diffusive reflectance UV/vis (DR-UV/vis) spectroscopy (Figure 9.1 in Appendix B). The modified ITO|*meso*-ITO slides were then used as working electrodes in CV experiments to investigate the hybrid systems under noncatalytic conditions in an aqueous environment.

In CV experiments, where the analyte is immobilized to the electrode, the number of electrons transferred during a reversible redox process directly reflects the total amount of analyte anchored to the electrode. The reversible redox process (Ru^{III}Ru^{II}/Ru^{II}Ru^{II}) thus is a measure of the number of anchored complexes on the ITO|*meso*-ITO surface. To evaluate the binding stability of the complexes on the surface, CVs of **1** - **3** on ITO|*meso*-ITO in the Ru^{III}Ru^{II}/Ru^{II}Ru^{II} potential range were recorded repetitively over several cycles at a scan rate of 10 mV/s in triflic acid (0.1 M, pH 1) (Figure 6.3).

The detachment of complexes is reflected by a decrease in the peak current. The trend in peak currents could be fitted satisfactorily with a biexponential fit (Figure 6.3D). The biexponential character of the desorption process reflects the different diffusion length scales in the mesoporous electrode, where k_d is the overall desorption rate constant and includes the detachment from the surface and subsequent diffusion into the solution^[109]. The two complexes anchored via carboxylate functionalities show k_d values on the same order of magnitude. The surface concentration could be significantly improved during the growing process when the bis-carboxylate complex **2** was used; however, **2** is even slightly more weakly attached to the electrode than the mono-carboxylate complex **1** under pH 1 conditions (Figure 6.3A,B). The best improvement in stability combined with a favorably increased surface concentration is observed when **3** equipped with a phosphonate anchor was used (Figure 6.3C; the

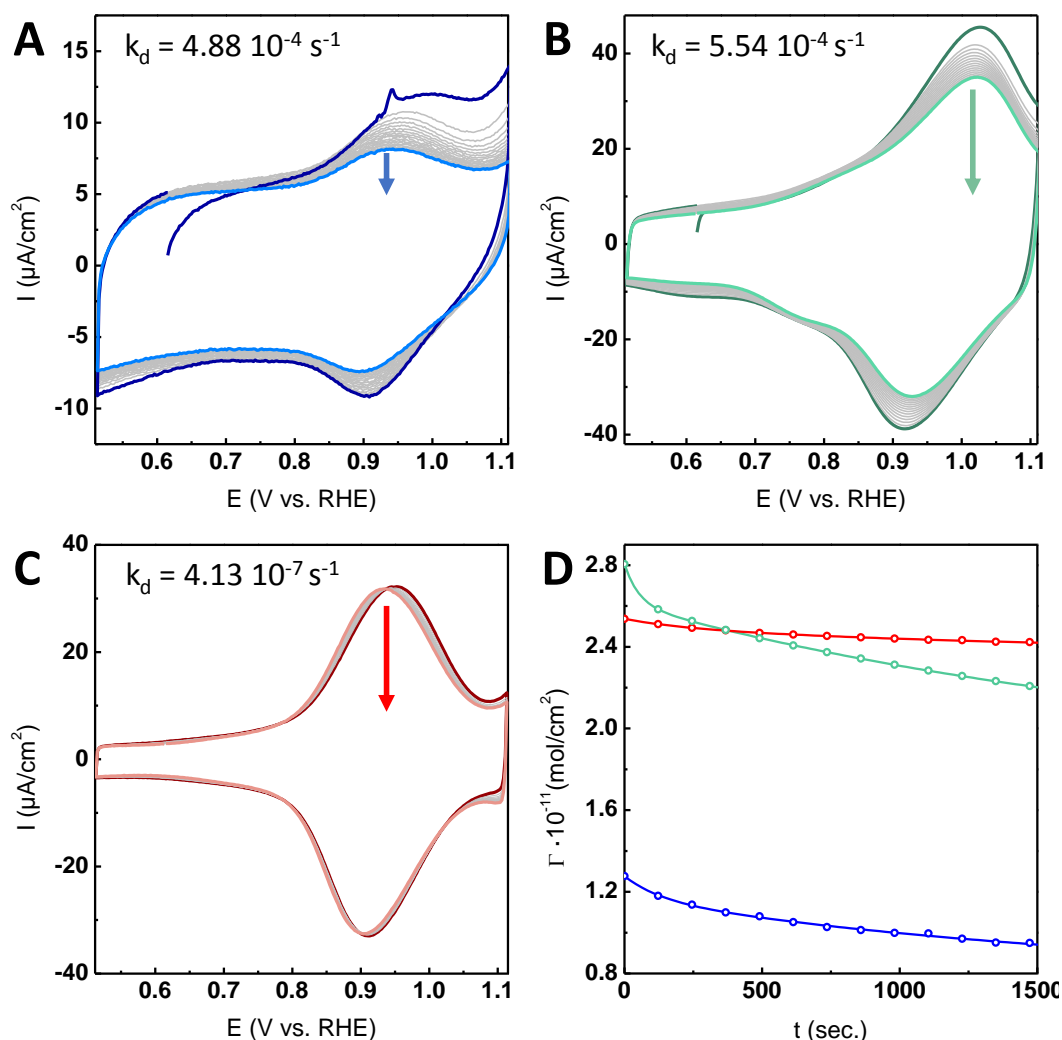


Figure 6.3: Cyclic voltammetry of (A) ITO|*meso*-ITO|**1** (WE), (B) ITO|*meso*-ITO|**2** (WE), (C) ITO|*meso*-ITO|**3** (WE) with the initial (dark color) and final (light color) traces highlighted. The arrows indicate the decline in peak current. (D) Desorption profiles of immobilized complexes extracted from peak currents. The colors in the plot conform to the colors of the respective CVs (data points correspond to the respective peak current of each scan, and the continuous lines show the biexponential fits of the data). All measurements have been performed at a scan rate of 10 mV/s in triflic acid (0.1 M, pH 1) with a Pt CE and a mercury sulfate reference electrode (MSE).

slight shift in anodic peak potential may result from partial hydrolysis of the bicarbonate bridge to give the diaqua complex). Insolubility is a key feature for stable anchoring. Complex **2** is more soluble in aqueous environment than **1**, whereas in methanol the solubility is reversed. The increasing number of binding sites of the bis-carboxylate complex **2** is counteracted by its higher solubility in water, thus leading to increasing desorption rates for **2**. Notably, k_d of the phosphonate anchored **3** is 3 orders of magnitude lower in comparison to **1** and **2**. In contrast to the latter complexes bearing carboxylate groups, **3** shows only a negligible decline in peak current during repetitive CV measurements up to 1.5 V vs RHE (Figure 9.9 in the Supporting Information). Hence the phosphonate complex **3** is stably anchored to the ITO surface even under high applied potentials (up to 1.5 V vs RHE).

Characterization of the Hybrid above the OER Threshold. Characterization of the hybrid electrodes at potentials below the threshold for water oxidation catalysis shows a significant influence of the anchoring group on stability, with **3** featuring the most favorable characteristics. However, the stability of the WOC in the catalytic region is crucial for further applications. To evaluate the behavior of ITO|*meso*-ITO|**3** under OER conditions, RRDE measurements were employed to assess its catalytic activity. The observed potentials for the $\text{Ru}^{\text{V}}\text{Ru}^{\text{IV}}/\text{Ru}^{\text{IV}}\text{Ru}^{\text{IV}}$ oxidation and the onset potential of the water oxidation catalysis of ITO|*meso*-ITO|**3** (onset potential 1.55 V vs RHE, $\text{Ru}^{\text{V}}\text{Ru}^{\text{IV}}/\text{Ru}^{\text{IV}}\text{Ru}^{\text{IV}}$ 1.69 V vs RHE in Figure 3) and the water-soluble $[(\text{bbp}^{\text{Me}})\text{Ru}_2(\text{O}_2\text{H}_3)-(3\text{-SO}_3\text{-py})_4]^{2-}$ studied under homogeneous conditions compare very well (bbpMe is the bis(bipyridyl)pyrazolate ligand with a methyl group at the pyrazolate- C_4 position and 3- $\text{SO}_3\text{-py}$ is pyridine-3-sulfonate; onset potential 1.50 V vs RHE, $\text{Ru}^{\text{V}}\text{Ru}^{\text{IV}}/\text{Ru}^{\text{IV}}\text{Ru}^{\text{IV}}$ 1.68 V vs RHE)^[34].

RRDE measurements demonstrate the ability of the hybrid to drive the oxygen evolution reaction catalytically. A potential of 0.25 V vs RHE was applied to the Pt ring electrode, which is sufficient to drive the oxygen reduction reaction (ORR) under diffusion-limited conditions (calibration measurements shown in Figure 9.10 in Appendix B). When CV measurements are performed at the ITO|*meso*-ITO|**3** disk electrode with rotation, the products formed during the reaction are transported outward to the Pt-ring electrode. Careful analysis of the ring currents is needed, as uncovered ITO can evolve dioxygen, and the potential at the Pt ring is sufficient to reduce not only dioxygen but also e.g.

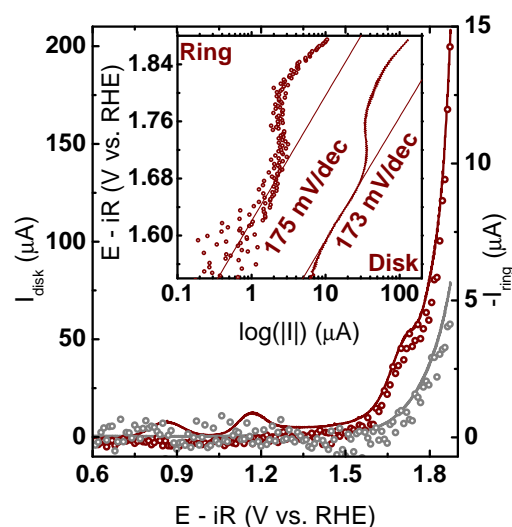


Figure 6.4: Rotating ring disk CV measurements of ITO|*meso*-ITO|**3** (dark red) and the blank ITO|*meso*-ITO electrode (solid grey line). The corresponding ring currents are shown as red, and grey dots corresponding to oxygen reduction ($V_{ring}=0.25$ V vs. RHE). Note that the background currents of the unmodified ITO electrode and the respective ring currents corresponding to complex desorption were subtracted (see text). The inset shows the Tafel analysis of both ring and disk current density as a function of disk voltage after subtraction of the background currents of blank electrodes. All measurements were performed with 0.1 M triflic acid supporting electrolyte (Ar-purged) at 10 mV/s and 1600 rpm. The voltage was corrected for uncompensated resistance. The positive-going direction of the first scan is shown.

desorbing complexes (further discussed below). By subtraction of background currents of oxygen evolution at the unmodified ITO (grey lines in Figure 6.4) and the currents due to desorbing complexes (Figure 6.3), we assume that the remaining ring currents solely correspond to oxygen evolved by the immobilized complexes. These ring currents showed significantly increased activity for the hybrid electrode ITO|*meso*-ITO|**3** (Figure 6.4) in comparison to unmodified ITO, which is analogous to our previous reports for immobilized **1**^[270]. The onset potential for water oxidation indicated by the increasing ring current was found at 1.55 V vs RHE.

Additionally, the ring currents can provide information about side reactions limiting the efficiency of the oxygen evolution. Note that the corresponding disk currents can only be corrected for the background currents of the ITO substrate. The sharp bend for ITO|*meso*-ITO|**3** between 1.7 and 1.76 V vs RHE in the Tafel slopes of both ring and disk reflects that additional charge is used for the oxidation to Ru^VRu^V rather than sustaining the previous reaction rate of Ru^{IV}Ru^V, thus further increasing the amount of evolved oxygen². At high potentials, comparison of the corrected ring and disk currents by Tafel analysis (inset of Figure 6.4) shows different Tafel slopes, which indicates that the disk currents are not solely reflecting the electron transfer of oxygen evolution. However, the Tafel slopes for ITO|*meso*-ITO|**3** differ only above the complete oxidation to Ru^VRu^V at 1.78 V vs RHE; below 1.7 V vs RHE the Tafel slopes are identical at ring and disk electrodes, thus suggesting high efficiency regarding water oxidation catalysis. Moreover, the ring Tafel slope measured for ITO|*meso*-ITO|**3** below 1.7 V vs RHE is essentially identical with our previously reported Tafel slope of 182 mV/dec for **1**, thereby suggesting the same reaction kinetics^[270]. The deviation of disk Tafel slopes in some regions from the reported value of 182 mV/dec indicates that oxygen evolution might be superimposed by additional processes such as desorption of highly oxidized complexes that presumably could evolve oxygen homogeneously. Because the Tafel analysis suggested that additional processes are operative, further evaluation of the stability under catalytic conditions needed to be performed.

To gain more insight into the additional processes, viz. the destabilization of the hybrid system, we again used RRDE measurements. Considering the step-wise oxidation of the anchored complexes, and assuming a higher desorption rate under reactive conditions, implies that a highly oxidized species is gener-

²Contributions from ligand-based oxidation cannot be safely excluded beyond the Ru^{IV}Ru^{IV} state

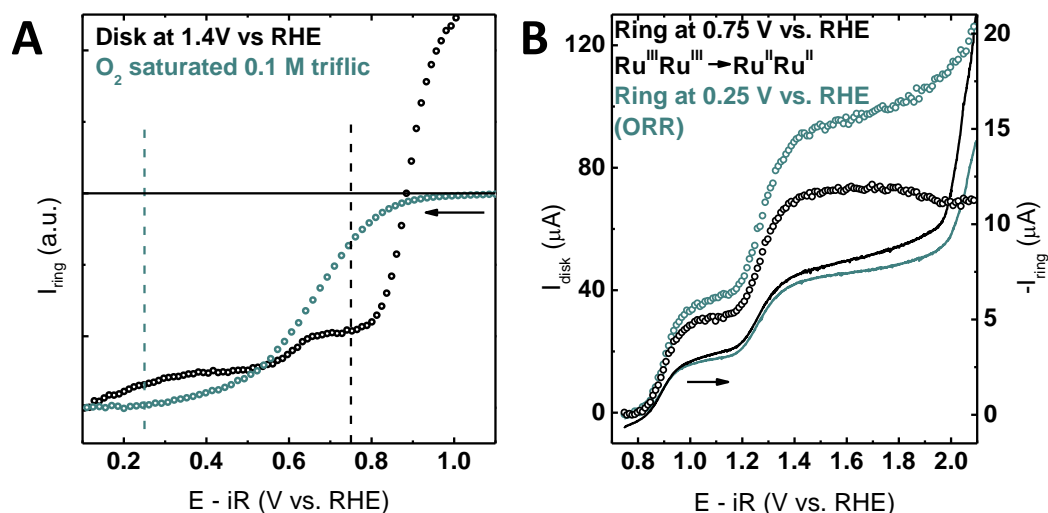


Figure 6.5: (A) Rotating ring disk measurements showing comparison between the CV measurements at the Pt-ring electrode for 0.5 mM $[(bbp^{Me})Ru_2(O_2H_3)-(3-SO_3-py)_4]^{2-}$ in Ar-saturated triflic acid (0.1 M, pH 1) and the ITO disk electrode at an oxidizing potential of 1.4 V vs RHE (black) and for an O_2 -saturated triflic acid (0.1 M, pH 1) without complex and the ITO disk at open circuit potential (OCP) (cyan). Note that the current scale was normalized to compare the onset of the CRR and ORR. At the potential of 0.75 V vs RHE the oxygen reduction contributes as the kinetically limited currents show. Nonetheless, (B) shows that for operating conditions with both dioxygen and oxidized complex present a clear distinction is possible. (B) RRDE measurement with 0.5 mM $[(bbp^{Me})Ru_2(O_2H_3)-(3-SO_3-py)_4]^{2-}$ in Ar-saturated triflic acid (0.1 M, pH 1) cycling the ITO disk electrode and holding the ring electrode at 0.75 V vs RHE to probe the complex reduction (black) and the ring electrode at 0.25 V vs RHE to probe the oxygen reduction (cyan). The ring currents for the complex reduction show no increase in the regime corresponding to oxygen evolution, which shows the suitability to exclusively probe the complex desorption. The rotation rate for all experiments was 1600 rpm.

ated and possibly partially detached^[109,270]. Therefore, one needs to disentangle the contributions of the detachment and the oxygen evolution to the ring current during OER activity. By convection enforced through the rotating electrode, the oxidized complexes are transported to the ring electrode. If the ring potential for the reduction of the complexes is sufficiently separable from the oxygen reduction potential at the Pt-ring electrode, it is possible to differentiate the evolved oxygen and the detached complexes. This offers a method for evaluating the stability under reactive conditions *in situ*.

Therefore, calibration measurements at the Pt ring electrode were performed to probe the reaction conditions for disentangling the oxygen reduction reaction (ORR) (Figure 9.10 in Appendix B) and the complex reduction reaction (CRR) (Figure 6.5 and Figure 9.12 in Appendix B). Careful calibration showed a superposition of the dioxygen reduction (calibration in O₂-saturated triflic acid (0.1 M, pH 1), Figure 9.10) and the reduction of the homogeneous [(bbp^{Me})Ru₂(O₂H₃)-(3-SO₃-py)₄]²⁻ complex^[34] that was oxidized at an ITO disk electrode. To avoid superposition with the dioxygen reduction, calibration of the ring electrode has been performed in Ar-saturated triflic acid (0.1 M, pH 1; Figure 6.5A). The Pt-ring electrode was held at a potential of 0.75 V vs RHE, which is sufficient to drive the diffusion-limited complex reduction. At this potential, the oxygen reduction reaction contributes through kinetically limited currents (Figure 6.5A). Under operating conditions, where both dioxygen and oxidized complexes are present, a clear distinction between them is possible (Figure 6.5B), and hence monitoring the oxygen evolution can be separated from the complex detachment. Note that the results shown in Figure 6.4 for the ORR were already corrected for the currents due to the CRR.

With the method established, we examined the stability in terms of desorption using the electrode setup described previously^[179], using **1** (Figure 6.6A), **3** (Figure 6.6B), and **3a** (Figure 6.6C) immobilized on ITO|*meso*-ITO electrodes; note that bicarbonate complexes **1** and **3** rapidly give the diaqua complexes in 0.1 M triflic acid (pH 1). To provide comparable conditions and sufficient concentrations, desorption under reactive conditions was probed using the first measured cycle of freshly prepared hybrid electrodes according to a common protocol (details in Appendix B).

The ring currents reveal the potential dependence of the desorption processes for both anchoring groups. In case of the hybrid anchored via a carboxylate, an increase in the ring currents corresponding to reduction of desorbed complexes (Figure 6.6A) above 1.2 V vs RHE was measured with only a small further in-

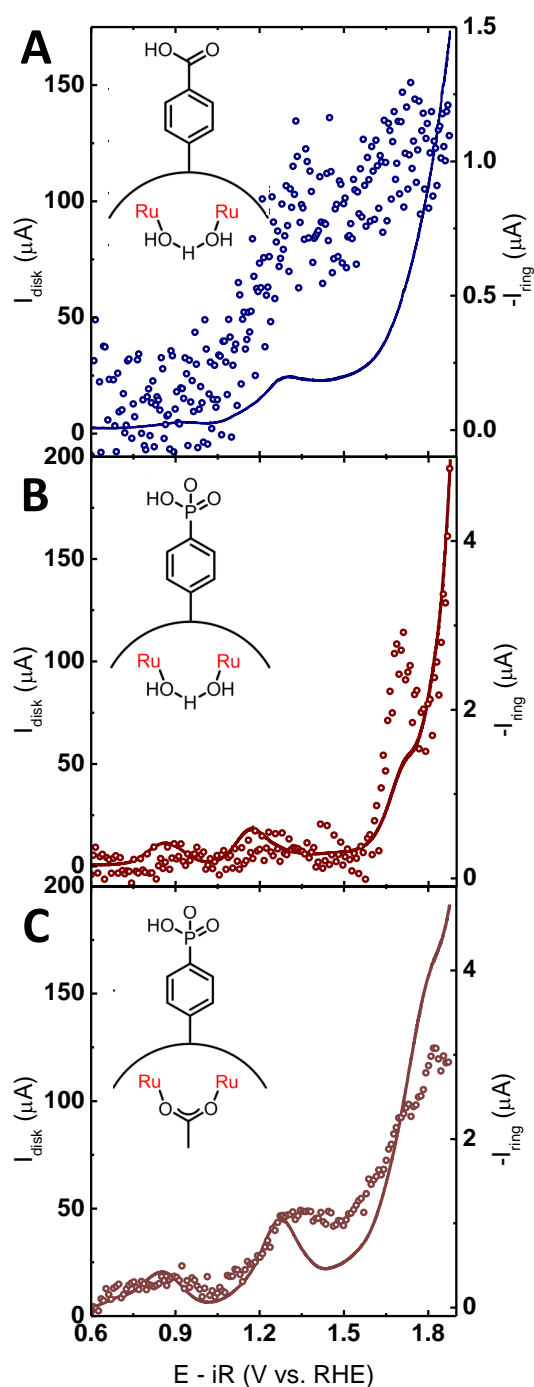


Figure 6.6: Rotating ring disk CV measurements of (A) $\text{ITO}|\text{meso-ITO}|1$ (dark blue line), (B) $\text{ITO}|\text{meso-ITO}|3$ (dark red line), and (C) acetate bridged $\text{ITO}|\text{meso-ITO}|3a$ (brown line). The corresponding ring currents are shown as dots. The ring currents represent the currents corresponding to reduction of the oxidized complexes ($V_{\text{ring}} = 0.75$ V vs. RHE). All measurements were performed in 0.1 M triflic acid (Ar-purged) at 10 mV/s and 1600 rpm. The voltage was corrected for uncompensated resistance. The positive-going direction of the first scan is shown. Note the amplitude of unnormalized ring currents does not reflect the differences in stability.

crease at potentials up to 1.9 V vs RHE. Note that desorption previously shown under noncatalytic conditions is only detectable for oxidation states of at least $\text{Ru}^{\text{II}}\text{Ru}^{\text{III}}$, hence above disk potentials of 0.9 V vs RHE. Therefore, the measured potential-dependent destabilization occurs in addition to the intrinsic desorption and well before the reactive regime of the water oxidation, but it shows no pronounced increase under the highly oxidizing conditions. The phosphonate hybrid $\text{ITO}|\text{meso-ITO}|3$ reveals a different behavior, evidenced by the ring currents shown in Figure 6.6B. In the noncatalytic regime, desorption is negligible but desorption is drastically increased under reactive conditions above 1.55 V vs RHE. The desorption shows a local maximum around 1.7 V vs RHE and proceeds to increase up to the turning potential. Interestingly the maximum in desorption at 1.7 V vs RHE coincides with the peak in disk current of the oxidation up to $\text{Ru}^{\text{V}}\text{Ru}^{\text{IV}}$, suggesting a detrimental effect of the high oxidation state on the stability of the hybrid system.

In order to validate that the Ru oxidation state effects the stability rather than the sole oxidation of the anchor in the case of the phosphonate-based hybrid, we compared the bicarbonate bridged **3** (Figure 6.6B) to the acetate-bridged **3a** (Figure 6.6C). In contrast to the bicarbonate -bridged complex, exchange of the acetate bridge to give the catalytically active diaqua compound is slow (see Appendix B)^[36]. Thus, in the acetate-bridged complex any PCET sequence to give $\text{Ru}=\text{O}$ species is prevented. The complex is therefore only oxidized to the $\text{Ru}^{\text{III}}\text{Ru}^{\text{III}}$ state, thus making the water oxidation catalysis inaccessible, whereas the diaqua complex can be oxidized via PCET steps to high-valent metal-oxo species in the same potential range. Remarkably, no local maximum for complex desorption is observed at the potential of 1.7 V vs RHE for the acetate-bridged complex (see Figure 6.6C). The increase in ring currents for higher potentials is due to the slow exchange of the acetate bridge under pH 1 conditions to give the diaqua species, which can then drive the water oxidation catalysis and possibly participate in the destabilization mechanism. Note that the ring response for the hybrid decorated with the acetate-bridged **3a** (Figure 6.6C) seems to reach relatively high currents, which is due to the currents not being concentration corrected. These results indicate that reaching the high-valent metal-oxo species in the formal $\text{Ru}^{\text{V}}\text{Ru}^{\text{IV}}$ state is responsible for the additional loss of complexes during water oxidation catalysis with $\text{ITO}|\text{meso-ITO}|3$.

In summary, the presented method using RRDE experiments allows evaluation of the stability of the immobilized complexes under reactive conditions *in situ*. We conclude that, despite the appearance of comparable orders of magnitude

scales for the desorption processes in Figure 6.6A,C, the initial trend of stability seen in Figure 6.3 is preserved. By normalization of the starting concentration, we observed ring currents per mole of immobilized complex more than 1 order of magnitude higher for the carboxylate anchor in comparison to the phosphonate anchor (Figure 9.13 in Appendix B). Since the ring currents for the CRR reflect the concentration of desorbing complexes, the normalized ring currents directly correspond to the fraction of initial complexes being detached. Furthermore, the CRR experiments reveal that the phosphonate anchor, despite the higher stability at positive potentials under noncatalytic conditions, is unstable under catalytic conditions due to the detrimental effect of the highly oxidized metal-oxo species in $\text{Ru}^{\text{V}}\text{Ru}^{\text{IV}}$.

Further experiments were then aimed at evaluating the identity of the species after electrochemical treatment to obtain insight into the cause of destabilization and catalyst detachment. The catalytic regime is known to be challenging, and even in reported examples of hybrid electrodes with very stable immobilized WOCs the oxygen evolution activity gradually decreases under catalytic conditions^[231,232,252,258]. Degradation can occur via different pathways. Under the highly oxidizing conditions, oxidative degradation of the ligand framework is known to lead to the thermodynamically most stable metal oxide product: viz., RuO_2 ^[90]. However, not only the ruthenium core and ligand backbone can decompose under such harsh conditions; the anchoring of acid functional groups on oxide surfaces is also known to be unstable^[109,110,114,243,270].

The chemical stability of the complex core remaining on the electrode was probed with XPS experiments by measuring the N 1s and Ru 3d states (Figure 9.16 in Appendix B) and by comparison of ITO|*meso*-ITO|₃ samples before and after chronoamperometry (CA) for 600 s at 1.813 V vs RHE. The ratio of these elements was determined on the basis of the peak intensity corrected by the relative sensitivity factors (rsf) provided by CasaXPS. The ratio determines the stoichiometry and probes the chemical stability of the ligand, as both Ru and N are only present in the complex. Other elements such as carbon, oxygen, indium, and tin were also measured (Figures 9.16 and 9.17 in Appendix B) but not evaluated in terms of stoichiometry, as they are not exclusively present in the complexes. The resulting stoichiometry in Figure 6.7A shows no significant change after the electrochemical treatment, while an increasing Ru to N ratio would have been expected for the formation of RuO_2 . Hence, we conclude that the ligand backbone and molecular diruthenium entities are chemically stable under reactive conditions and do not form RuO_2 . The role of the anchor that serves as

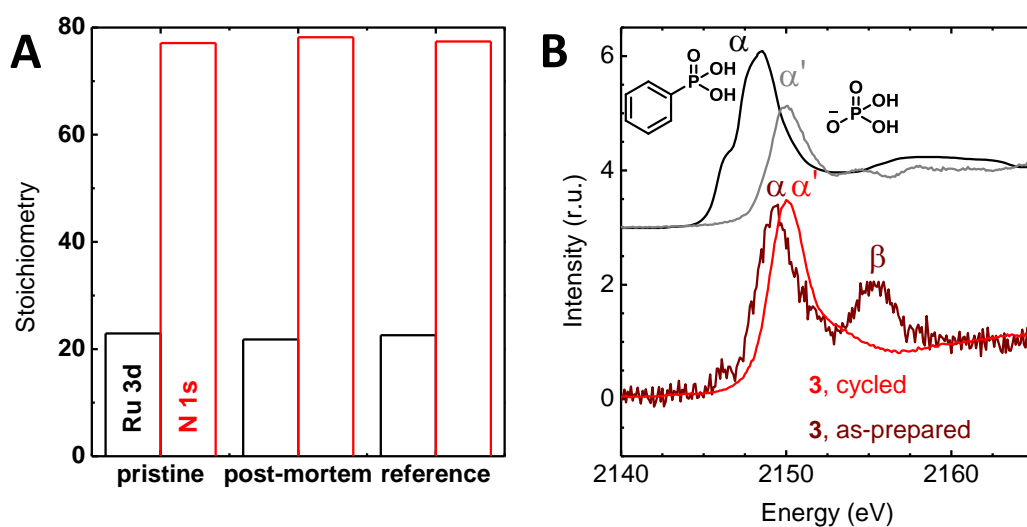


Figure 6.7: (A) Stoichiometry of ITO|*meso*-ITO|**3** as prepared in comparison to a dropcast reference sample of **3** on Au and ITO|*meso*-ITO|**3** after water oxidation catalysis. The stoichiometry was determined based on the intensity of N 1s and Ru 3d states (high resolution spectra in Figure 9.16). (B) Partial fluorescence yield XAS recorded at the P-K edge of as-prepared and cycled GC|*meso*-ITO|**3** as well as monobasic phosphate and phenyl phosphonate (extracted from literature^[271]) as references.

a link between substrate and complex was previously discussed^[108,109,270], but experimental access by, e.g., XPS is challenging due to low intensity for the P of the phosphonate anchor and strong overlap for the C of the carboxylate anchor. X-ray absorption spectroscopy (XAS) at the P K-edge was therefore used to elucidate the role and integrity of the anchor (Figure 6.7B). The spectrum of as-prepared GC|*meso*-ITO|**3** showed two peaks labeled α at 2149.2 and β at 2155.2 eV. The latter peak has not been discussed previously. It could be caused by electronic interaction with the backbone or be part of the extended X-ray absorption fine structure (EXAFS) originating from, e.g., a specific orientation of the anchor group. Peak β disappears after electrochemical cycling between 0.52 and 1.92 V vs RHE, so that the spectrum of cycled GC|*meso*-ITO|**3** only showed a single peak α' at 2150.0 eV with much greater intensity. As ruthenium is a rather heavy element and thus strong X-ray absorber, the enhanced peak intensity after cycling provides circumstantial evidence that the detected P-containing groups were not attached to a ruthenium complex. Overall, the spectrum of the cycled sample strongly resembles that of phosphates^[272–274], which is further supported by the energy position of the first maximum (Figure 6.7B). The peak at 2150.0 eV of cycled GC|*meso*-ITO|**3** is thus assigned to P^V in a phosphate. A

lower peak energy of peak α relative to peak α' is expected for phosphorus reduction, and the energy difference is similar to that between dihydrogen phosphate and phenylphosphonic acid (Figure 6.7B)^[271]. Peak α is thus assigned to the anchored phosphonate of the intact complex. The energy differences between phosphate and phosphonate vary in the literature, but the difference here is smaller than that previously reported^[271,273]. It is also known that an increase in the electronegativity of the neighboring atoms may shift peak maxima to higher energies^[273]. This would explain the less than expected peak shift, as it is likely that the P-based states overlap with the electronegative π system of the phenyl group in immobilized **3**. The XAS data thus strongly suggest that the phosphonate group of the anchor remains on the surface, where it oxidizes to phosphate upon P-C(aryl) bond cleavage.

The degradation mechanism explains the differences in stability for the hybrids based on the carboxylate and the phosphonate anchors. **3** is abruptly desorbed by oxidative cleavage of the P-C(aryl) bond rather than desorbed due to weak phosphonate binding to the surface, while **1** is rather desorbed due to weak binding. The observed correlation of desorption with the ruthenium oxidation state suggests a dependence of the corrosion mechanisms on the electronic structure of the anchor and its change due to an increase in Ru oxidation state. On the basis of these findings and the previous homogeneous studies, we propose the WOC scenario for the ITO|*meso*-ITO|**3** hybrid shown in Scheme 6.8, which includes a competing corrosion pathway via oxidative P-C(aryl) bond cleavage.

6.3 Conclusion

Robust anchoring of molecular water oxidation catalysts to solid oxide supports is a key challenge for the functional design of artificial photosynthesis devices. Furthermore, adequate stability of the anchor is required in order to elucidate basic principles of interfacial electron transfer and catalyst activity on surfaces. Starting from **1** bearing a single backbone carboxylate anchor^[270], we varied the anchoring groups and immobilized and finally characterized the resulting complexes on ITO substrates to improve and understand the binding functionalities of the previously established active Ru₂-bbp type complexes. By introducing an additional second carboxylate group in **2**, no improvement in the stability under noncatalytic conditions in comparison to complex **1** was

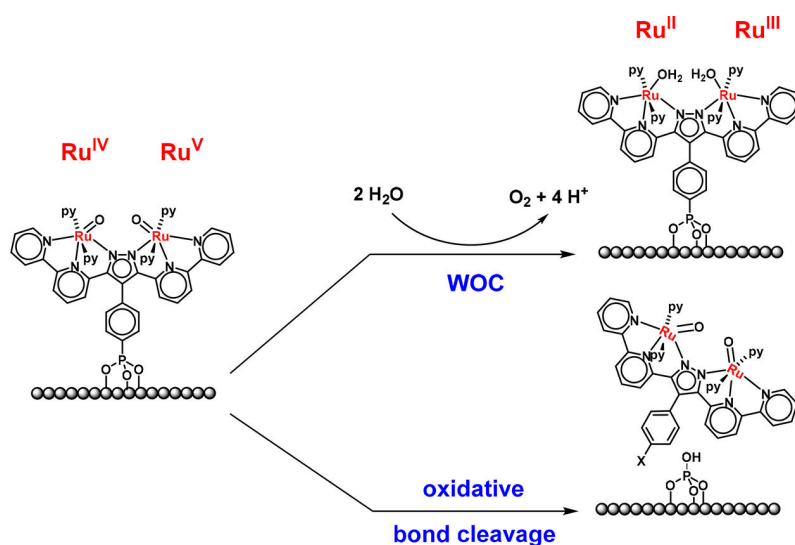


Figure 6.8: Two competing reaction pathways after oxidation of ITO|*meso*-ITO|**3** to $\text{Ru}^{\text{V}}\text{Ru}^{\text{IV}}$ either towards water oxidation catalysis or degradation of the phosphonate anchor.

observed. However, substitution of the carboxylate anchor with a phosphonate anchor led to a significant improvement in the stability for the hybrid electrode system ITO|*meso*-ITO|**3** with similarly high activity. RRDE experiments showed an onset potential of water oxidation catalysis for ITO|*meso*-ITO|**3** at 1.55 V vs RHE.

Further development of the RRDE methods allowed probing the desorption properties of the catalysts *in situ* under reactive conditions, where we observed significant distinctions in stability for the different anchoring groups. While **1** desorbs continuously already at low applied potentials, the stability of **3** is mainly corrupted after oxidation to high-valent metal-oxo species at the formal $\text{Ru}^{\text{V}}\text{Ru}^{\text{IV}}$ state. XAS and XPS experiments show chemical integrity of the bbp-based complex core and indicate a leaching mechanism where the P-C(aryl) bond is cleaved when the complex reaches the formal oxidation state $\text{Ru}^{\text{V}}\text{Ru}^{\text{IV}}$. With these findings we report a new decomposition pathway of immobilized molecular water oxidation catalysis systems on oxide supports, showing the boon and bane of highly oxidized ruthenium species with respect to stability and activity of hybrid WOCs. Overcoming the leaching problem thus requires the synthesis of anchoring groups which mediate facile electron transfer and can maintain stable covalent bonding even after the catalytic metal centers have reached high oxidation states. Recently, alternative new functional groups for surface immobilization have been presented which show significantly enhanced binding stabilities and electron transfer dynamics in comparison to carboxylic

and phosphonic acids. In addition to the most prominent candidate hydroxamic acid, also dipicolinic acid and silatranes (the latter bind to oxide surfaces as siloxanes) show promise for future generations of hybrid assemblies^[124,275,276]. Adaptation of the electron transfer chain between the catalyst and the anchoring group to avoid linkages susceptible to oxidative cleavage is also an important issue. The observed dependence of stability and activity on the applied anchors highlights the importance of the selection of appropriate anchoring groups for the construction of rugged hybrid systems in artificial photosynthesis, and this emphasizes the necessity of a detailed understanding of the interplay of the electronic structures of the catalyst, electron transfer chain, and anchor under operating conditions to achieve further improvement.

7 Conclusion

The key objective of the presented thesis is the realization and detailed analysis of a hybrid system for photoelectrochemical watersplitting with $\text{La}_{0.6}\text{Sr}_{0.4}\text{MnO}_3$ (LSMO) as photoabsorber and immobilized molecular bis(bipyridyl)pyrazolate diruthenium ($\text{Ru}_2\text{-bbp}$) catalyst. As a first step towards a full functioning photochemical device, the functionality of the hybrid assembly was elucidated electrochemically since the basic requirements for a photochemical device, such as stability and band alignment need to be also fulfilled for an electrochemical cell. The results herein focused on two main parts: (I) the role of LSMO as a solid support in terms of background activity and stability; (II) the behavior of the $\text{Ru}_2\text{-bbp}$ complex upon immobilization on a model oxide electrode. In these studies the method of rotating ring-disk electrodes (RRDE) played a key role and their advancements enabled in depth analysis on the activity and stability.

Key results of part I - the role of the substrate:

- LSMO was established as model electrode with high activity close to (110)-oriented IrO_2
- Mn was identified as active site and O-O formation as rate limiting step of the OER
- LSMO showed high structural stability under reactive conditions in alkaline media
- By control over defect chemistry, it was possible to further improve the stability of LSMO up to the very surface
- LSMO revealed the desired broad range absorption with long life times of excited states
- High background activity and low stability at acidic pH demonstrated the need for additional layers separating LSMO from the electrolyte

Development of RRDE setup: The developed electrode design allowed the implementation of epitaxial thin films in a RRDE setup for the first time. Thus providing an assembly scheme applicable to other oxide systems that can be prepared on Nb-doped STO. With only one crystal facet exposed to the electrolyte accurate evaluation of activity and efficiency is enabled with the RRDE method previously only applicable to oxide powders and electrodeposited films. By overcoming the uncertainties of undefined geometric and crystallographic surfaces it now is possible to access new experimental

questions such as accurate evaluation of oxygen reduction reactions of oxide electrodes. The adaptation of the use of the ring electrode provided an accurate measure for the evaluation of rougher surface. Here, the resemblance between the ring and the disk Tafel slopes can be used to estimate the catalytic efficiency. This is particularly interesting for electrode materials such as the investigated mesoporous ITO where the transport of the evolved species is affected by a rough surface or dense particle layer.

Electrochemical activity of LSMO: LSMO was established as model electrode with the very smooth surfaces and the high degree of structural control. This allowed to determine precise values for the Tafel slope with 60 mV/dec matching the value of 59 mV/dec of a chemical rate limiting step such as O-O formation predicted for LaMnO_3 ^[52]. Post-mortem analysis showed subtle changes in the surface stoichiometry and the amount of retained Mn. These changes correlated with the activity leading to the assumption of Mn as active site. While frequently assumed^[3,52] experimental evidence for the active B-site has been scarce to date and is important to differentiate the reaction mechanism to closely related manganites with redox active lattice oxygen^[61–63].

Stability of catalytic activity: The subtle changes in surface chemistry helped identify the formation of the V_{Mn}''' / D_{La}''' defect couple presumably as consequence of partial Sr^{2+} dissolution as possible mechanism to decreasing activity. By systematic variation of the stoichiometry of LSMO with Mn excess and deficiency of +7 and –4% both activity and stability were strongly affected. The correlation of the defect structure associated with the Mn off-stoichiometry led to the conclusion that Mn excess stabilizes the surface chemistry by restraining the formation of the V_{Mn}''' / D_{La}''' defect couple and might therefore improve the chemical stability of the surface under catalytic conditions.

Benchmarking LSMO as electrocatalyst: With LSMO established as model electrode it was possible to compare to other benchmarking oxide systems such as RuO_2 and IrO_2 as the measurements were conducted at pH 13. The comparison showed that the activity of LSMO is close to (110)-oriented IrO_2 ^[95,179].

LSMO as photoabsorber: Stationary absorption spectra (in Appendix C) show a broad range absorption. Moreover, transient absorption spectroscopy (TAS) experiments reveal excited states with a lifetime close to 1 ns (Appendix C). More importantly these long lifetimes were observed at excitation both in the infrared regime $\lambda = 800$ nm and the visible region at $\lambda = 400$. Therefore, LSMO is a promising choice as photoabsorber showing the desired long life times and broad range absorption shown for other photoabsorber^[9].

Key results of part II - the role of the anchor:

- Molecular Ru₂-bbp catalyst was successfully anchored on ITO as solid support
- The immobilized complex is active for the water oxidation without decomposition of the backbone ligand
- The surface coverage can be tuned by the employed anchor group
- The anchor strongly influences the stability with the phosphonate anchor binding the strongest
- The number of used anchoring groups increases solubility rather than the binding strength with biscarboxylate desorbing faster than carboxylate
- Interplay of the highly oxidized ruthenium oxo species with phosphate anchor enables new corrosion mechanism competing with OER
- Role of the interface in terms of anchor groups is the central parameter for the overall stability

Immobilization of Ru₂-bbp catalyst: By application of acid functional groups as anchor the Ru₂-bbp catalyst was immobilized on ITO as oxide support. ITO is highly stable at low pH and high surface area allowing to electrochemically analyze the complexes upon immobilization. The anchored complexes showed the expected behavior for immobilized species compared to the homogeneous complex, e.g. in scan rate dependent measurements. RRDE experiments revealed the activity of the anchored complexes with high efficiency. In addition, XPS experiments ruled out the formation of oxide particles as was reported for related catalysts^[90] thereby confirming the stability of the catalyst under working conditions.

Stability of the interface: The interface was identified as a key element for both the stability and activity due to rapidly decreasing activity despite the structural integrity of the backbone ligand. A systematic modification of the interface was achieved by employing three different anchor groups that resulted in different surface concentration varying by more than one order of magnitude. Additionally, the desorption rates differed by three orders of magnitude showing the differences in stability of the binding under non-reactive conditions. The differences show a pronounced effect of solubility on the stability rather than the number of anchor groups as the biscarboxylate desorbs faster than the carboxylate anchor. Among the employed anchor groups, the phosphonate

anchor reveals the slowest desorption.

Stability under reactive conditions: Under the reactive conditions of the OER, the combination of RRDE and XAS measurements allowed to identify the mechanism limiting the stability of the interface: While for the carboxylate anchor the leaching is the dominant effect limiting the stability, for the most stable phosphonate anchor a competition between an oxidative cleaving of the anchor and the desired water oxidation limits the stability. The oxidative cleaving of the anchor occurs presumably by electronic interaction of high valent metal oxo species and the anchor. The adaption of the RRDE method allowed to study the stability *in operando* highlighting the role of the interface under reactive conditions. Studies of the stability *in operando* are rarely performed due to the experimental challenges^[277] and evidence for the direct involvement of the anchor group has been scarce to date. The results show the importance of the frequently neglected interface in particular under the reactive conditions of the water oxidation and stress the need for theoretical understanding on interdependency of the reactive center and the ideally inert interface.

Outlook

The developed electrode design for the RRDE setup opens the door for the detailed analysis of (I) other molecular systems and (II) other oxide systems, e.g. for oxygen redox reactions. Here, the RRDE method will expand the experimental possibilities in particular for (I) the study of stability of other linker and ligand systems, and (II) the oxygen reduction that up until now have been limited to particle or electrodeposited electrodes. Moreover, the found influence of both activity and stability of LSMO on the defect chemistry might indicate new possibilities to tailor, in particular, the stability of oxides under reactive conditions.

For the hybrid system, the employed molecular Ru catalyst is a promising candidate as it can be crafted on the surface preserving the activity without decomposition. Moreover, the observed electrochemical activity is a promising step towards the realization of a photochemical device as the band alignment needed for the photochemical functionality is also required for the electrochemical activity. LSMO as absorber shows the desired broad range absorption and long life times making it a fitting choice and the developed electrode design

enables the combination of photoelectrochemistry with the RRDE method. Despite the promising properties of the molecular catalyst and the photoabsorber the stability of the interface including the absorber surface remains critical for the realization of a functional device and will pose the central task for future work. Possible approaches for improvement might be to add a carbon based separation layer and employ non-covalent anchor groups as their stability is not pH dependent. But additional theoretical support is needed to elucidate the interaction of the active ruthenium with the anchor in order to provide pathways for future catalyst design.

8 Appendix A

The following supporting information contains data and discussion concerning the first part, the role of LSMO. The displayed data is taken from the published supporting information of the respective article. To avoid multiple replication of figures, e.g. the oxygen reduction calibration at the ring electrode, only one version is given and reference adjusted accordingly.

8.1 Supporting information for chapter 3

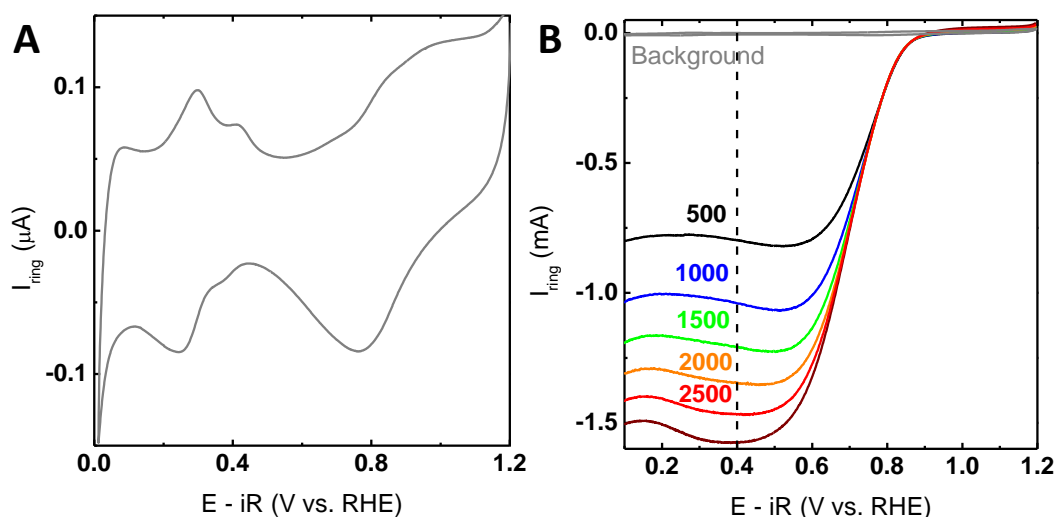


Figure 8.1: (A) Unrotated CV measurement of the freshly polished Pt-ring in Ar saturated 0.1 M KOH supporting electrolyte at 200 mV/s showing the expected features of a polycrystalline Pt metal without surface oxides^[278]. (B) Ring currents of a freshly polished Pt-ring in 0.1 M KOH supporting electrolyte (Ar-purged for the background measurement, O₂-purged for ORR measurements) at 200 mV/s. Rotation speeds were increased from 500 to 3000 rpm (lines). All measurements shown are the forward direction of the 2nd cycle. Data recorded using the IMP setup.

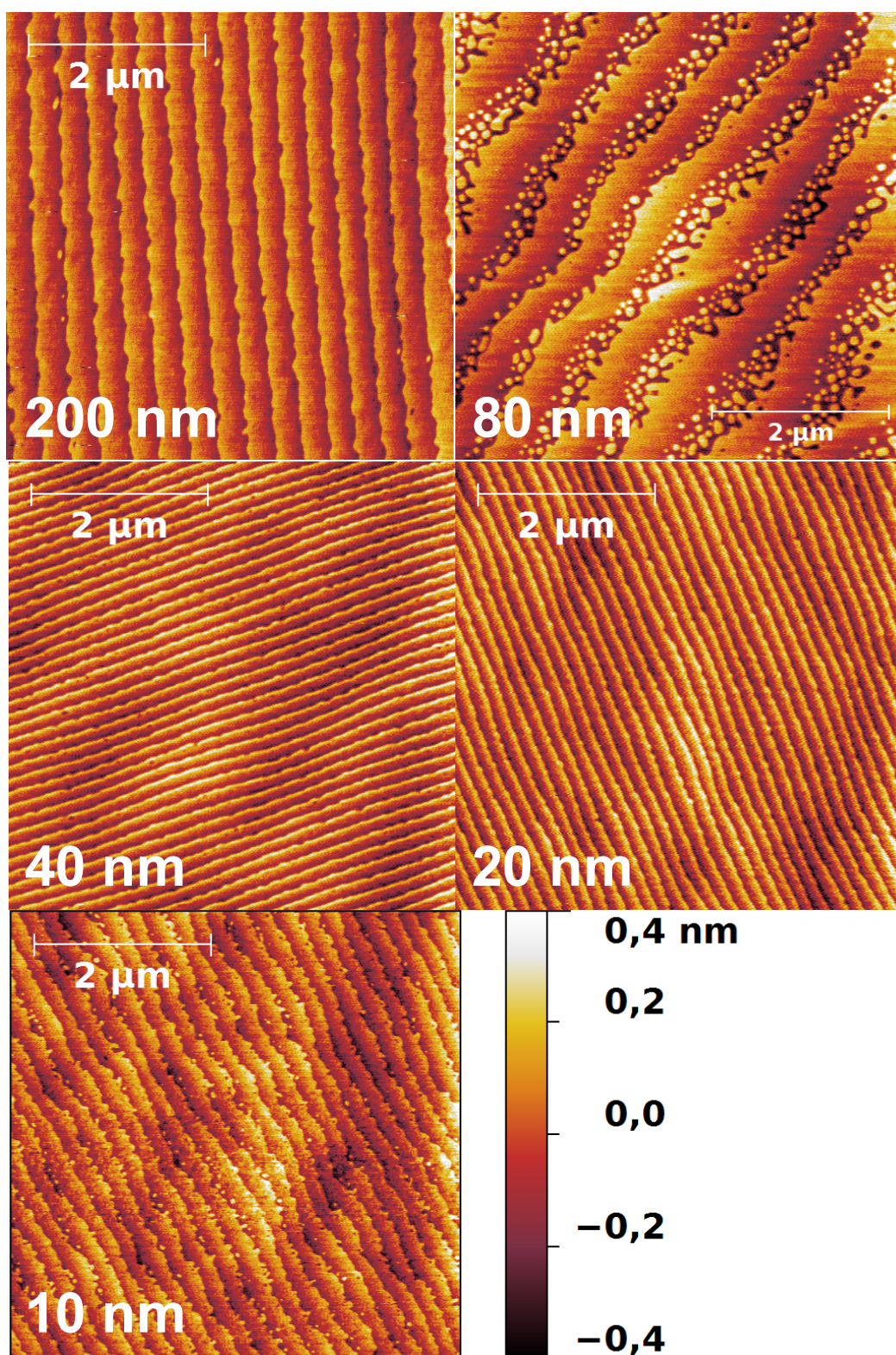


Figure 8.2: Exemplary AFM images of all prepared thicknesses indicated by the inset. The height scale is identical for all images and corresponds to two unit cells of LSMO (0.4 nm).

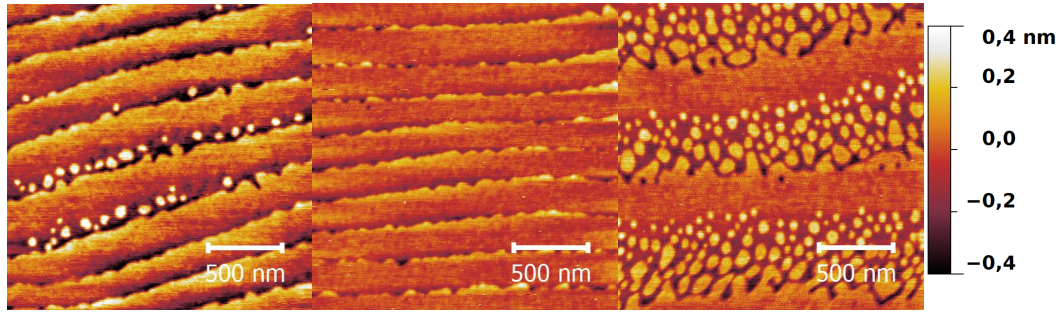


Figure 8.3: Typical variation in terrace width and surface morphology within one sample exemplarily shown for different positions on a 40 nm LSMO film. The height scale is identical for all images and corresponds to two unit cells of LSMO (0.4 nm).

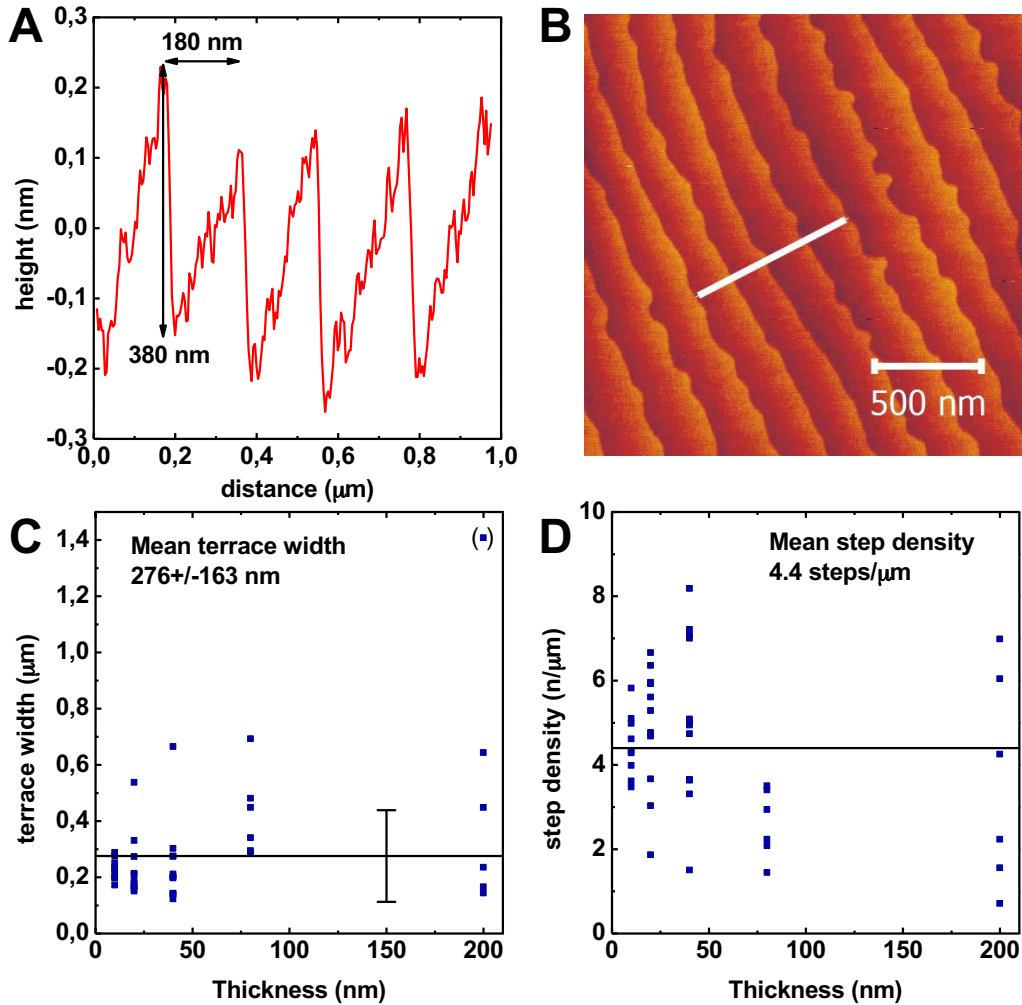


Figure 8.4: (A) Exemplary height profile extracted along the white line (B) of a 20 nm LSMO sample, (C) the extracted terrace width and mean terrace width for all samples measured at 3 different positions on each sample (the point in brackets was excluded), (D) the extracted step density and mean step density for all samples measured at 3 different positions on each sample.

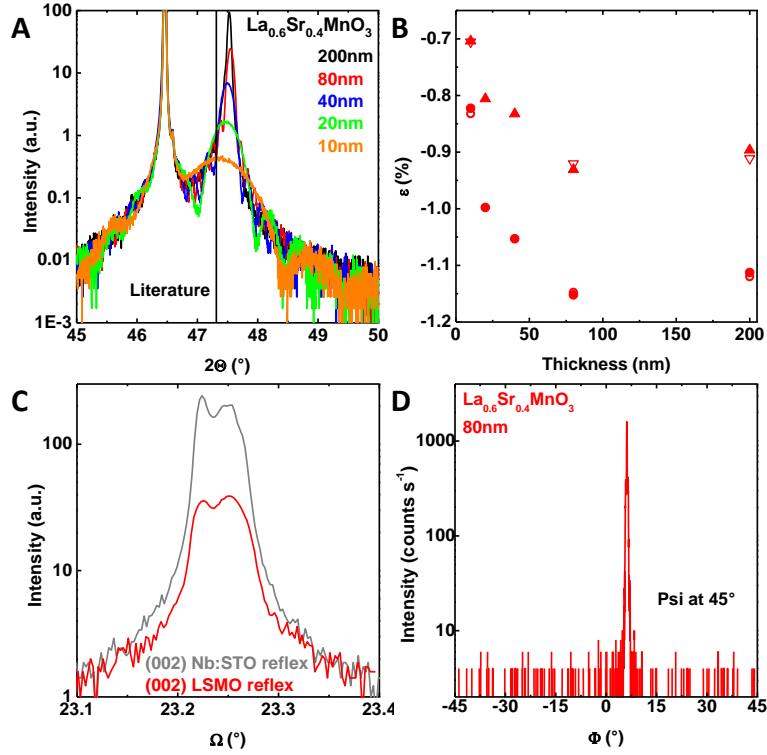


Figure 8.5: (A) Detailed 2θ XRD scan on (002) LSMO reflex for different thicknesses, (B) extrapolated strain state of LSMO films with respect to bulk value^[279], Red triangles represent samples prepared at position B, circles at position A. The hollow symbols show the strain after CA for 1 h at 1.7 V vs. RHE (C) Rocking curves on both the Nb:STO substrate reflex and the LSMO reflex, (D) 90° window of ϕ -scan with ψ at 45° on a typical $\text{La}_{0.6}\text{Sr}_{0.4}\text{MnO}_3$ film.

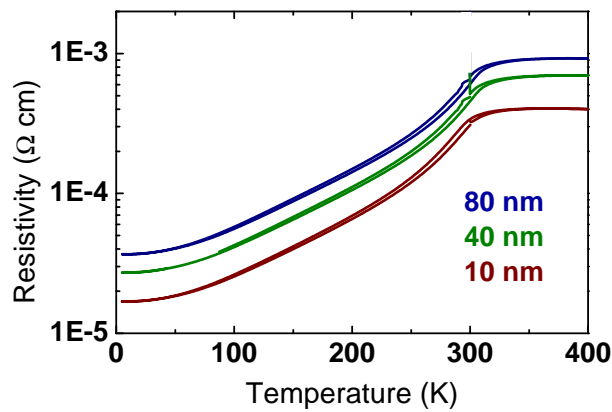


Figure 8.6: Bulk conductivity of $\text{La}_{0.6}\text{Sr}_{0.4}\text{MnO}_3$ films with thicknesses from 80 to 10 nm measured by PPMS

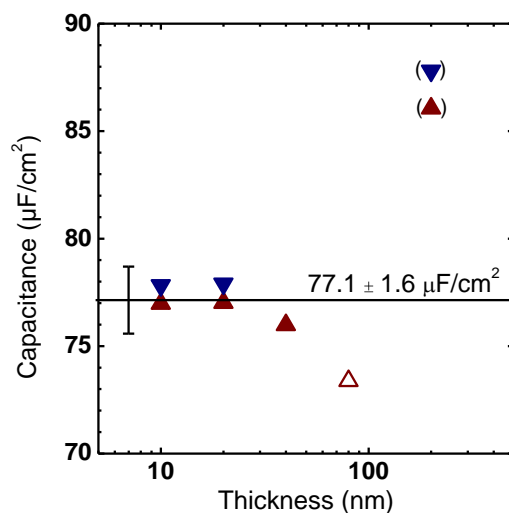


Figure 8.7: Capacitances measured using the EEL setup for measurements before electrolysis (up triangles) and after electrolysis and storage in air for a week or less (down triangles). Open and filled symbol denote different positions during deposition; the horizontal line indicates the average. The specific capacitance of a 200 nm LSMO film was clearly larger than the average specific capacitance. As this film was not an outlier in the AFM analysis of surface morphology, the deviation might relate to the measurement setup. For the IMP setup, the quality of CVs and resulting specific capacitance values depended strongly on the sampling mode (Figure A8) with the 'surface mode' yielding values comparable to those obtained by the EEL setup. See Table 3.1 in the main text for descriptions of the EEL and IMP setups.

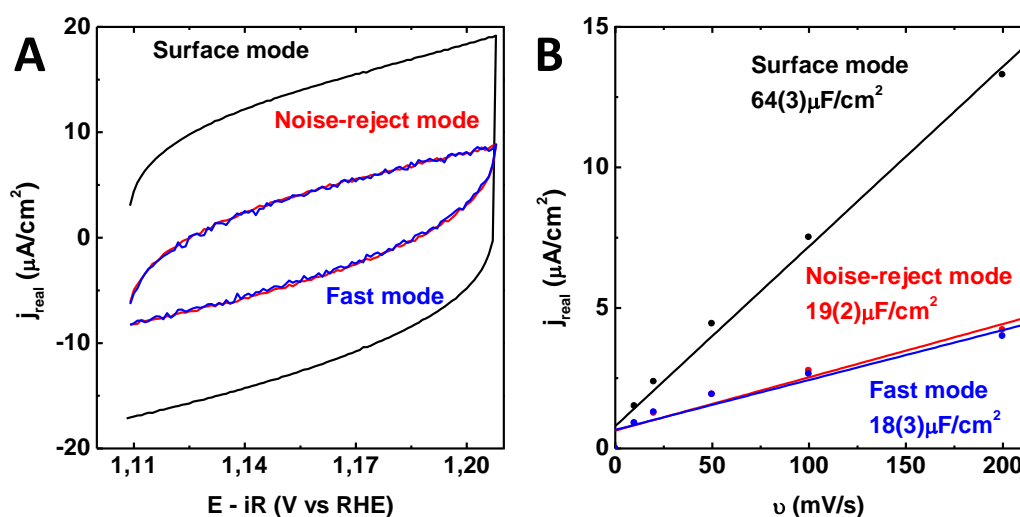


Figure 8.8: (A) Comparison of capacitance measurements using exemplary measurements at 200 mV/s taken with the EEL setup and the IMP setup for 3 sampling modes. (B) Variation in capacitance for the 3 sampling modes of the IMP setup. See Experimental section in the main text for description of the EEL and IMP setups.

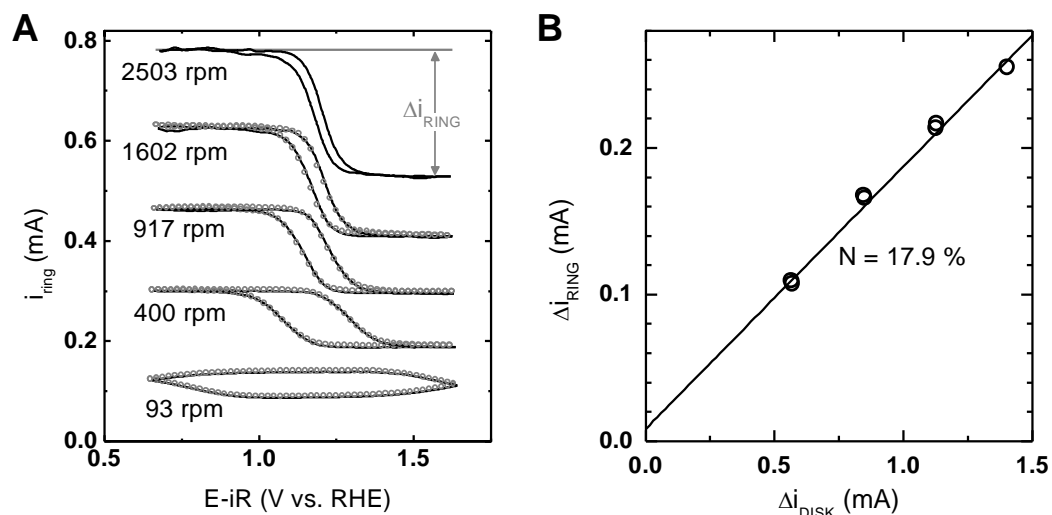


Figure 8.9: (A) Ring currents of $\text{La}_{0.6}\text{Sr}_{0.4}\text{MnO}_3$ films in 5 mM ferro- and ferricyanide with 0.1 M KOH supporting electrolyte (Ar-purged). Dotted lines indicate background currents at OCV. (B) Ring currents as function of disk currents and the collection efficiency, N , obtained by linear regression. Data recorded using the EEL setup.

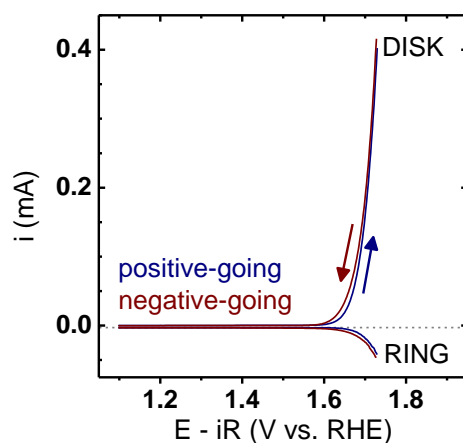


Figure 8.10: Exemplary raw data of the measurement shown in Figure 3.5 of the main text. A grey dashed line indicates a small background due to residual oxygen that was subtracted from the ring currents

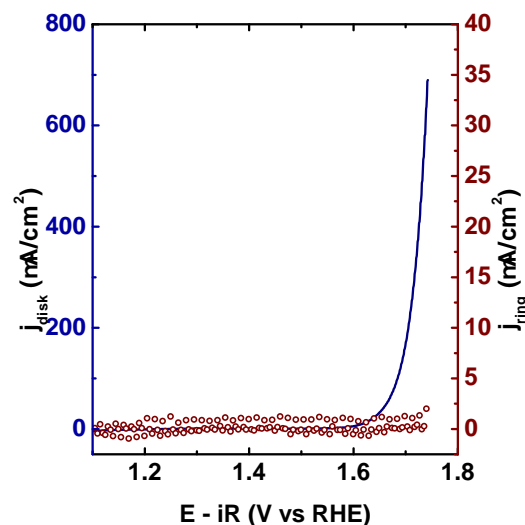


Figure 8.11: CV measurement of a 80 nm $\text{La}_{0.6}\text{Sr}_{0.4}\text{MnO}_3$ film (solid blue line) and the corresponding ring current (open red circles) obtained by CA at 1.2 V vs. RHE to probe for H_2O_2 acquired using the IMP setup. All measurements were performed with Ar-purged 0.1 M KOH supporting electrolyte at 10 mV/s and 2500 rpm and the positive-going direction of the 2nd scan is shown.

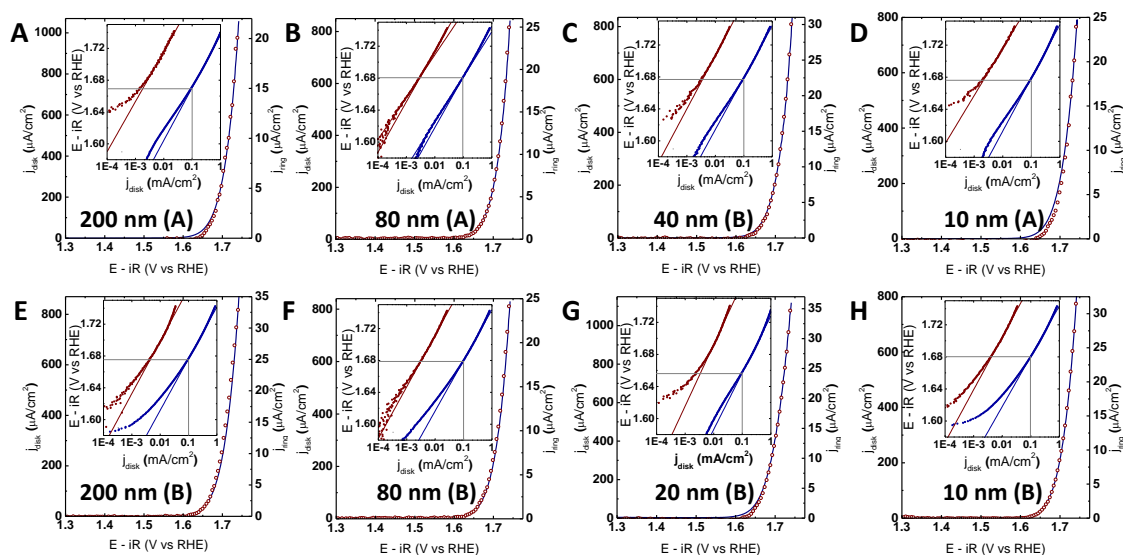


Figure 8.12: Disk currents of all LSMO samples measured using the IMP setup in 0.1 M Ar-saturated KOH at 10 mV/s and 2500 rpm (2nd cycle). Thicknesses were: (A, E) 200 nm; (B, F) 80 nm; (C) 40 nm; (G) 20 nm; (D, H) 10 nm. Tafel slopes can be found in Table 8.4. See Table 3.1 in the main text for description of the IMP setup. (A,B) denotation represents different positions during deposition resulting in small variations in the stoichiometry.

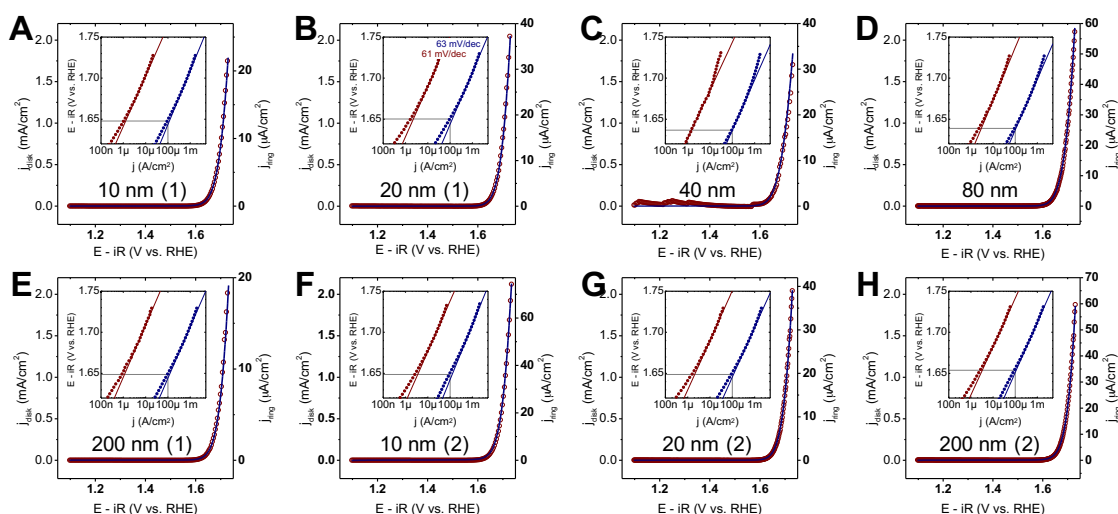


Figure 8.13: Disk currents of all LSMO samples measured using the EEL setup in 0.1 M Ar-saturated KOH at 10 mV/s and 2500 rpm (2nd cycle). First measurements: (A) 10 nm, (B) 20 nm, (C) 40 nm, (D) 80 nm, (E) 200 nm; second measurements (F) 10 nm, (G) 20 nm, (H) 200 nm. Tafel slopes and potentials at 100 $\mu\text{A}/\text{cm}^2$ can be found in Table 8.5. See Table 3.1 in the main text for description of the EEL setup.

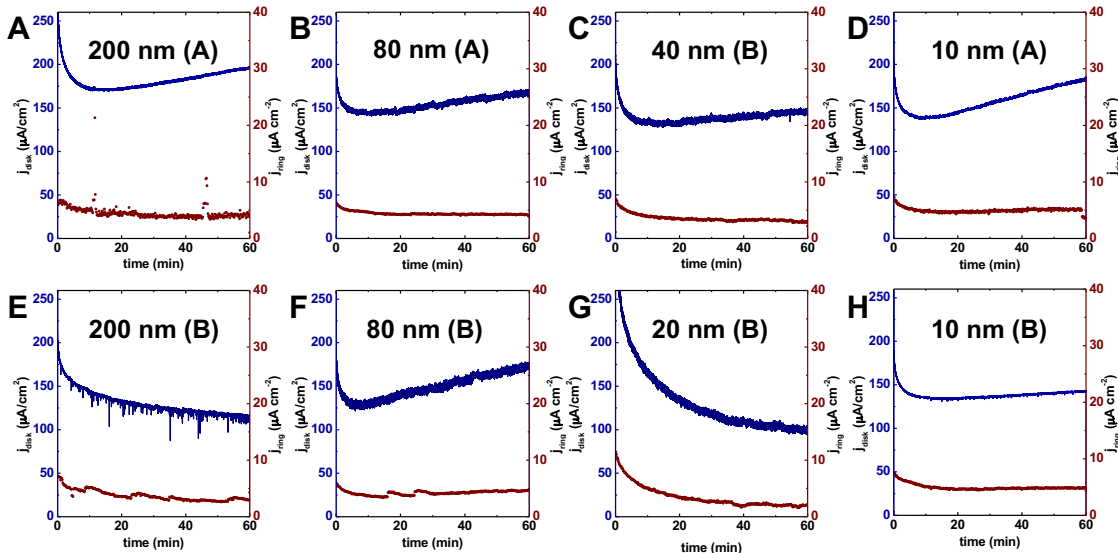


Figure 8.14: Disk currents of all LSMO samples in 0.1 M KOH supporting electrolyte (Ar) at 1.7 V vs. RHE and 2500 rpm. Previously and consecutively to the electrolysis the samples were held at 1.1 V vs. RHE for 10 min. The measurement protocol applied to the samples prior to electrolysis was identical for all samples with thicknesses of (A,E) 200 nm; (B, F) 80 nm; (C) 40 nm; (G) 20 nm; (D, H) 10 nm. Data recorded using the IMP setup; see Table 3.1 in the main text for description of the IMP setup. (A,B) denotation represents different positions during deposition resulting in small variations in the stoichiometry.

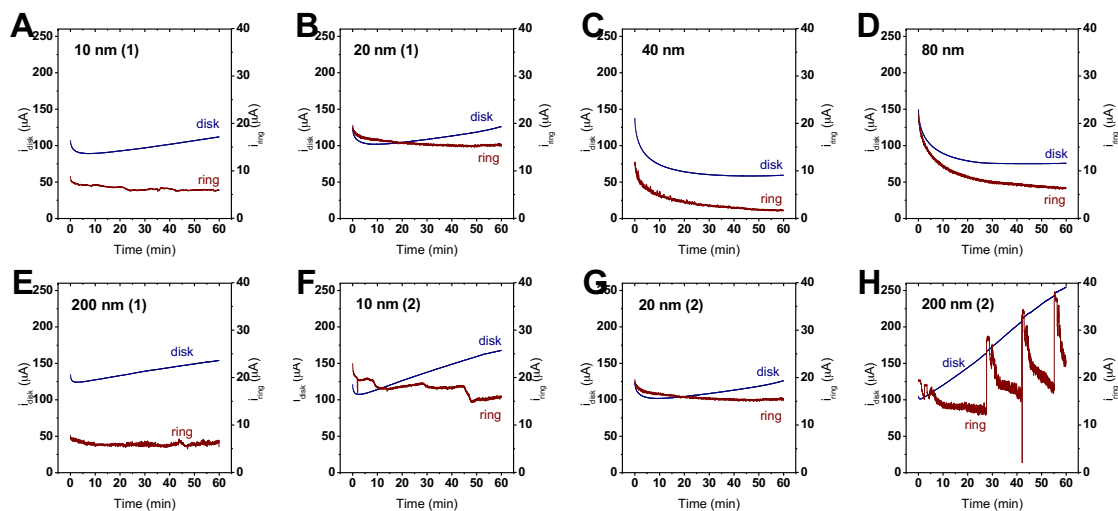


Figure 8.15: Disk currents of all LSMO samples in 0.1 M KOH supporting electrolyte (Ar) at 1.7 V vs. RHE and 2500 rpm. The samples were held at open-circuit for 10 min before and after electrolysis. The measurement protocol applied to the samples prior to electrolysis was identical for all samples. First measurements: (A) 10 nm, (B) 20 nm, (C) 40 nm, (D) 80 nm, (E) 200 nm; second measurements (F) 10 nm, (G) 20 nm, (H) 200 nm. Data recorded using the EEL setup; see Table 3.1 in the main text for description of the EEL setup.

8.1.1 Supporting discussion

1. Calculation of hypothetical Mn corrosion during OER at 1.7 V vs. RHE:

According to the Pourbaix diagram the formation of permanganate is possible^[73,79]. Considering the increasing region of current density (Figure A14D) which might possibly be caused by oxidation of Mn we made an estimate of magnitude of the total possible consumed Mn. The current we accounted for hypothetical Mn oxidation was calculated assuming a constant activity for OER after the initial minimum and only considering the additional current during the increase (highlighted section in Figure 8.22). The following calculation is based on the measurement on a 10 nm $\text{La}_{0.6}\text{Sr}_{0.4}\text{Mn}^{+3.4}\text{O}_3$ sample presented in Figure A14D. The total charge in the presented case adds up $Q = I_{\text{total}} t_{\text{total}} = 8.25 \text{ mC}$. Under the assumption the total corresponds to the maximum oxidation from Mn^{III} to Mn^{VII} (i.e. oxidation of $\text{LaMn}^{+3}\text{O}_3$) to result in permanganate ($\text{Mn}^{\text{VII}}\text{O}_4^-$) the consumed charge per manganese is $z=4$. Using Faraday's law^[51] the total

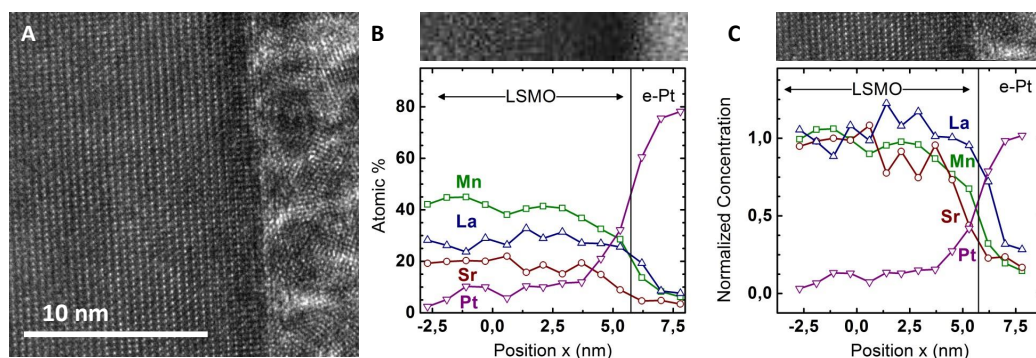


Figure 8.16: Post-mortem TEM characterization of a 80 nm LSMO electrode (80B) after performing cyclic voltammetry and CA at 1.7 V vs. RHE for 1 h at the IMP. (A) HR-TEM cross-section image of the LSMO electrode showing crystallinity up to the interface to the electron beam deposited Pt as protection layer. The protection layer is needed for preparation of the electron transparent TEM lamella by Focused Ion Beam (FIB). A STEM image corresponding to the EDX line profile below is shown above the data plots in (B). The contrast was enhanced by 40% to emphasize contrast changes along the interface between LSMO and Pt. (B) EDX line scan at the area of the STEM image in atomic percent with the interface located at the point where the Mn concentration is half the bulk concentration. (C) Correlation of a HRTEM image and the EDX line scan at an area close to the STEM image. The data is normalized to the bulk concentration, in order to better compare the change in material concentration along the interface. The normalization was performed by dividing all data by the averaged concentrations of the 5 points between ~ 2.6 and 0.1 . For Pt, the normalization was performed accordingly using the points at 7.0 and 7.8 . The normalization clearly shows that the surface is enriched in La in agreement with the XPS data in Figure 3.8.

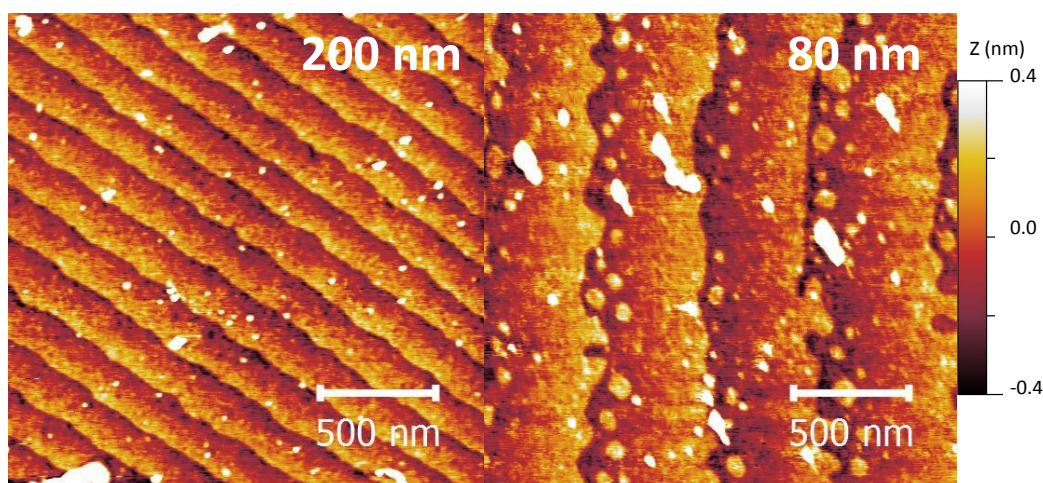


Figure 8.17: AFM images on LSMO samples measured in Göttingen after 1h electrolysis at 1.7 V vs. RHE. Exemplary images of all prepared thicknesses indicated by the inset are presented. The height scale is identical for all images and corresponds to two unit cells of LSMO (0.4 nm).

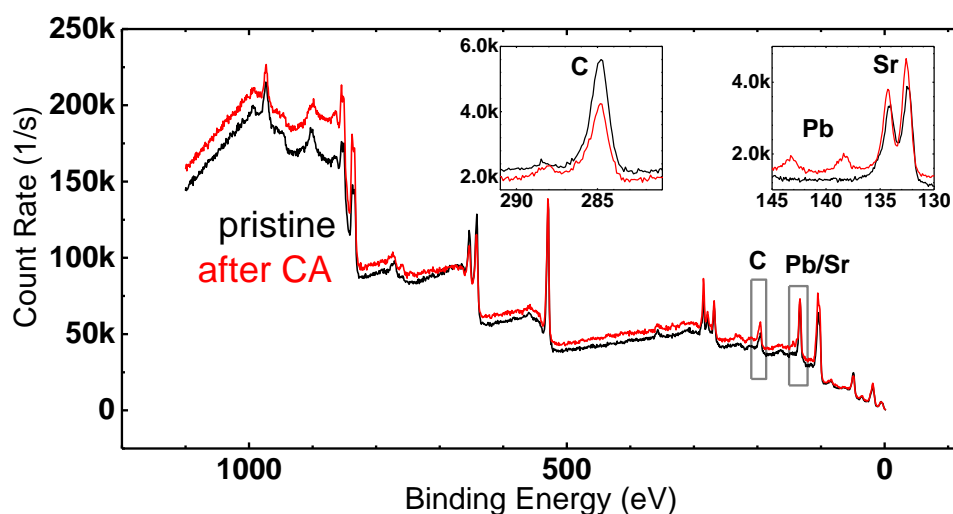


Figure 8.18: XPS survey of the 20 nm thin $\text{La}_{0.6}\text{Sr}_{0.4}\text{MnO}_3$ shown in Figure 3.8 of the main text. The insets show higher resolution spectra of the C 1s core level used for energy calibration and the Sr 3d core level where trace amounts of Pb were found after electrolysis.

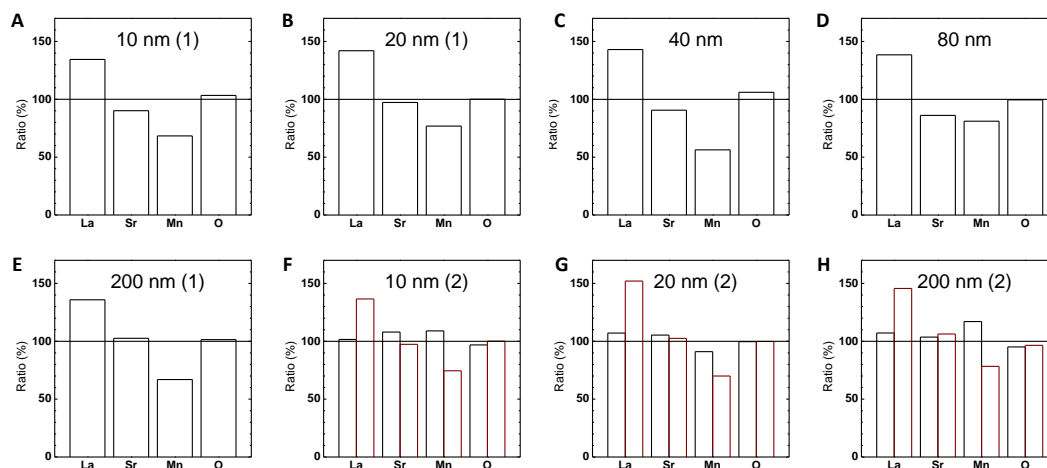


Figure 8.19: Ratio of electrolyzed (X_e) to pristine stoichiometry (X_p) of La, Sr, Mn and O obtained by XPS for LSMO with thickness (A) 10 nm, (B) 20 nm, (C) 40 nm, (D) 80 nm, (E) 200 nm. Repeated measurements are also shown for (F) 10 nm, (G) 20 nm and (H) 200 nm where black bars compare subsequent measurements (i.e. 1st and 2nd measurement) and red bars the 2nd measurement to pristine.

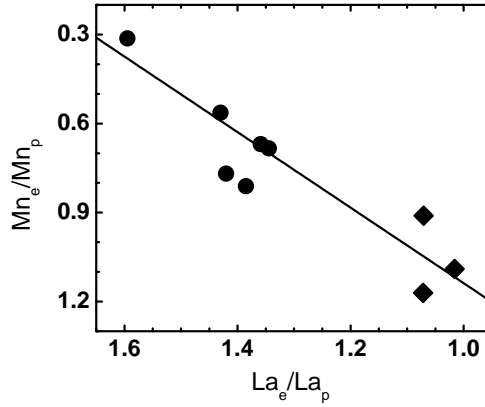


Figure 8.20: Correlation between changes in the surface stoichiometric ratio of electrolyzed (after 1 h CA at 1.7 V vs. RHE) to pristine manganese (Mn_e/Mn_p) and lanthanum (La_e/La_p) determined by XPS. Electrolysis was either performed on pristine surfaces (circles) or repeated measurements (diamonds) using the EEL setup. For more detail, please see section 3.4 in the main text.

amount of permanganate would therefore yield:

$$n = \frac{Q}{Fz} = 2.1379 \cdot 10^{-8} \text{ mol} \quad (8.1)$$

With the Faraday constant $F=96485.33 \text{ C/mol}^{[51]}$. The total amount of Mn in the presented sample can be calculated from the dimension of the sample ($A = 0.1257 \text{ cm}^2$, $d=10 \text{ nm}$ and the density of Mn per unit cell ($\rho = 1 \text{ Mn}/(0.388)^3$), giving a total amount of $n \approx 3.57 \times 10^{-9} \text{ mol}$. The discrepancy between the available Mn in the film and the oxidative charge can hence rule out an electrochemical corrosion process of Mn as the main source of the increasing disk currents.

2. **Calculation of time for oxygen saturation in diffusion layer during OER at 1.7 V vs. RHE:** The diffusion layer thickness is defined as^[51]:

$$\delta_L = 1.61 D_{O_2}^{1/3} \gamma^{1/3} \omega^{-1/2} \quad (8.2)$$

With the diffusion constant of oxygen in 0.1 M KOH $D_{O_2}=1.85 \times 10^{-5} \text{ cm}^2/\text{s}^{[280]}$, the kinematic viscosity for oxygen in 0.1 M KOH $\gamma=1.02 \times 10^{-2} \text{ cm}^2/\text{s}^{[166]}$, and the angular rotation rate, ω . For the applied rotation rate of 2500 rpm, the diffusion layer thickness would be $\delta_L=119.8 \text{ }\mu\text{m}$, hence resulting in a volume of the diffusion layer in the area of the disk ($r=2 \text{ mm}$) of $V= \pi r^2 \delta_L = 1.505 \times 10^{-4} \text{ cm}^3$.

We now can calculate the time needed to saturate the volume of the dif-

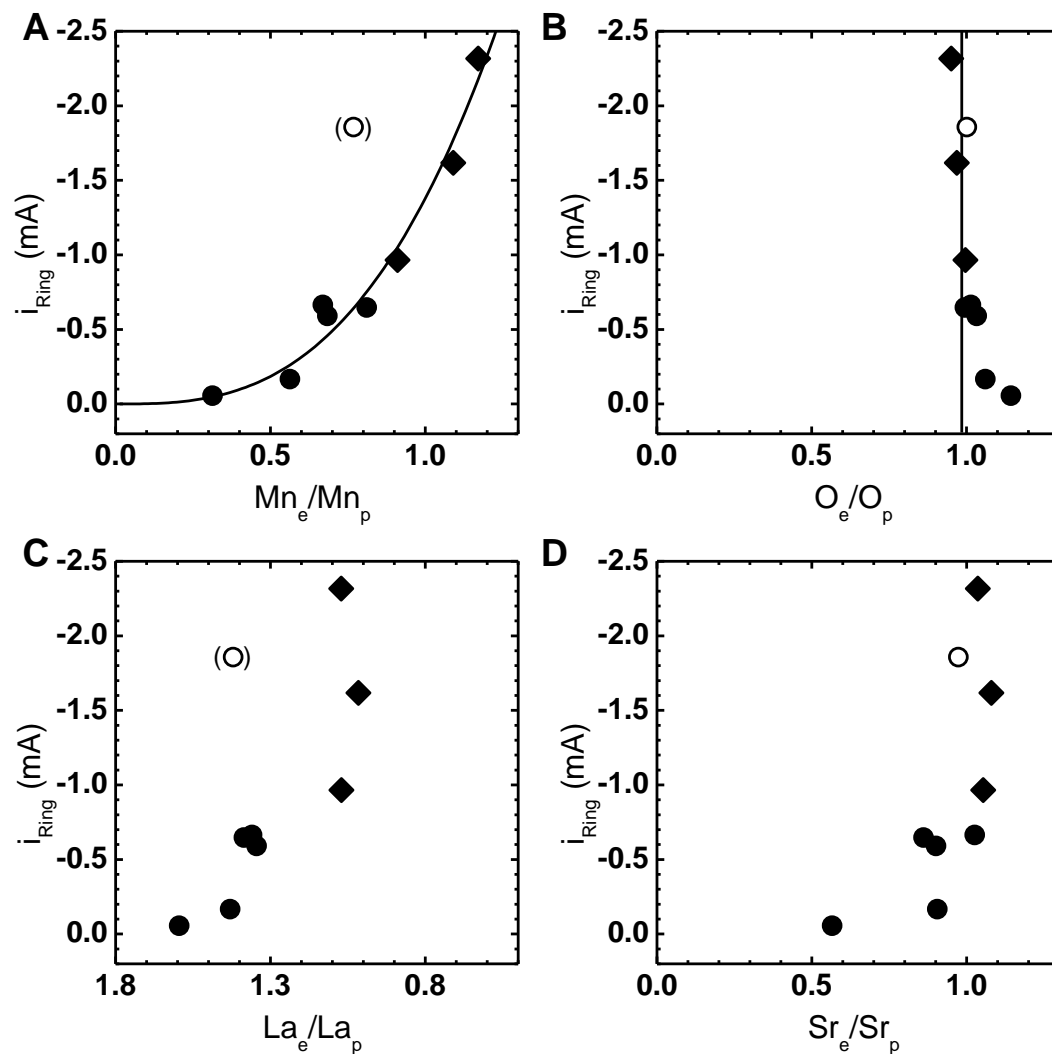


Figure 8.21: Correlation between the change in the background-corrected ring current at 1 h CA and surface stoichiometry obtained from XPS. CA data was either obtained at pristine surfaces (circles) or after repeated measurements (diamonds) using the EEL setup. The surface concentration after electrolysis X_e is normalized to that of the pristine state of all samples X_p . An outlier (open circle) was not considered in the fit in (A) and (B).

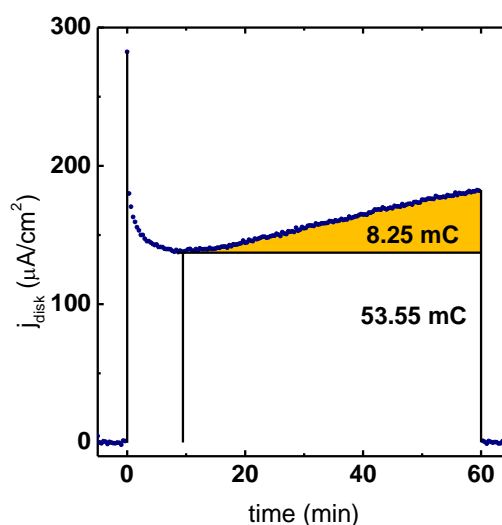


Figure 8.22: Disk currents of 10 nm LSMO samples in 0.1 M KOH supporting electrolyte (Ar) at 1.7 V vs. RHE and 2500 rpm. Previously and following to the electrolysis the samples were held at 1.1 V vs. RHE for 10 min. The highlighted area indicates the charge considered for corrosion effects.

fusion layer above the disk using Faraday's law^[51] under the assumption that the current from electrolysis corresponds solely to the formation of O₂ and the current remains constant at the value observed for the minimum (Figure A14D):

$$n = \frac{Q}{Fz} = \frac{it}{Fz} = n_{O_2} = c_{O_2}V \quad (8.3)$$

With Faraday constant $F=96485.33 \text{ C/mol}^{[51]}$, the current corresponding to the minimum observed for a 10 nm LSMO sample (Figure A 14D) $i=17.4 \text{ } \mu\text{A}$, the charge corresponding to the formation of O₂ $z=4$, and the saturation concentration of oxygen in 0.1 M KOH $c_{O_2}=1.21 \times 10^{-6} \text{ mol/cm}^3$ ^[280]. By transforming the equation the time needed to saturate the diffusion layer with oxygen therefore result as $t = 4.15 \text{ s}$.

8.1.2 Supporting Tables

Table 8.1: Root-mean squared roughness values (RMS) for the IMP samples, the roughness factor was calculated by surface area divided by the projected area based on the AFM images.

Thickness (nm)	RMS (nm)	Roughness factor
200 (A)	0.112	1.00011
200 (B)	0.101	1.00002
80 (A)	0.141	1.00003
80 (B)	(0.361)	1.00005
40 (B)	0.157	1.00014
20 (B)	0.089	1.00015
10 (A)	0.114	1.00008
10 (B)	0.096	1.00012
Avg (A)*	0.122 ± 0.032	1.00007 ± 0.00008
Avg (B)*	0.111 ± 0.031	1.00010 ± 0.00012
Avg*	0.116 ± 0.025	1.00009 ± 0.00010

* 95% confidence interval (2σ), excludes values in parentheses

(A,B) represent different positions during deposition resulting in small variations in the stoichiometry

Table 8.2: Root-mean squared roughness values (RMS) for the EEL samples, the roughness factor was calculated by surface area divided by the projected area based on the AFM images. The specific capacitance was calculated based on double capacitance layer measurements.

Thickness (nm)	RMS (nm)	Roughness factor	Specific Capacitance ($\mu\text{F}/\text{cm}^2$)
200 (A)	0.134	1.00002	86.1
200 (B)	0.169	1.00003	<i>n.d.</i>
80 (A)	0.095	1.00002	<i>n.d.</i>
80 (B)	(0.233)	1.00003	73.4
40 (A)	0.122	1.00004	76.0
40 (B)	0.141	1.00004	<i>n.d.</i>
20 (A)	0.130	1.00002	77.0
20 (B)	0.136	1.00004	<i>n.d.</i>
10 (A)	0.124	1.00003	77.0
10 (B)	0.120	1.00004	<i>n.d.</i>
Avg (A)*	0.121 ± 0.031	1.00003 ± 0.00002	–
Avg (B)*	0.142 ± 0.041	1.00004 ± 0.00001	–
Avg*	0.130 ± 0.039	1.00003 ± 0.00002	77.1 ± 1.6

* 95% confidence interval (2σ), excludes values in parentheses

(A,B) represent different positions during deposition resulting in small variations in the stoichiometry

Table 8.3: Analysis of the CVs in Figure 3.4B.

Thickness (nm)	E_c (V)	E_a (V)	E (mV)	E_0 (V)	i_c (mA)	i_a (mA)	i_c/i_a	R (Ω)*
40	1.14	1.23	90	1.18	-0.55	0.57	0.97	41
200	1.13	1.23	102	1.18	-0.48	0.51	0.95	63

* in Ar-saturated 0.1 M KOH (before addition of 5 mM ferri- and ferrocyanide)

Table 8.4: Tafel analysis for all samples measured using the IMP setup (see Table 3.1 in main text).

Thickness (nm)	E (V vs. RHE)*	LSMO DISK		Ring		R (Ω)
		Tafel low (mV/dec)	Tafel high (mV/dec)	Tafel low (mV/dec)	Tafel high (mV/dec)	
200 (A)	1.669	53.1	66.2	45	63	48
200 (B)	1.675	45.4	64.9	46.5	66	48
80 (A)	1.683	56.3	63	53	63.3	47
80 (B)	1.679	47	63	51.1	64	53
40 (B)	1.677	53.2	65	50.7	66.9	48
20 (B)	1.656	58.3	70.7	41.8	76.7	49
10 (A)	1.677	53.1	66.4	42.5	59.1	46
10 (B)	1.679	45.7	62.8	48.3	65.6	44
Avg**	1.67 ± 0.02	52 ± 10	65 ± 5	47 ± 8	66 ± 10	48 ± 5

* at 100 $\mu\text{A}/\text{cm}^2$

** 95% confidence interval (2σ)

(A,B) represent different positions during deposition resulting in small variations in the stoichiometry. Calculations based on the positive-going scan direction of the 2nd scan in 0.1 M KOH supporting electrolyte (Ar) at 10 mV/s and 2500 rpm

Table 8.5: Tafel analysis for all samples measured using the EEL setup (see Table 3.1 in the main text).

Thickness (nm)	E (V vs. RHE)*	LSMO DISK		Ring		R (Ω)
		Tafel low (mV/dec)	Tafel high (mV/dec)	Tafel low (mV/dec)	Tafel high (mV/dec)	
10	1.649	51.3	65.6	46.4	61.3	53
20	1.651	45.4	63.4	42.0	61.3	53
40	1.639	<i>n.d.</i>	61.3	<i>n.d.</i>	58.2	47
80	1.640	50.2	61.9	49.3	64.2	45
200	1.651	50.1	62.5	45.3	63.3	40
Avg**1	1.65 \pm 0.01	49 \pm 5	63 \pm 3	46 \pm 6	62 \pm 5	48 \pm 11
10 ⁺	1.650	53.7	66.8	43.8	61.5	32
20 ⁺	1.651	46.0	60.4	41.0	56.8	46
200 ⁺	1.655	51.1	61.0	44.6	60.4	46
Avg**2	1.65 \pm 0.01	50 \pm 8	63 \pm 7	43 \pm 4	60 \pm 5	41 \pm 16
Avg**	1.65 \pm 0.01	50 \pm 6	63 \pm 5	45 \pm 6	61 \pm 5	45 \pm 14

* at 100 $\mu\text{A}/\text{cm}^2$ ** 95% confidence interval (2σ)

⁺ Measurement protocol applied for the 2nd time, * * 1,2 Average after completion of first, second application of the protocol
 Calculations based on the positive-going scan direction of the 2nd scan in 0.1 M KOH supporting electrolyte (Ar) at 10 mV/s and 2500 rpm

Table 8.6: Voltages of select highly active electrocatalysts for the OER at $100 \mu A/cm_{oxide}^2$ in 0.1 M KOH.

Material	E (V vs. RHE)*	Conditions	Reference
La _{0.6} Sr _{0.4} MnO ₃ , EEL	1.65 ± 0.01	Epitaxial thin film on 0.5 wt% Nb:SrTiO ₃	This work
La _{0.6} Sr _{0.4} MnO ₃ , IMP	1.68 ± 0.02	Epitaxial thin film on 0.5 wt% Nb:SrTiO ₃	This work
La _{0.8} Sr _{0.2} MnO ₃	1.695	Epitaxial thin film on 0.5 wt% Nb:SrTiO ₃	[131]
La _{0.8} Sr _{0.2} MnO ₃	1.68	Polycrystalline film on Pt	[142]
Ba _{0.5} Sr _{0.5} Co _{0.8} Fe _{0.2} O ₃	1.525	Epitaxial thin film on La _{0.8} Sr _{0.2} MnO ₃	[131]
RuO ₂ (100)	1.516	Epitaxial thin film on MgO	[95]
RuO ₂ (110)	1.547	Epitaxial thin film on MgO	[95]
IrO ₂ (100)	1.62	Epitaxial thin film on SrTiO ₃	[95]
IrO ₂ (110)	1.689	Epitaxial thin film on SrTiO ₃	[95]
SrIrO ₃	1.548	Epitaxial thin film on DyScO ₃	[281]
LaCoO ₃	1.592	Epitaxial thin film on Nb:SrTiO ₃	[3]
RuO ₂	1.5681	Nanoparticle on GC	[94]
IrO ₂	1.5821	Nanoparticle on GC	[94]
LaMnO ₃	1.682	Nanoparticle on GC	[3]
Ba ₆ Mn ₅ O ₁₆	1.664	Nanoparticle on GC	[65]
Co ₃ O ₄	1.612	Nanoparticle on GC	[65]
LaCoO ₃	1.583	Nanoparticle on GC	[65]
La _{0.4} Sr _{0.6} CoO ₃	1.564	Nanoparticle on GC	[65]
La _{0.8} Sr _{0.2} MnO ₃	1.771	Nanoparticle on GC	[131]
La _{0.6} Sr _{0.4} MnO ₃	1.97**	Pellet	[39,44]

* Data extrapolated using <http://arohatgi.info/WebPlotDigitizer>.

** Using the roughness factor of 1200, $100 \mu A/cm_{ox}^2$ equals $0.12 A/cm_{pellet}^2$. The voltage was calculated by extrapolation using the Tafel equation with a Tafel slope of 125 mV/dec and exchange current density of $1.4 \times 10^{-7} A/cm_{pellet}^2$.

8.2 Supporting information for chapter 4

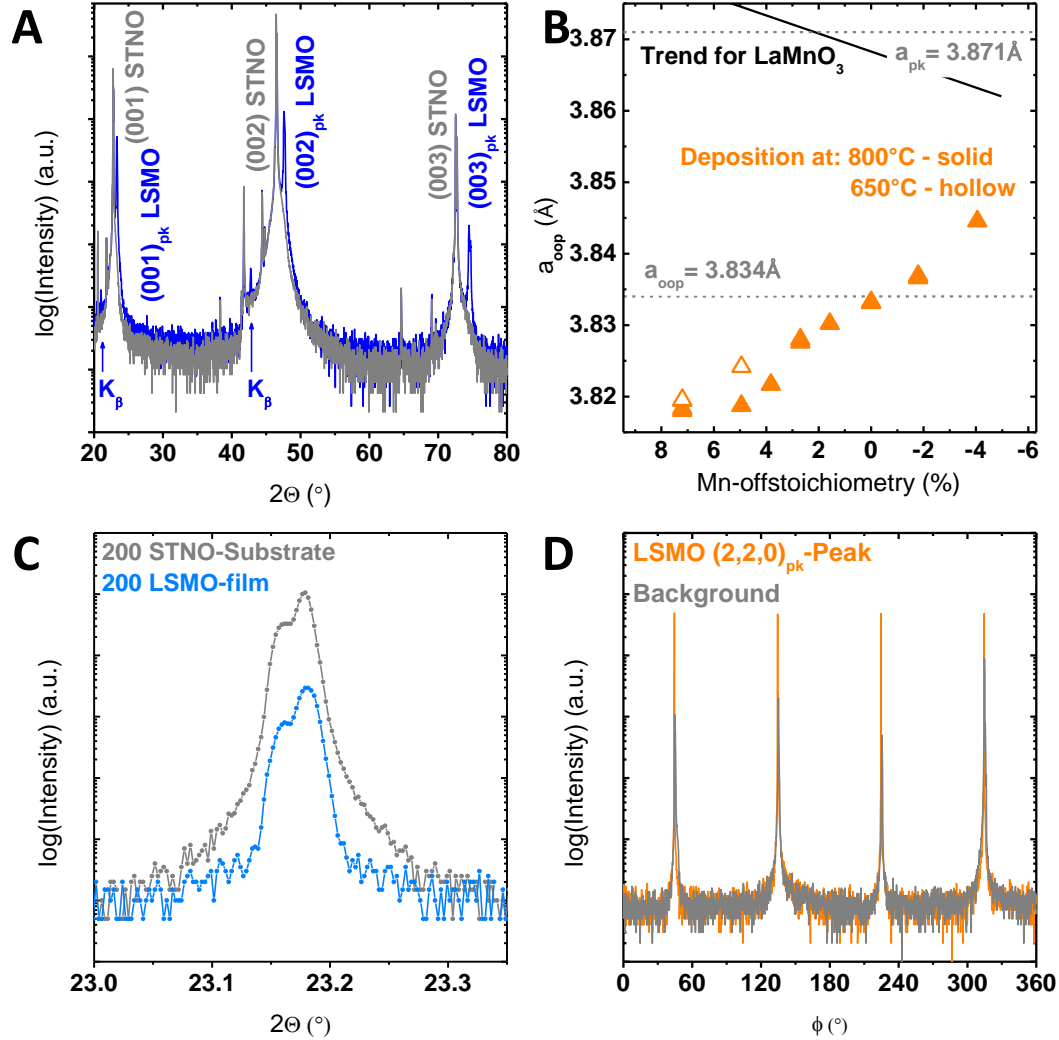


Figure 8.23: (A) Wide angle 2θ XRD scan on Mn-rich LSMO overlaid by wide angle 2θ XRD scan on Nb:STO substrate; (B) calculated lattice constants of LSMO films with respect to the bulk value; (C) rocking curves on both the Nb:STO substrate reflex and the LSMO reflex of the same sample as presented in (D); (D) ϕ - scan with ψ at 45° on a typical LSMO film.

Table 8.7: Analysis of surface roughness based on AFM images on all samples. The roughness factor is the ratio between the surface area and the projected area.

sample	RMS (nm)	Roughness factor
Mn deficient	0.16 ± 0.04	1.000 ± 0.000
Mn rich (800 °C deposition temp.)	17.75 ± 4.29	1.006 ± 0.001
Stoichiometric LSMO	0.12 ± 0.03	1.000 ± 0.000

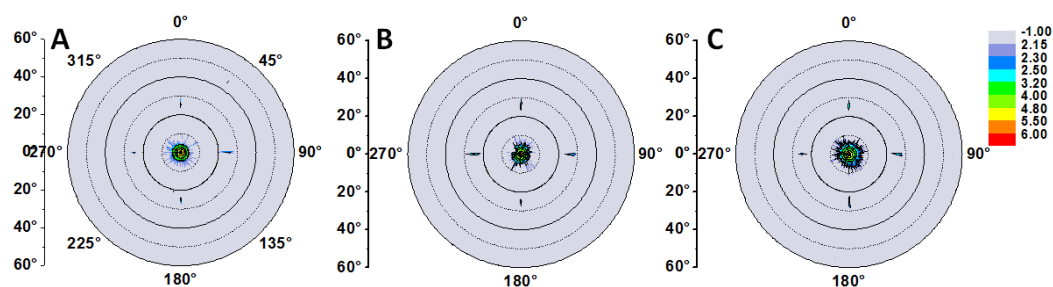


Figure 8.24: Pole figures of all investigated stoichiometries: **(A)** Mn deficient; **(B)** stoichiometric; **(C)** Mn-rich deposited. Note the logarithmic scale is identical for all pole figures.

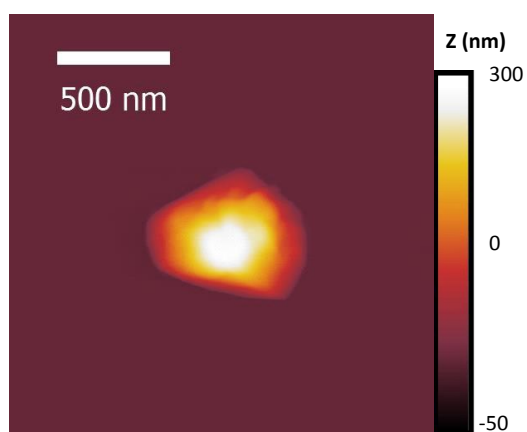


Figure 8.25: AFM image of LSMO with Mn excess showing a Mn_3O_4 precipitate presented in Figure 4.1B with a different height scale. Note the chosen height scale here resolves the full height of the Mn_3O_4 precipitate.

Table 8.8: List of all measured samples with their initial thickness and the relative changes after employing the electrochemical measurements based on fitted XRR spectra

sample	Mn stoichiometry (%)	off- film thickness (nm)	Change in thickness (nm)
GS2a	-2	75.8	-0.17
GS2b	-4.1	76.3	-0.33
GS2c	-2	75.3	-0.28
GS3a	7.2	76.5	0.13
GS3b	5.4	82.5	-0.2
GS3c	7.2	77.1	-1.74
GS6a	0	72.4	-0.51
GS6b	0	76.9	-0.31

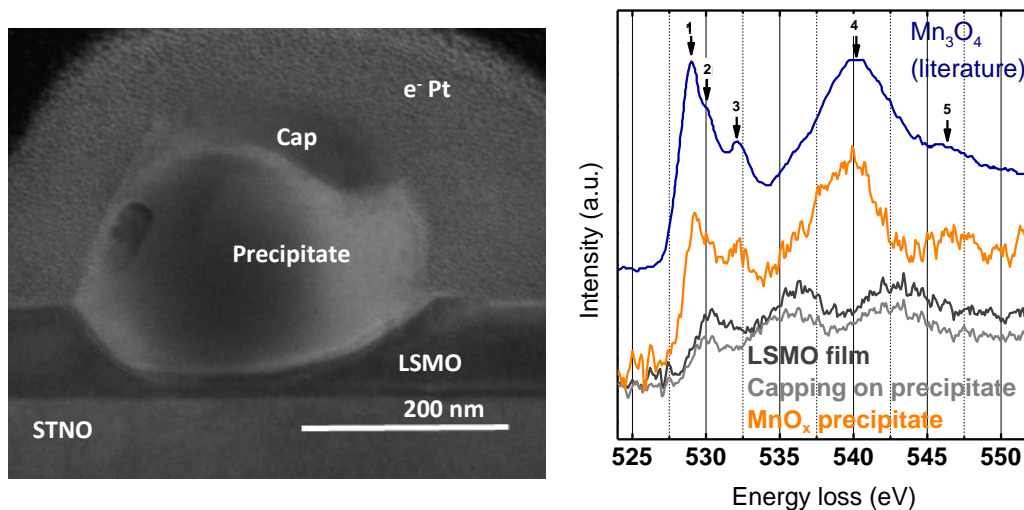


Figure 8.26: Bright field TEM image a LSMO film with a typical precipitate embedded taken with an acceleration voltage of 120 keV. Indicated are the STNO substrate, the LSMO film, the precipitate and the used protective layer of electron deposited Pt. On top of the precipitate, an additional capping can be seen. O K-edge EELS scans on the LSMO film and the capping suggest that the additional layer consists of LSMO. The comparison of the O K-edge of the precipitate with data from literature in Mn₃O₄ shows similar features (indicated by 1-5) that are only present in the precipitate. The data were taken from ref. [192].

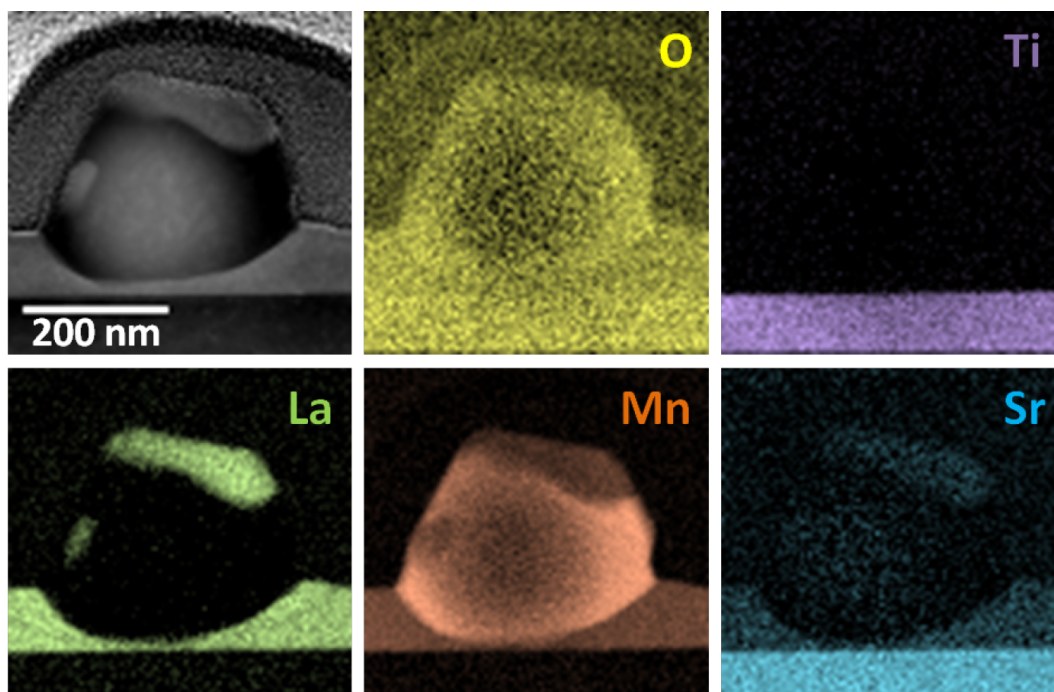


Figure 8.27: Dark field STEM image showing the LSMO film, the precipitate and the substrate. EELS maps for every involved element reveal the elemental distribution, indicating that the precipitate consists predominantly of Mn and O, while the film and the capping on the precipitate appear to have similar stoichiometries.

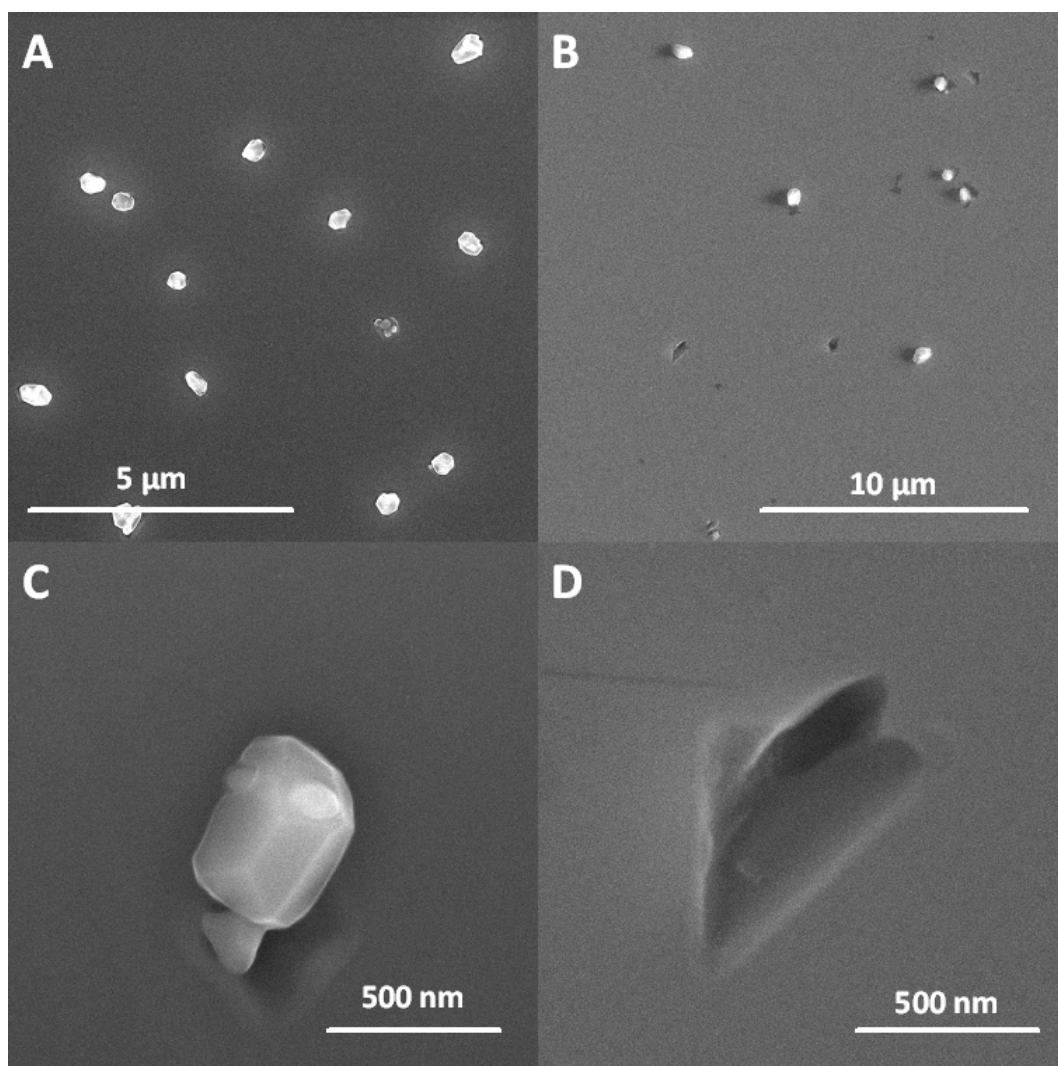


Figure 8.28: SEM images taken with 15 kV acceleration voltage on Mn-rich LSMO samples. **(A)** A representative section on a pristine Mn-rich sample with the typical density of Mn_3O_4 precipitates. **(B)** Large- area scan showing a representative section of a Mn-rich sample after application of the electrochemical measurements. **(C)** High resolution image on typical Mn_3O_4 precipitate after the electrochemical treatment revealing the preservation of the facets of the precipitate indicating the crystallinity shown by TEM (Figure 8.26). **(D)** Example of remaining sink in the LSMO surface where presumably the Mn_3O_4 precipitate was located.

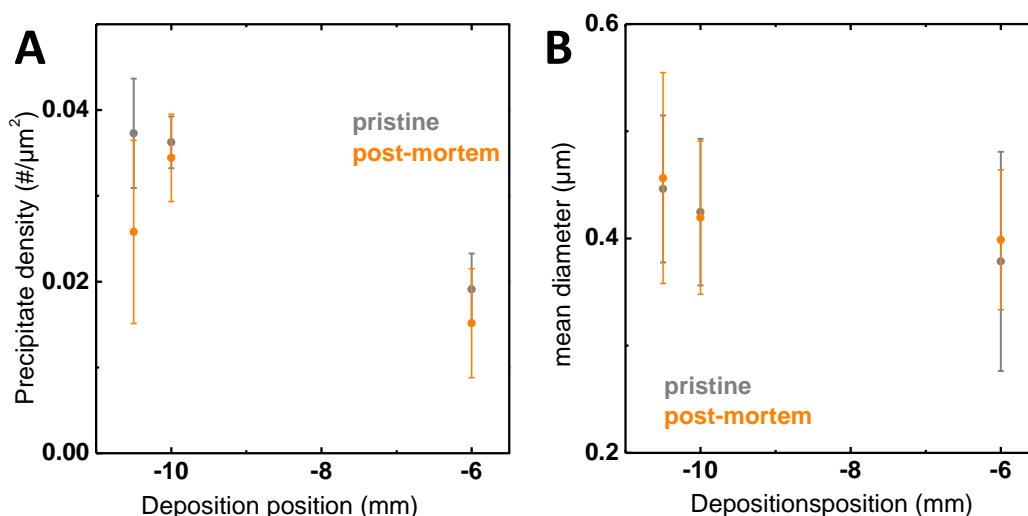


Figure 8.29: (A) Precipitate density evaluated by imaging the complete surface of the Mn-rich LSMO samples by SEM. The precipitate density was correlated with the deposition position corresponding to a Mn content of +5.4% in the case of the sample GS3b and +7.2% in the case of the samples GS3a and GS3c. (B) The mean diameter of the Mn_3O_4 precipitates imaged by SEM. The error bars indicate in both cases the statistical spread for the complete sample surface in both cases.

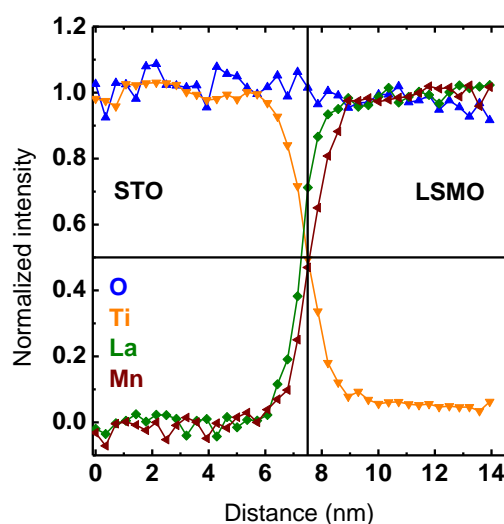


Figure 8.30: Normalized EELS scans across the interface of a Mn-rich LSMO film on an STNO substrate. The interface is indicated by the black lines based on the error function of a beam with a 1.5 nm dispersion showing the spread of the electron beam. As the point of half intensity for Mn and Ti coincide at the point predicted by the error function, the obtained resolution of the EELS scan has to be close to the dimension of the electron beam.

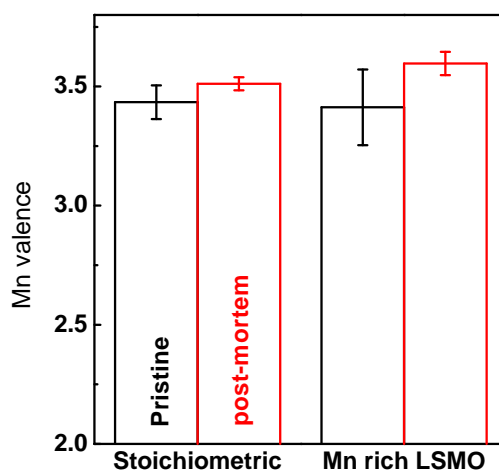


Figure 8.31: Mn valence states determined by the energy difference between the pre-peak of the O K-edge and the Mn L-edge according to refs.^[192,193] for (A) the Mn-rich LSMO and (B) the stoichiometric LSMO comparing the pristine state (black) to the effects of electrochemical treatment (red). The values were determined by averaging the EEL spectra far from the surface in order to obtain bulk values. The indicated error results from the fitting error assuming the accuracy of the energy position to ± 1 eV.

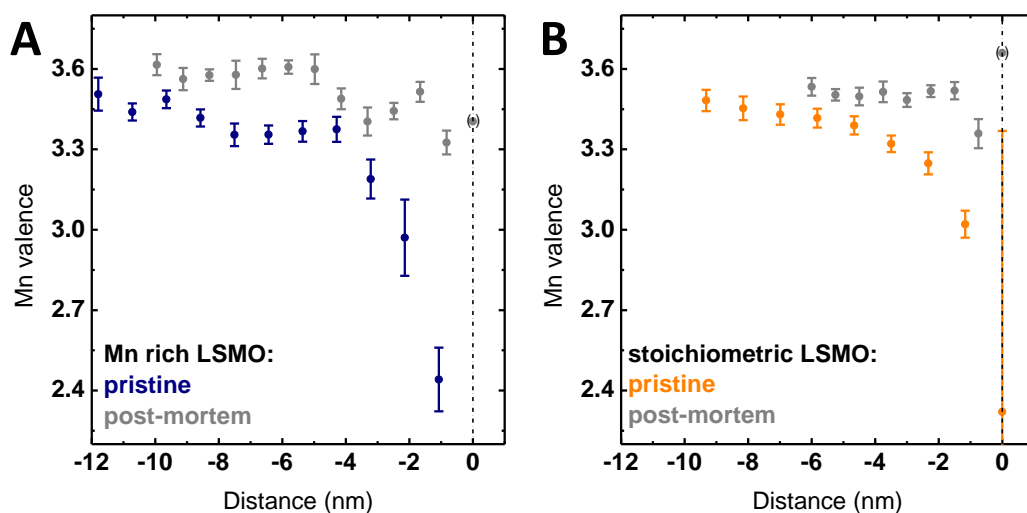


Figure 8.32: Local variation of Mn valence states determined by the energy difference between the pre-peak of the O K-edge and the Mn L-edge according to refs.^[192,193] for (A) the Mn-rich LSMO and (B) the stoichiometric LSMO comparing the pristine state to the effects of electrochemical treatment. The indicated error results from the fitting error assuming the accuracy of the energy position to ± 1 eV. The grey symbols indicate the local distribution of the Mn valence resulting from the electrochemical treatment. The dashed lines indicate the interface between the LSMO film and the electron deposited Pt.

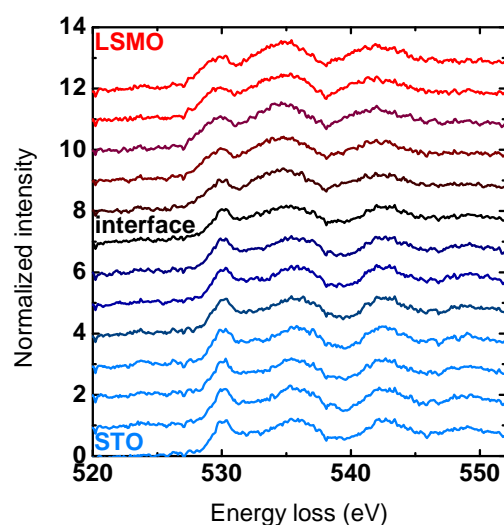


Figure 8.33: EELS scans at the O K-edge across the interface between a Mn-rich LSMO sample and the STO substrate. The step size of the separation for the spectra was 1.1 nm, resulting in a total mapped spread of 12.9 nm.

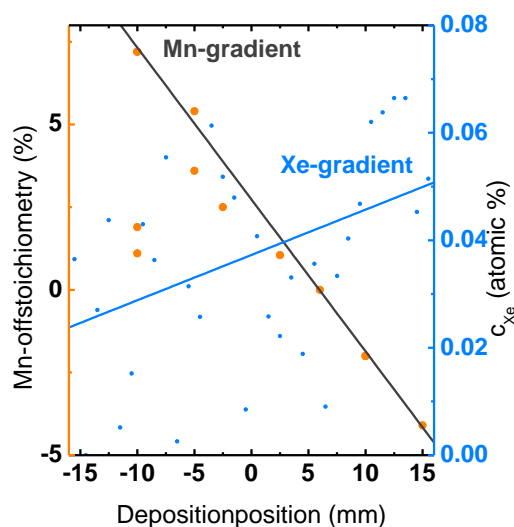


Figure 8.34: Mn gradient with deposition position resulting from different sputter yields of used elements. Data based on EMP measurements. Xe gradient extracted by EMP measurements as an example for residues of sputter gases present in samples prepared at room temperature.

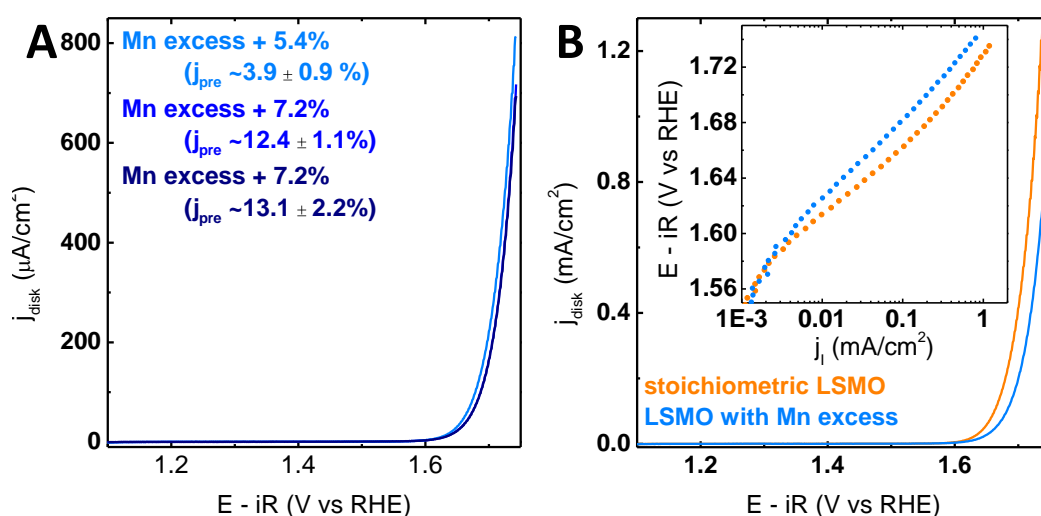


Figure 8.35: (A) CV measurement of all evaluated Mn-rich LSMO films with the amount of Mn excess shown and indicated by the used color code. (B) Comparison of CV measurements of stoichiometric LSMO and LSMO with Mn excess, but without precipitates. All measurements were performed with Ar-purged 0.1 M KOH supporting electrolyte at 10 mV/s and 1600 rpm. The voltage was corrected for electrolyte resistance ($\sim 47 \Omega$ for all samples). The forward direction of the second cycle is shown.

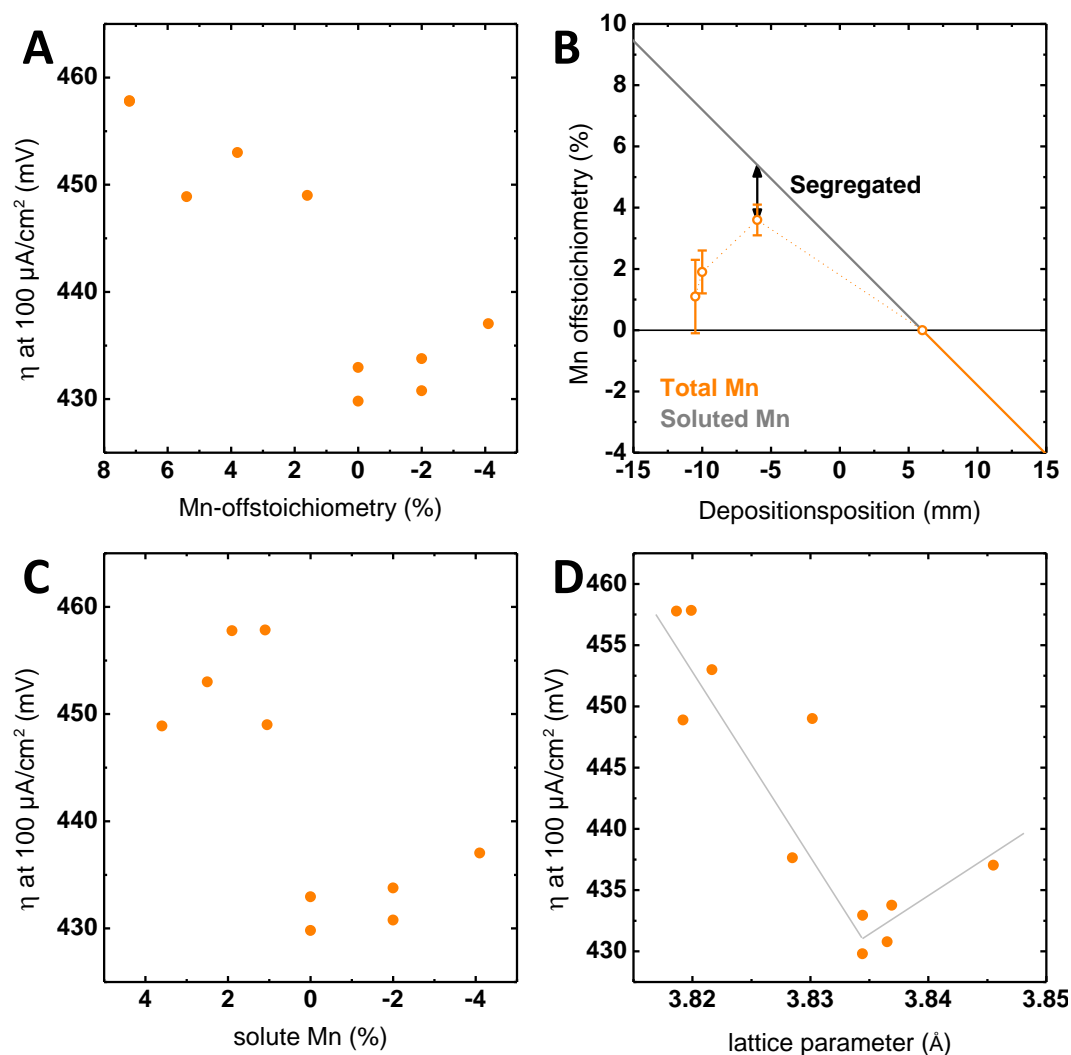


Figure 8.36: (A) Overpotential to obtain a current density of $100 \mu\text{A}/\text{cm}^2$ for all evaluated samples correlated with the Mn off stoichiometry based on the Mn gradient determined by EMP measurements. (B) Correction of the Mn content of the LSMO matrix in the case of the Mn-rich LSMO samples. The correction is based on the density of the Mn_3O_4 precipitates and their total volume estimated by a spherical volume. The total volume of Mn_3O_4 precipitates removes the amount of Mn from the LSMO indicated in (B). (C) Overpotential to obtain a current density of $100 \mu\text{A}/\text{cm}^2$ for all evaluated samples correlated with the amount of solute Mn in the LSMO film based on the correction shown in (B). (D) Overpotential to obtain a current density of $100 \mu\text{A}/\text{cm}^2$ for all evaluated samples correlated with the lattice parameter shown in Figure 4.7A.

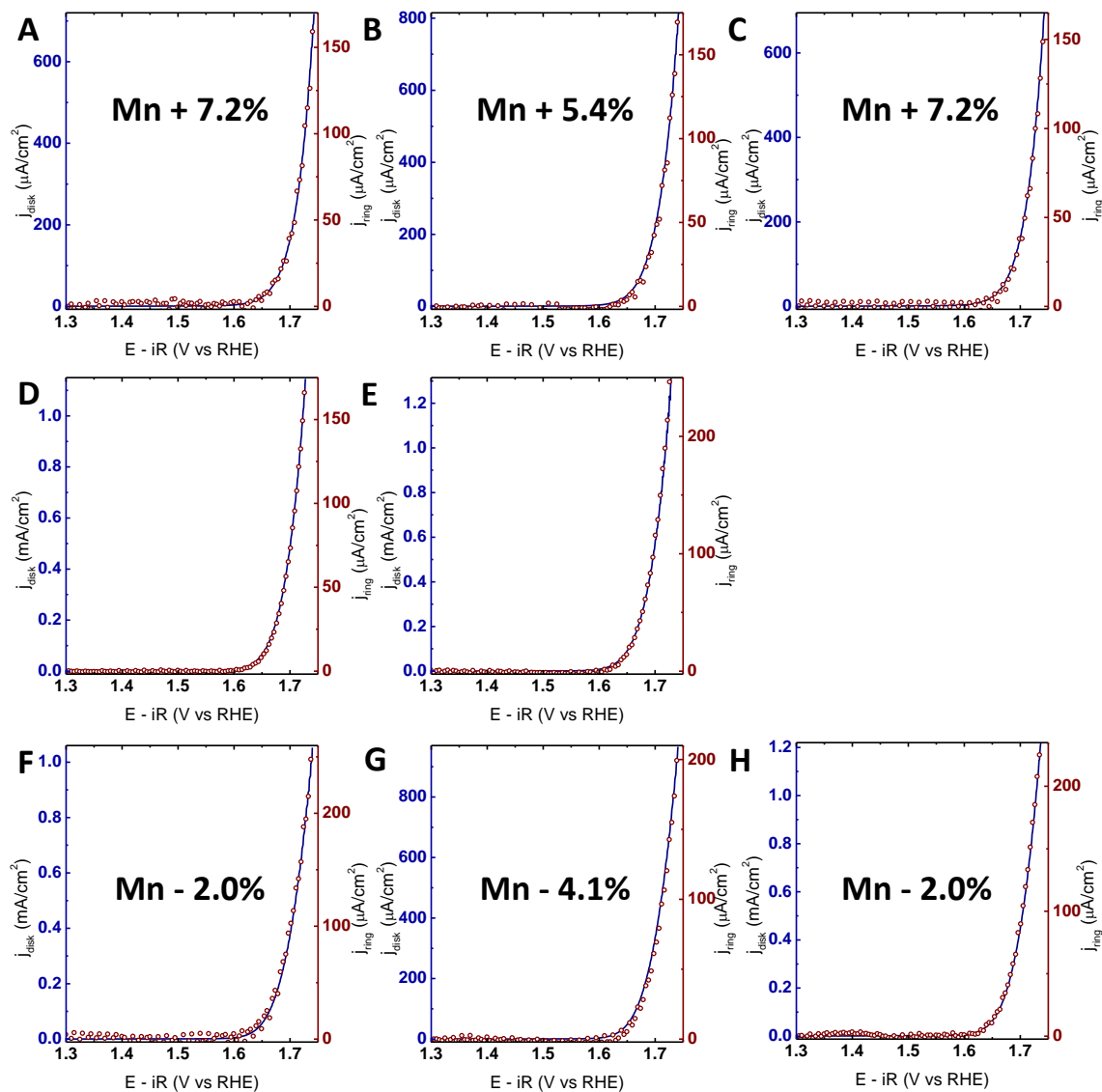


Figure 8.37: CV measurements of all evaluated $\text{La}_{0.6}\text{Sr}_{0.4}\text{Mn}_{1-\delta}\text{O}_3$ films (solid blue lines) and the corresponding ring currents (open red circles) obtained by CA at 0.4 V vs. RHE. All measurements were performed with Ar-purged 0.1 M KOH supporting electrolyte at 10 mV/s and 1600 rpm. The voltage was corrected for electrolyte resistance ($\sim 47 \Omega$ for all samples). (A-C) The Mn-rich samples; (D-E) the stoichiometric samples; (F-H) the Mn - deficient LSMO samples. Their respective Mn off - stoichiometry is indicated in each figure.

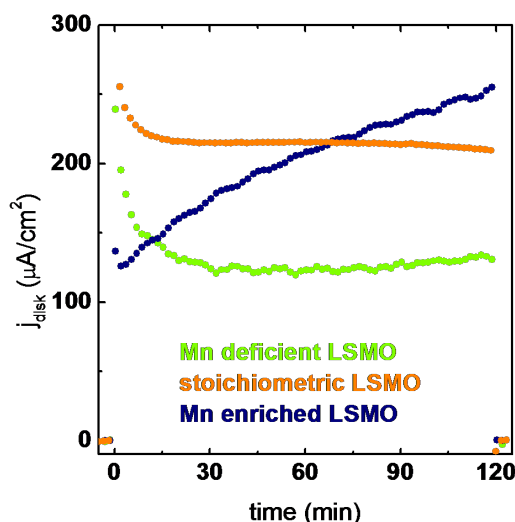


Figure 8.38: Disk currents of CA measurements for one LSMO of each stoichiometry for 2 h at 1.7 V vs. RHE. Previously and consecutively to the electrolysis, the samples were held at 1.1 V vs. RHE for 10 min. All electrochemical measurements were performed in Ar-saturated 0.1 M KOH and 1600 rpm. The measurement protocol applied to the samples prior to electrolysis/extensive CV measurements was identical for all samples.

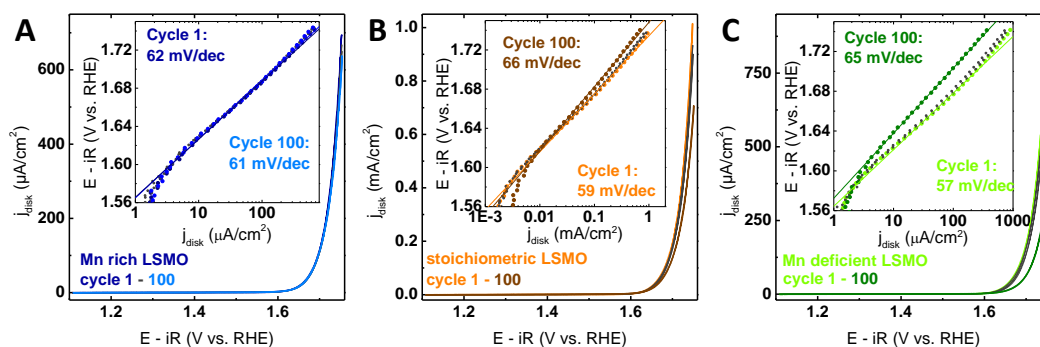


Figure 8.39: Comparison of CV measurements made prior to the applied long-term measurement and subsequent to the long-term measurement. Representative CV measurements are shown for all evaluated stoichiometries. All measurements were performed with Ar-purged 0.1 M KOH supporting electrolyte at 10 mV/s and 1600 rpm. The voltage was corrected for electrolyte resistance ($\sim 47 \Omega$ for all samples). The forward direction of the second cycle is shown. The inset shows the Tafel analysis comparing the CV before and after the long-term measurement with the determined Tafel slope stated. (A-C) The comparison of the effects extensive cycling comparing the first cycle and the 100th cycle of each sample.

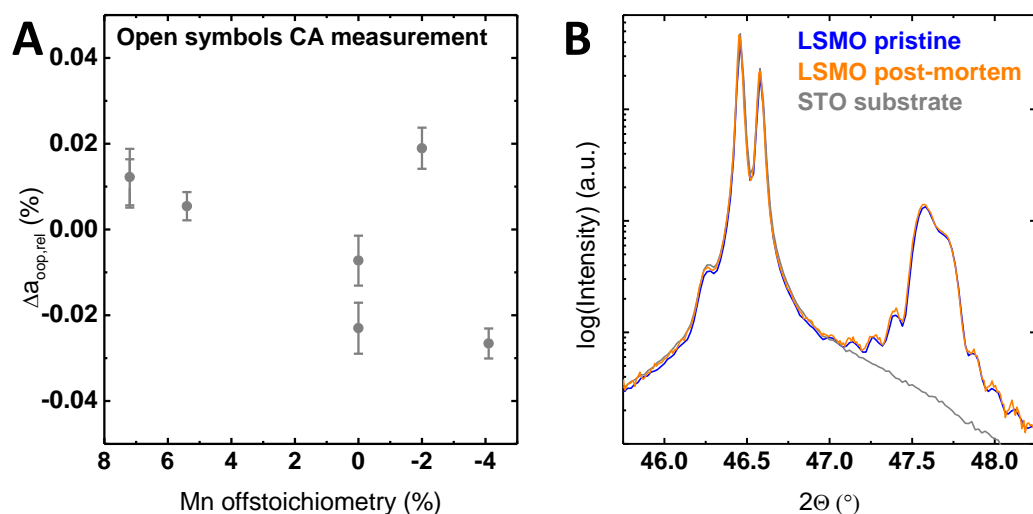


Figure 8.40: (A) Relative changes in the lattice parameters of the initial samples and after the electrochemical measurements based on wide angle out-of-plane X-ray diffraction spectra using a monochromator. (B) A detailed 2θ XRD scan at the 200 LSMO reflex comparing the blank substrate and a Mn-rich LSMO film prior to electrochemical measurements and directly after the applied electrochemical measurement (in this case, extensive cycling).

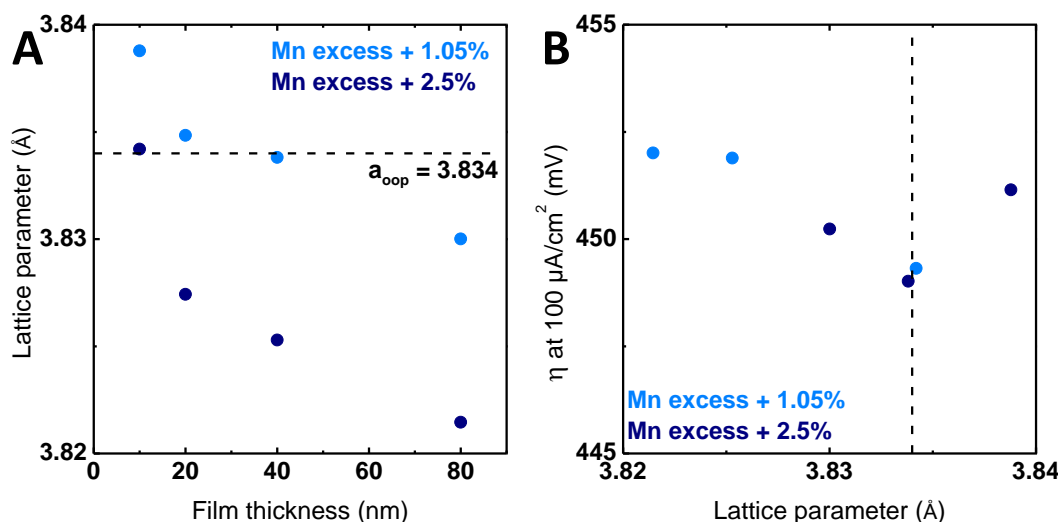


Figure 8.41: (A) Thickness decency of lattice parameters based on the sample series reported in ref. [179] for LSMO with small Mn excess. (B) Overpotential required to obtain $100 \mu\text{A}/\text{cm}^2$ in dependence of the lattice parameter for two offstoichiometries analogous to Figure 4.7A. The dashed line corresponds to the lattice parameter with the highest activity, as can be seen in Figure 4.6B.

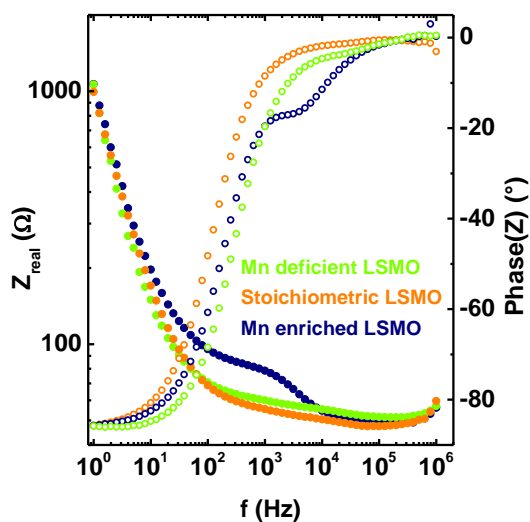


Figure 8.42: Electrochemical impedance spectroscopy (EIS) exemplarily shown for each stoichiometry. The EIS was conducted with an amplitude of 10 mV/s at open circuit potential and used to determine the uncompensated electrolyte resistance by the high frequency intercept. The additional feature for Mn-rich LSMO can be attributed to the additional interface due to the Mn_3O_4 precipitates.

9 Appendix B

The following supporting information contains data and discussion concerning the second part, the immobilization of the Ru₂-bbp catalyst on ITO. Note the herein shown part covers only the part of the supplementary information required for the preparation and analysis of the electrodes. Please refer to the complete published supporting information (SI of^[270]) and the PhD thesis of Jann Odrobina for detailed information on the synthetic routes of the complex synthesis and the extensive characterization. They contain the complete characterization via chromatography, NMR spectroscopy, mass spectrometry, UV-vis spectroscopy, and X-ray crystallography of the complexes.

9.1 Electrode preparation

Materials: The majority of the chemicals was purchased from commercial suppliers (ABCR, ALDRICH, ACROS, FLUKA, DEUTERON and MERCK) and used without further purification. Solvents were HPLC and p.a. grade. Whenever dry solvents needed to be used, they were dried according to standard procedures. All reactions were routinely performed under a dry nitrogen atmosphere by using standard SCHLENK techniques. RuCl₂(dmsO)₄,^[282] 3,5-bis6-(2,2'-bipyridyl)-4-iodo-1H-methoxymethyl pyrazole (MOML)¹² and 4-(Bis(pincolateto)boryl)-phenyl-ethylester³ were prepared according to literature procedures. All aqueous solutions were prepared with deionized water (Millipore). Trifluoromethanesulfonic acid (99+%) (triflic acid) packed in ampules, was purchased from STREAM/CYMIT and ceric ammonium nitrate (Ce(IV), CAN) was used obtained from ABCR (99% ACS grade, for catalysis experiments). The ITO coated glass slides (surface resistivity 8-12 Ω) and ITO nano powder (<50 nm particle size) were received from ALDRICH. GC slides for XAS measurements were purchased from HTW-HOCHTEMPERATUR-WERKSTOFFE GmbH.

Preparation of ITO|*meso*-ITO electrodes^[241]: The ITO slides (25 x 75 mm) were sonicated for 30 min in a soap solution (2 % Hellmanex[®]III in water), than sonicated for 30 min in water and finally sonicated in 2-propanol for additional 30 min. The slides were dried in air at 100 °C for 30 min. *meso*-ITO powder (100 mg), was suspended in ethanol (0.34 ml) and acetic acid (0.1 ml). The

suspension was sonicated in an ultrasonic bath for 20 min after manual shaking. Subsequently the suspension was sonicated in an ultrasonic horn sonicator (10 min, 5 cycles, 65 %). The suspension was sonicated for 30 sec in an ultrasonic bath directly before coating on the ITO glass slide. The *meso*-ITO dispersion (10 μ l) was distributed on the ITO slide by doctor blading. The sides of the slides were masked with TESA tape to maintain a constant surface thickness. After drying the slides in air, the tape was removed. The ITO|*meso*-ITO substrates were annealed with heating the samples up to 500 °C within two hours, the temperature was kept for one hour. In a subsequent annealing step the ITO|*meso*-ITO substrates were heated up to 300 °C in a 3% H₂/N₂ atmosphere for 1 h and cooled back to room temperature. The slides were cut with a diamond knife into smaller pieces with a *meso*-ITO coated area of (7 x 5 mm).

Preparation of GC|*meso*-ITO disk electrodes for RRDE (chapter 5): The GC disk electrode was polished initially with a diamond paste (ϕ = 1 μ m), after that with an alumina paste (ϕ = 0.05 μ m), washed with water and methanol and dried in air. *meso*-ITO powder (100 mg) was suspended in ethanol (0.34 ml) and acetic acid (0.1 ml). The suspension was sonicated in an ultrasonic bath for 20 min after manual shaking. Subsequently the suspension was sonicated in an ultrasonic horn sonicator (10 min, 5 cycles, 65 %). The mixture was diluted 1:2 with ethanol. One drop (3 μ l) of the diluted suspension was placed in the middle of the GC disk and dried in air.

LSMO film fabrication (chapter 5): La_{0.6}Sr_{0.4}MnO₃ (LSMO) thin films were prepared by ion-beam sputtering (IBS). Rectangular undoped SrTiO₃ (STO) with (100)-orientation (CRYSTEC GmbH) was used as substrates. The films were deposited at 800 °C in an oxygen atmosphere of 1.7×10^{-4} mbar. To reduce the number of preparation-induced defects, the prepared films were kept under preparation conditions for 1 h, and carefully cooled down to room temperature including a resting point of 30 min at 500 °C.

Preparation of GC|*meso*-ITO disk electrodes for XAS (chapter 6): *meso*-ITO powder (100 mg) was suspended in ethanol (0.34 ml) and acetic acid (0.1 ml). The suspension was sonicated in an ultrasonic bath for 20 min after manual shaking. Subsequently the suspension was sonicated in an ultrasonic horn sonicator (10

min, 5 cycles, 65 %). The mixture was diluted 1:2 with ethanol. 15 μ l of the diluted suspension was placed in the middle of the GC slide and dried in air. The GC|*meso*-ITO electrodes were soaked in a 0.1 mM solution of **3** in methanol overnight subsequently rinsed with methanol and dried in air. One GC|*meso*-ITO|**3** sample was cycled 3 times in a cyclic voltammetry experiment as WE in the current range of 0.313 and 1.713 V vs. RHE with CE: Pt and ref. MSE in pH 7 (0.1 M Na₃SO₄). The sample was subsequently rinsed with water.

Preparation ITO-RRD Electrode (chapter 6): The In_xSn_{1-x}O₃ (ITO) electrodes used for the electrochemical characterization by RRDE measurements were prepared by ion beam sputtering (IBS). Round 0.5 wt% Nb doped SrTiO₃ (STNO) with (100) orientation were used as substrates purchased from CrysTec GmbH. The deposition temperature was at 650 °C in an oxygen atmosphere of 1.8×10^{-4} mbar.

In order to minimize preparation induced defects the films were kept under preparation conditions for 20 min and subsequently carefully cooled down to room temperature. To ensure stable back contact Ti contacts (5 nm thickness) with a protective Au layer (100 nm thickness) were deposited on the backside prior to the film preparation. The mesoporous particles were prepared according to the procedure published by Hoertz et al^[241]. The assembly of the prepared STNO|ITO|*meso*-ITO electrode was performed according to our previously established electrode design published in Scholz et al^[179].

Anchoring of [L^xRu₂(CO₃H)] on the oxide electrodes: To anchor the complexes [L^xRu₂(CO₃H)] (x=COOH, POOOH, COOH₂) to the oxide electrodes and the GC|*meso*-ITO disk electrodes, the electrodes were soaked in a solution of [L^xRu₂(CO₃H)] (0.1 mmol/l, 2 ml) in methanol at room temperature for 1 d. Afterwards the electrodes were rinsed with methanol (15 ml).

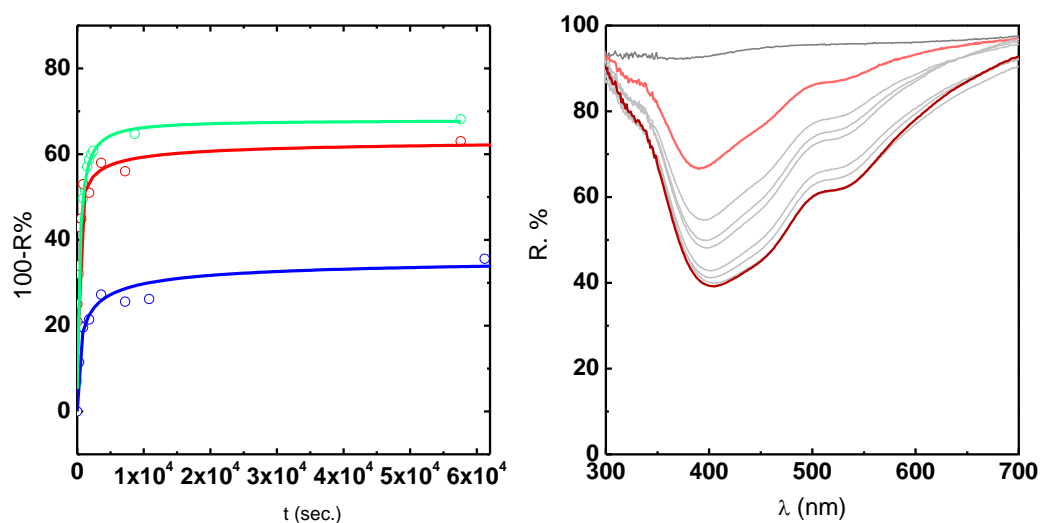


Figure 9.1: Chapter 6: **left:** anchoring curves of $[L^{COOH}Ru_2(CO_3H)(py)_4]$ **1** (blue), $[L^{(COOH)_2}Ru_2(CO_3H)(py)_4]$ **2** (cyan), $[L^{(POOOH)}Ru_2(CO_3H)(py)_4]$ **3** (red) concentrations extracted from peak value at 396 nm in DR-UV/vis spectroscopy on ITO|*meso*-ITO, **right:** growing of $[L^{(POOOH)}Ru_2(CO_3H)(py)_4]$ **3** (0.1 mM in MeOH) on ITO|*meso*-ITO monitored by DR-UV/vis.

9.2 Experimental Section

9.2.1 Electrochemistry

Cyclic voltammetry: Cyclic voltammetry experiments were carried out at a PGSTAT 101 (METROHM). For experiments with dissolved complex (in 0.1 M tBu_4NPF_6 propylene carbonate), a glassy carbon (GC) disk electrode ($\varnothing = 3$ mm) was used as working electrode (WE), a platinum disk electrode ($\varnothing = 2$ mm) was used as counter electrode (CE) and Hg/Hg₂SO₄ electrode (MSE) served as reference electrode. In the hybrid case, the WE was substituted by the modified *meso*-ITO glass slides. These glass slides were connected via an alligator clamp to the wire of the potentiostat. The GC and Pt electrodes were polished initially with a diamond paste ($\varnothing = 1$ μm), then with an alumina paste ($\varnothing = 0.05$ μm), washed with water and methanol and dried in air.

Cyclic voltammetry experiments were performed in propylene carbonate (PC) with tBu_4NPF_6 (0.1 M) as conduction salt, or in aqueous triflic acid (0.1 M, pH 1). The potentials measured in aqueous solution were referenced to the reversible hydrogen electrode (RHE) scale.

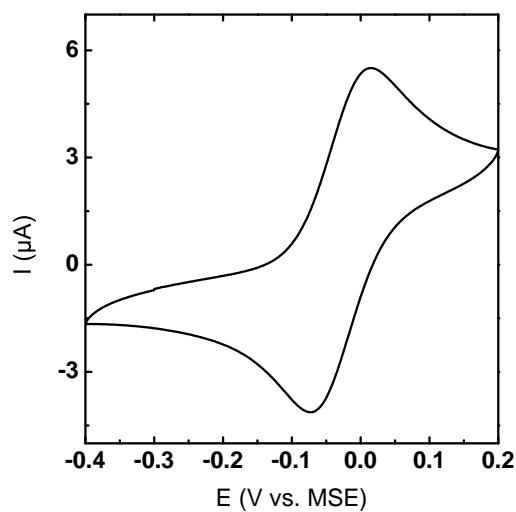


Figure 9.2: Chapter 5: Ferrocene measured in PC containing $t\text{Bu}_4\text{NPF}_6$ (0.1 M) with WE: GC, CE: Pt and Ref. MSE (scan rate 100 mV/s).

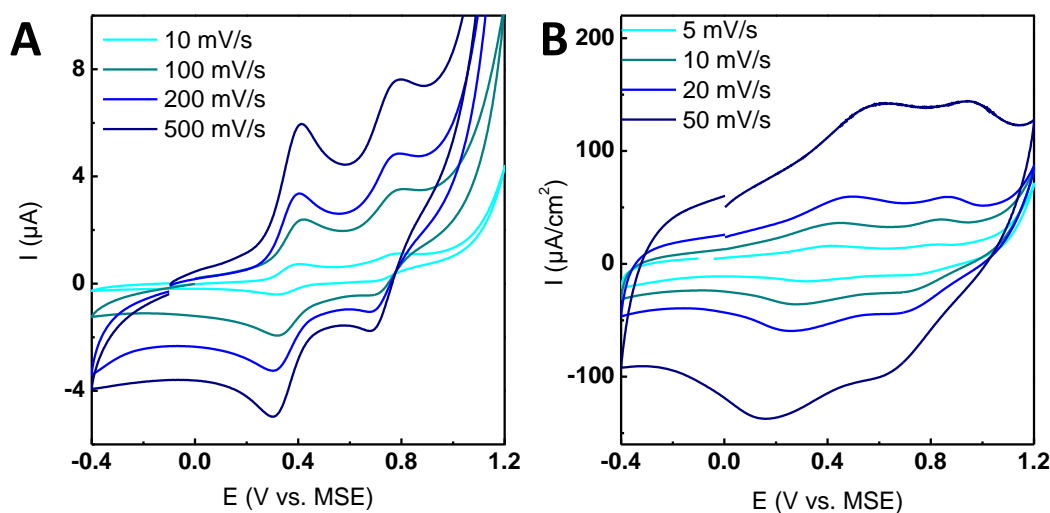


Figure 9.3: Chapter 5: left: CVs of complex $[\text{L}^{\text{COOH}}\text{Ru}_2(\text{CO}_3\text{H})](\text{PF}_6)_2$ (**4**) measured in PC containing $t\text{Bu}_4\text{NPF}_6$ (0.1 M) with WE: GC, CE: Pt and Ref. MSE at different scan rates, right: CVs of complex $[\text{L}^{\text{COOH}}\text{Ru}_2(\text{CO}_3\text{H})](\text{PF}_6)_2$ (**4**) on ITO|*meso*-ITO measured in PC containing $t\text{Bu}_4\text{NPF}_6$ (0.1 M) with WE: ITO|*meso*-ITO, CE: Pt and Ref. MSE at different scan rates

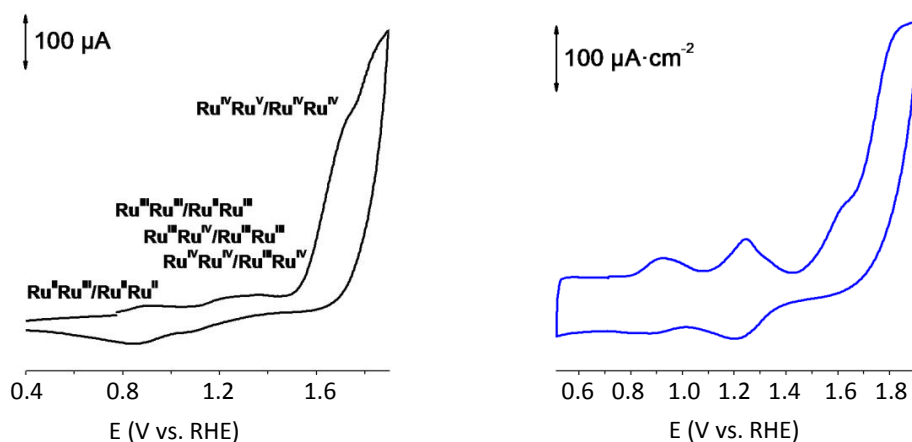


Figure 9.4: Chapter 5: left: CV of complex $[L^{COOH}Ru_2(CO_3H)](PF_6)_2$ (**4**) on ITO|*meso*-ITO measured in 0.1 M triflic acid solution pH 1; WE: ITO|*meso*-ITO, CE: Pt and Ref. MSE, right: CV of a water soluble diaqua complex measured in 0.1 M triflic acid solution pH 1 with WE: GC, CE: Pt and Ref. SCE^[36].

9.2.1.1 RRDE setup:

For the rotating ring-disk electrode experiments the RRDE-3A (ALS Co. Ltd) with a Pt ring electrode were used. Two Interface 1000E (Gamry Instruments Inc.) were driven in bipotentiostatic mode for the collection experiments. All electrochemical measurements with the RRDE setup were performed in 0.1 M triflic acid at pH 1. The electrolyte was saturated with Ar gas (Air Liquide, 99.999%) for at least 30 min prior the measurement and continuously purged with Ar throughout the measurement. The rotation rate used for all experiments was 1600 rpm. A Pt coil was used as counter electrode and a mercury sulfate electrode (MSE) (ALS Co. Ltd) was used as reference electrode. The potentials for analysis were converted to the RHE scale using $E_{RHE} = E_{applied} + E_{reference}$. Prior to each measurement, the Pt ring electrode was polished and electrochemically scanned to ensure reliable ring measurements.

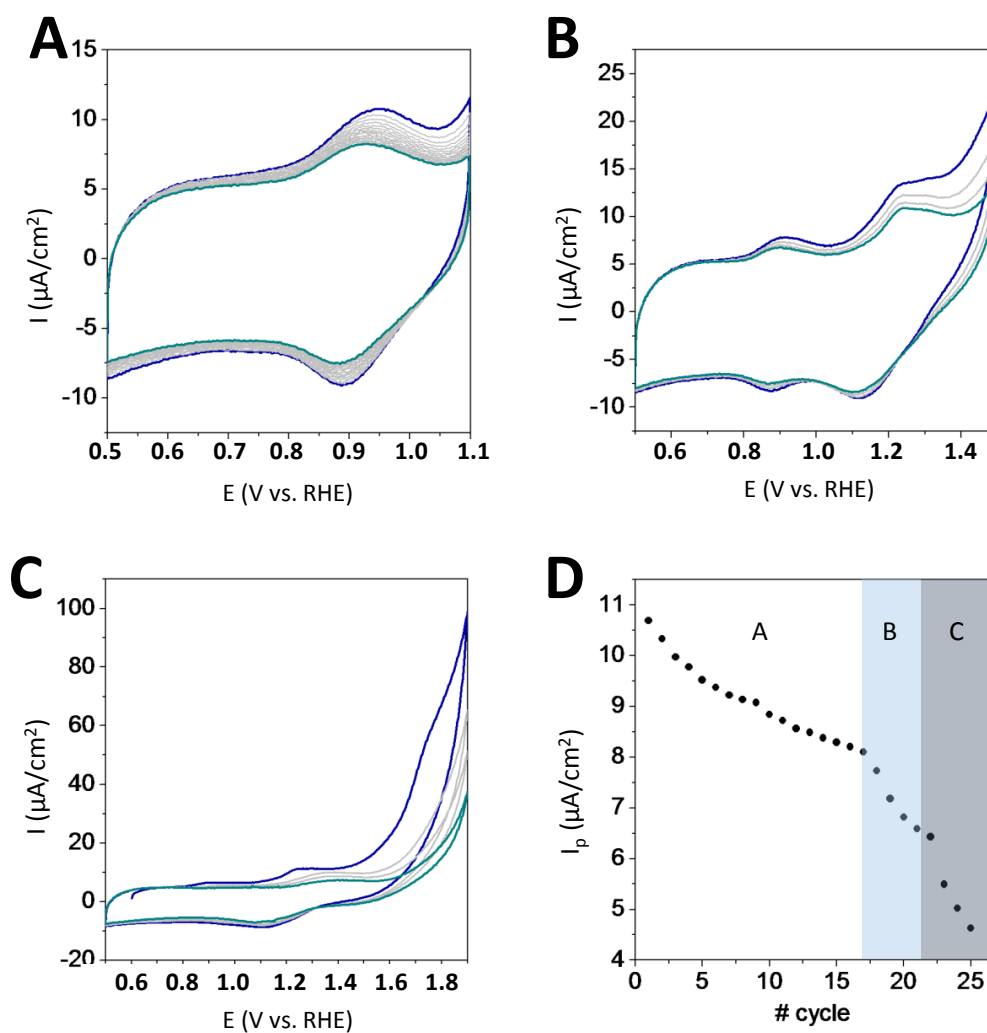


Figure 9.5: Chapter 5: **A:** repetitive CVs (scan rate 10 mV/s) of the first redox reaction $^{III}\text{Ru}/^{II}\text{Ru} \mid ^{II}\text{Ru}/^{II}\text{Ru}$ of **4** anchored on *meso*-ITO, **B:** repetitive CVs (scan rate 10 mV/s) up to $^{IV}\text{Ru}/^{IV}\text{Ru}$, **C:** repetitive CVs (scan rate 10 mV/s) into the catalytic region, **D:** change of anodic peak current for the $^{III}\text{Ru}/^{II}\text{Ru} \mid ^{II}\text{Ru}/^{II}\text{Ru}$ wave with number of scans, A related to **A** (up 1.1 V), B related to **B** (up to 1.5 V) and C (up to 1.9 V) related to **C**. WE: ITO|*meso*-ITO, CE: Pt and Ref. MSE (first scan blue, last scan cyan).

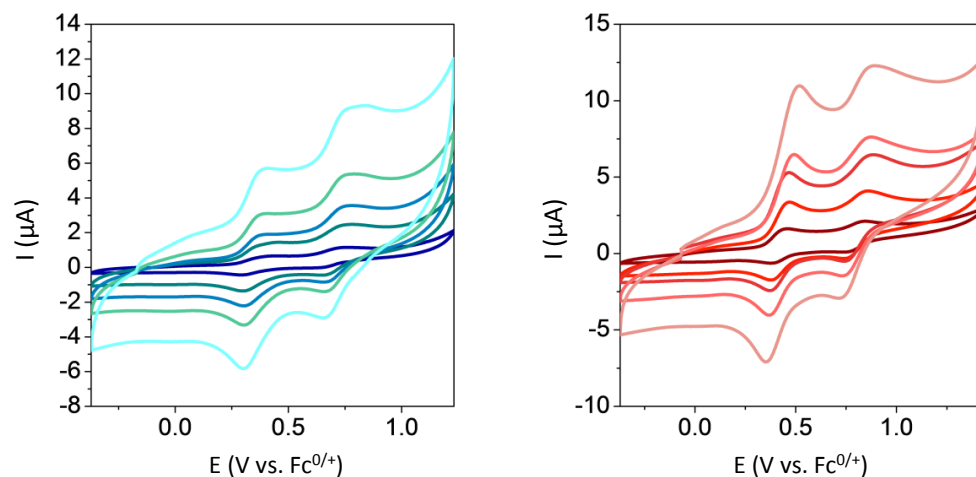


Figure 9.6: Chapter 6: **left:** CV of $[L^{(COOH)_2}Ru_2(CO_3H)(py)_4]$ **2** in 0.1 M $[Bu_4N]PF_6$ PC with WE: GC, CE: Pt measured at different scan rates (10, 50, 100, 200, 500 mV/s), **right:** CV of $[L^{(POOOH)}Ru_2(CO_3H)(py)_4]$ **3** in 0.1 M $[Bu_4N]PF_6$ PC with WE: GC, CE: Pt measured at different scan rates (10, 50, 100, 200, 500 mV/s).

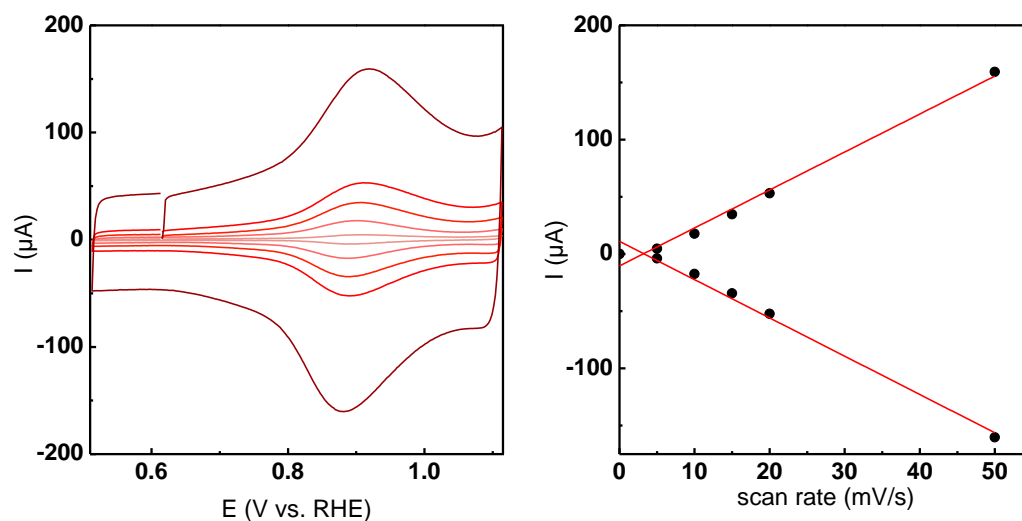


Figure 9.7: Chapter 6: **left:** scan rate dependent CV (5, 10, 15, 20, 50 mV/s) and **right:** scan rate vs. peak current plot of $Ru^{III}Ru^{II}/Ru^{II}Ru^{II}$ of $ITO|meso-ITO|3$ in 0.1 M triflic acid (pH 1) with WE: $ITO|meso-ITO|3$, CE: Pt, ref.: MSE.

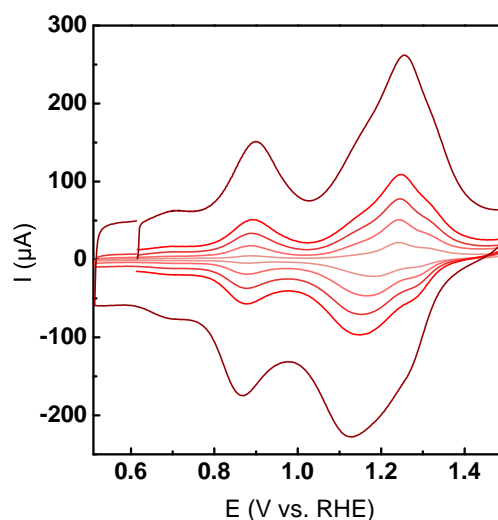


Figure 9.8: Chapter 6: scan rate dependent CV (5, 10, 15, 20, 50 mV/s) of $\text{Ru}^{\text{V}}\text{Ru}^{\text{V}}/\text{Ru}^{\text{II}}\text{Ru}^{\text{II}}$ of $\text{ITO}|\text{meso-ITO}|_3$ in 0.1 M triflic acid (pH 1) with WE: $\text{ITO}|\text{meso-ITO}|_3$, CE: Pt, ref.: MSE.

RRDE measurement protocols for chapter 5: The measurement protocol was identical for all samples. The OER activity was investigated by cycling three times from 0.54 V vs. RHE to 1.94 V vs. RHE with 10 and once with 200 mV/s at 1600 rpm. Subsequently the samples were held at open circuit potential (OCP) for 20 min in order to remove all unbound complexes. Afterwards the samples were cycled once with 10 mV/s and 200 mV/s with the previous parameters. Chronoamperometric measurements were performed subsequently, consisting of 1 min holding at the OCP, then 1 min holding at potentials between 1.69 and 1.94 V vs. RHE in steps of 50 mV, and a final step of 1 min at OCP. The ring electrode was constantly held at 0.2 V vs. RHE to probe for O_2 (calibration data shown in Figure C7.4). Before each measurement series, electrochemical impedance spectroscopy (EIS) was conducted with an amplitude of 10 mV at open circuit potential. A platinum wire was used as counter electrode (CE) and a MSE electrode served as reference electrode. The potentials were referenced to the RHE scale in 0.1 M triflic acid and corrected for the electrolyte resistance extracted from the high frequency intercept of the real impedance.

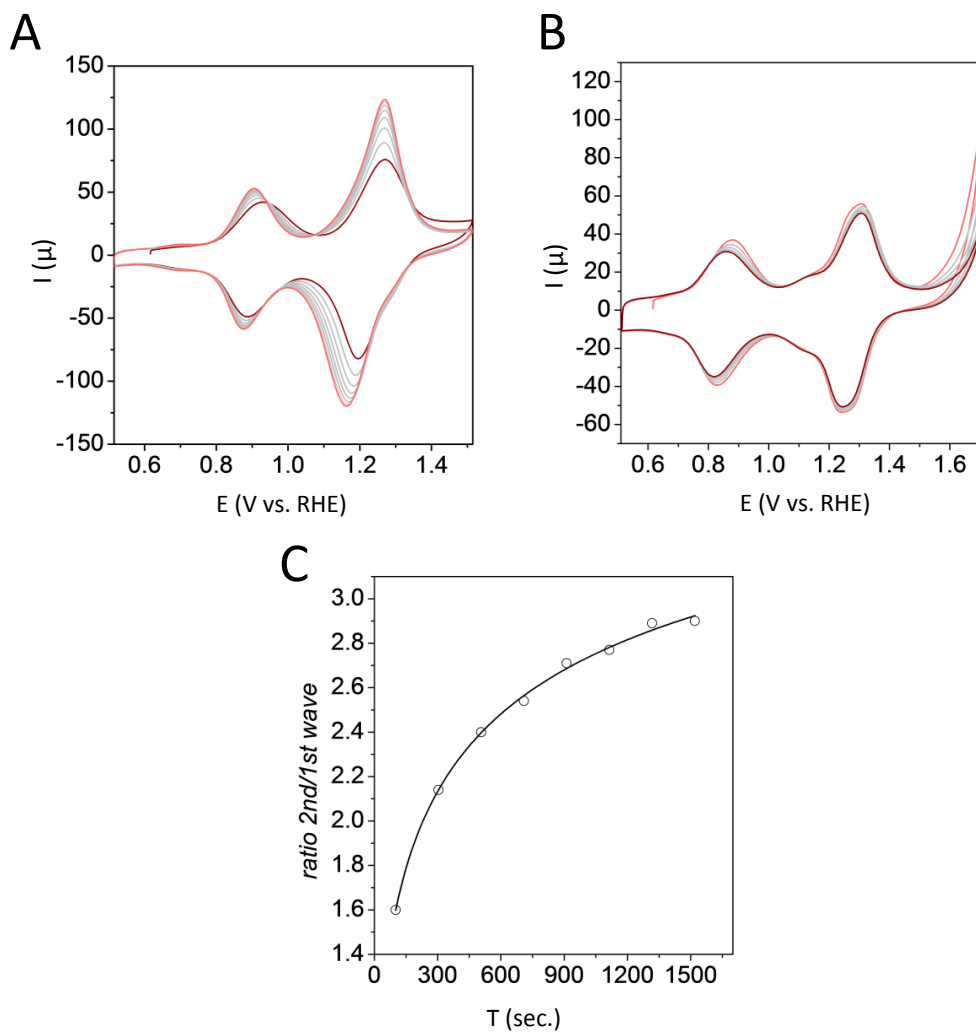


Figure 9.9: Chapter 6: **A:** repetitive CV of ITO|*meso*-ITO|**3** in 0.1 M triflic acid (pH 1) with WE: ITO|*meso*-ITO|**3**, **B:** repetitive CV of ITO|*meso*-ITO|**3a** in 0.1 M triflic acid (pH 1) with WE: ITO|*meso*-ITO|**3a**, CE: Pt, ref.: MSE CE: Pt, ref.: MSE, **C:** integrated current ratio of first and second redox process for repetitive CVs of ITO|*meso*-ITO|**3**. The desired diaqua complex should show a ratio of 3:1, for carbonate bridged complex the ratio should be 1:1.

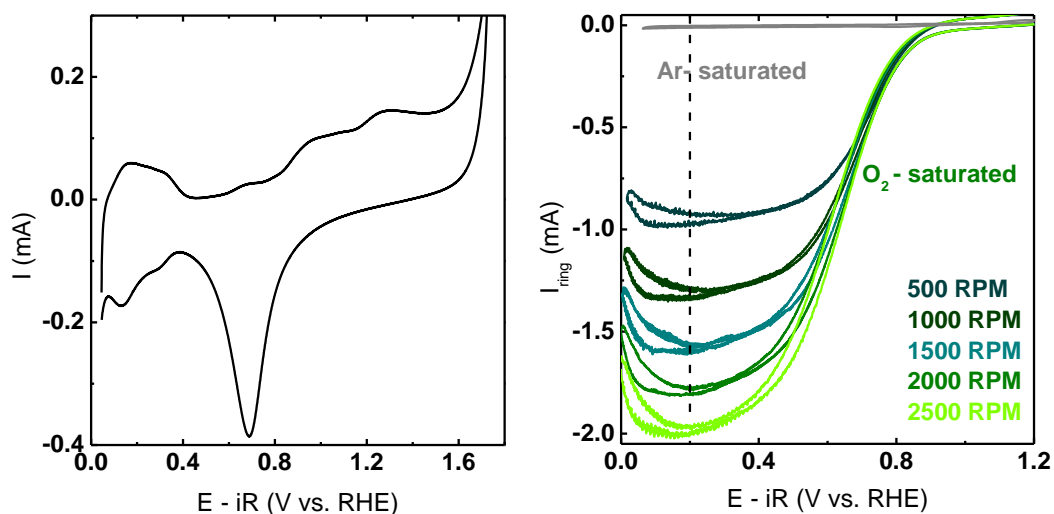


Figure 9.10: **A:** Unrotated CV measurement of the freshly polished Pt-ring electrode in Ar saturated 0.1 M triflic (pH 1) at 200 mV/s. The features represent the known characteristics of a polycrystalline Pt metal. **B:** Ring currents of a freshly polished Pt- ring electrode in 0.1 M triflic acid (pH 1) supporting electrolyte (Ar-purged for the background measurement, O₂ purged for the oxygen reduction measurements) at 200 mV/s.

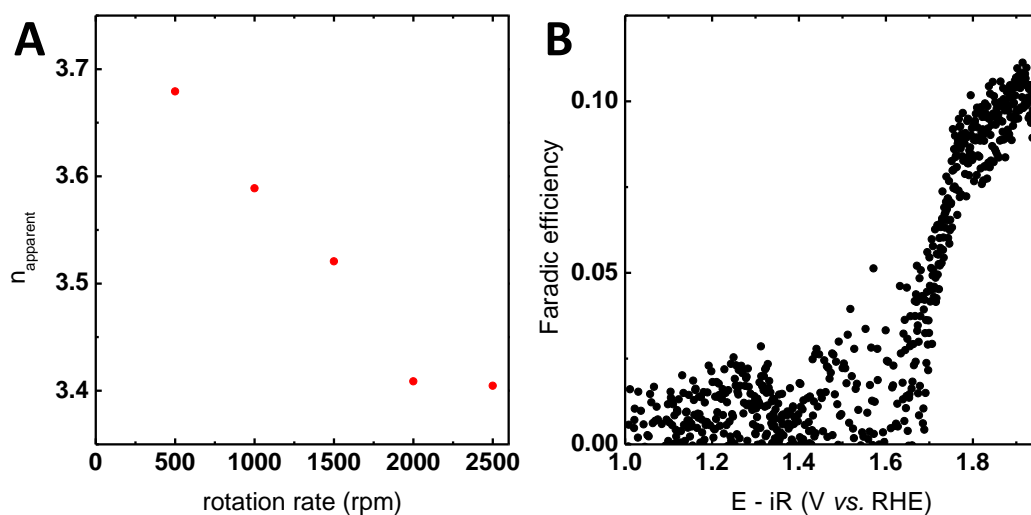


Figure 9.11: **A:** the calculated transferred electrons based on the currents under diffusion limiting conditions at 0.2 V vs. RHE (Details in the text). **(B)** Evaluation of the faradic efficiency based on the calculated number of electrons (3.5) for the oxygen reduction at the Pt ring electrode at 1500 rpm. The currents considered are background corrected by subtraction of the respective blank currents for both the ring and the disk currents.

RRDE measurement protocols for chapter 6: Identical measurement protocols were applied to all electrodes except for the order of the ring experiment during the desorption measurements. Initially electrochemical impedance spectroscopy was conducted with an amplitude of 10 mV at open circuit potential. In addition to the conversion to the RHE scale the potentials were corrected for the uncompensated electrolyte resistance extracted from the high-frequency intercept of the real impedance. Additionally, the double layer capacitance was measured for all electrodes by cycling two times between 0.54 to 1.14 V vs. RHE with 10, 20, 50, 100, and 200 mV/s. The linear scaling relation between peak current of the $\text{Ru}^{\text{II}}\text{Ru}^{\text{III}}$ oxidation and the employed scan rate was checked after subtraction of the double layer capacitance extracted at 0.65 V vs. RHE. Subsequently the electrodes were cycled two times between 0.54 to 1.89 V vs. RHE with 120 s open circuit potential in between. The corresponding ring measurements probed either first the complex reduction at 0.75 V vs. RHE and then the oxygen reduction at 0.25 V vs. RHE or vice versa. The analysis of either complex desorption or oxygen evolution was performed with ring electrode probing the first cycle of the respective reaction. For the reaction rate experiments the disk electrodes were held at open circuit potential for 180 s prior and subsequent to each potential step. The measured potentials between 1.64 and 1.94 V vs. RHE with 0.05 V steps were applied for 60 sec. Between each chronoamperometry CA measurement the remaining complex concentration was measured by one cycle between 0.54 and 1.14 V vs. RHE with 10 mV/s.

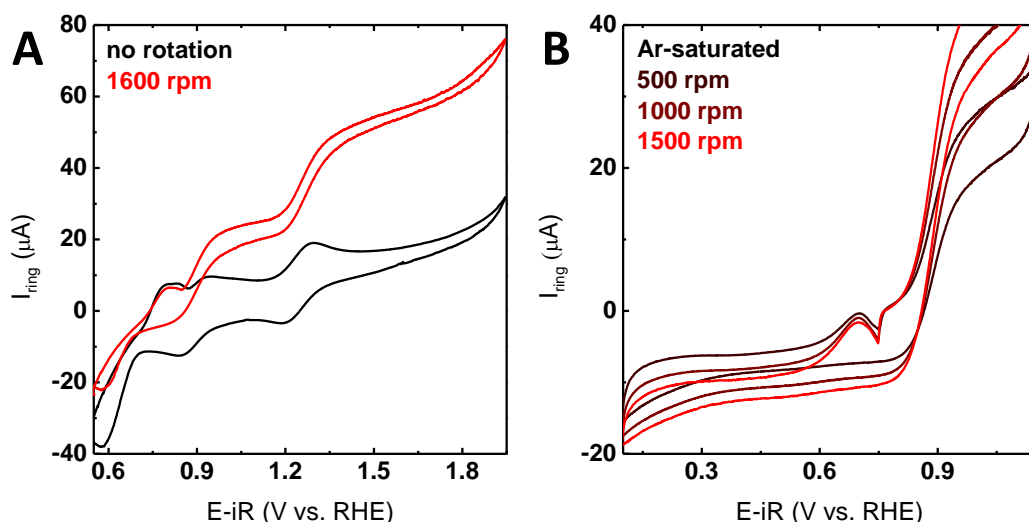


Figure 9.12: Chapter 6: (A) CV measurements of 0.5 mM $\text{Na}_2[(\text{bbp}^{\text{Me}})\text{Ru}_2(\text{O}_2\text{H}_3)(3\text{-SO}_3\text{-py})_4]$ in Ar saturated 0.1 M triflic (pH 1) and ITO disk electrode without rotation (black) and with rotation (red) at 1600 rpm. (B) CV measurements at the Pt ring electrode and the ITO disk at the oxidizing potential of 1.1 V vs. RHE in Ar saturated 0.1 M triflic (pH 1) with 0.5 mM $\text{Na}_2[(\text{bbp}^{\text{Me}})\text{Ru}_2(\text{O}_2\text{H}_3)(3\text{-SO}_3\text{-py})_4]$.

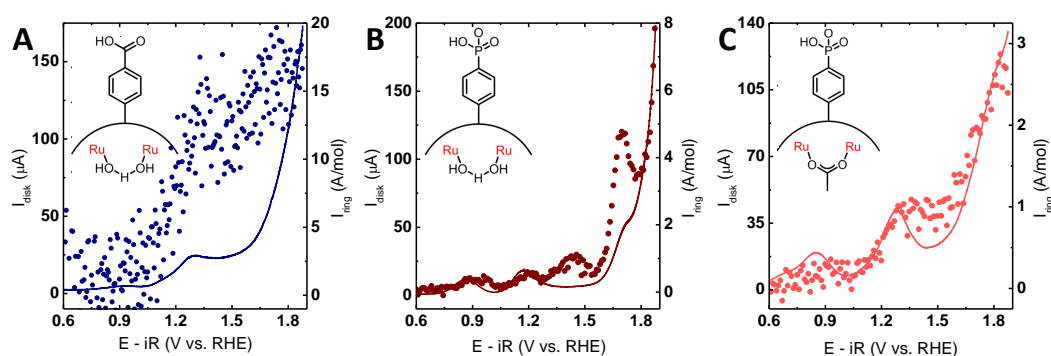


Figure 9.13: Chapter 6: Rotating ring disc CV measurements of (A) surface anchored complex $[\text{L}^{\text{COOH}}\text{Ru}_2(\text{CO}_3\text{H})(\text{py})_4]$ **1** (ITO|*meso*-ITO|**1**, dark blue line), (B) surface anchored complex $[\text{L}^{(\text{POOOH})}\text{Ru}_2(\text{CO}_3\text{H})(\text{py})_4]$ **3** (ITO|*meso*-ITO|**3**, dark red line), and (C) surface anchored acetate bridged complex $[\text{L}^{(\text{POOOH})}\text{Ru}_2(\text{OAc})(\text{py})_4]$ **3a** (ITO|*meso*-ITO|**3a**, brown line). The corresponding ring currents are shown as dots. The ring currents represent the currents corresponding to reduction of the oxidized complexes ($V_{\text{ring}} = 0.75$ V vs. RHE) normalized on the concentration of complexes determined by integration of the first oxidation. All measurements were performed with 0.1 m triflic acid supporting electrolyte (Ar-purged) at 10 mV/s and 1600 rpm. The voltage was corrected for uncompensated resistance. The positive-going direction of the first scan is shown.

9.2.1.2 Water Oxidation Experiments:

Water oxidation experiments using CAN as chemical oxidant were performed in a self-made two cell glass reactor (each $V = 16.5$ ml) whose temperature was controlled at $25\text{ }^{\circ}\text{C}$. The rise in pressure during catalysis was monitored by on-line manometry using a differential pressure manometer (TESTO 521-1). The pressure difference was measured between the reaction cell and a reference cell (same size, same ratio between liquid and gas). To monitor the increasing oxygen concentration, a Clark oxygen sensor (UNISENSE, Ox-N sensor and Oxy-meter) was placed in the gas phase of the reactor. The oxygen sensor had to be calibrated prior to the catalysis experiment. Therefore, defined amounts of dioxygen were added to the degassed reactor (2 ml, 0.1 M triflic acid, pH 1).

The complex was added to the degassed reactor (1.85 ml, 0.1 M triflic acid, pH 1). After pressure equilibration with the reference cell (filled with 1.85 ml, 0.1 M triflic acid, pH 1), 150 μl of the triflic acid solution containing the ruthenium catalyst were added to the reference cell. When the dioxygen value measured in the reactor was stable, 150 μl of a CAN solution in triflic acid (100 eq. Ce^{IV}) were added to the reactor. Progress of the catalysis was monitored based on the difference in pressure and dioxygen concentration between reactor and reference cell.

The TOF_i value (TOF_i initial turnover frequency) was determined from the manometry experiment after adding 100 eq. of CAN to the pH 1, complex solution. To calculate the TOF_i value, the increasing TONs were linear fitted within the first 30 s after $\text{Ce}(\text{IV})$ addition.

Table 9.1: Chapter 5: Turnover frequency's (TOF) and turnover numbers (TON) for WOC of the water soluble bbp-type complex^[34] in comparison with complexes **5** and **6** after addition of ~ 100 eq. of Ce^{IV} at $25\text{ }^{\circ}\text{C}$ in 0.1 M triflic acid solution pH 1, $\text{TON}(\text{p})$ measured by manometry, $\text{TON}(\text{O}_2)$ measured with a Clark electrode.

Water soluble bbp-type	$\text{TOF}_i(\text{p})$	$6.8 \times 10^{-2} \text{ s}^{-1}$	$\text{TON}(\text{p})$	22.6 ± 1.5
			$\text{TON}(\text{theo})$	24.8 ± 0.2
5	$\text{TOF}_i(\text{p})$	$3.5 \times 10^{-2} \text{ s}^{-1}$	$\text{TON}(\text{p})$	22.9 ± 1.8
			$\text{TON}(\text{theo})$	25.4 ± 0.2
6	$\text{TOF}_i(\text{p})$	$3.1 \times 10^{-2} \text{ s}^{-1}$	$\text{TON}(\text{p})$	23.3 ± 1.4
			$\text{TON}(\text{theo})$	25.1 ± 0.1

Table 9.2: Chapter 6: Turn over frequency's (TOF) and turn over numbers (TON after addition of ~ 100 eq. of Ce^{IV} at 25°C in 0.1 M triflic acid solution pH 1, TON(p) measured by manometry, TON(O_2) measured with a Clark electrode.

Complex	TON(p)	TOF _i (p) (1/s)
$\text{Na}_2[(\text{bbp}^{\text{Me}})\text{Ru}_2(\text{O}_2\text{H}_3)(3\text{-SO}_3\text{-py})_4]^{[34]}$	22.6	6.8×10^{-2}
1 ^[270]	23.3	3.1×10^{-2}
2	22.3	2.5×10^{-2}
3	23.2	3.5×10^{-2}
3a	22.2	2.5×10^{-2}

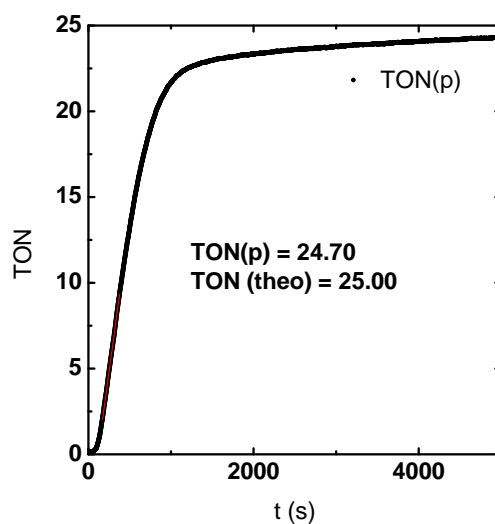


Figure 9.14: Chapter 5: Water oxidation with complex **5** in 0.1 M triflic acid solution pH 1 upon addition of 100 eq. of Ce_{IV} (CAN) at 25°C , measured by manometry.

9.2.2 XPS Measurements:

Procedure for Chapter 5: The elemental composition was measured using an Omicron EA 125 analyzer and Mg K_{α} (1253.6 eV) X-ray source. The binding energy scale was calibrated by defining the fitted Au 4f 7/2 peak of the sputtered Au holder at 84 eV^[249]. For analysis of stoichiometry, the atomic area intensities were normalized by the 'corrected RSF' (relative sensitivity factor) provided by the manufacturer.

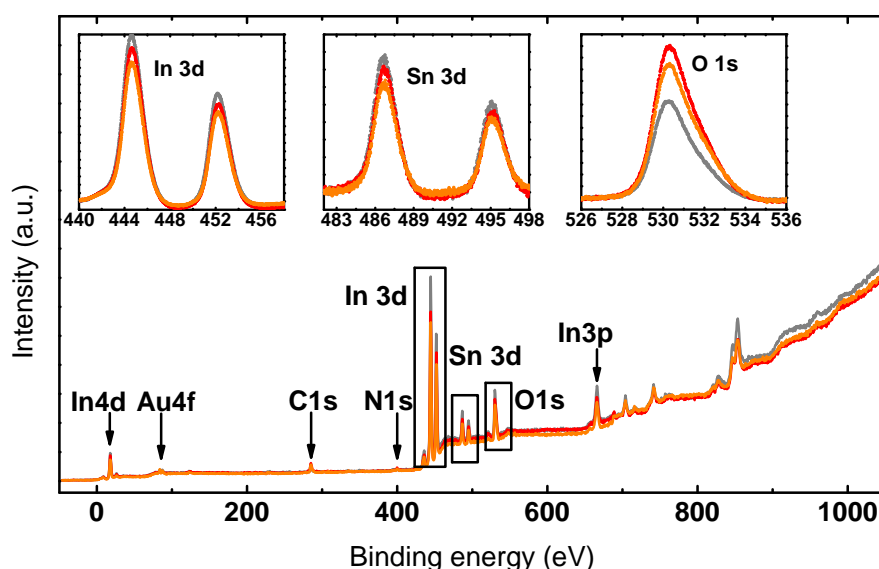


Figure 9.15: Chapter 5: XPS survey of *meso*-ITO unmodified (grey), modified with **4** before electrochemical treatment (red) and after CV measurements and CA in WOC (orange). The inset correspond to the substrate specific In 3d, Sn 3d and O 1s spectra. Energy calibration was done with respect to the Au 4f spectra of the sputtered Au holder.

Procedure for Chapter 6: The elemental composition of the prepared hybrid electrodes consisting of $[L^{(POOOH)}Ru_2(CO_3H)(py)_4]$ **3** on *meso*-ITO was evaluated prior and after electrochemical treatment.

In the electrochemical treatment, the ITO|*meso*-ITO|**3** was implemented in a three-electrode setup as WE with CE: Pt and ref. MSE in pH 1 (0.1 M triflic acid). In a chronoamperometry experiment a potential of 1.813 V vs. RHE was applied for 600 sec., afterwards the sample was rinsed with water. The elemental composition was determined using X-ray photoemission spectroscopy (XPS) using a monochromatic Mg K_{α} X-ray source (1253.6 eV) and an Omicron EA 125 analyzer. The binding energy scale was calibrated using In 3d 5/2 at a binding

energy of 444.2 eV^[283]. The stoichiometry as parameter for the chemical stability was calculated using the atomic area intensities normalized by the 'corrected RSF' provided by the manufacturer and the casaXPS software.

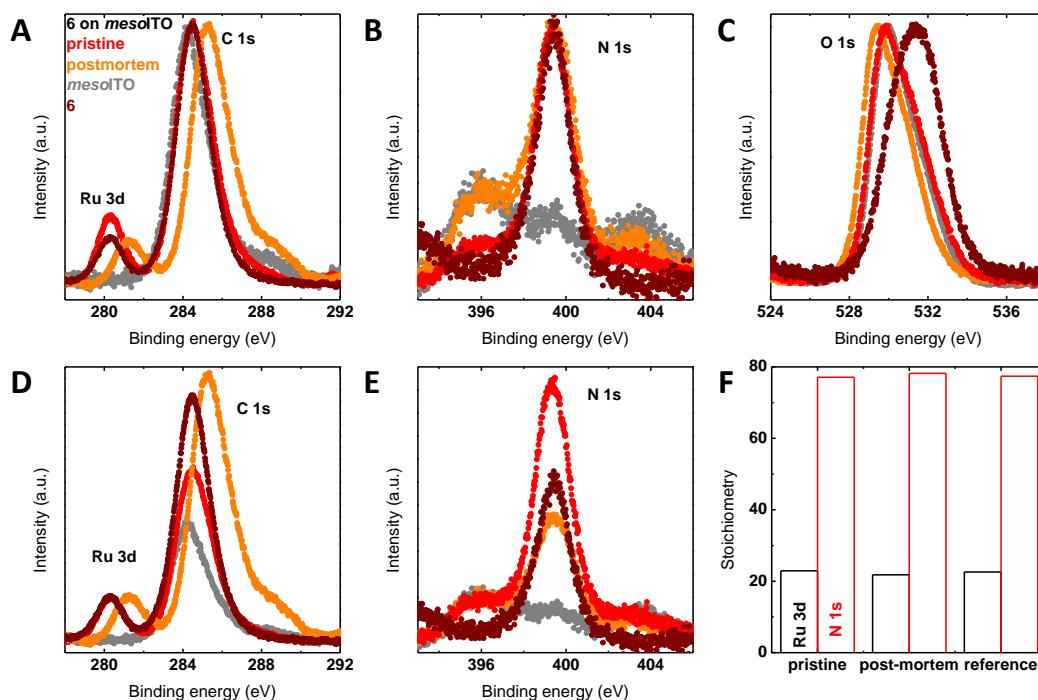


Figure 9.16: Chapter 6: High resolution XPS spectra referenced to the In 3d states at 444.2 eV: (A) C 1s and Ru 3d spectra normalized on the intensity of the C 1s peak; (B) N 1s with the intensity normalized on the main peak; (C) O 1s with the intensity normalized; (D) C 1s and Ru 3d spectra normalized on the intensity of the Ru 3d peak; (E) N 1s with the intensity normalized on the pre-peak; The color code is identical for all high resolution spectra and refers to a unmodified ITO electrode (grey), a dropcast of $[L^{(POOH)}Ru_2(CO_3H)(py)_4]_3$ on a sputtered Au-holder, a ITO|*meso*-ITO|₃ electrode pristine (red) and after CA at 1.813 V vs. RHE (orange). (F) The stoichiometry was determined based on the N 1s:Ru 3d ratio by the relative sensitivity factors.

9.2.3 X-ray Absorption Spectroscopy:

In chapter 6 X-ray absorption at the P-K edge was collected in fluorescence yield mode using a 4-element Vortex SDD detector in a helium atmosphere at the 9-BM-B beamline station (Advanced Photon Source). A double monochromator (Si-111) was used to scan the energy axis, which was calibrated by setting the first inflection point in the spectra of P₂O₅ to 2149 eV. All spectra were normalized by the incident beam intensity obtained from an ionization chamber. Further

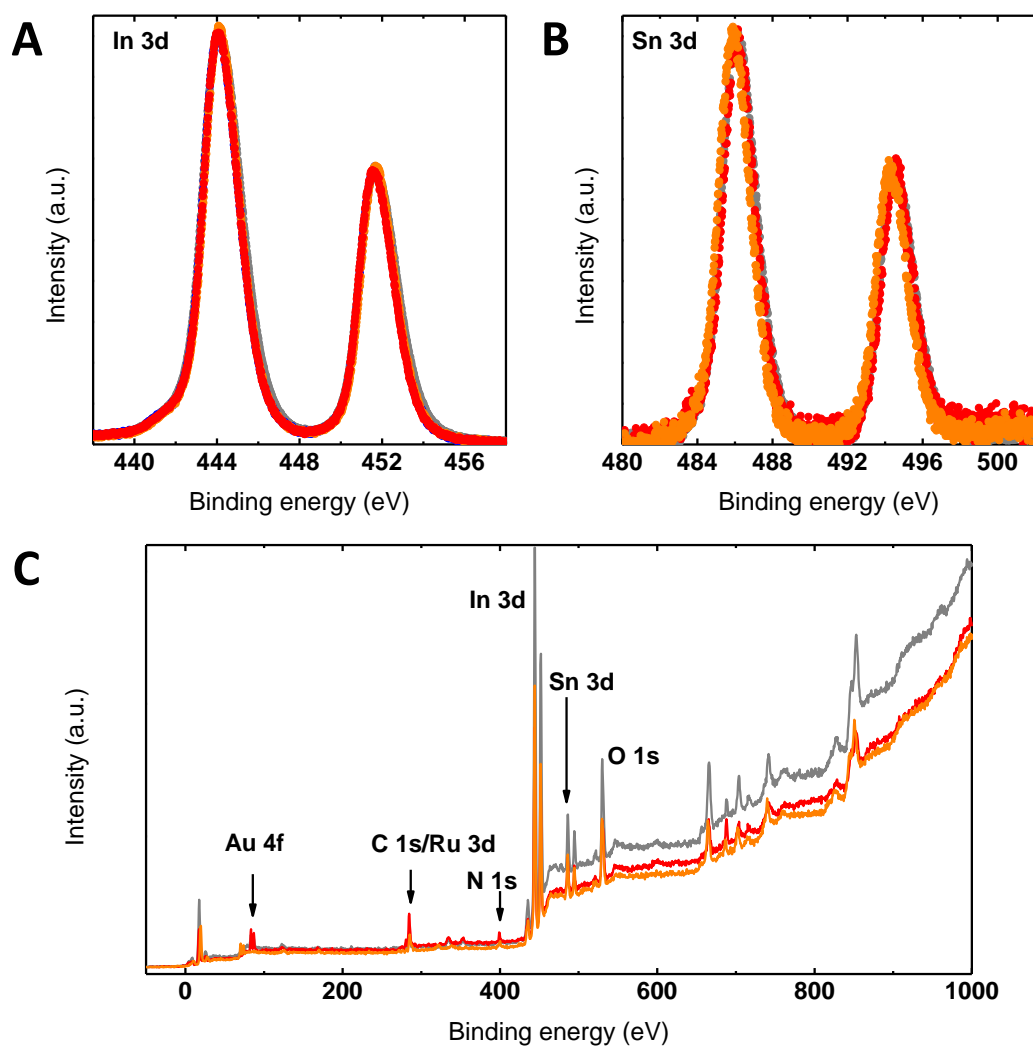


Figure 9.17: Chapter 6: High resolution XPS spectra referenced to the In 3d states at 444.2 eV: (A) In 3d spectra normalized on the intensity of the first peak; (B) Sn 3d with the intensity normalized on the first peak. The color code is identical to the previous XPS spectra and identical for all panels. (C) Survey scan showing only the peaks corresponding to the ITO electrode and the complex indicated by the arrows.

normalization included fitting of a straight line to the pre-edge region and subtraction thereof over the whole scan range. The average intensity between 2175 and 2177 was subset to unity for P-K spectra. Three XAS measurement were averaged for as-prepared GC|*meso*-ITO|**3** and two measurements for all other samples to exclude beam drifts at the P-K edge and photo-damage.

9.2.4 Atomic force microscopy:

In chapter 5 the surface morphology after modification of lanthanum strontium manganite ($\text{La}_{0.6}\text{Sr}_{0.4}\text{MnO}_3$, LSMO) with **4** was characterized by atomic force microscopy (AFM) using a MFP-3D Classic (ASYLUM RESEARCH) in tapping mode. Image analysis was performed using Gwyddion software^[148].

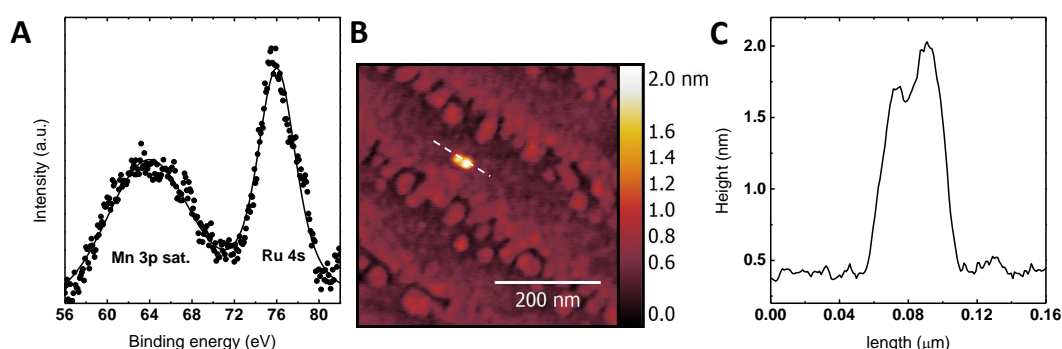


Figure 9.18: Chapter 5: (A) High resolution XPS spectrum of **4** immobilized on $\text{La}_{0.6}\text{Sr}_{0.4}\text{MnO}_3$ (LSMO) prepared by identical methods as presented for *meso*-ITO. (B) AFM image of LSMO modified by solution growth of **4**. (C) Height profile along the line indicated by the dashed line in (B). The height corresponds to the crystallographically determined height of **4**.

9.3 Discussion

Electrochemical Measurements and data

Dependence of the peak current I_p on the scan rate^[51]

(i) for homogeneous measurements:

$$I_p = 0.4463 \left(\frac{F^3}{RT} \right)^{1/2} n^{2/3} A D_0^{1/2} c_0^* \nu^{1/2} \quad (9.1)$$

(ii) for heterogeneous measurements:

$$I_p = \frac{n^2 F^2}{4RT} \nu A \Gamma_0^* \quad (9.2)$$

F: Faraday coefficient, R: universal gas constant, T: temperature, n: number of transferred electrons, A: surface of the electrode, D_0 : diffusion coefficient, c_0^* bulk concentration of complex, ν scan rate, Γ_0^* surface excess of complex at equilibrium.

Oxygen reduction on Pt-ring electrode

The ratio between disk and ring currents can be translated to the faradic efficiency using the following formula:

$$\varepsilon = \frac{I_{ring}/n_{ring}}{I_{disk}/n_{disk}N} = \frac{4I_{ring}}{n_{ring}I_{disk}N} \quad (9.3)$$

This assumes that the number of electrons being transferred on the disk (n_{disk}) corresponds to the four electron process of the OER. The collection efficiency N can either be calculated using the geometrical dimensions of the setup or measured using the ferri-/ferrocyanide redoxreaction. The number of transferred electrons on the ring electrode (n_{ring}) depends on the underlying mechanism for the ORR occurring at the ring. It can easily be determined measuring the ORR for the given ring electrode and calculating the number of electrons at the given

potential by the Levich equation^[51]:

$$I_L = 0.62n_{app}F\pi(r_2^3 - r_1^3)^{2/3}D^{2/3}\omega^{1/2}\nu^{-1/6}c_{O_2} \quad (9.4)$$

Where I_L is the measured plateau current, $F = 96,485.33 \text{ C/mol}$ is the Faraday constant, $r_2 = 6 \text{ mm}$ is the outer ring radius, $r_1 = 3.5 \text{ mm}$ the inner ring radius, $c_{O_2} = 0.63 \times 10^{-6} \text{ mol/cm}^3$ is the concentration of dissolved O_2 in 1 M triflic^[284], $D = 9.67 \times 10^{-6} \text{ cm}^2/\text{s}$ the diffusion coefficient of O_2 in 1 M triflic^[284], $\nu = 0.917 \times 10^{-2} \text{ cm}^2\text{s}^{-1}$ is the kinematic viscosity of O_2 in 1 M triflic^[284] and ω is the rotation speed. The measured ORR data for the present setup can be seen in Figure 9.10.

It should be stressed that the differences in the oxygen reduction is dependent on electrode assembly and preparation of the Pt surfaces in advance to the measurements. The diffusion rate will strongly differ from the smooth surfaces such as the polished Pt electrode for the dense particle layer of the prepared *meso*-ITO electrodes. The resulting delay is clearly visible in slowly increasing ring currents during application of potential on the disk electrode and slow decrease after the potential step.

Effect of changing oxygen partial pressure

To consider the effect of increasing oxygen partial pressure the effect on the applied potential has been calculated by the Nernstian equation:

$$E = E_0 + \frac{0.059V}{n} \log Q \text{ with } Q = \frac{p_{O_2}[H^+]^4}{[H_2O]^2} \quad (9.5)$$

For the water oxidation in triflic the concentration of water and the change in pH can be neglected, and the number of electrons per oxygen molecule is known so that the relative change assigned to the oxygen concentration is:

$$\Delta E = \frac{0.059V}{4} \log p_{O_2} \quad (9.6)$$

The concentration for oxygen saturated 1 M triflic is $p_{O_2} = 0.63 \times 10^{-6} \text{ mol/cm}^3$ ^[285], resulting in an effective decrease in the applied potential by $\Delta E = -0.091 \text{ V}$.

Evaluation of saturation time

Calculation of time for oxygen saturation in the diffusion layer during OER at 1.94 V vs. RHE: The diffusion layer thickness is defined as:

$$\delta_L = 1.61 D_{O_2}^{1/3} \gamma^{1/3} \omega^{-1/2} \quad (9.7)$$

With the diffusion constant of oxygen in 1 M triflic $D_{O_2} = 9.67 \times 10^{-6} \text{ cm}^2/\text{s}$, the kinematic viscosity for oxygen in 1 M triflic $\gamma = 0.917 \times 10^{-2} \text{ cm}^2/\text{s}$ ^[267], and the angular rotation rate. For the applied rotation rate of 1600 rpm the diffusion layer thickness would be $\delta_L = 12.1 \text{ }\mu\text{m}$, hence resulting in a volume of the diffusion layer in the area of the disk ($r=2 \text{ mm}$) of $V = \pi r^2 \delta_L = 1.523 \times 10^{-4} \text{ cm}^3$. Note that due to the porous layer of *meso*-ITO we assume that the particle layer is not affected by the rotation rate thereby increasing the diffusion layer by the particle layer thickness.

One now can calculate the time needed to saturate the volume of the diffusion layer above the disk using Faraday's law under the assumption that the current from electrolysis corresponds solely to the formation of O_2 and the current difference between hybrid and background currents of the blank ITO remains constant at the value observed for the value after 10 seconds:

$$n = \frac{Q}{Fz} = \frac{It}{Fz} = n_{O_2} = c_{O_2} V \quad (9.8)$$

With Faraday constant $F=96,485.33 \text{ C/mol}$, the current difference after 10 seconds (Figure 5.8) $I = 10 \text{ }\mu\text{A}$, the charge corresponding to the formation of O_2 $z=4$, and the saturation concentration of oxygen in 1 M triflic $c_{O_2} = 0.63 \times 10^{-6} \text{ mol/cm}^3$ ^[243]. By transforming the equation the time needed to saturate the diffusion layer with oxygen therefore results as $t = 1.85 \text{ s}$.

Table 9.3: Literature known WOCs compared with the experimental conditions and the turnover frequency (TOF) at an overpotential η . In addition the applied methods used to evaluate the immobilized complexes and methods for postmortem stability analysis are indicated. Due to different configurations of the working electrodes the overpotential was not given for specific current densities but the TOF determined per complex.

η (mV)	TOF(1/s)	Conditions	Characterization, post-mortem Investigations	Ref.
479	0.06	0.1 M HNO ₃ <i>nano</i> ITO on GC disk	advanced RRD experiments, CV on surface, postmortem investigation with cyclic voltammetry	[110]
479	0.18	0.1 M HNO ₃ <i>nano</i> ITO on GC disk	advanced RRD experiments, CV on surface, postmortem investigation with cyclic voltammetry	[110]
429	0.35	0.1 M HClO ₄ on FTO and <i>nano</i> ITO on GC disk	CV on surface, RRD experiments, Pourbaix diagram on surface, no postmortem investigation	[243]
629	0.3	0.1 M HNO ₃ on ITO	CV in solution and on surface, Pourbaix, fluorescence-based O ₂ detection YSI ProODO, no postmortem investigations	[267]

* TOF reaches maximum and decreases if scanned to higher potential

10 Appendix C

The following supporting information shows the first results for optical pump-probe experiments of Jennifer Ahrens on $\text{La}_{0.6}\text{Sr}_{0.4}\text{MnO}_3$ (LSMO). Detailed analysis and discussion will be the scope of future work and is therefore not included.

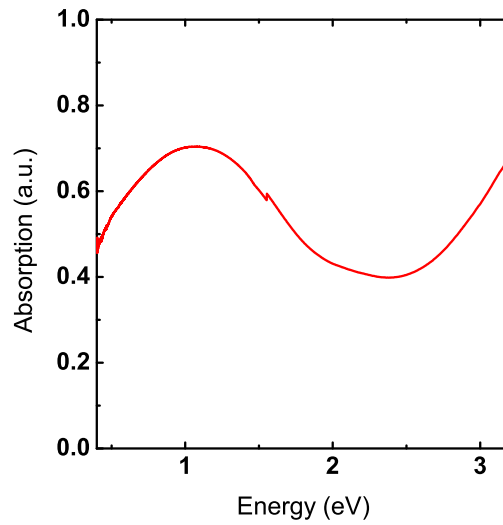


Figure 10.1: Stationary absorption spectra on 80 nm $\text{La}_{0.6}\text{Sr}_{0.4}\text{MnO}_3$ (LSMO) sample on SrTiO_3 (STO). Due to the bandgap of 3.2 eV of the STO, the absorption for energies > 3.2 eV could not be evaluated. The spectra were measured in transmission on a Cary Varian 5e spectrometer with unpolarized light in a wavelength range of 250-3300 nm at room temperature.

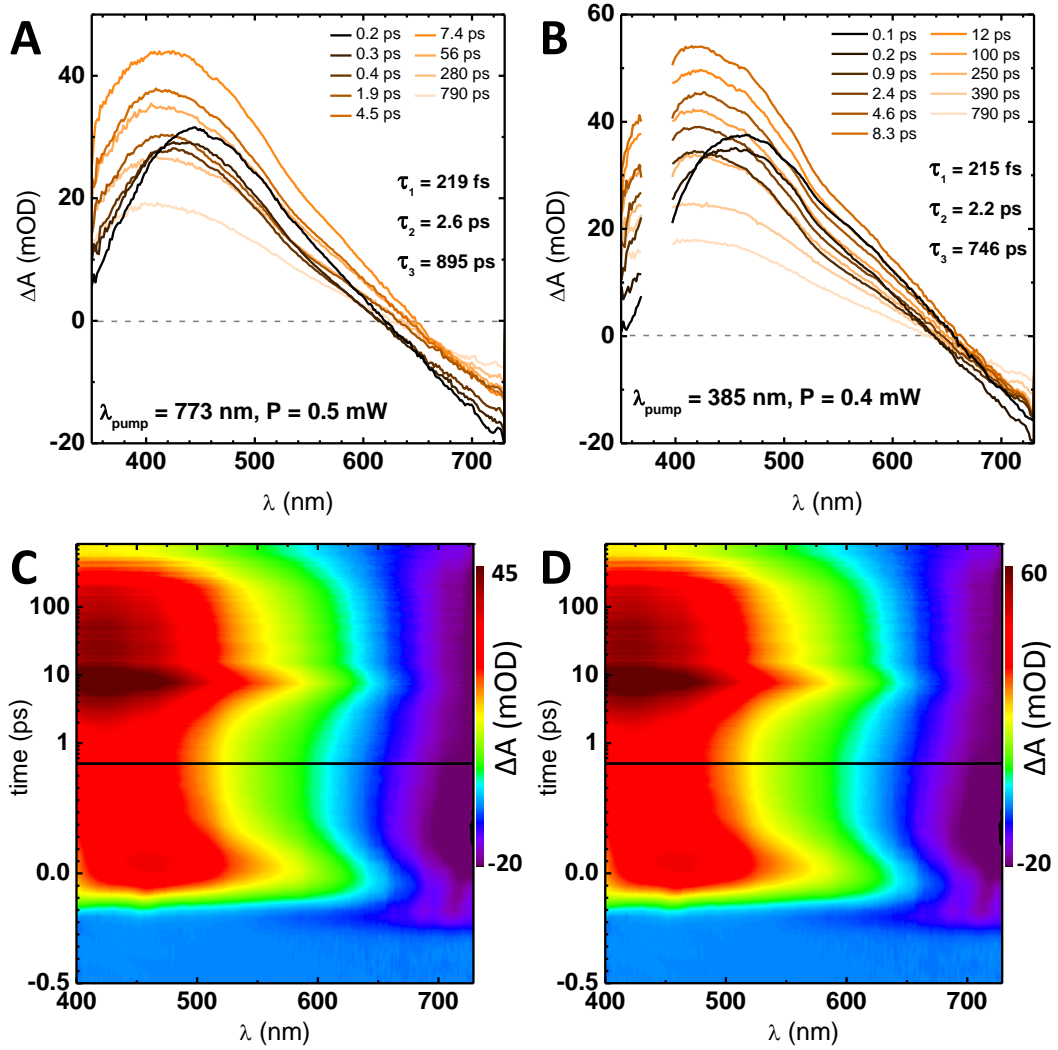


Figure 10.2: Transient absorption spectra for 40 nm LSMO film on MgO. The excitation energy was $\lambda=773$ nm with $P=0.5$ mW for (A) and $\lambda=385$ nm with $P=0.4$ mW for (B) with a half width of the pulses of 150 fs. Note that the half width of the pump pulse might be affected by small deviations in the experimental setup. The excitation energies were chosen according to the absorption features of LSMO (see Figure 10.1). The used pump power was set low to avoid radiation damage and multiple photon processes. At both excitation energies two processes can be observed: After primary excitation an excited state at ~ 465 eV develops, that transforms into a second species at ~ 415 eV as can be seen by the presence of the isosbestic points. The fitted time constant correspond to the initial rise of the first excited state τ_1 , the transformation to the second stated τ_2 , and the life time of the second state τ_3 . The first short lived excited state, followed by a fast charge transfer process to a long lived state can be observed for both pump pulse excitation wavelengths at $\lambda=773$ nm (C) and $\lambda=385$ nm (D). Note that the given values for the time constants depend on the half width of the pump pulse causing an experimental uncertainty of 150 fs for all calculated values. The measurements and their analysis were performed by Jennifer Ahrens in the group of Dirk Schwarzer at the Max-Planck Institute for biophysical chemistry Göttingen.

Bibliography

- [1] Ciamician, G. *Science* **1912**, 36, 385–394.
- [2] Galán-Mascarós, J. R. *ChemElectroChem* **2015**, 2, 37–50.
- [3] Hong, W. T.; Risch, M.; Stoerzinger, K. A.; Grimaud, A.; Suntivich, J.; Shao-Horn, Y. *Energy Environ. Sci.* **2015**, 8, 1404–1427.
- [4] Wiechen, M.; Berends, H.-M.; Kurz, P. *Dalton Trans.* **2012**, 41, 21–31.
- [5] Nocera, D. G. *Accounts of Chemical Research* **2012**, 45, 767–776.
- [6] Concepcion, J. J.; Jurss, J. W.; Brennaman, M. K.; Hoertz, P. G.; Patrocínio, A. O. T.; Murakami Iha, N. Y.; Templeton, J. L.; Meyer, T. J. *Accounts of Chemical Research* **2009**, 42, 1954–1965.
- [7] Umena, Y.; Kawakami, K.; Shen, J.-R.; Kamiya, N. *Nature* **2011**, 473, 55–60.
- [8] Grätzel, M. *Nature* **2001**, 414, 338–44.
- [9] Raiser, D.; Mildner, S.; Ifland, B.; Sotoudeh, M.; Blöchl, P.; Techert, S.; Jooss, C. *Advanced Energy Materials* **2017**, 1602174.
- [10] Joya, K. S.; de Groot, H. J. M. *ChemSusChem* **2014**, 7, 73–76.
- [11] Gust, D.; Moore, T. A.; Moore, A. L. *Accounts of Chemical Research* **2009**, 42, 1890–1898.
- [12] Van de Krol, R.; Grätzel, M. *Photoelectrochemical hydrogen production*; Springer, 2012; Vol. 90.
- [13] Frischmann, P. D.; Mahata, K.; Würthner, F. *Chem. Soc. Rev.* **2013**, 42, 1847–1870.
- [14] Xagas, A.; Bernard, M.; Hugot-Le Goff, A.; Spyrellis, N.; Loizos, Z.; Falaras, P. *Journal of Photochemistry and Photobiology A: Chemistry* **2000**, 132, 115–120.
- [15] Concepcion, J. J.; Jurss, J. W.; Brennaman, M. K.; Hoertz, P. G.; Patrocínio, A. O. T.; Murakami Iha, N. Y.; Templeton, J. L.; Meyer, T. J. *Accounts of Chemical Research* **2009**, 42, 1954–1965.
- [16] Fujishima, A. *Nature* **1972**, 238, 37–38.

-
- [17] Abdi, F. F.; Han, L.; Smets, A. H. M.; Zeman, M.; Dam, B.; van de Krol, R. *Nature Communications* **2013**, *4*, 1–7.
- [18] Ni, M.; Leung, M. K.; Leung, D. Y.; Sumathy, K. *Renewable and Sustainable Energy Reviews* **2007**, *11*, 401–425.
- [19] Maeda, K.; Domen, K. *The Journal of Physical Chemistry Letters* **2010**, *1*, 2655–2661.
- [20] Sivula, K.; Formal, F. L.; Grätzel, M. *Chemistry of Materials* **2009**, *21*, 2862–2867.
- [21] Berardi, S.; Francàs, L.; Neudeck, S.; Maji, S.; Benet-Buchholz, J.; Meyer, F.; Llobet, A. *ChemSusChem* **2015**, *8*, 3688–3696.
- [22] Berardi, S.; Drouet, S.; Francàs, L.; Gimbert-Suriñach, C.; Guttentag, M.; Richmond, C.; Stoll, T.; Llobet, A. *Chem. Soc. Rev.* **2014**, *43*, 7501–7519.
- [23] Lauinger, S. M.; Sumliner, J. M.; Yin, Q.; Xu, Z.; Liang, G.; Glass, E. N.; Lian, T.; Hill, C. L. *Chemistry of Materials* **2015**, *27*, 5886–5891.
- [24] Youngblood, W. J.; Lee, S.-H. A.; Maeda, K.; Mallouk, T. E. *Accounts of chemical research* **2009**, *42*, 1966–1973.
- [25] Ashford, D. L.; Song, W.; Concepcion, J. J.; Glasson, C. R.; Brennaman, M. K.; Norris, M. R.; Fang, Z.; Templeton, J. L.; Meyer, T. J. *Journal of the American Chemical Society* **2012**, *134*, 19189–19198.
- [26] Gersten, S. W.; Samuels, G. J.; Meyer, T. J. *Journal of the American Chemical Society* **1982**, *104*, 4029–4030.
- [27] Matheu, R.; Ertem, M. Z.; Benet-Buchholz, J.; Coronado, E.; Batista, V. S.; Sala, X.; Llobet, A. *Journal of the American Chemical Society* **2015**, *137*.
- [28] Wang, L.; Duan, L.; Wang, Y.; Ahlquist, M. S. G.; Sun, L. *Chem. Commun.* **2014**, *50*, 12947–12950.
- [29] Hong, W. T.; Stoerzinger, K. a.; Moritz, B.; Devereaux, T. P.; Yang, W.; Shao-Horn, Y. *The Journal of Physical Chemistry C* **2015**, *119*, 2063–2072.
- [30] Jung, J. H.; Kim, K. H.; Noh, T. W.; Choi, E. J.; Yu, J. *Phys. Rev. B* **1998**, *57*, R11043–R11046.

- [31] Quijada, M.; Černe, J.; Simpson, J.; Drew, H.; Ahn, K.; Millis, A.; Shree-kala, R.; Ramesh, R.; Rajeswari, M.; Venkatesan, T. *Physical Review B* **1998**, 58, 16093.
- [32] Mildner, S.; Hoffmann, J.; Blöchl, P. E.; Techert, S.; Jooss, C. *Physical Review B* **2015**, 92, 035145.
- [33] Moritomo, Y.; Machida, A.; Matsuda, K.; Ichida, M.; Nakamura, A. *Physical Review B* **1997**, 56, 5088–5091.
- [34] Neudeck, S.; Maji, S.; López, I.; Meyer, S.; Meyer, F.; Llobet, A. *Journal of the American Chemical Society* **2014**, 136, 24–27.
- [35] Neudeck, S.; Maji, S.; López, I.; Dechert, S.; Benet-Buchholz, J.; Llobet, A.; Meyer, F. *Inorganic Chemistry* **2016**, 55, 2508–2521.
- [36] Neudeck, S. Establishing Dinuclear Ruthenium Complexes Based on the Bis (bipyridyl) pyrazolate Ligand System for Catalytic Water Catalytic Activity and Mechanistic Investigations Oxidation: Synthetic Access. Ph.D. thesis, Georg-August-University Göttingen, 2016.
- [37] Matheu, R.; Neudeck, S.; Meyer, F.; Sala, X.; Llobet, A. *ChemSusChem* **2016**, 9, 3361–3369.
- [38] Rincón, R. A.; Ventosa, E.; Tietz, F.; Masa, J.; Seisel, S.; Kuznetsov, V.; Schuhmann, W. *ChemPhysChem* **2014**, 15, 2810–2816.
- [39] Bockris, J. O.; Otagawa, T. *The Journal of Physical Chemistry* **1983**, 87, 2960–2971.
- [40] McCrory, C. C. L.; Jung, S.; Peters, J. C.; Jaramillo, T. F. *Journal of the American Chemical Society* **2013**, 135, 16977–16987.
- [41] Suntivich, J.; May, K. J.; Gasteiger, H. A.; Goodenough, J. B.; Shao-Horn, Y. *Science* **2011**, 334, 1383–1385.
- [42] Matsumoto, Y.; Sato, E. *Materials Chemistry and Physics* **1986**, 14, 397–426.
- [43] Coehn, A.; Gläser, M. *Zeitschrift für anorganische und allgemeine Chemie* **1902**, 33, 9–24.
- [44] Matsumoto, Y.; Sato, E. *Electrochimica Acta* **1979**, 24, 421–423.

-
- [45] Trasatti, S. *Electrochimica Acta* **1984**, 29, 1503–1512.
- [46] Bockris, J. O.; Otagawa, T. *Journal of The Electrochemical Society* **1984**, 131, 290.
- [47] Ramadass, N. *Materials Science and Engineering* **1978**, 36, 231–239.
- [48] Bockris, J. O. *The Journal of Chemical Physics* **1956**, 24, 817.
- [49] Doyle, R. L.; Godwin, I. J.; Brandon, M. P.; Lyons, M. E. G. *Physical Chemistry Chemical Physics* **2013**, 15, 13737.
- [50] Fletcher, S. *Journal of Solid State Electrochemistry* **2009**, 13, 537–549.
- [51] Bard, A. J.; Faulkner, L. R. *Electrochemical Methods: Fundamentals and Applications*; Wiley, 2000; Vol. 6.
- [52] Man, I. C.; Su, H.-Y.; Calle-Vallejo, F.; Hansen, H. A.; Martínez, J. I.; Inoglu, N. G.; Kitchin, J.; Jaramillo, T. F.; Nørskov, J. K.; Rossmeisl, J. *ChemCatChem* **2011**, 3, 1159–1165.
- [53] Sabatier, P. *Catalysis in Organic Chemistry (translated by Reidl. EE)*, Van Nostrand: Princeton, NJ **1913**, 923.
- [54] Koper, M. T. *Journal of Electroanalytical Chemistry* **2011**, 660, 254–260.
- [55] Rossmeisl, J.; Logadottir, A.; Nørskov, J. *Chemical Physics* **2005**, 319, 178–184.
- [56] Mefford, J. T.; Rong, X.; Abakumov, A. M.; Hardin, W. G.; Dai, S.; Kolpak, A. M.; Johnston, K. P.; Stevenson, K. J. *Nature Communications* **2016**, 7, 11053.
- [57] Rong, X.; Kolpak, A. M. *Journal of Physical Chemistry Letters* **2015**, 6, 1785–1789.
- [58] Rong, X.; Parolin, J.; Kolpak, A. M. *ACS Catalysis* **2016**, 6, 1153–1158.
- [59] Grimaud, A.; Hong, W. T.; Shao-Horn, Y.; Tarascon, J.-M. *Nature Materials* **2016**, 15, 121–126.
- [60] Grimaud, A.; Diaz-Morales, O.; Han, B.; Hong, W. T.; Lee, Y.-L.; Giordano, L.; Stoerzinger, K. A.; Koper, M. T. M.; Shao-Horn, Y. *Nature Chemistry* **2017**, 9, 111–115.

- [61] Mierwaldt, D.; Mildner, S.; Arrigo, R.; Knop-Gericke, A.; Franke, E.; Blumenstein, A.; Hoffmann, J.; Jooss, C. *Catalysts* **2014**, *4*, 129–145.
- [62] Mildner, S.; Beleggia, M.; Mierwaldt, D.; Hansen, T. W.; Wagner, J. B.; Yazdi, S.; Kasama, T.; Ciston, J.; Zhu, Y.; Jooss, C. *The Journal of Physical Chemistry C* **2015**, *119*, 5301–5310.
- [63] Raabe, S.; Mierwaldt, D.; Ciston, J.; Uijtewaal, M.; Stein, H.; Hoffmann, J.; Zhu, Y.; Blöchl, P.; Jooss, C. *Advanced Functional Materials* **2012**, *22*, 3378–3388.
- [64] May, K.; Carlton, C.; Stoerzinger, K. a.; Risch, M.; Suntivich, J.; Lee, Y.-l.; Grimaud, A.; Shao-Horn, Y. *Journal of Physical Chemistry Letters* **2012**, *3*, 3264–3270.
- [65] Grimaud, A.; Carlton, C. E.; Risch, M.; Hong, W. T.; May, K. J.; Shao-Horn, Y. *The Journal of Physical Chemistry C* **2013**, *117*, 25926–25932.
- [66] Lee, Y.-L.; Kleis, J.; Rossmeisl, J.; Morgan, D. *Physical Review B* **2009**, *80*, 224101.
- [67] Ebrahimizadeh Abrishami, M.; Risch, M.; Scholz, J.; Roddatis, V.; Osterthun, N.; Jooss, C. *Materials* **2016**, *9*, 921.
- [68] Hong, W. T.; Welsch, R. E.; Shao-Horn, Y. *The Journal of Physical Chemistry C* **2016**, *120*, 78–86.
- [69] Sotoudeh, M.; Rajpurohit, S.; Blöchl, P.; Mierwaldt, D.; Norpoth, J.; Roddatis, V.; Mildner, S.; Kressdorf, B.; Ifland, B.; Jooss, C. **2016**, 1–26.
- [70] Lazzeri, M.; Selloni, A. *Physical Review Letters* **2001**, *87*, 266105.
- [71] Pentcheva, R.; Wendler, F.; Meyerheim, H. L.; Moritz, W.; Jedrecy, N.; Scheffler, M. *Physical Review Letters* **2005**, *94*, 126101.
- [72] McCrory, C. C. L.; Jung, S.; Ferrer, I. M.; Chatman, S. M.; Peters, J. C.; Jaramillo, T. F. *Journal of the American Chemical Society* **2015**, *137*, 4347–4357.
- [73] Su, H.-y.; Gorlin, Y.; Man, I. C.; Calle-Vallejo, F.; Nørskov, J. K.; Jaramillo, T. F.; Rossmeisl, J. *Physical Chemistry Chemical Physics* **2012**, *14*, 14010.

- [74] Han, B.; Risch, M.; Lee, Y.-L.; Ling, C.; Jia, H.; Shao-Horn, Y. *Phys. Chem. Chem. Phys.* **2015**, *17*, 22576–22580.
- [75] Burke, L. D.; Murphy, O. J.; O'Neill, J. F.; Venkatesan, S. *Journal of the Chemical Society, Faraday Transactions 1: Physical Chemistry in Condensed Phases* **1977**, *73*, 1659.
- [76] Frydendal, R.; Paoli, E. A.; Knudsen, B. P.; Wickman, B.; Malacrida, P.; Stephens, I. E. L.; Chorkendorff, I. *ChemElectroChem* **2014**, *1*, 2075–2081.
- [77] Burke, M. S.; Zou, S.; Enman, L. J.; Kellon, J. E.; Gabor, C. A.; Pledger, E.; Boettcher, S. W. *The Journal of Physical Chemistry Letters* **2015**, *6*, 3737–3742.
- [78] Chang, S. H.; Danilovic, N.; Chang, K.-c.; Subbaraman, R.; Paulikas, A. P.; Fong, D. D.; Highland, M. J.; Baldo, P. M.; Stamenkovic, V. R.; Freeland, J. W.; Eastman, J. A.; Markovic, N. M. *Nature Communications* **2014**, *5*, 1–9.
- [79] Pourbaix, M. *Atlas of electrochemical equilibria in aqueous solutions*, 2nd ed.; National Association of Corrosion Engineers, 1974.
- [80] Lopes, P. P.; Strmcnik, D.; Tripkovic, D.; Connell, J. G.; Stamenkovic, V.; Markovic, N. M. *ACS Catalysis* **2016**, *6*, 2536–2544.
- [81] Danilovic, N.; Subbaraman, R.; Chang, K.-C.; Chang, S. H.; Kang, Y. J.; Snyder, J.; Paulikas, A. P.; Strmcnik, D.; Kim, Y.-T.; Myers, D.; Stamenkovic, V. R.; Markovic, N. M. *The Journal of Physical Chemistry Letters* **2014**, *5*, 2474–2478.
- [82] Barbier, A.; Renaud, G.; Stierle, A. *Surface Science* **1998**, *402-404*, 757–760.
- [83] Kitakatsu, N.; Maurice, V.; Marcus, P. *Surface Science* **1998**, *411*, 215–230.
- [84] Aruta, C.; Minola, M.; Galdi, A.; Ciancio, R.; Petrov, A. Y.; Brookes, N.; Ghiringhelli, G.; Maritato, L.; Orgiani, P. *Physical Review B* **2012**, *86*, 115132.
- [85] Marozau, I.; Das, P. T.; Döbeli, M.; Storey, J. G.; Uribe-Laverde, M. a.; Das, S.; Wang, C.; Rössle, M.; Bernhard, C. *Physical Review B* **2014**, *89*, 174422.
- [86] Töpfer, J.; Goodenough, J. *Journal of Solid State Chemistry* **1997**, *130*, 117–128.

- [87] Kobayashi, S.; Tokuda, Y.; Ohnishi, T.; Mizoguchi, T.; Shibata, N.; Sato, Y.; Ikuhara, Y.; Yamamoto, T. *Journal of Materials Science* **2011**, *46*, 4354–4360.
- [88] Benck, J. D.; Pinaud, B. A.; Gorlin, Y.; Jaramillo, T. F. *PLoS ONE* **2014**, *9*, e107942.
- [89] Michaelos, T. K.; Shopov, D. Y.; Sinha, S. B.; Sharninghausen, L. S.; Fisher, K. J.; Lant, H. M.; Crabtree, R. H.; Brudvig, G. W. *Accounts of Chemical Research* **2017**,
- [90] Matheu, R.; Francàs, L.; Chernev, P.; Ertem, M. Z.; Batista, V.; Haumann, M.; Sala, X.; Llobet, A. *ACS Catalysis* **2015**, *5*, 3422–3429.
- [91] Blakemore, J. D.; Schley, N. D.; Olack, G. W.; Incarvito, C. D.; Brudvig, G. W.; Crabtree, R. H. *Chem. Sci.* **2011**, *2*, 94–98.
- [92] Hintermair, U.; Hashmi, S. M.; Elimelech, M.; Crabtree, R. H. *Journal of the American Chemical Society* **2012**, *134*, 9785–9795.
- [93] Trasatti, S. *Journal of Electroanalytical Chemistry and Interfacial Electrochemistry* **1980**, *111*, 125–131.
- [94] Lee, Y.; Suntivich, J.; May, K. J.; Perry, E. E.; Shao-Horn, Y. *The Journal of Physical Chemistry Letters* **2012**, *3*, 399–404.
- [95] Stoerzinger, K. A.; Qiao, L.; Biegalski, M. D.; Shao-Horn, Y. *The Journal of Physical Chemistry Letters* **2014**, *5*, 1636–1641.
- [96] Kügler, M.; Scholz, J.; Kronz, A.; Siewert, I. *Dalton Trans.* **2016**, *45*, 6974–6982.
- [97] Wu, X.; Li, F.; Zhang, B.; Sun, L. *Journal of Photochemistry and Photobiology C: Photochemistry Reviews* **2015**, *25*, 71–89.
- [98] Duan, L.; Bozoglian, F.; Mandal, S.; Stewart, B.; Privalov, T.; Llobet, A.; Sun, L. *Nature Chemistry* **2012**, *4*, 418–423.
- [99] Ishii, H.; Sugiyama, K.; Ito, E.; Seki, K. *Advanced Materials* **1999**, *11*, 605–625.
- [100] Greiner, M. T.; Helander, M. G.; Tang, W.-M.; Wang, Z.-B.; Qiu, J.; Lu, Z.-H. *Nature Materials* **2011**, *11*, 76–81.

- [101] Ley, L.; Smets, Y.; Pakes, C. I.; Ristein, J. *Advanced Functional Materials* **2013**, *23*, 794–805.
- [102] Pujari, S. P.; Scheres, L.; Marcelis, A. T. M.; Zuilhof, H. *Angewandte Chemie* **2014**, *126*, 6438–6474.
- [103] Petit, M.; Janvier, P.; Knight, D. A.; Bujoli, B. *Chemical Reviews* **2012**, *112*, 3777–3807.
- [104] Muresan, N. M.; Willkomm, J.; Mersch, D.; Vaynzof, Y.; Reisner, E. *Angewandte Chemie International Edition* **2012**, *51*, 12749–12753.
- [105] Lakadamyali, F.; Reynal, A.; Kato, M.; Durrant, J. R.; Reisner, E. *Chemistry - A European Journal* **2012**, *18*, 15464–15475.
- [106] Chen, Z.; Concepcion, J. J.; Hull, J. F.; Hoertz, P. G.; Meyer, T. J. *Dalton Transactions* **2010**, *39*, 6950.
- [107] Brewster, T. P.; Konezny, S. J.; Sheehan, S. W.; Martini, L. A.; Schmuttenmaer, C. A.; Batista, V. S.; Crabtree, R. H. *Inorganic Chemistry* **2013**, *52*, 6752–6764.
- [108] Hanson, K.; Brennaman, M. K.; Luo, H.; Glasson, C. R. K.; Concepcion, J. J.; Song, W.; Meyer, T. J. *ACS Applied Materials & Interfaces* **2012**, *4*, 1462–1469.
- [109] Hyde, J. T.; Hanson, K.; Vannucci, A. K.; Lapides, A. M.; Alibabaei, L.; Norris, M. R.; Meyer, T. J.; Harrison, D. P. *ACS Applied Materials & Interfaces* **2015**, *7*, 9554–9562.
- [110] Concepcion, J. J.; Binstead, R. A.; Alibabaei, L.; Meyer, T. J. *Inorganic Chemistry* **2013**, *52*, 10744–10746.
- [111] Park, H.; Bae, E.; Lee, J.-J.; Park, J.; Choi, W. *The Journal of Physical Chemistry B* **2006**, *110*, 8740–8749.
- [112] Young, K. J.; Martini, L. A.; Milot, R. L.; Snoeberger, R. C.; Batista, V. S.; Schmuttenmaer, C. A.; Crabtree, R. H.; Brudvig, G. W. *Coordination Chemistry Reviews* **2012**, *256*, 2503–2520.
- [113] Wee, K.-R.; Brennaman, M. K.; Alibabaei, L.; Farnum, B. H.; Sherman, B.; Lapides, A. M.; Meyer, T. J. *Journal of the American Chemical Society* **2014**, *136*, 13514–13517.

- [114] Vannucci, A. K.; Alibabaei, L.; Losego, M. D.; Concepcion, J. J.; Kalanyan, B.; Parsons, G. N.; Meyer, T. J. *Proceedings of the National Academy of Sciences of the United States of America* **2013**, *110*, 20918–20922.
- [115] Lapides, A. M.; Sherman, B. D.; Brennaman, M. K.; Dares, C. J.; Skinner, K. R.; Templeton, J. L.; Meyer, T. J. *Chem. Sci.* **2015**, *6*, 6398–6406.
- [116] Tong, L.; Göthelid, M.; Sun, L. *Chemical Communications* **2012**, *48*, 10025–10027.
- [117] Chen, H. M.; Chen, C. K.; Liu, R.-S.; Zhang, L.; Zhang, J.; Wilkinson, D. P. *Chemical Society Reviews* **2012**, *41*, 5654.
- [118] Donley, C.; Dunphy, D.; Paine, D.; Carter, C.; Nebesny, K.; Lee, P.; Alloway, D.; Armstrong, N. R. *Langmuir* **2002**, *18*, 450–457.
- [119] Frank, G.; Köstlin, H. *Applied Physics A: Materials Science & Processing* **1982**, *27*, 197–206.
- [120] Nüesch, F.; Forsythe, E.; Le, Q.; Gao, Y.; Rothberg, L. *Journal of Applied Physics* **2000**, *87*, 7973–7980.
- [121] Kim, J.-S.; Cacialli, F.; Friend, R. *Thin Solid Films* **2003**, *445*, 358–366.
- [122] Popovich, N. D.; Yen, B. K.; Wong, S.-S. *Langmuir* **2003**, *19*, 1324–1329.
- [123] Prasittichai, C.; Hupp, J. T. *The Journal of Physical Chemistry Letters* **2010**, *1*, 1611–1615.
- [124] Brewster, T. P.; Konezny, S. J.; Sheehan, S. W.; Martini, L. A.; Schmuttenmaer, C. A.; Batista, V. S.; Crabtree, R. H. *Inorganic Chemistry* **2013**, *52*, 6752–6764.
- [125] Giordano, L.; Han, B.; Risch, M.; Hong, W. T.; Rao, R. R.; Stoerzinger, K. A.; Shao-Horn, Y. *Catalysis Today* **2016**, *262*, 2–10.
- [126] Paoli, E. A.; Masini, F.; Frydendal, R.; Deiana, D.; Schlaup, C.; Malizia, M.; Hansen, T. W.; Horch, S.; Stephens, I. E. L.; Chorkendorff, I. *Chem. Sci.* **2015**, *6*, 190–196.
- [127] Jiráček, Z.; Krupička, S.; Šimša, Z.; Dlouhá, M.; Vratislav, S. *Journal of Magnetism and Magnetic Materials* **1985**, *53*, 153–166.

-
- [128] Raveau, B. *Philosophical Transactions of the Royal Society A: Mathematical, Physical and Engineering Sciences* **2008**, 366, 83–92.
- [129] Dau, H.; Limberg, C.; Reier, T.; Risch, M.; Roggan, S.; Strasser, P. *ChemCatChem* **2010**, 2, 724–761.
- [130] Petrie, J. R.; Jeen, H.; Barron, S. C.; Meyer, T. L.; Lee, H. N. *Journal of the American Chemical Society* **2016**, 138, 7252–7255.
- [131] Risch, M.; Stoerzinger, K. A.; Maruyama, S.; Hong, W. T.; Takeuchi, I.; Shao-Horn, Y. *Journal of the American Chemical Society* **2014**, 136, 5229–5232.
- [132] Morita, M.; Iwakura, C.; Tamura, H. *Electrochimica Acta* **1979**, 24, 357–362.
- [133] Suntivich, J.; Gasteiger, H. A.; Yabuuchi, N.; Shao-Horn, Y. *Journal of The Electrochemical Society* **2010**, 157, B1263.
- [134] Ashton, S. J.; Arenz, M. *Journal of Power Sources* **2012**, 217, 392–399.
- [135] Fabbri, E.; Nachttegaal, M.; Cheng, X.; Schmidt, T. J. *Advanced Energy Materials* **2015**, 5, 1402033.
- [136] Maiyalagan, T.; Chemelewski, K. R.; Manthiram, A. *ACS Catalysis* **2014**, 4, 421–425.
- [137] Stoerzinger, K. A.; Choi, W. S.; Jeen, H.; Lee, H. N.; Shao-Horn, Y. *The Journal of Physical Chemistry Letters* **2015**, 6, 487–492.
- [138] Markovic, N. M.; Gasteiger, H. A.; Ross, P. N. *The Journal of Physical Chemistry* **1996**, 100, 6715–6721.
- [139] Paulus, U.; Schmidt, T.; Gasteiger, H.; Behm, R. *Journal of Electroanalytical Chemistry* **2001**, 495, 134–145.
- [140] Hu, Y.; Tolmachev, Y. V.; Scherson, D. A. *Journal of Electroanalytical Chemistry* **1999**, 468, 64–69.
- [141] Gao, Q.; Ranjan, C.; Pavlovic, Z.; Blume, R.; Schlögl, R. *ACS Catalysis* **2015**, 5, 7265–7275.
- [142] Miyahara, Y.; Miyazaki, K.; Fukutsuka, T.; Abe, T. *Journal of the Electrochemical Society* **2014**, 161, F694–F697.

- [143] Izumi, M.; Konishi, Y.; Nishihara, T.; Hayashi, S.; Shinohara, M.; Kawasaki, M.; Tokura, Y. *Applied Physics Letters* **1998**, *73*, 2497–2499.
- [144] Sirena, M.; Steren, L.; Guimpel, J. *Thin Solid Films* **2000**, *373*, 102–106.
- [145] Stoerzinger, K. A.; Risch, M.; Suntivich, J.; Lü, W. M.; Zhou, J.; Biegalski, M. D.; Christen, H. M.; Ariando,; Venkatesan, T.; Shao-Horn, Y. *Energy & Environmental Science* **2013**, *6*, 1582.
- [146] Mori, M.; Hiei, Y.; Sammes, N. M.; Tompsett, G. A. *Journal of The Electrochemical Society* **2000**, *147*, 1295.
- [147] Trasatti, S.; Petrii, O. *Journal of Electroanalytical Chemistry* **1992**, *327*, 353–376.
- [148] Nečas, D.; Klapetek, P. *Open Physics* **2012**, *10*, 181–188.
- [149] Wagner, C. In *Applied Surface Analysis*; Barr, T. L., Davis, I. E., Eds.; ASTM International: 100 Barr Harbor Drive, PO Box C700, West Conshohocken, PA 19428-2959, 1980; pp 137–137–11.
- [150] Savitzky, A.; Golay, M. J. E. *Analytical Chemistry* **1964**, *36*, 1627–1639.
- [151] Li, D.; Wang, C.; Strmcnik, D. S.; Tripkovic, D. V.; Sun, X.; Kang, Y.; Chi, M.; Snyder, J. D.; van der Vliet, D.; Tsai, Y.; Stamenkovic, V. R.; Sun, S.; Markovic, N. M. *Energy Environ. Sci.* **2014**, *7*, 4061–4069.
- [152] Zemni, S.; Dhahri, J.; Cherif, K.; Dhahri, J.; Oummezzine, M.; Ghedira, M.; Vincent, H. *Journal of Solid State Chemistry* **2004**, *177*, 2387–2393.
- [153] Aruta, C.; Ghiringhelli, G.; Tebano, A.; Boggio, N. G.; Brookes, N. B.; Medaglia, P. G.; Balestrino, G. *Physical Review B* **2006**, *73*, 235121.
- [154] Méchin, L.; Wu, S.; Guillet, B.; Perna, P.; Fur, C.; Lebargy, S.; Adamo, C.; Schlom, D. G.; Routoure, J. M. *Journal of Physics D: Applied Physics* **2013**, *46*, 202001.
- [155] Mitchell, R. H.; Chakhmouradian, A. R.; Woodward, P. M. *Physics and Chemistry of Minerals* **2000**, *27*, 583–589.
- [156] Stoerzinger, K. A.; Lü, W.; Li, C.; Ariando,; Venkatesan, T.; Shao-Horn, Y. *The Journal of Physical Chemistry Letters* **2015**, *6*, 1435–1440.

-
- [157] Memming, R. *Semiconductor Electrochemistry*; John Wiley & Sons, 2015.
- [158] Giancoli, D. C. *Prentice Hall, 4th edition*; Prentice Hall, 1995.
- [159] Zouari, A.; Boudaya, C.; Dhahri, E. *physica status solidi (a)* **2001**, *188*, 1177–1186.
- [160] Nicholson, R. S.; Shain, I. *Analytical Chemistry* **1964**, *36*, 706–723.
- [161] Pharr, C. M.; Griffiths, P. R. *Analytical Chemistry* **1997**, *69*, 4673–4679.
- [162] Petrovic, S. *The Chemical Educator* **2000**, *5*, 231–235.
- [163] Lin, K.; Chen, Q.; Gerhardt, M. R.; Tong, L.; Kim, S. B.; Eisenach, L.; Valle, A. W.; Hardee, D.; Gordon, R. G.; Aziz, M. J.; Marshak, M. P. *Science* **2015**, *349*, 1529–1532.
- [164] Goldstein, E.; Van de Mark, M. *Electrochimica Acta* **1982**, *27*, 1079–1085.
- [165] Bott, A. W.; Jackson, B. P. *Current Separations* **1996**, *15:1*, 25–30.
- [166] Arvíá, A.; Marchiano, S.; Podestá, J. *Electrochimica Acta* **1967**, *12*, 259–266.
- [167] Lu, H.; George, T. A.; Wang, Y.; Ketsman, I.; Burton, J. D.; Bark, C.-W.; Ryu, S.; Kim, D. J.; Wang, J.; Binek, C.; Dowben, P. A.; Sokolov, A.; Eom, C.-B.; Tsymbal, E. Y.; Gruverman, A. *Applied Physics Letters* **2012**, *100*, 232904.
- [168] Lodi, G.; Sivieri, E.; De Battisti, A.; Trasatti, S. *Journal of Applied Electrochemistry* **1978**, *8*, 135–143.
- [169] Brown, A. P.; Krumpelt, M.; Loutfy, R.; Yao, N. *Electrochimica Acta* **1982**, *27*, 557–560.
- [170] Stoerzinger, K. A.; Hong, W. T.; Azimi, G.; Giordano, L.; Lee, Y.-L.; Crumlin, E. J.; Biegalski, M. D.; Bluhm, H.; Varanasi, K. K.; Shao-Horn, Y. *The Journal of Physical Chemistry C* **2015**, *119*, 18504–18512.
- [171] Lide, D. R. *CRC Handbook of Chemistry and Physics*; 2007; p 47.
- [172] Lambert, I.; Clever, H. L. *Alkaline Earth Hydroxides in Water and Aqueous Solutions*; 1992; Vol. 52; p 388.
- [173] Connell, J. G.; Isaac, B. J.; Ekanayake, G. B.; Strachan, D. R.; Seo, S. S. A. *Applied Physics Letters* **2012**, *101*, 251607.

- [174] Ngai, J. H.; Schwendemann, T. C.; Walker, A. E.; Segal, Y.; Walker, F. J.; Altman, E. I.; Ahn, C. H. *Advanced Materials* **2010**, 22, 2945–2948.
- [175] Hem, J. D. *Chemical Equilibria and Rates of Manganese Oxidation*; 1963; p 71.
- [176] Kröger, F.; Vink, H. *Journal of Physics and Chemistry of Solids* **1958**, 5, 208–223.
- [177] Ebel, H.; Pöhn, C.; Svagera, R.; Wernle, M.; Ebel, M.; Jabłonski, A. *Journal of Electron Spectroscopy and Related Phenomena* **1990**, 50, 109–116.
- [178] Satpathy, S.; Popović, Z. S.; Vukajlović, F. R. *Physical Review Letters* **1996**, 76, 960–963.
- [179] Scholz, J.; Risch, M.; Stoerzinger, K. A.; Wartner, G.; Shao-Horn, Y.; Jooss, C. *The Journal of Physical Chemistry C* **2016**, 120, 27746–27756.
- [180] Calle-Vallejo, F.; Inoglu, N. G.; Su, H.-Y.; Martínez, J. I.; Man, I. C.; Koper, M. T. M.; Kitchin, J. R.; Rossmeisl, J. *Chemical Science* **2013**, 4, 1245.
- [181] Lee, Y.-L.; Gadre, M. J.; Shao-Horn, Y.; Morgan, D. *Phys. Chem. Chem. Phys.* **2015**, 17, 21643–21663.
- [182] Jalili, H.; Han, J. W.; Kuru, Y.; Cai, Z.; Yildiz, B. *Journal of Physical Chemistry Letters* **2011**, 2, 801–807.
- [183] Petrie, J. R.; Cooper, V. R.; Freeland, J. W.; Meyer, T. L.; Zhang, Z.; Lutterman, D. A.; Lee, H. N. *Journal of the American Chemical Society* **2016**, 138, 2488–2491.
- [184] Augustynski, J.; Koudelka, M.; Sanchez, J.; Conway, B. *Journal of Electroanalytical Chemistry and Interfacial Electrochemistry* **1984**, 160, 233–248.
- [185] Goniakowski, J.; Finocchi, F.; Noguera, C. *Reports on Progress in Physics* **2008**, 71, 016501.
- [186] Strmcnik, D.; Li, D.; Lopes, P. P.; Tripkovic, D.; Kodama, K.; Stamenkovic, V. R.; Markovic, N. M. *Topics in Catalysis* **2015**, 58, 1174–1180.
- [187] Jeen, H.; Bi, Z.; Choi, W. S.; Chisholm, M. F.; Bridges, C. A.; Paranthaman, M. P.; Lee, H. N. *Advanced Materials* **2013**, 25, 6459–6463.

- [188] Chang, S. H.; Danilovic, N.; Chang, K.-c.; Subbaraman, R.; Paulikas, A. P.; Fong, D. D.; Highland, M. J.; Baldo, P. M.; Stamenkovic, V. R.; Freeland, J. W.; Eastman, J. A.; Markovic, N. M. *Nature Communications* **2014**, *5*, 1–9.
- [189] Ifland, B.; Hoffmann, J.; Kramer, T.; Scherff, M.; Mildner, S.; Jooss, C. *Journal of Nanomaterials* **2015**, *2015*, 1–12.
- [190] Grundy, A. N.; Hallstedt, B.; Gauckler, L. J. *Calphad* **2004**, *28*, 191–201.
- [191] Töpfer, J.; Goodenough, J. B. *Chemistry of Materials* **1997**, *9*, 1467–1474.
- [192] Paterson, J. H.; Krivanek, O. L. *Ultramicroscopy* **1990**, *32*, 319–325.
- [193] Rask, J. H.; Miner, B. A.; Buseck, P. R. *Ultramicroscopy* **1987**, *21*, 321–326.
- [194] Riedl, T.; Gemming, T.; Gruner, W.; Acker, J.; Wetzig, K. *Micron* **2007**, *38*, 224–230.
- [195] Varela, M.; Oxley, M. P.; Luo, W.; Tao, J.; Watanabe, M.; Lupini, A. R.; Pantelides, S. T.; Pennycook, S. J. *Physical Review B* **2009**, *79*, 085117.
- [196] Nishida, S.; Kobayashi, S.; Kumamoto, A.; Ikeno, H.; Mizoguchi, T.; Tanaka, I.; Ikuhara, Y.; Yamamoto, T. *Journal of Applied Physics* **2013**, *114*, 054906.
- [197] Norpoth, J.; Mildner, S.; Scherff, M.; Hoffmann, J.; Jooss, C. *Nanoscale* **2014**, *6*, 9852–9862.
- [198] Ramírez, A.; Hillebrand, P.; Stellmach, D.; May, M. M.; Bogdanoff, P.; Fiechter, S. *The Journal of Physical Chemistry C* **2014**, *118*, 14073–14081.
- [199] Shannon, R. D. *Acta Crystallographica Section A* **1976**, *32*, 751–767.
- [200] Berardi, S.; Drouet, S.; Francàs, L.; Gimbert-Suriñach, C.; Guttentag, M.; Richmond, C.; Stoll, T.; Llobet, A. *Chem. Soc. Rev.* **2014**, *43*, 7501–7519.
- [201] Kärkäs, M. D.; Liao, R.-Z.; Laine, T. M.; Åkerman, T.; Ghanem, S.; Siegbahn, P. E. M.; Åkerman, B. *Catal. Sci. Technol.* **2016**, *6*, 1306–1319.
- [202] Joya, K. S.; Joya, Y. F.; Ocakoglu, K.; van de Krol, R. *Angewandte Chemie International Edition* **2013**, *52*, 10426–10437.
- [203] Wen, F.; Li, C. *Accounts of chemical research* **2013**, *46*, 2355–2364.

- [204] Kalyanasundaram, K.; Graetzel, M. *Current opinion in Biotechnology* **2010**, *21*, 298–310.
- [205] Lewis, N. S.; Nocera, D. G. *Proceedings of the National Academy of Sciences* **2006**, *103*, 15729–15735.
- [206] Prévot, M. S.; Sivula, K. *The Journal of Physical Chemistry C* **2013**, *117*, 17879–17893.
- [207] Dau, H.; Zaharieva, I. *Accounts of chemical research* **2009**, *42*, 1861–1870.
- [208] Kang, D.; Kim, T. W.; Kubota, S. R.; Cardiel, A. C.; Cha, H. G.; Choi, K.-S. *Chemical Reviews* **2015**, *115*, 12839–12887.
- [209] Parent, A. R.; Sakai, K. *ChemSusChem* **2014**, *7*, 2070–2080.
- [210] Dismukes, G. C.; Brimblecombe, R.; Felton, G. A.; Pryadun, R. S.; Sheats, J. E.; Spiccia, L.; Swiegers, G. F. *Accounts of Chemical Research* **2009**, *42*, 1935–1943.
- [211] Artero, V.; Chavarot-Kerlidou, M.; Fontecave, M. *Angewandte Chemie International Edition* **2011**, *50*, 7238–7266.
- [212] Kanan, M. W.; Surendranath, Y.; Nocera, D. G. *Chemical Society Reviews* **2009**, *38*, 109–114.
- [213] Najafpour, M. M.; Renger, G.; Hołyńska, M.; Moghaddam, A. N.; Aro, E.-M.; Carpentier, R.; Nishihara, H.; Eaton-Rye, J. J.; Shen, J.-R.; Al-lakhverdiev, S. I. *Chemical reviews* **2016**, *116*, 2886–2936.
- [214] Sala, X.; Maji, S.; Bofill, R.; García-Antón, J.; Escriche, L.; Llobet, A. *Accounts of chemical research* **2013**, *47*, 504–516.
- [215] Karkas, M. D.; Verho, O.; Johnston, E. V.; Åkermark, B. *Chemical reviews* **2014**, *114*, 11863–12001.
- [216] Hetterscheid, D. G.; Reek, J. N. *Angewandte Chemie International Edition* **2012**, *51*, 9740–9747.
- [217] Blakemore, J. D.; Crabtree, R. H.; Brudvig, G. W. *Chemical reviews* **2015**, *115*, 12974–13005.
- [218] Duan, L.; Wang, L.; Li, F.; Li, F.; Sun, L. *Accounts of Chemical Research* **2015**, *48*.

- [219] Kaveevivitchai, N.; Chitta, R.; Zong, R.; El Ojaimi, M.; Thummel, R. P. *Journal of the American Chemical Society* **2012**, *134*, 10721–10724.
- [220] Gilbert, J. A.; Eggleston, D. S.; Murphy, W. R.; Geselowitz, D. A.; Gersten, S. W.; Hodgson, D. J.; Meyer, T. J. *Journal of the American Chemical Society* **1985**, *107*, 3855–3864.
- [221] Concepcion, J. J.; Jurss, J. W.; Templeton, J. L.; Meyer, T. J. *Journal of the American Chemical Society* **2008**, *130*, 16462–16463.
- [222] Zong, R.; Thummel, R. P. *Journal of the American Chemical Society* **2005**, *127*, 12802–12803.
- [223] Staehle, R.; Tong, L.; Wang, L.; Duan, L.; Fischer, A.; Ahlquist, M. S.; Sun, L.; Rau, S. *Inorganic chemistry* **2014**, *53*, 1307–1319.
- [224] Tong, L.; Inge, A. K.; Duan, L.; Wang, L.; Zou, X.; Sun, L. *Inorganic chemistry* **2013**, *52*, 2505–2518.
- [225] Sens, C.; Romero, I.; Rodríguez, M.; Llobet, A.; Parella, T.; Benet-Buchholz, J. *Journal of the American Chemical Society* **2004**, *126*, 7798–7799.
- [226] Bozoglian, F.; Romain, S.; Ertem, M. Z.; Todorova, T. K.; Sens, C.; Mola, J.; Rodriguez, M.; Romero, I.; Benet-Buchholz, J.; Fontrodona, X.; Cramer, C. J.; Gagliardi, L.; Llobet, A. *Journal of the American Chemical Society* **2009**, *131*, 15176–15187.
- [227] Sander, A. C.; Maji, S.; Francàs, L.; Böhnisch, T.; Dechert, S.; Llobet, A.; Meyer, F. *ChemSusChem* **2015**, *8*, 1697–1702.
- [228] Romain, S.; Bozoglian, F.; Sala, X.; Llobet, A. *Journal of the American Chemical Society* **2009**, *131*, 2768–2769.
- [229] Duan, L.; Bozoglian, F.; Mandal, S.; Stewart, B.; Privalov, T.; Llobet, A.; Sun, L. *Nature Chemistry* **2012**, *4*, 418–423.
- [230] Fan, K.; Li, F.; Wang, L.; Daniel, Q.; Chen, H.; Gabrielsson, E.; Sun, J.; Sun, L. *ChemSusChem* **2015**, *8*, 3242–3247.
- [231] Li, F.; Zhang, B.; Li, X.; Jiang, Y.; Chen, L.; Li, Y.; Sun, L. *Angewandte Chemie International Edition* **2011**, *50*, 12276–12279.

- [232] Li, F.; Li, L.; Tong, L.; Daniel, Q.; Göthelid, M.; Sun, L. *Chem. Commun.* **2014**, 50, 13948–13951.
- [233] Ashford, D. L.; Lapidés, A. M.; Vannucci, A. K.; Hanson, K.; Torelli, D. A.; Harrison, D. P.; Templeton, J. L.; Meyer, T. J. *Journal of the American Chemical Society* **2014**, 136, 6578–6581.
- [234] Chen, Z.; Concepcion, J. J.; Jurss, J. W.; Meyer, T. J. *Journal of the American Chemical Society* **2009**, 131, 15580–15581.
- [235] Chen, Z.; Concepcion, J. J.; Luo, H.; Hull, J. F.; Paul, A.; Meyer, T. J. *Journal of the American Chemical Society* **2010**, 132, 17670–17673.
- [236] Gao, Y.; Ding, X.; Liu, J.; Wang, L.; Lu, Z.; Li, L.; Sun, L. *Journal of the American Chemical Society* **2013**, 135, 4219–4222.
- [237] Yu, Z.; Li, F.; Sun, L. *Energy & Environmental Science* **2015**, 8, 760–775.
- [238] Ashford, D. L.; Gish, M. K.; Vannucci, A. K.; Brennaman, M. K.; Templeton, J. L.; Papanikolas, J. M.; Meyer, T. J. *Chemical reviews* **2015**, 115, 13006–13049.
- [239] Willkomm, J.; Muresan, N. M.; Reisner, E. *Chemical Science* **2015**, 6, 2727–2736.
- [240] Reynal, A.; Lakadamyali, F.; Gross, M. A.; Reisner, E.; Durrant, J. R. *Energy & Environmental Science* **2013**, 6, 3291–3300.
- [241] Hoertz, P. G.; Chen, Z.; Kent, C. A.; Meyer, T. J. *Inorganic Chemistry* **2010**, 49, 8179–8181.
- [242] Kato, M.; Cardona, T.; Rutherford, A. W.; Reisner, E. *Journal of the American Chemical Society* **2012**, 134, 8332–8335.
- [243] Norris, M. R.; Concepcion, J. J.; Fang, Z.; Templeton, J. L.; Meyer, T. J. *Angewandte Chemie International Edition* **2013**, 52, 13580–13583.
- [244] Alibabaei, L.; Brennaman, M. K.; Norris, M. R.; Kalanyan, B.; Song, W.; Losego, M. D.; Concepcion, J. J.; Binstead, R. A.; Parsons, G. N.; Meyer, T. J. *Proceedings of the National Academy of Sciences* **2013**, 110, 20008–20013.

- [245] Steinert, M. Defektgitter und Gitterkomplexe - Einflüsse von Gegenionen und Lösungsmitteln auf ihre magnetischen Eigenschaften. Ph.D. thesis, Georg-August-University Göttingen, 2016.
- [246] Odrobina, J. . Ph.D. thesis, Georg-August-University Göttingen, 2017.
- [247] Macyk, W.; Szaciłowski, K.; Stochel, G.; Buchalska, M.; Kuncewicz, J.; Łabuz, P. *Coordination Chemistry Reviews* **2010**, *254*, 2687–2701.
- [248] Weroński, P.; Nosek, M.; Batys, P. *Journal of Chemical Physics* **2013**, *124*705.
- [249] Shen, J.; Adnot, A.; Kaliaguine, S. *Applied surface science* **1991**, *51*, 47–60.
- [250] Francàs, L.; Richmond, C.; Garrido-Barros, P.; Planas, N.; Roeser, S.; Benet-Buchholz, J.; Escriche, L.; Sala, X.; Llobet, A. *Chemistry - A European Journal* **2016**, *22*.
- [251] Mola, J.; Mas Marza, E.; Sala, X.; Romero, I.; Rodríguez, M.; Viñas, C.; Parella, T.; Llobet, A. *Angewandte Chemie* **2008**, *120*, 5914–5916.
- [252] Creus, J.; Matheu, R.; Peñafiel, I.; Moonshiram, D.; Blondeau, P.; Benet-Buchholz, J.; García-Antón, J.; Sala, X.; Godard, C.; Llobet, A. *Angewandte Chemie International Edition* **2016**, *55*, 15382–15386.
- [253] Song, W.; Glasson, C. R.; Luo, H.; Hanson, K.; Brennaman, M. K.; Concepcion, J. J.; Meyer, T. J. *The Journal of Physical Chemistry Letters* **2011**, *2*, 1808–1813.
- [254] Wang, L.; Ashford, D. L.; Thompson, D. W.; Meyer, T. J.; Papanikolas, J. M. *The Journal of Physical Chemistry C* **2013**, *117*, 24250–24258.
- [255] Li, F.; Li, L.; Tong, L.; Daniel, Q.; Göthelid, M.; Sun, L. *Chem. Commun.* **2014**, *50*, 13948–13951.
- [256] Zhang, L.; Gao, Y.; Ding, X.; Yu, Z.; Sun, L. *ChemSusChem* **2014**, *7*.
- [257] Fan, K.; Li, F.; Wang, L.; Daniel, Q.; Gabrielsson, E.; Sun, L. *Physical Chemistry Chemical Physics* **2014**, *16*, 25234–25240.
- [258] Wang, L.; Fan, K.; Daniel, Q.; Duan, L.; Li, F.; Philippe, B.; Rensmo, H.; Chen, H.; Sun, J.; Sun, L. *Chemical Communications* **2015**, *51*, 7883–7886.
- [259] Bonke, S. A.; Wiechen, M.; MacFarlane, D. R.; Spiccia, L. *Energy Environ. Sci.* **2015**, *8*, 2791–2796.

- [260] Verlage, E.; Hu, S.; Liu, R.; Jones, R. J. R.; Sun, K.; Xiang, C.; Lewis, N. S.; Atwater, H. A. *Energy Environ. Sci.* **2015**, *8*, 3166–3172.
- [261] Reece, S. Y.; Hamel, J. a.; Sung, K.; Jarvi, T. D.; Esswein, a. J.; Pijpers, J. J. H.; Nocera, D. G. *Science* **2011**, *334*, 645–648.
- [262] Lutterman, D. A.; Surendranath, Y.; Nocera, D. G. *Journal of the American Chemical Society* **2009**, *131*, 3838–3839.
- [263] Shaffer, D. W.; Xie, Y.; Szalda, D. J.; Concepcion, J. J. *Inorganic Chemistry* **2016**, *55*, 12024–12035.
- [264] Duan, L.; Wang, L.; Inge, A. K.; Fischer, A.; Zou, X.; Sun, L. *Inorganic Chemistry* **2013**, *52*, 7844–7852.
- [265] Collin, J.; Sauvage, J. P. *Inorganic Chemistry* **1986**, *25*, 135–141.
- [266] Liu, F.; Cardolaccia, T.; Hornstein, B. J.; Schoonover, J. R.; Meyer, T. J. *Journal of the American Chemical Society* **2007**, *129*, 2446–2447.
- [267] Concepcion, J. J.; Jurss, J. W.; Hoertz, P. G.; Meyer, T. J. *Angewandte Chemie International Edition* **2009**, *48*, 9473–9476.
- [268] Sugiyama, K.; Ishii, H.; Ouchi, Y.; Seki, K. *Journal of Applied Physics* **2000**, *87*, 295–298.
- [269] Sheehan, S. W.; Thomsen, J. M.; Hintermair, U.; Crabtree, R. H.; Brudvig, G. W.; Schmittenmaer, C. a. *Nature Communications* **2015**, *6*, 6469.
- [270] Odrobina, J.; Scholz, J.; Pannwitz, A.; Francàs, L.; Dechert, S.; Llobet, A.; Jooss, C.; Meyer, F. *ACS Catalysis* **2017**, *7*, 2116–2125.
- [271] Brandes, J. A.; Ingall, E.; Paterson, D. *Marine Chemistry* **2007**, *103*, 250–265.
- [272] Engemann, C.; Franke, R.; Hormes, J.; Lauterbach, C.; Hartmann, E.; Clade, J.; Jansen, M. *Chemical physics* **1999**, *243*, 61–75.
- [273] Myneni, S. *Reviews in Mineralogy and Geochemistry* **2002**, *49*, 485–579.
- [274] Rouff, A. A.; Rabe, S.; Nachtegaal, M.; Vogel, F. *The Journal of Physical Chemistry A* **2009**, *113*, 6895–6903.

-
- [275] Gabrielsson, E.; Tian, H.; Eriksson, S. K.; Gao, J.; Chen, H.; Li, F.; Oscarsson, J.; Sun, J.; Rensmo, H.; Kloo, L. *Chemical Communications* **2015**, 51, 3858–3861.
- [276] Materna, K. L.; Crabtree, R. H.; Brudvig, G. W. *Chemical Society Reviews* **2017**, 46, 6099–6110.
- [277] Rosser, T. E.; Reisner, E. *ACS Catalysis* **2017**, 7, 3131–3141.
- [278] Sheng, W.; Gasteiger, H. A.; Shao-Horn, Y. *Journal of The Electrochemical Society* **2010**, 157, B1529.
- [279] Urushibara, A.; Moritomo, Y.; Arima, T.; Asamitsu, A.; Kido, G.; Tokura, Y. *Physical Review B* **1995**, 51, 14103–14109.
- [280] Davis, R. E.; Horvath, G. L.; Tobias, C. W. *Electrochemistry* **1967**, 12, 287–297.
- [281] Tang, R.; Nie, Y.; Kawasaki, J. K.; Kuo, D.-y.; Petretto, G.; Rignanes, G.-m.; Shen, K. M.; Schlom, D. G.; Suntivich, J. *Journal of Materials Chemistry A* **2016**,
- [282] Evans, I.; Spencer, A.; Wilkinson, G. *Dalton Trans* **1973**, 204.
- [283] Szörényi, T.; Laude, L.; Bertoti, I.; Kantor, Z.; Geretovszky, Z. *Journal of Applied Physics* **1995**, 78, 6211–6219.
- [284] Murthi, V. S.; Urian, R. C.; Mukerjee, S. *The Journal of Physical Chemistry B* **2004**, 108, 11011–11023.
- [285] Geng, D.; Chen, Y.; Chen, Y.; Li, Y.; Li, R.; Sun, X.; Ye, S.; Knights, S. *Energy & Environmental Science* **2011**, 4, 760.

Author contributions

The presented thesis consists of four chapters based on the following publications and one manuscript prepared for submission:

1. Chapter 3: *Rotating Ring-Disk Electrode Study of Oxygen Evolution at a Perovskite Surface: Correlating Activity to Manganese Concentration*, J. Phys. Chem. C **120** (49), 2016
2. Chapter 4: *Tailoring the Oxygen Evolution Activity and Stability Using Defect Chemistry*, Catalysts **7** (5), 2017
3. Chapter 5: *Backbone Immobilization of the Bis(bipyridyl)pyrazolate Diruthenium Catalyst for Electrochemical Water Oxidation*, ACS catalysis **7** (3), 2017
4. Chapter 6: *Chasing the Achilles' Heel in Hybrid Systems of Diruthenium Water Oxidation Catalysts Anchored on Indium Tin Oxide: the Stability of the Anchor*, ACS catalysis **7**, (9), 2017

All articles present original research of the author. The research for the article published in the Journal of physical chemistry C was performed in collaboration to the Electrochemical Energy Lab at the Massachusetts Institute of Technology (MIT) led by Prof. Yang Shao-Horn. Both the research of chapter 5 and chapter 6 was performed in close collaboration to the group of Franc Meyer in the inorganic chemistry department and their experimental facilities. Furthermore, the XAS measurements displayed in chapter 6 were performed at the 9-BM-B beamline station at the Advanced Photon Source (ALS) in Chicago. All collaborators are listed as coauthors of the respective articles. The disclosure of the authors contributions will be listed in the following for each article.

All samples investigated in chapter 3 were prepared by the author according to the electrode design of the author. The structural characterization including AFM, XRD, XRR, and SEM analysis was performed by the author. The electrochemical measurements were executed according to identical protocols by Marcel Risch at MIT and by the author in Göttingen. The measurements of the surface composition by XPS was performed by Kelsey Stoerzinger supported by Magali Gauthier at MIT. The analysis of the XPS measurements

was performed by Kelsey Stoerzinger and Marcel Risch. Furthermore, Marcel Risch, Christian Jooß, Kelsey Stoerzinger and Yang Shao-Horn have contributed to the interpretation and the writing of the manuscript. The main parts of the manuscript have been prepared by the author.

For chapter 4 Garlef Wartner prepared the samples, performed the X-ray diffraction measurements and the electrochemical measurements together with the author. AFM measurements and their analysis was executed by the author. Christoph Luderer and Vladimir Roddatis conducted the TEM experiments including the preparation and the analysis of the data. The planning of the experiments was done by Christian Jooß together with the author. The interpretation and writing of the manuscript was performed by Christian Jooß, Marcel Risch and the author.

The synthesis of the various molecular complexes and their structural analysis representing the central material component of chapter 5 and 6 was performed by Jann Odrobina in the group of Franc Meyer. The synthetic route for bbp-Ru₂ complex with the carboxylate anchor was the result of the Master thesis of Andrea Pannwitz. The further development of the synthetic route for the phosphonate and biscarboxylate anchor was done by Jann Odrobina. Sebastian Dechert contributed the X-ray crystallography for all investigated molecular complexes. Furthermore homogeneous and quiescent electrochemical measurements on commercially available ITO samples was performed by Jann Odrobina. The preparation of the samples for RRDE measurements and their electrochemical characterization was performed by the author. The XPS measurements and analysis was performed by the author, XAS measurements and analysis were conducted by Marcel Risch at the facilities of ALS. Antoni Llobet, Franc Meyer, and Christian Jooß contributed in the interpretation and the composition of the manuscript. The main parts of the article were prepared by Jann Odrobina and the author.

The transient absorption spectroscopy displayed in the appendix was conducted by Jennifer Ahrens in the group of Dirk Schwarzer at the Max-Planck Institute for Biophysical chemistry in Göttingen on samples prepared by the author.

Acknowledgment

For this thesis has not been the work of one but the effort of many and would not have been possible without the help and the support of others along the way this is the time to express my gratitude. First, I want to thank my adviser Prof. Christian Jooß for his support at all times providing me with the freedom and the resources to follow my ideas along with the encouraging and lively discussion within and outside the field of science. Only his broad support and the discussions challenging to push the project further made the thesis possible.

Due to the interdisciplinary nature of this thesis, special thank is owed to Prof. Franc Meyer not only for helping as a co-adviser but also for his discussion challenging my physical point of view and broadening my knowledge.

In addition, my thank goes to Prof. Sven Schneider who kindly agreed to co-referee this thesis.

Since part of this work was done during a research scholarship at MIT my thank goes to Prof. Yang Shao-Horn for giving me the opportunity to experience the unique and inspiring world at MIT. Needless to say that the gratitude extends to the friends and colleagues who made this time truly special. Among them Marcel Risch needs to be highlighted as he continued to teach me numerous things on both sides of the Atlantic from electrochemistry to the value of Hawaiian shirt friday. As this scholarship and the whole thesis was financed by the DFG and the collaborative research center (CRC) 1073 I would like to express my thank for the funding.

But not only my colleagues and friends at MIT deserve my gratitude. The time in Göttingen and the work at the IMP would not have been the same without my colleagues and friends. And there are many to thank for but first and, in light of this thesis, foremost Jann Odrobina. Your part in all this cannot be emphasized enough, thank you for everything! You made this not only possible but more importantly a truly inspiring and great time bringing physics and chemistry together whether in the lab or at the brew kettle.

Besides him I need to thank my former Bachelor and Master student namely Kai-Moritz Kumkar, Garlef Wartner, and Christoph Luderer which directly and indirectly helped to push this thesis forward; along with Jörg Hoffmann, Malte Scherff, Stephanie Mildner, Benedikt Iland, Birte Kressdorf and the others who helped to create the vivid, friendly working atmosphere and always had encouraging words when things were not working out as they were intended. And a special thanks to all the additional set of eyes for the final proofreading in par-

ticular as many of you so kindly agreed on very short notice.

Last but not least my parents deserve my greatest gratitude for the generous support throughout my studies enabling me to follow this pursue and teaching me the value of hard work. And lastly my thank belongs to Leonie who was the greatest motivator, cheerleader and through all ups and downs this journey entailed.